Synthesis and Properties of New Oxychalcogenide Materials

FREE, DAVID,GEORGE

Abstract

"Synthesis and Properties of New Oxychalcogenide Materials"

Ph.D. Thesis David G. Free December 2010

Chapter 1 gives a brief review of oxychalcogenide materials and their properties, particularly those with structures similar to systems discussed in the later chapters. Particular attention is paid to the structural and magnetic properties of $La_2O_2Fe_2OSe_2$-type materials, work on which is presented in chapters 3–5. These oxychalcogenides, along with ZrCuSiAs-related materials, are of interest due to their potentially interesting magnetic and conducting properties. In particular they are close relatives of the LaOFeAs superconductors.

Chapter 2 describes the synthetic and analytical techniques used in this project. The theory behind the powder diffraction techniques used throughout is described, and information on specific methodology used in the data collections and analysis of this work is given. SQUID magnetometry is also discussed.

Chapter 3 discusses the variable temperature structural and magnetic properties of $La_2O_2Mn_2OSe_2$ and $Pr_2O_2Mn_2OSe_2$, as well as those of the newly prepared material $Ce_2O_2Mn_2OSe_2$. These materials are observed to undergo a phase transition on cooling revealed by a change in the thermal expansion of the *c* cell parameter, and show evidence for the static disorder of oxide ions from the $[Mn_2O]^{2+}$ plane below this temperature. $Pr_2O_2Mn_2OSe_2$ is also shown to undergo a further transition on cooling below 36 K to an orthorhombic unit cell. Neutron diffraction data have also shown that the Mn^{2+} moments in these materials order with an AFM1 structure on cooling below ~180 K.

Chapter 4 describes the study of both $La_2O_2Fe_2OS_2$ and $La_2O_2Fe_2OSe_2$ by variable temperature neutron powder diffraction. These materials have been demonstrated to order with an AFM3 structure on cooling below ~100 K, which is coincident with a subtle structural change observed in the thermal expansion of the *a* cell parameter. The unexpected adoption of the AFM3 magnetic structure is discussed in relation to structurally similar iron-based superconductors.

Chapter 5 presents the synthesis of several new $La_2O_2Fe_2OSe_2$-type materials, and the magnetic structure of $La_2O_2Co_2OSe_2$. The stability range over which these materials form is discussed with respect to the size of the metal ions present. A comparison of the structural properties of all the $A_2O_2M_2OSe_2$ materials is given and the various magnetic structures they adopt discussed.

Chapter 6 reports the synthesis of a new family of transition metal oxychalcogenides (β-$La_2O_2MnSe_2$). Their structure has been solved from laboratory X-ray diffraction data, using a combination of charge-flipping and direct methods, and confirmed by neutron diffraction. Variable temperature structural properties are discussed and show these materials undergo a phase transition on cooling associated with ordering of transition metal ions. SQUID magnetometry and neutron powder diffraction have both demonstrated these materials order antiferromagnetically at low temperatures.

Chapter 7 describes the synthesis of two new ZrCuSiAs-related transition metal containing oxychalcogenides: $Ce_2O_2FeSe_2$ and $La_2O_2ZnSe_2$. The structure solution of $Ce_2O_2FeSe_2$ by charge-flipping is reported, alongside the determination of the magnetic structure from neutron powder diffraction data collected at 12 K. The variable temperature structural properties of $La_2O_2ZnSe_2$ are also reported.

Synthesis and Properties of New Oxychalcogenide Materials

David G. Free, M.Chem. (Dunelm)
Collingwood College
Durham University

Supervisor: Prof. John S. O. Evans

A thesis submitted in partial fulfilment of the requirements for the degree of Doctor of Philosophy.

Department of Chemistry
Durham University
2010

Contents

Abbreviations

ADP	Anisotropic thermal displacement parameter
AFM	Antiferromagnetic
bs	Backscattering
CCR	Closed circuit refrigerator
CIF	Crystallographic information file
DFT	Density functional theory
FC	Field cooled
FM	Ferromagnetic
GGA	Generalised gradient approximation
GSAS	General structure analysis system
HRPD	High resolution powder diffractometer
ICSD	Inorganic crystal structure database
IPNS	Intense pulsed neutron source
irrep	Irreducible representation
LSDA	Local spin-density approximation
MPMS	Magnetic properties measurement system
n.n.	Nearest-neighbour
n.n.n.	Next-nearest-neighbour
RMM	Relative molecular mass
R_{wp}	Weighted *R*-factor
SARAh	Simulated annealing and representational analysis
SEPD	Special environment powder diffractometer
SQUID	Superconducting quantum interference device
TA	TOPAS Academic
TOF	Time-of-flight
VT	Variable temperature
XRD	X-ray diffraction
XRPD	X-ray powder diffraction
ZFC	Zero-field cooled

Declaration & Statement of Copyright

The work described in this thesis is entirely my own, except where I have acknowledged help from, or collaboration with, a named person, or given reference to a published source or thesis. Aspects of research on the materials described in chapters 6 and 7 were performed with Dr. Emma McCabe (Durham University), and led to joint publications. Selected results from these are included in the text for clarity, and attribution is given at the relevant points.

The research presented was performed in the Department of Chemistry, Durham University, between October 2007 and December 2010, the result of which have not been submitted for a degree in this or any other university.

This thesis conformed to the word limit set out in the Degree Regulations.

Acknowledgements

First and foremost I would like to thank John for all your help and support over the past 4 years both academically and personally. Thank you for all of the confidence and motivation you have given me throughout my Ph.D., and especially for the amount of time you have been able to give to me in spite of your departmental commitments. Whilst I am sure I'll be glad to see the back of it at first, I'm sure I will grow to miss the endless scribbles of pink pen over any piece of work I've given you. *In Iohannes speramus.*

Secondly I would like to thank all those who have helped in a scientific capacity. For MPMS data I would like to thank Kosmas Prassides & Yasuhiro Takabayashi (Chemistry), and Ian Terry (Physics). Also, for HRPD data, thanks to Richard Ibberson and Aziz Daoud-Aladine.

Thanks also to Ivana for all the help you have given, and for making your office a very welcoming place, even if it is always rather warm in there!

Thanks must go to all the members of "Team Evans" who have helped, amused and listened to me rant on about a certain rubbish cricket player for the past 4 and a bit years (although I'm sure it seems much longer to you guys). Firstly to my fellow oxychalcogenide people: Alex, Andrew and Emma. A special mention must go to Emma, however, for all of the work we have done together trying to prove reactions can work more than once, and also for all the synthetic work you did for me after I burned my arm. Thanks to Lars for giving me plenty of tuneful ways to annoy Sarah. Jenny, for the amazing Kevin Pietersen spoofs (I still listen to them today). Julia, for those rare occasions when you'd walk into the office surprised to see me there already! Thanks in advance to Andrew for solving the structure of the $A_2O_2Mn_2OSe_2$ materials at low temperature from single crystal data! Big thanks to Gary for the endless football knowledge and, more importantly, Sporcle!!! Obviously thanks go to all of the project students that have kept me amused over the years, Tom H., May, (a.k.a. bamboo), Yuandi, Oliver, Francesca, Erin, Vicky R., Zoe, Tom D., Adam and this year's brave souls Ian, Alistair and Vicky W. Also thanks to Anne, Xiaojun and Bex (get well soon seems like a relevant statement!). To Sam, "You're going to Leeds… to see Leeds…?!", yes we were, because Leeds are awesome! Thank you for all things Yorkshire, for teaching Sarah that one "mashes" tea and most importantly for letting me sit next to you on the train. Finally to Sarah (previously known as "the Listertron"), thank you for listening to me going on and on and on and on about cricket, and Doctor Who, and Yorkshire, and… well… pretty much everything. You've been a great help both scientifically and personally. Is it time to go home yet?

I would also like to thank mum, dad and Louise for the endless times you have pretended to understand what I'm talking about when I tell you about work… it's all in here… it shouldn't take too long to read!

"*I'm wasted on Chemistry… well actually Chemistry is probably wasted on me…*" (DGF, 2008)

Introduction and Literature Review

1.1 Introduction

Oxychalcogenides are mixed-anion materials that contain both oxide ions and anions of another of the group 6 elements, most commonly S, Se or Te. There has been a recent surge in the study of mixed-anion materials following the 2006 discovery of superconductivity in oxyphosphides and the 2008 >26 K LaOFeAs superconductors.[1, 2] Whilst superconductivity has not yet been observed in oxychalcogenide materials there are many examples of materials with interesting electronic, magnetic and optical properties. The structural similarity of oxychalcogenides to the pnictide phases, and the wide potential for doping these systems across the insulator-metal boundary, suggests further research into oxychalcogenides is warranted. The main focus of this review will be on synthetic mixed-anion materials containing edge-sharing $[A_2O_2]^{2+}$ layers, in particular ZrCuSiAs and $La_2O_2Fe_2OSe_2$-type materials. It is also worth noting that only three naturally occurring oxychalcogenide minerals are known: kermesite, sarabauite and cetineite.[3-5] Throughout this report "*A*" will indicate a trivalent rare-earth metal ion (including Bi and Y), "*M*" will indicate a transition metal ion, and "*Q*" a chalcogenide ion (S, Se or Te). Other cations will be identified as "*B*" and pnictide ions as "*Pn*". A review of the known layered oxychalcogenide and oxypnictide structures, to 2008, has been written by Clarke *et al.*.[6]

The simplest oxychalcogenides are, of course, ternary phases. Most commonly these are found containing rare-earth metals, although a small number of transition metal oxychalcogenides have also been reported. The best studied rare-earth containing materials have the general formula A_2O_2Q and contain layers of distorted A_4O tetrahedra separated by chalcogenide ions (*Figure 1.1*). Whilst there is an extensive series of materials known for each of S^{2-} (*A* = La–Lu, Pu, Sc, Y, Bi), Se^{2-} (*A* = La–Lu, Y, Bi) and Te^{2-} (*A* = La–Dy, U), the most intense current interest is in the application of the oxysulphides as oxygen storage materials (achieved by oxidation of the chalcogenide ions to produce SO_4^{2-} layers).[7-22] Other ternary *f*-block oxychalcogenides include $A_4O_4Se_3$-type materials, (*A* = La–Sm) which contain fluorite-type $[A_2O_2]^{2+}$ layers separated by Se^{2-} ions and discrete $[Se\text{-}Se]^{2-}$ units, and those with the formula *BOQ* (*B* = Th, U, Np; *Q* = S–Te), which are similar in structure to $A_4O_4Se_3$, but contain edge-sharing $[B_2O_2]^{4+}$ layers separated by two layers of chalcogenide ions (*Figure 1.1*).[23-30] A description of different oxychalcogenide phases formed by praseodymium is given by Weber *et al.*.[23] Ternary materials containing transition metals include ZrOS and HfOS, Sc_2O_2S and the Cr_2Se_3 derived material $Cr_2Se_{0.7}O_{2.3}$.[22, 31-33] More recently a drive in nano-technology has given rise to several new nanoscale oxychalcogenide materials, with the general formula A_2O_2Q or $A_2O_2Q_2$ (A = La, Nd–Gd).[34, 35]

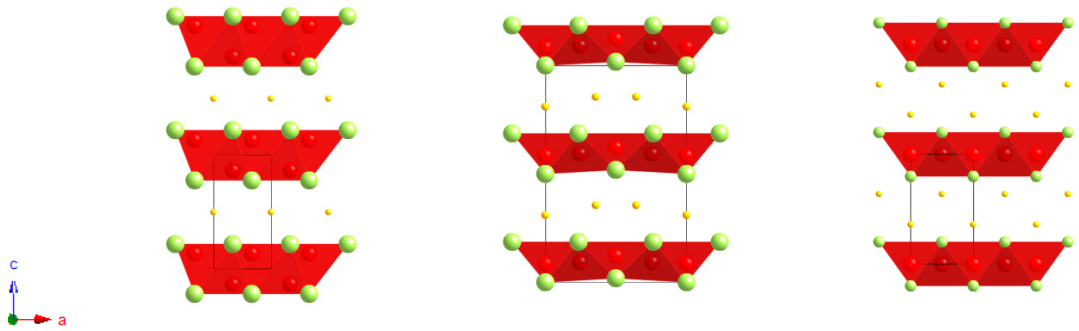

a) A_2O_2Q *b)* $A_4O_4Se_3$ *c) BOQ*

Figure 1.1 *Structures of (a) A_2O_2Q, (b) $A_4O_4Se_3$ and (c) BOQ; A/B = green, O = red, Q = yellow, the unit cells are outlined.*

A large number of the known oxychalcogenide materials adopt 2-dimensional, layered, structures. The reason for this is that layering allows separation of the different anions into different layers. By far the most explored materials in this category are quaternary phases with the ZrCuSiAs-type structure and consist of fluorite-type lanthanide-oxide and anti-fluorite-type metal-chalcogenide layers, particularly copper containing materials. The stability of these materials is enhanced by the complementary sizes of the A_4O and CuQ_4 tetrahedra, and, additionally, the "soft" nature of copper and the "hard" nature of the lanthanide ion aids anion selectivity. These materials will be discussed in greater depth in section 1.2.1. These "building-block" layers are also found in a variety of different oxychalcogenides, for example $[La_2O_2]^{2+}$ layers in $La_2O_2CdSe_2$, a potential electron blocking layer in LED technology (section 1.2.2), and $[Cu_2Se_2]^{2-}$ layers in $Bi_2YO_4Cu_2Se_2$ (*Figure 1.2*).[36, 37] Most importantly they are also observed in $La_2O_2Fe_2OSe_2$-type materials (section 1.3), which will be at the centre of this work.[38]

a) *b)*

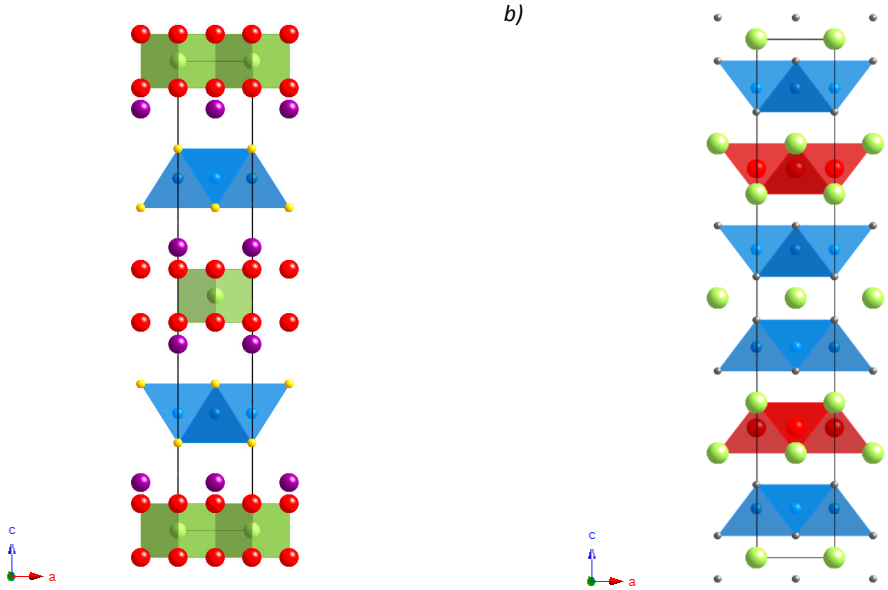

Figure 1.2 *Structures of (a) $Bi_2YO_4Cu_2Se_2$ and (b) $La_3Cu_4P_4O_2$; Bi = purple, Cu = blue, La/Y = green, O = red, P = grey, Se = yellow, the unit cells are outlined.*

Oxypnictide materials can also be built from similar building-blocks to those discussed. The most topical example is the *A*OFeAs family (*A* = La–Gd), which has the ZrCuSiAs structure, and has been demonstrated to superconduct at temperatures up to 55 K ($Sm(O_{0.9}F_{0.1})FeAs$).[2, 39-46] As in the

oxychalcogenides these contain fluorite-type $[A_2O_2]^{2+}$ layers, however the replacement of Q^{2-} by Pn^{3-} ions changes the oxidation state of the transition metal from M^{+} to M^{2+}. These will be discussed in more depth in section 1.2.3 with regard to their superconducting and magnetic properties. Other oxypnictide materials include $Na_2Sb_2Ti_2O$, a layered material consisting of octahedral $TiSb_4O_2$ layers separated by Na^+ ions (section 1.3.4), Ruddlesden-Popper-type materials, *e.g.* Ba_2TaO_3N, and also $La_3Cu_4P_4O_2$ (*Figure 1.2*) which contains $[La_2O_2]^{2+}$ layers separated by $ThCr_2Si_2$-type $LaCu_2P_2$ layers.[47-49]

As well as forming layered structures, oxychalcogenides can also crystallise with 3-dimensional structures. Within these structure-types there a few materials known that incorporate fragments of the layered building-blocks discussed earlier. A good example of this is $Gd_4TiSe_4O_4$, which contains fragments of $[Gd_2O_2]^{2+}$ layers.[50] This will be discussed alongside other examples (section 1.4) in light of the synthesis of a new oxychalcogenide structure type, to be discussed in chapter 6. Other materials with 3-dimensional structures include $A_2Ta_3Q_2O_8$ (A = La–Sm; Q = S, Se; *Figure 1.3*), $A_{20}Ti_{11}S_{44}O_6$ (*A* = La, Ce) and $La_5Ti_{3.25}Zr_{0.25}S_5O_{9,25}$.[51-56]

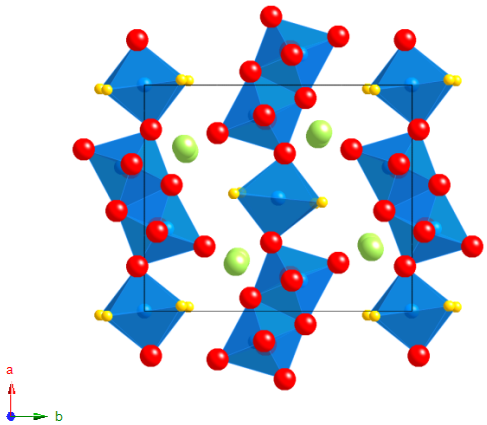

Figure 1.3 *Structure of $La_2Ta_3Se_2O_8$; La = green, Ta = blue, O = red, Se = yellow, the unit cell is outlined.*

1.2 ZrCuSiAs-type Materials

The ZrCuSiAs structure is the basis of a large family of mixed anion materials, particularly oxychalcogenides and oxypnictides.[57] As mentioned earlier, the main reason for this is the layered nature of the structure, which allows for separation of the anionic species into different metal coordination environments. These materials crystallise with a tetragonal structure, *P4/nmm*, and are best described as containing PbO-type $[A_2O_2]^{2+}$ layers, separated by anti-PbO-type $[M_2Q_2]^{2-}$ layers (*Figure 1.4*). These layers are arranged such that the lanthanide ions sit in the 8-coordinate square anti-prismatic holes created by the O^{2-} and Q^{2-} ions. A summary of the known oxychalcogenide and iron-based oxypnictide materials with the ZrCuSiAs structure is given in *Table 1.1*. Here we will discuss the chemistry and applications of these oxychalcogenides, as well as the iron-based oxypnictides. In addition to this, anti-PbO-type iron-chalcogenide materials will also be discussed.

Table 1.1 *Summary of the known ZrCuSiAs-type oxychalcogenides and iron-containing oxypnictides.*

Series	*A*	Refs.
*A*OCuS	La–Eu, Bi	58-62
*A*OCuSe	La–Er, Y, Bi	60, 61, 63
*A*OCuTe	La–Nd, Bi	61, 64-66
*A*OAgS	La, Ce	67, 68
*A*OAgSe	La–Nd	69
*A*OAgTe	La	69
*A*OFeP	La–Sm, Gd	70
*A*OFeAs	La–Sm, Gd	39

1.2.1 Oxychalcogenides

There are an extensive number of oxychalcogenides with the ZrCuSiAs structure, with sulphide, selenide and telluride examples known. These are predominantly copper-containing, however a number of silver-containing materials are known, as well as related cadmium and manganese-containing materials. There are two important reasons for the abundance of these copper containing materials. Firstly, the chalcophilic nature of copper allows for easy separation of the two anionic species present. Secondly, the size of the $[Cu_2Q_2]^{2-}$ layers is such that they naturally stack with the $[A_2O_2]^{2+}$ layers. The known ZrCuSiAs-type oxychalcogenides are summarised in *Table 1.1*. Although no superconducting oxychalcogenide materials have been formed (apart from those where chalcogenide ions have been doped into the parent oxide), these materials have been demonstrated to posses several interesting optical and electronic properties.

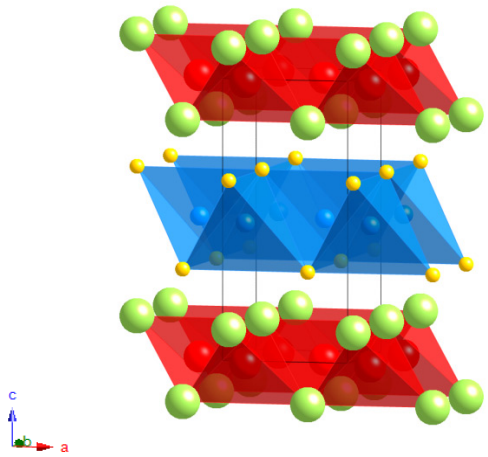

Figure 1.4 *Structure of LaOCuSe; La = green, Cu =blue, O =red, Se = yellow, the unit cell is outlined.*

Structural trends

Figure 1.5 shows the variation in the reported unit cell volumes for each of the *A*OCuS, *A*OCuSe and *A*OCuTe series of materials, relative to the volume of the lanthanum containing materials. The figure shows that, except for the Bi^{3+} materials, the volume of the unit cell decreases smoothly with decreasing rare-earth cation radius. Smaller volumes and shorter *A*-O and *A*-*Q* bond lengths for the bismuth containing samples, relative to the lanthanum containing materials, are observed despite the larger ionic radius of bismuth. Closer inspection of the lattice parameters also shows that, whilst *a* decreases in size, *c* is seen to increase. These observations can be explained by the electronegativity of Bi (2.02),

which is much larger than that of La (1.10), meaning that the Bi-anion bonds are much more covalent than the La-anion bonds, and hence are shorter.[71] Secondly, the electronic configuration of Bi^{3+} is such that it has a lone pair of electrons which repels the oxide ions such that the O-Bi-O bond angle decreases and hence the cell expands in the *c* direction and shrinks in *a*. The figure also shows that the La^{3+} materials have a slightly larger cell volume than observed for the other rare-earth ions. The reason for this is unknown, however is reflected in reported values for lanthanide-phosphide materials.[72]

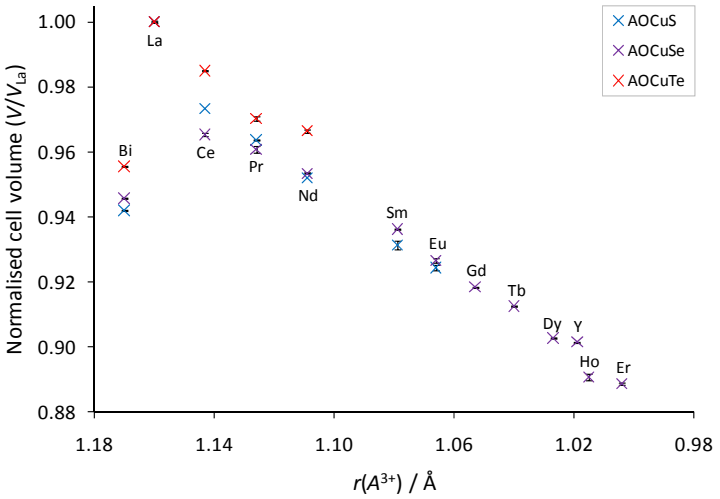

Figure 1.5 *The effect of decreasing lanthanide cation radii on the normalised cell volume for AOCuQ materials; values are normalised relative to A = La and therefore LaOCuS, LaOCuSe and LaOCuTe data points are all coincident.*

It is also worth noting that studies of the cerium-based phases have shown a tendency to form copper deficient materials.[61, 68] This is caused by variation of the cerium oxidation state from Ce^{3+} towards Ce^{4+}, and hence Cu^{+} ions are lost from the material to achieve charge balance. The consequence of this is that lattice parameters observed for "CeOCuS" samples are smaller than would be expected. These materials have been studied in depth, and an approximately stoichiometric material, $Ce_{0..987(2)}OCuS$, has been reported by Pitcher *et al.*; it is the lattice parameters of that cell that are given in *Figure 1.5*.[73] This study also demonstrated that this material readily oxidises in moist air.

Electronic properties

The main point of interest in the LaOCuS materials is their transparent *p*-type semiconducting nature. This behaviour is made possible by the large band-gaps observed in these materials (~3.1 eV for LaOCuS).[74] The contrast between the highly covalent $[Cu_2Q_2]^{2-}$ and highly ionic $[A_2O_2]^{2+}$ layers creates a quantum well type material, with the highly conducting chalcogenide layers separated by hole-blocking oxide layers.[75] The valence band maxima and conduction band minima consist of the Cu 3*d* and *Q np*, and Cu 4*s* states, respectively (*Figure 1.6*). Charge transfer in these materials is therefore via hole-conduction pathways in the $[Cu_2Q_2]^{2-}$layers. This band gap can then be tuned by variation of the lanthanide or chalcogenide ions involved. Studies have shown that, on changing the lanthanide ion from La^{3+} to a smaller ion, *e.g.* Sm^{3+}, the unit cell dimensions decrease, and hence Cu-Cu distances in the chalcogenide layer decrease. This decrease leads to increased orbital overlap, and hence broadening of the valence and conduction bands, decreasing the band gap. This is well illustrated by a systematic

decrease in band gap from 3.1 eV in LaOCuS to 2.9 eV in SmOCuS.[76, 77] Substituting La^{3+} for Bi^{3+} also decreases the band gap, owing to the lower energy of the Bi 6*p* orbitals.[78] This is reflected in the black colour of the material. Varying the chalcogenide ion from S^{2-} to Se^{2-} decreases the band gap from 3.1 to 2.8 eV, respectively, and in turn increases conductivity.[76, 79] This decrease in band gap reflects the decrease in electronegativity between these two anions (2.58 and 2.55, respectively) and hence an increase in the hybridisation of the Cu 3*d* and *Q np* orbitals, leading to increased band width and higher conductivity.[71] On replacing Se^{2-} with Te^{2-} (electronegativity 2.51) the band gap decreases sufficiently that the material behaves as a degenerate semiconductor, reflecting the more dramatic decrease in band gap to 2.3 eV.[65, 71]

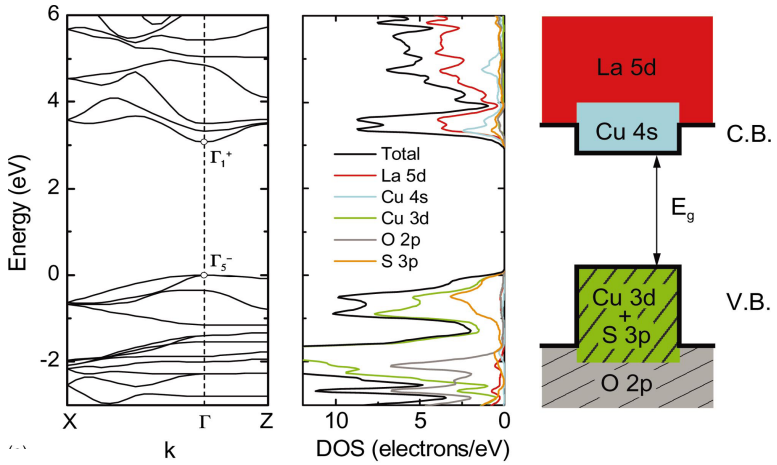

Figure 1.6 *The calculated and schematic band structure and density of states for LaOCuS taken from Ueda et al.*.[i]

The electronic properties discussed mean that the LaOCu*Q* materials (*Q* = S, Se) have potential application as a transparent light-emitting layer in LED devices.[80, 81] This is best illustrated by LaOCuSe, which can be combined with amorphous $InGaZn_5O_8$ (an *n*-type semiconductor) to produce a hetero *p*/*n*-junction.[82] This junction has been demonstrated to emit blue light on application of a potential difference (~8 V) at room temperature. The applied potential difference introduces electrons into the $InGaZn_5O_8$ layer, which then combine with holes from chalcogenide layers in LaOCuSe, producing excitons (binding energy ≈ 50 meV) that emit radiation with λ = 430 nm.[83]

Whilst the majority of these materials are copper-containing there are also examples of silver containing materials, as summarised in *Table 1.1*. Unlike their copper analogues, these materials are fast ion conductors, with band gaps of 0.22 eV in LaOAgS and 0.71 eV in CeOAgS; reflecting a change in colour from green to black.[59, 67, 84, 85] The large difference between the band gap for LaOAgS and LaOCuS (3.1 eV) is the result of the increased *M*-S orbital overlap for LaOAgS, due to more diffuse Ag^+ 4*d* orbitals, leading to more disperse bands and hence a smaller band gap. Neutron data reported for LaOAgS have exhibited a large thermal displacement of the Ag^+ ions in the *x* and *y* directions, suggesting conduction occurs via interstitial sites in the *ab* plane.

[i] Reprinted Figure 2a with permission from K. Ueda *et al.*, *Phys. Rev. B*, 2004, **69**, 155305. Copyright 2004 by the American Physical Society.

Magnetic properties

As the copper cations of the *A*OCu*Q* materials are formally monovalent, and therefore d^{10}, they do not contribute to the magnetic properties of the material. Instead magnetism arises from the rare-earth cations involved. Susceptibility data show paramagnetic contributions from each of the Pr^{3+}, Nd^{3+}, Sm^{3+} and Eu^{3+} cations with no evidence of ordering at low temperature; the La^{3+} containing materials show diamagnetic behaviour.[77, 86-88]

1.2.2 Related Oxychalcogenides

There are several materials closely related to LaOCuS, either by composition or structure. Two structurally similar materials are $La_2O_2CdSe_2$ and $CeOMn_{0.5}Se$.[37, 89, 90] Due to the divalent nature of the metal ions these materials contain $[A_2O_2]^{2+}$ layers separated by half-occupied metal-selenide layers, $[MSe_2]^{2-}$. Whilst no ordering of the metal cation sites is observed in $CeOMn_{0.5}Se$, those in $La_2O_2CdSe_2$ order such that all tetrahedra are corner sharing, producing a checkerboard arrangement of tetrahedra (*Figure 1.7*). The most studied of these materials is $La_2O_2CdSe_2$, which has been demonstrated to have a wide band gap (3.3 eV), giving it a yellow-white appearance, however due to the lower energy of the Cd 4*d* bands, compared with the Cu 3*d* bands in LaOCuS, conductivity is low and hence the material is insulating. Optical measurements for $CeOMn_{0.5}Se$ indicate a band gap energy of 2.01 eV, however electrical and magnetic properties have not yet been reported.[90]

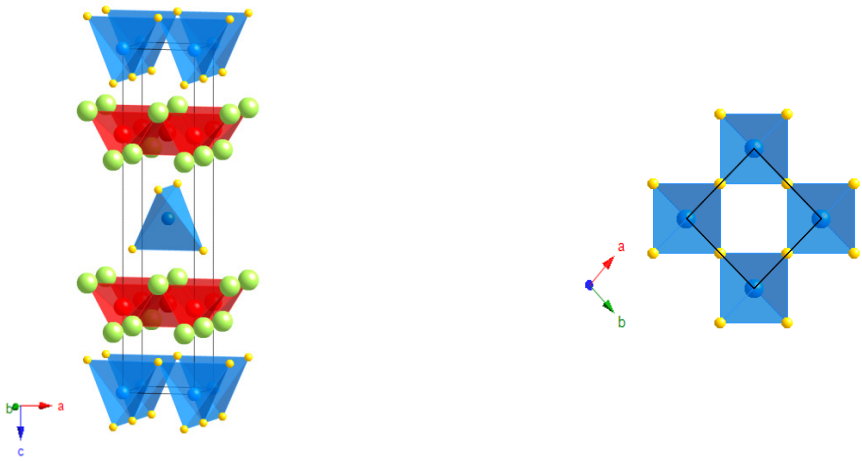

Figure 1.7 *Structure of $La_2O_2CdSe_2$ with the checkerboard $[MSe_2]^{2-}$ layer also shown; La = green, Cd = blue, O = red, Se = yellow, the unit cell is outlined.*

Other structurally related materials include $(NdO)_4Ga_2S_5$ and $La_5Cu_6O_4S_7$.[91, 92] The latter of these materials (*Figure 1.8a*) contains edge-sharing $[Cu_2S_2]^{2-}$ layers separated by fragments of $[La_2O_2]^{2+}$ layers, which are coupled by square-planar S^{2-} ions in every fifth O^{2-} site along the *b* axis. The introduction of this S^{2-} ion into the $[La_2O_2]^{2+}$ layers causes the copper layers to undulate slightly. Layer distortion is also observed in $(NdO)_4Ga_2S_5$, where $[Nd_2O_2]^{2+}$ layers are separated by layers of corner sharing GaS_4 tetrahedra (*Figure 1.8b*), and the relative sizes of these layers causes an undulating effect.[91]

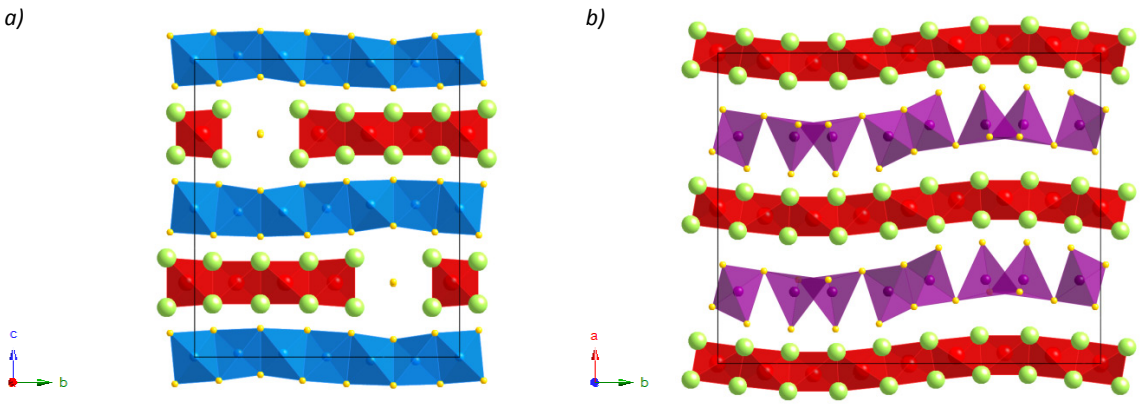

Figure 1.8 *Structures of (a) $La_5Cu_6O_4S_7$ and (b) $(NdO)_4Ga_2S_5$; Cu = blue, Ga = purple, La/Nd = green, O = red, S = yellow, unit cells are outlined.*

Materials that form different structures, despite having the same general formula are the *B*ZnOS materials (*B* = Ba, Ca).[93-95] The structure of the Ba and Ca containing materials differ, and both are shown in *Figure 1.9*. BaZnOS contains layers of corner sharing ZnO_2S_2 tetrahedra, with Zn^{2+} ions lying above and below a layer of O^{2-} ions and with Ba^{2+} ions in 8-coordinate sites. CaZnOS, however, is better described as containing distorted, corner sharing, $ZnOS_3$ tetrahedral layers, with all the Zn^{2+} ions in the same plane, and Ca^{2+} ions in 6-coordinate sites between the layers. The band gaps for these materials are calculated as 3.9 and 3.7 eV for BaZnOS and CaZnOS respectively. Cu-activated BaZnOS has been shown to display blue phosphorescence, on exposure to UV light.[95]

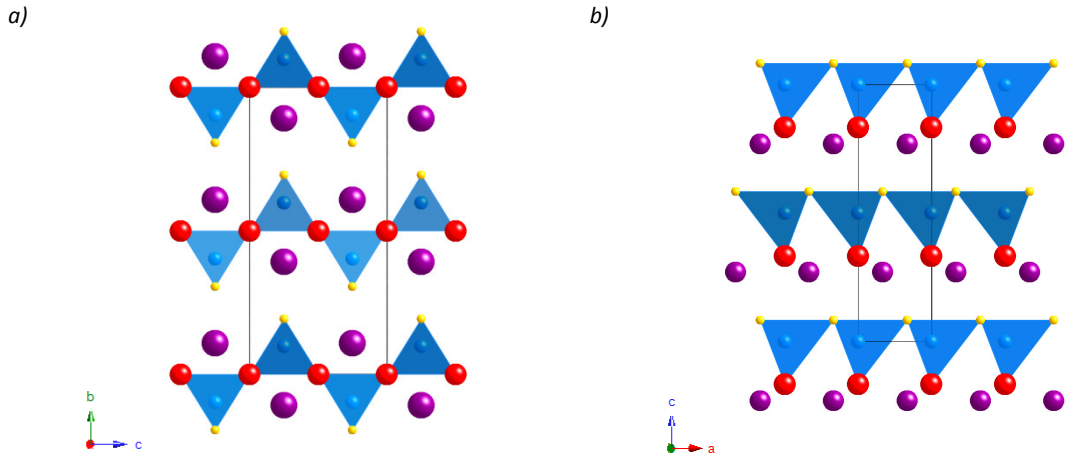

Figure 1.9 *Structures of (a) BaZnOS and (b) CaZnOS; Ba/Ca = purple, Zn = blue, O = red, S = yellow, unit cells are outlined.*

1.2.3 Oxypnictides

Unlike ZrCuSiAs-type oxychalcogenides, oxypnictide analogues are stable for a variety of different transition metal ions, including Mn–Zn, Ag, Cd, Ru and Os. As stated earlier, the replacement of Q^{2-} ions for Pn^{3-} ion means that divalent transition metal ions are required for overall charge balance. It is this move from univalent to divalent cations that allows these materials to form for a wider range of transition metals. Good reviews of all these materials have been provided by Pöttgen & Johrendt, and Ozawa & Kauzlarich.[57, 96] Here we will focus on the iron-containing oxypnictides, which have been found to superconduct, with a highest T_c of 55 K for F-doped SmOFeAs.[43] Known materials and their critical temperatures are summarised in *Table 1.2*.

Superconductivity in these materials was originally reported for LaOFeP, with a T_c of 3.2 K, which was demonstrated to increase to ~7 K on doping of the $[La_2O_2]^{2+}$ layers with 6 % F^- ions.[1, 97] Substitution of the pnictide ion from P^{3-} to As^{3-} resulted in an increase of T_c to 26 K for $La(O_{0.95}F_{0.05})FeAs$.[2] Furthermore, in the arsenide series of materials, T_c is observed to increase with decreasing lanthanide radius, reaching a maximum of 55 K for F-doped SmOFeAs; the maximum T_c for F-doped GdOFeAs is 36 K.[41, 43]

Table 1.2 *Summary of T_c's for selected AOFePn materials.*

Material	T_C / K	Refs.
"LaOFeP"	*7*	97
"PrOFeP"	*3.2*	98
"NdOFeP"	*3.1*	98
$LaO_{0.89}F_{0.11}FeAs$	*26*	2
$CeO_{0.84}F_{0.16}FeAs$	*35 / 41*	45, 99
$PrO_{0.85}F_{0.15}FeAs$	*52*	46
$NdO_{0.89}F_{0.11}FeAs$	*52*	100
$SmO_{0.9}F_{0.1}FeAs$	*55*	43
$GdO_{0.83}F_{0.17}FeAs$	*36*	41
$LaOFe_{0.9}Rh_{0.1}As$	*16*	101
$Nd_{0.8}Th_{0.2}OFeAs$	*38*	102

Investigation of LaOFeP by McQueen *et al.* indicated a lack of superconductivity in stoichiometrically precise LaOFeP, and therefore attributed observed superconductivity to doping caused by oxygen vacancies in the $[La_2O_2]^{2+}$ layers.[103] This is also highlighted by the arsenide materials, for example both $PrO_{0.85}F_{0.15}FeAs$ and $PrO_{0.85}FeAs$ exhibit superconductivity below 52 K, whereas PrOFeAs does not.[46, 104] Other doping mechanisms have been investigated, for example aliovalent substitution of Nd^{3+} for Th^{4+} in $Nd_{0.8}Th_{0.2}OFeAs$, and isovalent substitution of Fe^{2+} for Rh^{2+} in $LaOFe_{0.9}Rh_{0.1}As$, however neither shows an improvement of T_c over the F-doped samples.[101, 102]

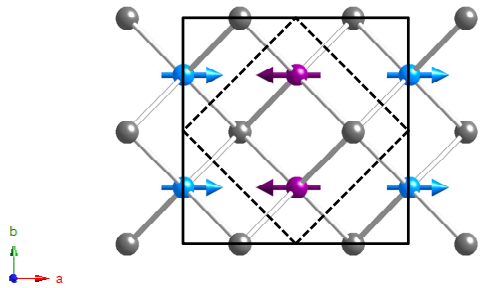

Figure 1.10 *Magnetic ordering of Fe^{2+} moments in the $[Fe_2As_2]^{2+}$ layers of LaOFeAs; Fe = blue/purple, As = grey; the blue/purple colour of the Fe ions relates similar spins; the outline of the room temperature cell is dashed and the low temperature is solid.*

The presence of Fe^{2+} ions in these materials means that magnetic ordering can occur on cooling. For the *A*OFeAs series this results in a striped antiferromagnetic (AFM) arrangement of moments (AFM2, *Figure 1.10*), and follows a structural phase transition from a tetragonal to an enlarged orthorhombic cell; the magnetic cell is then related to the orthorhombic nuclear cell by doubling along the *c* axis. A good review of the magnetic properties of these materials, and other iron-based superconductors has been provided by Lynn & Dai.[105] As well as the Fe^{2+} moments ordering, the rare earth atoms are also seen to order with an AFM arrangement, however at significantly lower temperatures. A summary of the

ordering temperatures and magnetic lattices adopted is given in *Table 1.3*. A systematic study of the $CeO_{1-x}F_xFeAs$ system, has shown that AFM ordering of the Fe^{2+} ions is observed for compositions between $x = 0$ and 0.06, beyond which point it is suppressed in favour of superconductivity.

Table 1.3 *Summary of ordering temperatures for Fe^{2+} and A^{3+} moments in selected AOFeAs materials.*

Material	T_N^{Fe} / K	T_N^{A} / K	Refs.
LaOFeAs	*137*	-	42
CeOFeAs	*140*	*4.0*	45, 99
PrOFeAs	*127*	*14*	46, 104
NdOFeAs	*141*	*1.96*	40, 106
SmOFeAs	*135*	*~5*	107

Following the discovery of superconductivity in the oxypnictides, interest surged in other materials containing $[Fe_2As_2]^{2-}$ layers. These include LiFeAs, $BaFe_2As_2$ and more recently $Sr_3Sc_2O_5Fe_2As_2$-type materials.[108-111] The structural similarities between these materials are highlighted in *Figure 1.11*. There are many good papers reviewing these materials including work by Paglione & Greene, and Lynn & Dai.[105, 112]

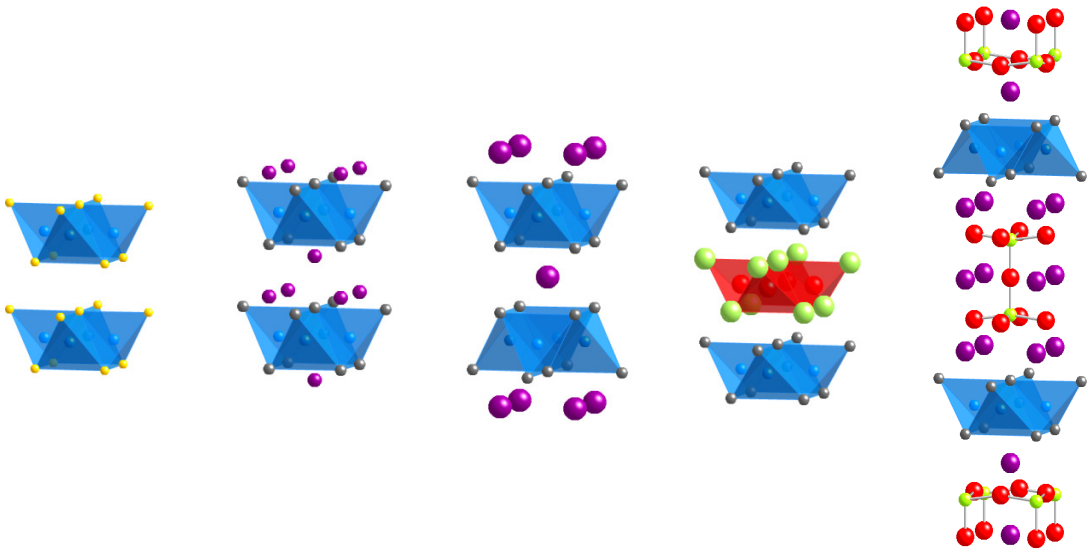

a) α-FeSe *b) LiFeAs* *c) $BaFe_2As_2$* *d) LaOFeAs* *e) $Sr_3Sc_2O_5Fe_2As_2$*

Figure 1.11 *Structures of iron-based superconductors; Ba/Li/Sr = purple, Fe = blue, La/Sc = green, As = grey, O = red, Se = yellow.*

1.2.4 Anti-PbO-type Materials

The superconducting materials discussed above all contain anti-PbO-type $[Fe_2As_2]^{2-}$ layers, separated either by cations, or oxide layers. α-FeSe has a similar structure, made of anti-PbO-type $[Fe_2Se_2]$ layers, but with no cations or oxide layers separating them (*Figure 1.11*). Recently, work by Hsu *et al.*, demonstrated that $\alpha\text{-}FeSe_{1-x}$ becomes superconducting below 8 K, for $x = 0.12$, whilst work by Margadonna *et al.* increased this to 13.5 K, for $x = 0.08$ at ambient pressure, and further work to 36.7 K under 8.9 GPa pressure.[113-115] Whilst superconductivity in these materials was originally attributed to selenium deficiencies in the layers, stoichiometric FeSe was prepared and exhibited superconductivity

with T_c = 8.9 K.[116] Further research on α-FeSe explored how superconductivity varied as Se^{2-} was substituted for Te^{2-} ions.

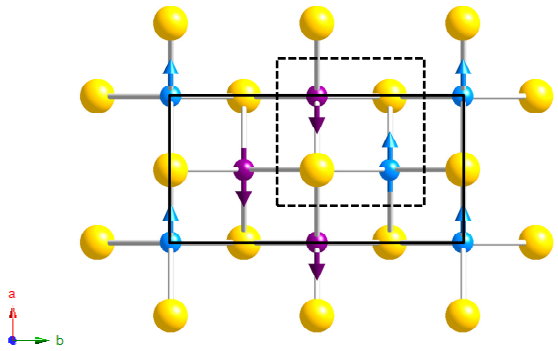

Figure 1.12 *Magnetic ordering of Fe^{2+} moments in the $Fe_{1.086}Te$; Fe = blue/purple, Te = yellow; the blue/purple colour of the Fe ions relates similar spins; the outline of the room temperature cell is dashed and the low temperature cell is solid.*

Studies by Yeh *et al.* demonstrated an increase of T_c with increasing Te^{2-} content, reaching a maximum of 15.2 K for $FeSe_{0.5}Te_{0.5}$, above this point the T_c is observed to decrease again until superconductivity is completely suppressed in favour of magnetic ordering in FeTe.[117] Unlike in LaOFeAs, this ordering does not coincide with a reduction from tetragonal to orthorhombic symmetry. Instead $Fe_{1.068}Te$ is observed to undergo a transition to monoclinic symmetry at 67 K.[118, 119] The observed magnetic ordering, for $Fe_{1+y}Te$ with $y < 0.1$, is also different to that in LaOFeAs, and is shown in *Figure 1.12*. This frustrated arrangement requires a doubling of the nuclear unit cell along the *a* and *c* axes and is labelled as AFM3. The reduction in symmetry naturally leads to subtle differences in exchange energies, and the region of the magnetic phase diagram in which the AFM3 structure is stable has been explored by Fang *et al.*.[120]

1.3 $La_2O_2Fe_2OSe_2$-type Materials

The $La_2O_2Fe_2OSe_2$ structure type was originally reported from single crystal studies by Mayer *et al.*, who published the synthesis, magnetic properties and conductivities of $La_2O_2Fe_2OS_2$ and $La_2O_2Fe_2OSe_2$.[38] Since this was originally reported a number of other materials with this structure have been prepared by our group. Work by Hickey reported a series of Fe^{2+}-containing materials $A_2O_2Fe_2OSe_2$ (*A* = La, Nd, Sm) and $A_2O_2Fe_2OS_2$ (*A* = La, Nd), whilst work by Withers investigated the structure and properties of $La_2O_2Mn_2OSe_2$ and $La_2O_2Co_2OSe_2$.[121, 122] These materials were initially reported in 2004 and 2005, respectively, however in 2010 more work was published concerning $La_2O_2Co_2OSe_2$ and $Nd_2O_2Fe_2OSe_2$, and also the Ti^{4+}-containing pnictide analogue $Sm_2O_2Ti_2OSb_2$.[123-126]

1.3.1 Structure and Previous Work on $A_2O_2M_2OSe_2$ Materials

These materials are best described as containing $[A_2O_2]^{2+}$ layers, as seen in the ZrCuSiAs materials, separated from anti-CuO_2-type $[M_2O]^{2+}$ layers by a layer of Se^{2-} ions (*Figure 1.13*). This unusual geometry with 2-coordinate transition metals and 4-coordinate oxide ions is not found in oxides, and therefore the possibility of unusual electronic, and magnetic, behaviour in this layer was one motivation for this study. The coordination of the transition metal sites can also be described as face-sharing octahedral,

each M^{2+} ion bonding to two axial O^{2-} ions, and four equatorial Q^{2-} ions. The coordination of the lanthanide ions is similar to that in the ZrCuSiAs structure type, with four oxide ions and four chalcogenide ions creating a square anti-prismatic arrangement. Other materials with similar structures include a family of oxychalcogenides and oxypnictides where transition metal octahedra are separated by $[B_2F_2]^{2+}$ (B = Sr, Ba) layers.[125, 127]

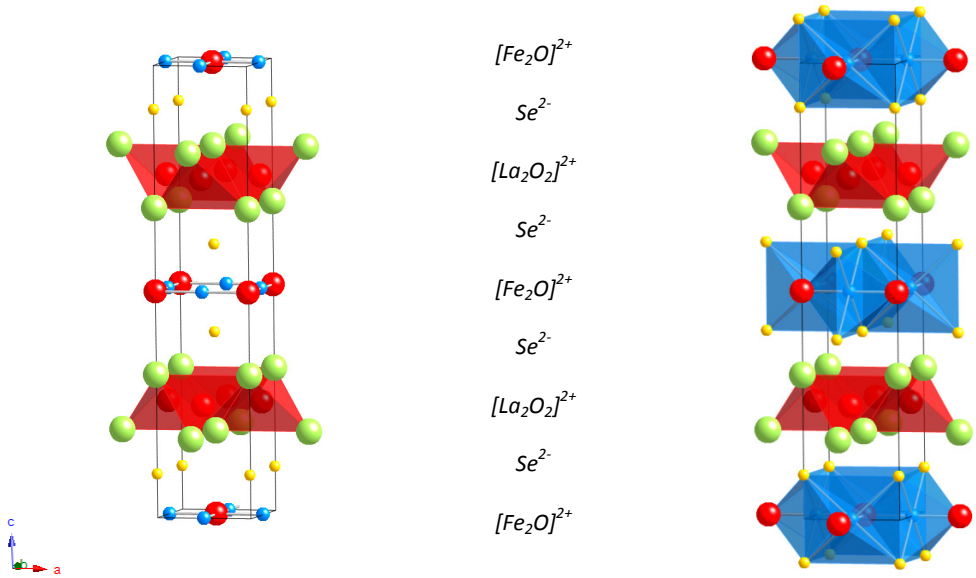

Figure 1.13 *Structure of $La_2O_2Fe_2OSe_2$ with different transition metal coordination geometries depicted; Fe = blue, La = green, O = red, Se = yellow, the unit cell is outlined.*

Previous work, reported in my masters project, expanded this family to include $Pr_2O_2Mn_2OSe_2$ and $Pr_2O_2Fe_2OSe_2$, and demonstrated that the $La_2O_2FeOSe_2$-type materials form over a narrow range of transition metal radii.[128] In addition to this, variation of the lanthanide ion demonstrated that no further cobalt containing materials could be produced and that manganese containing materials were restricted to $La_2O_2Mn_2OSe_2$ and $Pr_2O_2Mn_2OSe_2$. *Figure 1.14* gives a summary of both successful (black circles) and unsuccessful (white circles) syntheses, plotted relative to the radii of the cations involved, and reveals a relatively narrow range of radii over which these materials form (radii used are the high spin radii reported by Shannon which are consistent with recently acquired neutron data reported here).[129] Overall, results suggest that size of both metals, as well the stability of competing phases, play a major role in phase formation. The formation of competing phases will be discussed in greater depth in chapter 5, however those observed included transition metal selenides (*e.g.* MnSe), rare-earth oxyselenides (*e.g.* La_2O_2Se and $La_4O_4Se_3$) and also perovskite based phases (*e.g.* $LaVO_3$). The attempted doping of half of the La^{3+} sites in $La_2O_2Co_2OSe_2$ with Nd^{3+} ions produced the material $(La_{1-x}Nd_x)_2O_2Co_2OSe_2$ with ($x \approx 0.2$), demonstrating the limiting rare-earth radius in the cobalt containing materials; this conclusion is supported up by the lack of formation of $Pr_2O_2Co_2OSe_2$.

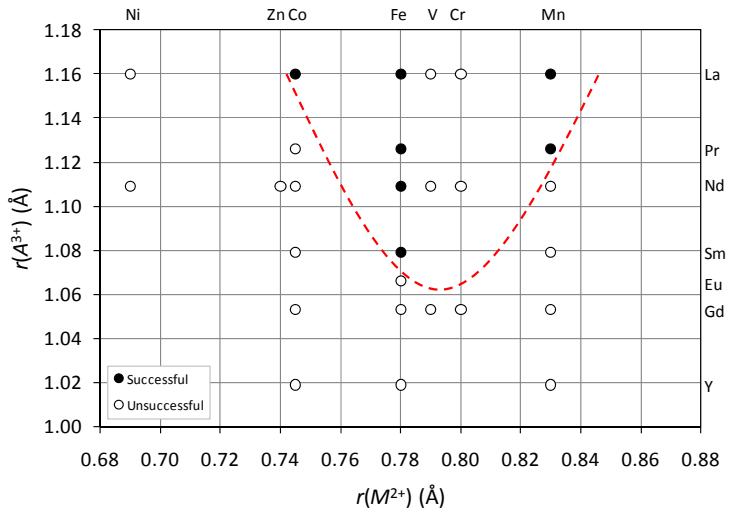

Figure 1.14 *Plot summarising successfully isolated members of the $A_2O_2M_2OSe_2$ family of materials by comparison of cation radii; the dotted red line serves as a guide to the eye.*

1.3.2 Magnetic Properties

Magnetic measurements suggest that the square planar transition metal layers in these materials order antiferromagnetically on cooling. Whilst susceptibility measurements have been recorded for each of the materials, preliminary neutron data have only been reported for $La_2O_2Mn_2OSe_2$ and $La_2O_2Co_2OSe_2$.[121] A summary of the magnetic transitions for these materials is given in *Table 1.4*. The arrangement of the magnetic moments suggested for these materials can be seen in *Figure 1.15*. $La_2O_2Mn_2OSe_2$ adopts an AFM1 structure, where all the 180° interactions are ferromagnetic (FM) and the direct 90° Mn-Mn interactions are AFM. The magnetic structure suggested for $La_2O_2Co_2OSe_2$, however, contains moments aligned in the *ab* plane, such that they are directed along, and in the adjacent layers perpendicular to, the Co-O bonds. Unlike $La_2O_2Mn_2OSe_2$ the 180° interactions are reported as AFM. This arrangement is contrary to theoretical studies by Wu, which predicted that the material would adopt an AFM6 arrangement of atoms (*Figure 1.15*).

Table 1.4 *Summary of ordering temperatures for M^{2+} in selected $La_2O_2Fe_2OSe_2$-type materials.*

Material	T_N^{Fe} / K	Measurement	Refs.
$La_2O_2Mn_2OSe_2$	*~160*	Susceptibility	121
$La_2O_2Fe_2OS_2$	*100*	Susceptibility	38
$La_2O_2Fe_2OSe_2$	*100*	Susceptibility	38
$Nd_2O_2Fe_2OSe_2$	*88*	Mössbauer	123
$La_2O_2Co_2OSe_2$	*220*	Susceptibility	123, 126
$Ba_2F_2Fe_2OS_2$	*94-95*	Susceptibility	127
$Ba_2F_2Fe_2OSe_2$	*83.6*	Neutron	127
$Sr_2F_2Fe_2OS_2$	*106.2*	Mössbauer	127
$Sr_2F_2Fe_2OSe_2$	*95-97*	Susceptibility	127

Whilst neutron data have not been reported for the remainder of the materials, recent theoretical studies have suggested possible structures. Studies by Zhu *et al.,* have suggested two possible magnetic structures for $La_2O_2Fe_2OQ_2$ (Q = S, Se), AFM1 and AFM6 (*Figure 1.15*), depending on the magnitude of the Mott-Hubbard interaction energy (U).[130] Similar studies of the $B_2F_2Fe_2OQ_2$ family also suggested that the AFM1 and AFM6 structures would be most stable for the $[Fe_2O]^{2+}$ layers, despite the different

PbO-type layers present.[127] Mössbauer spectroscopy on $Nd_2O_2Fe_2OSe_2$, whilst not revealing the magnetic structure, has suggested that the Fe^{2+} moments lie along the Fe-O-Fe bond direction, with T_N = 88 K.[124] Both of the two suggested models for the arrangement of the moments are similar to that suggested for $La_2O_2Co_2OSe_2$, however one has AFM Fe^{2+} chains coupled AFM, and the other has FM chains coupled AFM. In addition, recent studies by Wu have suggested that $La_2O_2Co_2OSe_2$ orders with an AFM6 structure.[131] One aim of this project was to determine the magnetic structures of these materials. Experimental results, and their relationship to the emerging theoretical papers, are discussed in chapters 3, 4 and 5.

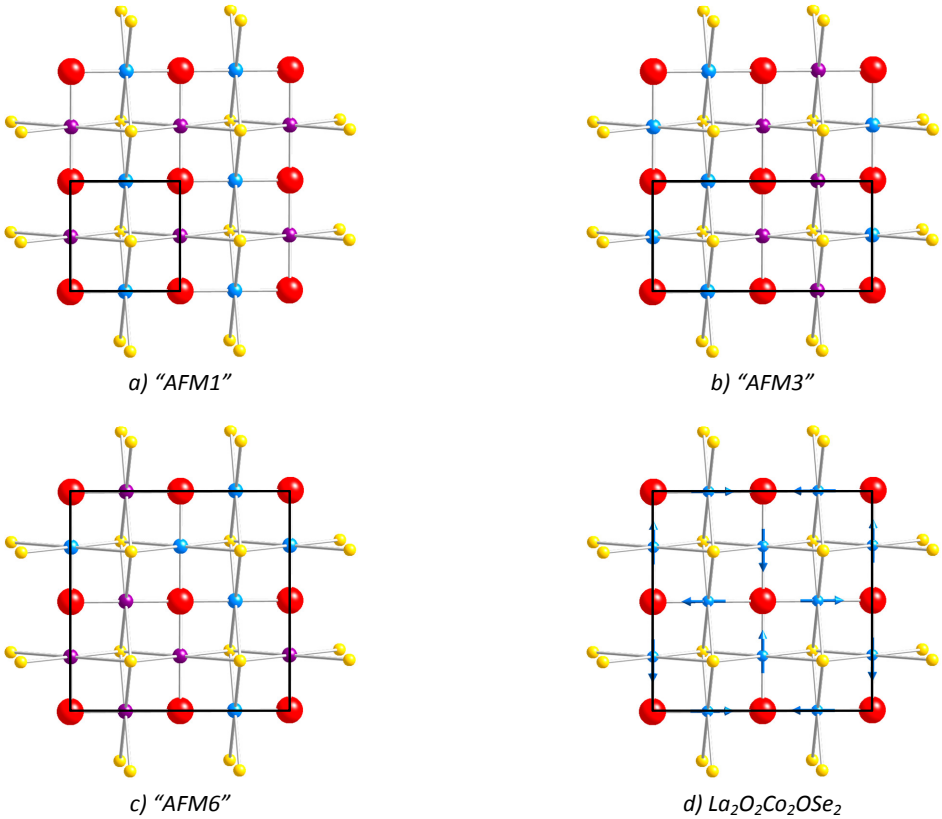

a) "AFM1" *b) "AFM3"*

c) "AFM6" *d) $La_2O_2Co_2OSe_2$*

Figure 1.15 *Observed and theoretical magnetic structures for the metal-oxychalcogenide layers in $La_2O_2Fe_2OSe_2$-type materials; Fe = blue/purple, O = red, Se = yellow; the blue/purple colour of the Fe^{2+} ions relates similarly orientated moments; the magnetic cells are outlined in black.*

1.3.3 Resistivity and Electronic Structure

Resistivity measurements for $La_2O_2M_2OSe_2$ (*M* = Mn, Fe), $La_2O_2Fe_2OS_2$, and the $B_2F_2Fe_2OQ_2$ family suggest these materials are semiconducting at room temperature.[38, 121, 127] Separate reports of $La_2O_2Co_2OSe_2$, by Withers and Wang *et al.* suggest the material is also semiconducting at room temperature, with a room temperature resistivity of 10^7 Ωm and an activation energy of 0.35 eV.[121, 126]

Electronic structure calculations by Zhu *et al.* showed that, for both $La_2O_2Fe_2OS_2$ and $La_2O_2Fe_2OSe_2$, the primary contribution to the density of states near the Fermi level is from the Fe 3*d* electrons, and that the 3*d* bandwidths observed are appreciably narrower than those observed for LaOFeAs (*Figure 1.16*); 3.2 and 4.4 eV for $La_2O_2Fe_2OSe_2$ and LaOFeAs, respectively.[130] Studies by Wu have shown that these

bands are even narrower in $La_2O_2Co_2OSe_2$, with a Co 3*d* bandwidth of 2.8 eV.[131] Both studies have shown these materials to be Mott insulators.

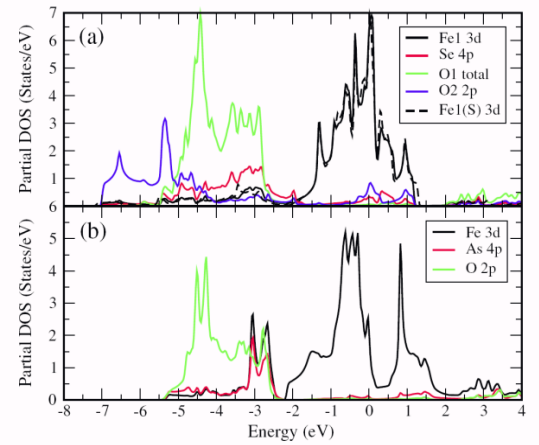

Figure 1.16 *The calculated density of states for (a) $La_2O_2FeOSe_2$ and (b) LaOFeAs taken from Zhu et al.; the dashed line represents the Fe contribution for $La_2O_2Fe_2OS_2$.*[ii]

1.3.4 Related [M_2O]-containing Materials

As discussed earlier, there are a small number of materials containing similar [M_2O] layers, including the oxypnictide analogues, $Sr_2F_2Ti_2OPn_2$ (*Pn* = As, Sb) and $Sm_2O_2Ti_2OSb_2$, and also $Na_{1.9}Cu_2Se_2.Cu_2O$.[125, 132] $Na_{1.9}Cu_2Se_2.Cu_2O$ was originally reported by Park *et al.*, and was synthesised using an $NaSe_x$ flux.[132] Unlike the $La_2O_2Fe_2OSe_2$ materials, $Na_{1.9}Cu_2Se_2.Cu_2O$ contains anti-PbO-type $[Cu_2Se_2]^{2-}$ layers separated from square-planar $[Cu_2O]$ layers by a layer of Na^+ ions (*Figure 1.17*). Whilst the presence of Na^+ vacancies means that charge carriers are introduced into the material, it is was not initially known whether these were contained in the copper-selenide or oxide layers. Subsequent theoretical studies by Chacon *et al.*, however demonstrated that these holes were confined to the chalcogenide layers, with the oxide layers being charge reservoir layers.[133]

a) *b)*

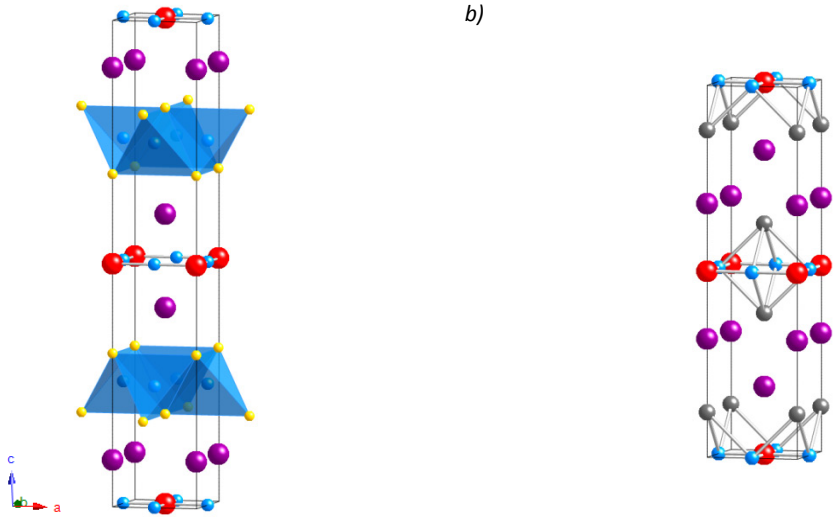

Figure 1.17 *Structures of (a) $Na_{1.9}Cu_2Se_2.Cu_2O$ and (b) $Na_2Ti_2Sb_2O$; Cu = blue, Na = purple, O = red, Sb = grey, Se = yellow, unit cells are outlined.*

[ii] Reprinted Figure 2 with permission from J-X. Zhu *et al.*, *Phys. Rev. Lett*, 2010, **104**, 216405. Copyright 2010 by the American Physical Society.

The pnictide analogues are also similar in structure to the $Na_2Ti_2Pn_2O$ materials, where *Pn* = As & Sb.[134] Instead of containing PbO-type $[A_2O_2]^{2+}$ layers, the $[M_2O]$ transition metal layers are separated by a layer of Na^+ ions (*Figure 1.17*). On cooling, the magnetic susceptibility of $Na_2Ti_2Sb_2O$ undergoes a sharp drop, which is coincident with a metal-to-metal transition observed from resistivity data. Powder neutron diffraction studies have shown that these observations are consistent with a change in the thermal expansion of both the *a* and *c* cell parameters, however no magnetic ordering, or changes in symmetry have been observed.[135] These observations suggest the presence of a charge (or spin) density wave in the material, similar to that observed in undoped LaOFeAs.[42, 136, 137]

1.4 3-D Oxychalcogenides

Whilst the majority of oxychalcogenide materials are layered, there are also several known materials with 3-dimensional structures. Here we will discuss materials that contain fragments of the infinite $[A_2O_2]^{2+}$ layers seen in the 2-dimensional phases. These phases can be organised in terms of the size of the $[A_2O_2]^{2+}$ fragments, in particular by the number of tetrahedra that are formed between breaking points. This is quantified by the value of *x* in xA_4O, and this section will give examples of $2A_4O$, $3A_4O$ and $4A_4O$ materials. The structures of these phases are relevant for the new transition metal oxychalcogenides described in chapter 6.

Figure 1.18 shows the structure of two materials, $Sm_7VO_4Se_8$ and $Eu_5V_3O_7S_6$, which both contain $[A_2O_2]^{2+}$ fragments joined at corners by vanadium ions.[138, 139] In $Sm_7VO_4Se_8$ these $[A_2O_2]^{2+}$ layers are broken such that they are two tetrahedra across ($2A_4O$), whereas in $Eu_5V_3O_7S_6$ we observed a 1:1 mixture of $2A_4O$ and $3A_4O$ fragments, and we can therefore label the system as $2.5A_4O$. In each material these fragments coordinate in a *trans* fashion about a vanadium ion, which is also coordinated by four Q^{2-} ions to produce a VQ_4O_2 octahedron, similar to that observed in the $La_2O_2Fe_2OSe_2$-type materials discussed previously. In $Sm_7VO_4Se_8$ the remaining Sm^{3+} ions are coordinated by Se^{2-} ions to create chains of edge-sharing $SmSe_6$ octahedra, and in $Eu_5V_3O_7S_6$ the remaining vanadium ions form another set of edge-sharing VO_2Se_4 octahedral chains. These materials are therefore good examples of more complex arrangements of the building blocks discussed throughout this chapter.

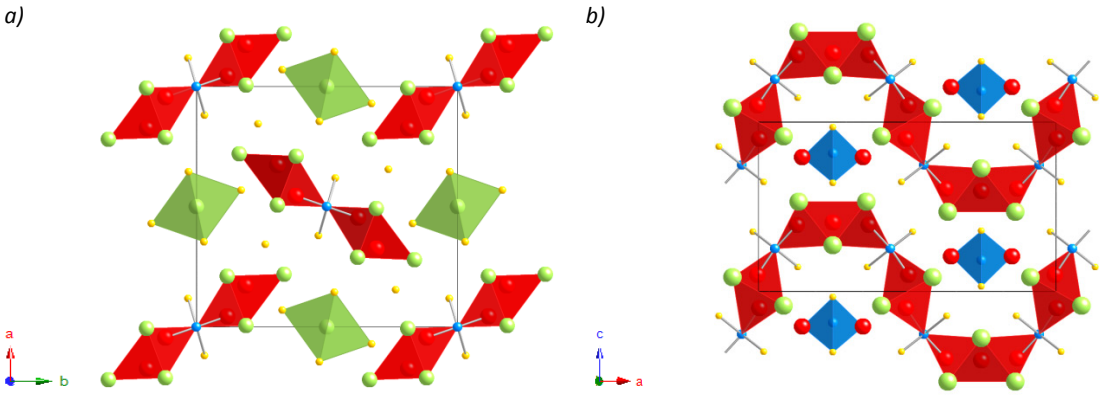

Figure 1.18 *Structures of (a) $Sm_7VO_4Se_8$ and (b) $Eu_5V_3O_7S_6$; Eu/Sm = green; V = blue, O = red, S/Se = yellow, unit cells are outlined.*

Two examples of 3A_4O materials are shown in *Figure 1.19*, and show the variety of structures that can be formed, ranging from pseudo-layered arrangements, as in $UY_4O_3S_5$, to more complex 3-dimensional arrangements, as in $La_{16}Ti_5S_{17.75}O_{17}$.[140, 141] In both of these materials we can see that, as in the previous examples, $[A_2O_2]^{2+}$ layers are broken by transition metal ions. In $UY_4O_3S_5$ these fragments share corners in a *trans* fashion to produce oxide chains, separated by edge-sharing YSe_6 octahedra, whereas in $La_{16}Ti_5S_{17.75}O_{17}$ 3OA_4 fragments are arranged in a *cis* fashion, forming a square (with an extra O^{2-} ion at each corner to complete the Ti^{4+} coordination sphere) that encases chains of corner-sharing $TiSe_6$ octahedra.

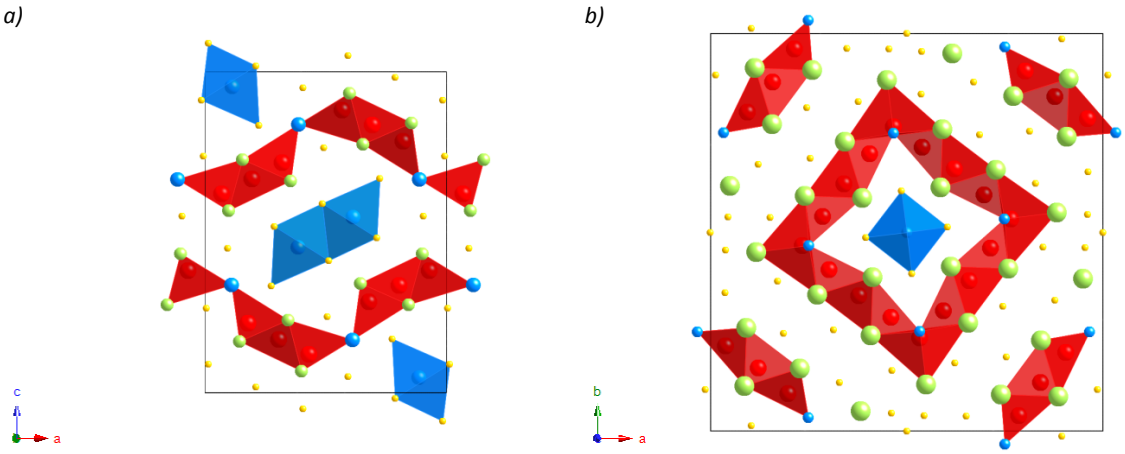

Figure 1.19 *Structures of (a) $UY_4O_3S_5$ and (b) $La_{16}Ti_5S_{17.75}O_{17}$ (right); La/U = green, Ti/Y = blue, O = red, S = yellow, unit cells are outlined.*

A pseudo-layered material that contains both MQ_4O_2 octahedra and $[A_2O_2]^{2+}$ fragments is the 4A_4O material $Gd_4TiSe_4O_4$ (*Figure 1.20*).[50] This material is closely related to the ternary material $La_4O_4Se_3$ (*Figure 1.1*), which contains infinite layers of edge-sharing La_4O tetrahedra separated by Se^{2-} ions. These layers are then broken into fragments, four tetrahedra across, which are linked by an octahedrally coordinated titanium ion. Magnetic measurements have suggested that this material remains paramagnetic on cooling, although the magnetic susceptibility does increase dramatically below 4 K. This increase has been attributed to ordering of the Gd^{3+} ions, however the ordering of these ions cannot be readily investigated using neutron diffraction due to the highly absorbing nature of Gd^{3+}.

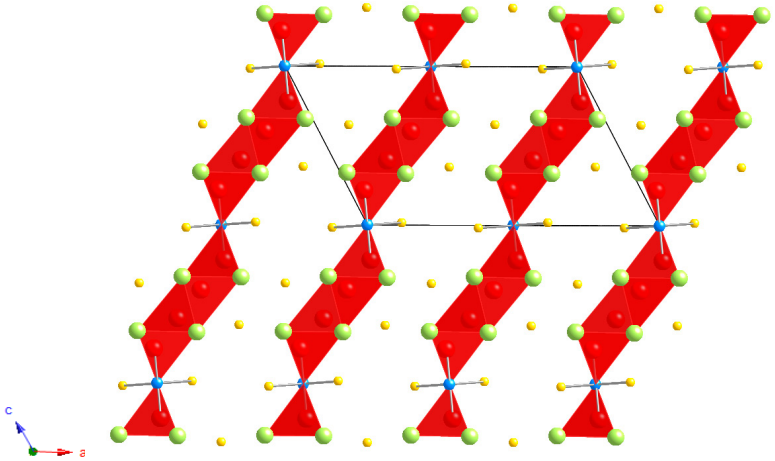

Figure 1.20 *Structure of $Gd_4TiSe_4O_4$; Gd = green, Ti = blue, O = red, Se = yellow, the unit cell is outlined.*

1.5 Conclusions & Project Aims

Whilst there are a range of different structures formed by transition metal oxychalcogenides, the most commonly observed crystallise with the ZrCuSiAs structure type. We have seen that there are a range of copper-containing materials that form with anti-PbO-type copper-chalcogenide layers, which, owing to their interesting electronic properties, have potential uses in LED technology. The iron-oxypnictide analogues of these materials contain iron-pnictide layers, and are demonstrated to superconduct at temperatures as high as 55 K. These iron-pnictide layers are a very important feature in these superconducting materials, and several other materials containing these layers have been demonstrated to superconduct. In addition to this α-FeSe has also been shown to superconduct, whilst this is suppressed in the tellurium analogue.

Work presented here will investigate related oxychalcogenides with the general formula $A_2O_2M Se_2$, where *A* is a lanthanide ion and *M* is a transition metal. These materials crystallise with two different structure-types. Chapter 7 will discuss the structure and magnetic properties of those similar to $CeOMn_{0.5}Se$ and $La_2O_2CdSe_2$, which adopt the ZrCuSiAs structure with only half of the transition metal sites occupied, whilst chapter 6 will discuss the structure solution of a new family of materials (termed β-$A_2O_2M Se_2$) that crystallise with a structure more akin to $Gd_4TiSe_2O_4$. The synthesis of ZrCuSiAs-type oxychalcogenides that contain Fe^{2+} ions is of particular interest due to the contrasting properties of Mott-insulating LaOCuSe and poor-metallic LaOFeAs.

The structures and properties of materials with the $La_2O_2Fe_2OSe_2$ structure have also been discussed and these should be viewed as key members (or even parent compounds) of the various superconducting families. These materials have been shown to order antiferromagnetically on cooling, although the magnetic structures proposed vary significantly. Chapter 3 will pay particular attention to the variable temperature structural and magnetic properties of the family of manganese containing materials, including the synthesis of a cerium-containing material, whilst chapter 4 will focus on the properties of $La_2O_2Fe_2OQ_2$ (*Q* = S, Se). Work presented in chapter 5 will further explore the range of transition and rare-earth metals over which materials with this structure can be prepared, and collate the conclusions of chapter 3–5.

1.6 References

1. Y. Kamihara, H. Hiramatsu, M. Hirano, K. Kawamura, H. Yanagi, T. Kamiya and H. Hosono, *J. Am. Chem. Soc.*, 2006, **128**, 10012-10013.
2. Y. Kamihara, T. Wantanbe, M. Hirano and H. Hosono, *J. Am. Chem. Soc.*, 2008, **130**, 3296-3297.
3. V. Kupčíc, *Naturwissenschaften*, 1967, **54**, 114-114.
4. I. Nakai, K. Koto, K. Nagashima and N. Morimoto, *Chem. Lett.*, 1977, 275-276.
5. C. Sabelli and G. Vezzalini, *Neues JB. Miner. Monat.*, 1987, 419-425.
6. S. J. Clarke, P. Adamson, S. J. C. Herkelrath, O. J. Rutt, D. R. Parker, M. J. Pitcher and C. F. Smura, *Inorg. Chem.*, 2008, **47**, 8473-8486.
7. W. Zachariasen, *Acta Cryst.*, 1949, **2**, 60-62.
8. H. A. Eick, *J. Am. Chem. Soc.*, 1958, **80**, 43-44.

9. H. A. Eick, *Acta Cryst.*, 1960, **13**, 161-161.
10. M. Guittard, J. Flahaut and L. Domange, *Acta Cryst.*, 1966, **21**, 832-832.
11. M. R. Ballestracci, *C. R. Acad. Sci. Hebd. Seances Acad. Sci. B*, 1967, **264**, 1736.
12. P. M. Raccah, J. M. Longo and H. A. Eick, *Inorg. Chem.*, 1967, **6**, 1471-1473.
13. Y. Abbas and J. Rossat-Mignod, *Solid State Commun.*, 1973, **12**, 985-991.
14. E. Koyama, I. Nakai and K. Nagashima, *Acta Cryst.*, 1984, **B40**, 105-109.
15. P. Schmidt, O. Rademacher, H. Oppermann and S. Däbritz, *Z. Anorg. Allg. Chem.*, 2000, **626**, 1999-2003.
16. R. Benz, *Acta Cryst.*, 1971, **B27**, 853-854.
17. F. A. Weber and T. Schleid, *Z. Anorg. Allg. Chem.*, 1999, **625**, 1833-1838.
18. E. W. Breeze and N. H. Brett, *J. Nucl. Mater.*, 1971, **40**, 113-115.
19. M. Machida, K. Kawamura, K. Iro and K. Ikeue, *Chem. Mater.*, 2005, **17**, 1487-1492.
20. M. Machida, T. Kawano, M. Eto, D. Zhang and K. Ikeue, *Chem. Mater.*, 2007, **19**, 954-960.
21. K. Ikeue, T. Kawano, M. Eto, D. Zhang and M. Machida, *J. Alloy Compd.*, 2008, **451**, 338-340.
22. M. Julien-Pouzol, S. Jaulmes, M. Guittard and P. Laruelle, *J. Solid State Chem.*, 1978, **26**, 185-188.
23. F. A. Weber and T. Schleid, *Z. Anorg. Allg. Chem.*, 2001, **627**, 1383-1388.
24. S. Strobel, A. Choudhury, P. K. Dorhout, C. Lipp and T. Schleid, *Inorg. Chem.*, 2008, **47**, 4936-4944.
25. J. Dugue, C. Adolphe and P. Khodadad, *Acta Cryst.*, 1970, **B26**, 1627-1628.
26. R. W. M. D'Eye, P. G. Sellman and J. R. Murray, *J. Chem. Soc.*, 1952, 2555-2562.
27. R. W. M. D'Eye and P. G. Sellman, *J. Chem. Soc.*, 1954, 3760-3766.
28. R. Ferro, *Z. Anorg. Allg. Chem.*, 1954, **275**, 320-326.
29. W. Trzebiatowski, J. Niemiec and A. Sepichowska, *B. Acad. Pol. Sci.-Chim.*, 1961, **9**, 373-377.
30. G. B. Jin, A. D. Raw, S. Skanthakumar, R. G. Haire, L. Soderholm and J. A. Ibers, *J. Solid State Chem.*, 2010, **183**, 547-550.
31. J. D. McCulloch, L. Brewer and L. A. Bromley, *Acta Cryst.*, 1948, **1**, 287-289.
32. G. A. Eisman and H. Steinfink, *J. Solid State Chem.*, 1982, **43**, 225-226.
33. N. D. Boscher, C. J. Carmalt, A. G. Prieto, Q. A. Pankhurst, R. G. Palgrave and I. P. Parkin, *Eur. J. Inorg. Chem.*, 2007, 4579-4582.
34. Y.-Z. Huang, L. Chen and L.-M. Wu, *Cryst. Growth. Des*, 2008, **8**, 739-743.
35. Z. Liu, X. Sun, S. Xu, J. Lian, X. Li, Z. Xiu, Q. Li, D. Huo and J.-G. Li, *J. Phys. Chem. C*, 2008, **112**, 2353-2358.
36. J. S. O. Evans, E. B. Brogden, A. L. Thompson and R. L. Cordiner, *Chem. Commun.*, 2002, 912-913.
37. H. Hiramatsu, K. Ueda, T. Kamiya, H. Ohta, M. Hirano and H. Hosono, *J. Mater. Chem.*, 2004, **14**, 2946-2950.
38. J. M. Mayer, L. F. Schneemeyer, T. Siegrist, J. V. Waszczak and B. v. Dover, *Angew. Chem. Int. Ed. Engl.*, 1992, **31**, 1645-1647.
39. P. Quebe, L. J. Terbüchte and W. Jeitschko, *J. Alloy Compd.*, 2000, **302**, 70-74.
40. Y. Chen, J. W. Lynn, J. Li, G. Li, G. F. Chen, J. L. Luo, N. L. Wang, P. Dai, C. de la Cruz and H. A. Mook, *Phys. Rev. B*, 2008, **78**, 064515.
41. P. Cheng, L. Fang, H. Yang, X. Zhu, G. Mu, H. Luo, Z. Wang and H. Wen, *Sci. China Ser. G*, 2008, **51**, 719-722.
42. C. de la Cruz, Q. Huang, J. W. Lynn, J. Li, W. Ratcliff II, J. L. Zarestky, H. A. Mook, G. F. Chen, J. L. Luo, N. L. Wang and P. Dai, *Nature*, 2008, **453**, 899-902.
43. Z. A. Ren, W. Lu, J. Yang, W. Yi, X.-L. Shen, Z.-C. Li, G.-C. Che, X. L. Dong, L. L. Sun, F. Zhou and Z. X. Zhao, *Chin. Phys. Lett.*, 2008, **25**, 2215-2216.
44. Y. Takahashi, K. Igawa, K. Arii, Y. Kamihara, M. Hirano and H. Hosono, *Nature*, 2008, **453**, 376-378.
45. J. Zhao, Q. Huang, C. de la Cruz, S. Li, J. W. Lynn, Y. Chen, M. A. Green, G. F. Chen, G. Li, Z. Li, J. L. Luo, N. L. Wang and P. Dai, *Nature Mater.*, 2008, **7**, 953-959.
46. J. Zhao, Q. Huang, C. de la Cruz, J. W. Lynn, M. D. Lumsden, Z. A. Ren, J. Yang, X. Shen, X. Dong, Z. Zhao and P. Dai, *Phys. Rev. B*, 2008, **78**, 132504.
47. R. J. Cava, H. W. Zandbergen, J. J. Krajewski, T. Siegrist, H. Y. Hwang and B. Batlogg, *J. Solid State Chem.*, 1997, **129**, 250-256.
48. W. E. Pickett, *Phys. Rev. B*, 1998, **58**, 4335-4340.
49. S. J. Clarke, B. P. Guinot, C. W. Michie, M. J. C. Calmont and M. J. Rosseinsky, *Chem. Mater.*, 2002, **14**, 288-294.
50. A. Meerschaut, A. Lafond, V. Meignen and C. Deudon, *J. Solid State Chem.*, 2001, **162**, 182-187.
51. T. D. Brennan, L. E. Aleandri and J. A. Ibers, *J. Solid State Chem.*, 1991, **91**, 312-322.
52. T. D. Brennan and J. A. Ibers, *J. Solid State Chem.*, 1992, **98**, 82-89.
53. C. Deudon, A. Meerschaut, L. Cario and J. Rouxel, *J. Solid State Chem.*, 1995, **120**, 164-169.

54. G. Guo, Y. Wang, J. Chen, H. Zhuang, J. Huang and Q. Zang, *Acta Cryst.*, 1995, **C51**, 1964-1966.
55. J. A. Cody, C. Deudon, L. Cario and A. Meerschaut, *Mater. Res. Bull.*, 1997, **32**, 1181-1192.
56. V. Meignen, A. Meerschaut, L. Cario and A. Lafond, *J. Solid State Chem.*, 2005, **178**, 1637-1643.
57. R. Pottgen and D. Johrendt, *Z. Naturforsch*, 2008, **63b**, 1135-1148.
58. M. Palazzi, *C. R. Acad. Sci. Hebd. Seances Acad. Sci. C*, 1981, **292**, 7899.
59. K. Ishikawa, S. Kinoshita, Y. Suzuki, S. Matsuura, T. Nakanishi, M. Aizawa and Y. Suzuki, *J. Electrochem. Soc.*, 1991, **138**, 1166-1170.
60. A. M. Kusainova, P. S. Berdonosov, L. G. Akselrud, L. N. Kholodkovskaya, V. A. Dolgikh and B. A. Popovkin, *J. Solid State Chem.*, 1994, **112**, 189-191.
61. D. O. Charkin, A. V. Akopyan and V. A. Dolgikh, *Russ. J. Inorg. Chem.*, 1999, **44**, 833-837.
62. K. Ueda, K. Takafuji, H. Ohta, T. Kamiya, M. Hirano and H. Hosono, *Chem. Mater.*, 2003, **15**, 3692-3695.
63. T. Ohtani, M. Hirose, T. Sato, K. Nagaoka and M. Iwabe, *Jpn. J. Appl. Phys.*, 1993, **32 (Suppl. 32-3)**, 316-318.
64. B. A. Popovkin, A. M. Kusainova, V. A. Dolgikh and L. G. Aksel'rud, *Russ. J. Inorg. Chem.*, 1998, **43**, 1471-1475.
65. M. L. Liu, L. B. Wu, F. Q. Huang, L. D. Cheng and J. A. Ibers, *J. Solid State Chem.*, 2007, **180**, 62-69.
66. H. Hiramatsu, H. Yanagi, T. Kamiya, K. Ueda, M. Hirano and H. Hosono, *Chem. Mater.*, 2008, **20**, 326-334.
67. M. Palazzi, C. Carcaly and J. Flahaut, *J. Solid State Chem.*, 1980, **35**, 150-155.
68. G. H. Chan, B. Deng, M. I. Bertoni, J. R. Ireland, M. C. Hersam, T. O. Mason, R. P. v. Duyne and J. A. Ibers, *Inorg. Chem.*, 2006, **45**, 8264-8272.
69. D. O. Charkin, P. S. Berdonosov, V. A. Dolgikh and P. Lightfoot, *Russ. J. Inorg. Chem.*, 2000, **45**, 182-189.
70. B. I. Zimmer, W. Jeitschko, J. H. Albering, R. Glaum and M. Reehuis, *J. Alloy Compd.*, 1995, **229**, 238-242.
71. A. L. Allred, *J. Inorg. Nucl. Chem.*, 1961, **17**, 215-221.
72. O. Schob and E. Parthe, *Acta Cryst.*, 1965, **19**, 214-224.
73. M. J. Pitcher, C. F. Smura and S. J. Clarke, *Inorg. Chem.*, 2009, **48**, 9054-9056.
74. K. Ueda, S. Inoue, S. Hirose, H. Kawazoe and H. Hosono, *Appl. Phys. Lett.*, 2000, **77**, 2701-2703.
75. K. Ueda, H. Hiramatsu, H. Ohta, M. Hirano, T. Kamiya and H. Hosono, *Phys. Rev. B*, 2004, **69**, 155305.
76. S.-i. Inoue, K. Ueda, H. Hosono and N. Hamada, *Phys. Rev. B*, 2001, **64**, 245211.
77. J. Llanos, R. Cortés, T. Guizouarn and O. Peña, *Mater. Res. Bull.*, 2006, **41**, 1266-1271.
78. W. C. Sheets, E. S. Stampler, H. Kabbour, M. I. Bertoni, L. Cario, T. O. Mason, T. J. Marks and K. P. Poeppelmeier, *Inorg. Chem.*, 2007, **46**, 10741-10748.
79. H. Hiramatsu, K. Ueda, H. Ohta, M. Hirano, T. Kamiya and H. Hosono, *Thin Solid Films*, 2003, **445**, 304-308.
80. K. Ueda, H. Hiramatsu, M. Hirano, T. Kamiya and H. Hosono, *Thin Solid Films*, 2006, **496**, 8-15.
81. H. Hosono, *Thin Solid Films*, 2007, **515**, 6000-6014.
82. H. Hiramatsu, K. Ueda, H. Ohta, T. Kamiya and M. Hirano, *Appl. Phys. Lett.*, 2005, **87**, 211107.
83. H. Hiramatsu, K. Ueda, H. Ohta and M. Hirano, *Appl. Phys. Lett.*, 2003, **82**, 1048-1050.
84. M. Palazzi and S. Jaulmes, *Acta Cryst.*, 1981, **B37**, 1337-1339.
85. D. Wilmer, J. D. Jorgensen and B. J. Wuensch, *Solid State Ionics*, 2000, **136-137**, 961-966.
86. J. Llanos, R. Cortés and V. Sánchez, *Mater. Res. Bull.*, 2008, **43**, 320-325.
87. J. Llanos and O. Pena, *J. Solid State Chem.*, 2005, **178**, 957-960.
88. H. Nakao, Y. Takano, K. Takase, H. Sato, S. Hara, S. Ikeda, Y. Takahashi and K. Sekizawa, *J. Alloy Compd.*, 2006, **408-412**, 104-106.
89. H. Hiramatsu, K. Ueda, T. Kamiya, H. Ohta, M. Hirano and H. Hosono, *J. Phys. Chem. B*, 2004, **108**, 17344-17351.
90. I. Ijjaali, K. Mitchell, C. L. Haynes, A. D. McFarland, R. P. van Duyne and J. A. Ibers, *J. Solid State Chem.*, 2003, **176**, 170-174.
91. J. Dugue and M. Guittard, *Acta Cryst.*, 1982, **B38**, 2368-2371.
92. F. Q. Huang, P. Brazis, C. R. Kannewurf and J. A. Ibers, *J. Solid State Chem.*, 2000, **155**, 366-371.
93. S. Broadley, Z. A. Gal, F. Cora, C. F. Smura and S. J. Clarke, *Inorg. Chem.*, 2005, **44**, 9092-9096.
94. T. Sambrook, C. F. Smura and S. J. Clarke, *Inorg. Chem.*, 2007, **46**, 2571-2574.
95. Y. Xia, F. Q. Huang, W. Wang, A. Wang and J. Shi, *Solid State Sci.*, 2007, **9**, 1074-1078.
96. T. C. Ozawa and S. M. Kauzlarich, *Sci. Technol. Adv. Mater.*, 2008, **9**, 033003.
97. M. Tegel, I. Schellenberg, R. Pottgen and D. Johrendt, *Z. Naturforsch*, 2008, **63b**, 1057-1061.

98. R. E. Baumbach and et al., *New J. Phys.*, 2009, **11**, 025018.
99. G. F. Chen, Z. Li, D. Wu, G. Li, W. Z. Hu, J. Dong, P. Zheng, J. L. Luo and N. L. Wang, *Phys. Rev. Lett.*, 2008, **100**, 247002.
100. Z.-A. Ren and et al., *Europhys. Lett.*, 2008, **82**, 57002.
101. S. Muir, A. W. Sleight and M. A. Subramanian, *Mater. Res. Bull.*, 2010, **45**, 392-395.
102. M. Xu, F. Chen, H.-W. Ou, J.-F. Zhao and D.-L. Feng, *Chem. Mater.*, 2008, **20**, 7201-7203.
103. T. M. McQueen, M. Regulacio, A. J. Williams, Q. Huang, J. W. Lynn, Y. S. Hor, D. V. West, M. A. Green and R. J. Cava, *Phys. Rev.*, 2008, **B78**, 024521.
104. S. A. J. Kimber, D. N. Argyriou, F. Yokaichiya, K. Habicht, S. Gerischer, T. Hansen, T. Chetterji, R. Klingeler, C. Hess, G. Behr, A. Kondrat and B. Buchner, *Phys. Rev. B*, 2008, **78**, 140503.
105. J. W. Lynn and P. Dai, *Physica C*, 2009, **469**, 469-476.
106. Y. Qui, W. Bao, Q. Huang, T. Yildirim, J. M. Simmons, M. A. Green, J. W. Lynn, Y. C. Gasparovic, J. Li, T. Wu, G. Wu and X. H. Chen, *Phys. Rev. Lett.*, 2008, **101**, 257002.
107. A. J. Drew, C. Niedermayer, P. J. Baker, F. L. Pratt, S. J. Blundell, T. Lancaster, R. H. Liu, G. Wu, X. H. Chen, I. Watanabe, V. K. Malik, A. Dubroka, M. Rossle, K. W. Kim, C. Baines and C. Bernhard, *Nat. Mater*, 2009, **8**, 310-314.
108. M. J. Pitcher, D. R. Parker, P. Adamson, S. J. C. Herkelrath, A. T. Boothroyd, R. M. Ibberson, M. Brunelli and S. J. Clarke, *Chem. Commun.*, 2008, 5918-5920.
109. J. H. Tapp, Z. Tang, B. Lv, K. Sasmal, B. Lorenz, P. C. W. Chu and A. M. Guloy, *Phys. Rev. B*, 2008, **78**, 060505.
110. M. Rotter, M. Tegel and D. Johrendt, *Phys. Rev. Lett.*, 2008, **101**, 107006.
111. X. Zhu, F. Han, G. Mu, B. Zeng, P. Cheng, B. Shen and H.-H. Wen, *Phys. Rev. B*, 2009, **79**, 024516.
112. J. Paglione and R. L. Greene, *Nat. Phys*, 2010, **6**, 645-658.
113. F. C. Hsu, J. Y. Luo, K. W. Yeh, T. K. Chen, T. W. Huang, P. M. Wu, Y. C. Lee, Y. L. Huang, Y. Y. Chu, D. C. Yan and M. K. Wu, *P. Natl. Acad. Sci. USA*, 2008, **105**, 14262-14264.
114. S. Margadonna, Y. Takabayashi, M. T. McDonald, K. Kasperkiewicz, Y. Mizuguchi, Y. Takano, A. N. Fitch, E. Suard and K. Prassides, *Chem. Commun.*, 2008, 5607-5609.
115. S. Medvedev, T. M. McQueen, I. A. Troyan, T. Palasyuk, M. I. Eremets, R. J. Cava, S. Naghavi, F. Casper, V. Ksenofontov, G. Wortmann and C. Felser, *Nat. Mater*, 2009, **8**, 630-633.
116. Y. Xia, F. Huang, X. Xie and M. Jiang, *Europhys. Lett.*, 2009, **86**, 37008.
117. K. W. Yeh, T. W. Huang, Y. L. Huang, T. K. Chen, F. C. Hsu, P. M. Wu, Y. C. Lee, Y. Y. Chu, C. L. Chen, J. L. Luo, D. C. Yan and M. K. Wu, *Europhys. Lett.*, 2008, **84**, 37002.
118. S. Li, C. de la Cruz, F. Q. Huang, Y. Chen, J. W. Lynn, J. Hu, Y. L. Huang, F. C. Hsu, K. W. Yeh, M. K. Wu and P. Dai, *Phys. Rev. B*, 2009, **79**, 054503.
119. D. Fruchart, P. Convert, P. Wolfers, R. Madar, J. P. Senateur and R. Fruchart, *Mater. Res. Bull.*, 1975, **10**, 169-174.
120. C. Fang, B. A. Bernevig and J. Hu, *Europhys. Lett.*, 2009, **86**, 67005.
121. N. D. Withers, *Synthesis and Characterisation of New Layered Oxychalcogenide Materials*, Durham University, *Ph.D.*, Durham, 2005.
122. P. Hickey, *Synthesis and Chemistry of New Layered Chalcogenides and Oxychalcogenides*, Durham University, *M.Chem.*, Durham, 2004.
123. Y. Fuwa, M. Wakeshima and Y. Hinatsu, *Solid State Commun.*, 2010, **150**, 1698-1701.
124. Y. Fuwa, M. Wakeshima and Y. Hinatsu, *J. Phys.: Condens. Matter*, 2010, **22**, 346003.
125. R. H. Liu, Y. A. Song, Q. J. Li, J. J. Ying, Y. J. Yan, Y. He and X. H. Chen, *Chem. Mater.*, 2010, **22**, 1503-1508.
126. C. Wang, M.-q. Tan, C.-m. Feng, Z.-f. Ma, S. Jiang, Z.-a. Xu, G.-h. Cao, K. Matsubayashi and Y. Uwatoko, *J. Am. Chem. Soc.*, 2010, **132**, 7069-7073.
127. H. Kabbour, E. Janod, B. Corraze, M. Danot, C. Lee, M.-H. Whangbo and L. Cario, *J. Am. Chem. Soc.*, 2008, **130**, 8261-8270.
128. D. G. Free, *Synthesis and Chemistry of New Layered Oxychalcogenides*, Durham University, *M.Chem.*, Durham, 2007.
129. R. D. Shannon, *Acta Cryst.*, 1976, **A32**, 751-767.
130. J. X. Zhu, R. Yu, H. Wang, L. L. Zhao, M. D. Jones, J. Dai, E. Abrahams, E. Morosan, M. Fang and Q. Si, *Phys. Rev. Lett.*, 2010, **104**, 216405.
131. H. Wu, *Phys. Rev. B*, 2010, **82**, 020410.
132. Y. B. Park, D. C. Degroot, J. L. Schindler, C. R. Kannewurf and M. G. Kanatzidis, *Chem. Mater.*, 1993, **5**, 8-10.
133. G. Chacon, X. Long and C. Zheng, *J. Alloy Compd.*, 1994, **216**, 177-182.
134. A. Adam and H. U. Schuster, *Z. Anorg. Allg. Chem.*, 1990, **584**, 150-158.

135. T. C. Ozawa, R. Pantoja, E. A. Axtell, S. M. Kauzlarich, J. E. Greedan, M. Bieringer and J. W. Richardson, *J. Solid State Chem.*, 2000, **153**, 275-281.
136. R. H. Liu, D. Tan, Y. A. Song, Q. J. Li, Y. J. Yan, J. J. Ying, Y. L. Xie, X. F. Wang and X. H. Chen, *Phys. Rev. B*, 2009, **80**, 144516.
137. T. C. Ozawa and S. M. Kauzlarich, *Chem. Mater.*, 2001, **13**, 1804-1810.
138. A. Meerschaut, A. Lafond, P. Palvadeau, C. Deudon and L. Cario, *Mater. Res. Bull.*, 2002, **37**, 1895-1905.
139. O. Tougait and J. A. Ibers, *J. Solid State Chem.*, 2000, **154**, 564-568.
140. G. B. Jin, E. S. Choi, D. M. Wells and J. A. Ibers, *J. Solid State Chem.*, 2009, **182**, 1861-1866.
141. V. Meignen, A. Lafond, L. Cario, C. Deudon and A. Meerschaut, *Acta Cryst.*, 2003, **C59**, i63-i64.

Experimental Details & Structure Analysis

2.1 Introduction

This chapter will discuss the methods used in the synthesis and structural analysis of the materials reported in this work. Due to the polycrystalline nature of all of the materials prepared, structural analysis was performed using X-ray, and in some cases neutron, powder diffraction. Magnetic properties were also investigated, using a combination of neutron diffraction and magnetic susceptibility measurements. The theory and application of these techniques, alongside the methods used in data analysis will be discussed.

2.2 Experimental Details

The starting materials used in the following synthesis of both $A_2O_2M_2OQ_2$ and $A_2O_2MSe_2$-type materials are given below (*Table 2.1)*. These syntheses can each be broken into two main parts, preparation of the A_xO_y starting material (where A = La–Gd), and synthesis of the target material. Preparation of the A_xO_y starting materials involved heating the materials prior to use, and storing them in an inert atmosphere (nitrogen filled glovebox), to ensure that unwanted CO_2 and moisture were not evolved during the final synthesis. This was important as all reactions took place in sealed quartz ampoules.

Table 2.1 *Summary of the starting materials used in the syntheses.*

Reagent		Supplier	Purity
A_xO_y	La_2O_3	Alfa Aesar	99.99 %
	CeO_2	Alfa Aesar	99.99 %
	Pr_6O_{11}	Alfa Aesar	99.99 %
	Nd_2O_3	Electronic Materials	99 %
	Sm_2O_3	BDH Chemicals	99.9 %
	Y_2O_3	Sigma-Aldrich	99.99 %
M	Ti	BDH Chemicals	unknown
	Mn	Avocado	99+ %
	Fe	Aldrich	99.9+ %
	Co	Fisons	unknown
	Cu	Aldrich (Goodfellow Metals)	99.99+ %
	Zn	Alfa-Aesar	99.9 %
Q	S	Aldrich	99.98 %
	Se	Alfa-Aesar	99.999 %

2.2.1 Preparation of the A_xO_y starting materials

All of the A_xO_y materials were prepared similarly apart from Pr_2O_3, which was made from Pr_6O_{11} using an method outlined by Faeth and Clifford.[1] This method was preferred to others reported, as it did not involve the use of H_2 gas.

A = La, Ce, Nd, Sm & Y

Weighed solid A_2O_3 (or CeO_2 in the case of cerium) was heated in an alumina crucible in a furnace at 800 ^oC for eight hours in order to remove any CO_2 or H_2O adsorbed to the surface. After cooling, the

sample was then re-weighed and placed in a glovebox, to ensure no further contamination. A small sample was retained for X-ray powder diffraction (XRPD) to ensure phase purity.

A = Pr

Solid, black, Pr_6O_{11} was measured into an alumina crucible and heated in a tube furnace under vacuum at 1000 ^{o}C for 15 h. The resulting, beige/green, material was then cooled, immediately characterised and used in the synthesis of the target phase. The change in colour of the material was consistent with that published.[2, 3]

2.2.2 Synthesis of $A_2O_2M_2OQ_2$ materials

In the case of La^{3+}, Pr^{3+}, Nd^{3+}, Sm^{3+} and Y^{3+}-containing target materials, stoichiometric amounts of A_2O_3, *M* and *Q* powders were weighed out to within ±0.0001 g (*Table 2.2*), and ground together in an agate mortar and pestle. Minimum time was spent weighing out the A_2O_3 material, and the process was carried out quickly to ensure minimal uptake of CO_2 / H_2O. The resulting powder was pressed into two 5 mm (diameter) pellets using a pellet die with a force of ~1 tonne. The pellets were then placed inside a 7 mm, high density, alumina crucible, and this placed inside an 11 mm (inner diameter) quartz tube. This was then evacuated for ~10 min at ~0.1 mbar and flame sealed. The sealed tube was then placed in a furnace and heated as follows:

- Ramp at 1 ^{o}C.min^{-1} to 600 ^{o}C and dwell for 12 h
- Ramp at ½ ^{o}C.min^{-1} to 800 ^{o}C and dwell for 1 h
- Ramp at 1 ^{o}C.min^{-1} to 1000 ^{o}C and dwell for 12 h
- Cool to room temperature

In the case of Ce^{3+}-containing materials, the procedure above was employed, however with a stoichiometric (by cerium content) amount of CeO_2. Excess oxygen was removed *in situ* by the presence of a second alumina crucible containing a 10 % molar excess of Al metal powder (*Figure 2.1*); for example, in the synthesis of $Ce_2O_2Mn_2OSe_2$, using the masses outlined in *Table 2.2*, 0.0297 g of Al was used (0.0270 + 0.0027 g). The contents of this crucible were later confirmed to be Al and Al_2O_3 powder by XRPD.

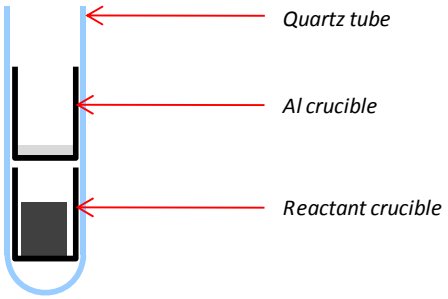

Figure 2.1 *Quartz tube contents for a reaction involving an Al getter.*

The equations for these syntheses are shown below:

$$A_2O_3 + 2M + 2Q \xrightarrow{1000\,^{o}C} A_2O_2M_2OQ_2$$

$$2CeO_2 + 2M + 2Q \xrightarrow[-\frac{1}{3}Al_2O_3]{1000\,^{\circ}C,\ +\frac{2}{3}Al} Ce_2O_2M_2OQ_2$$

The samples were removed at room temperature and the ampoules broken open, using a hammer. The resulting pellets were removed from the crucibles using tweezers. These were then ground, taking care to remove any surface impurities and analysed using XRPD. A summary of all the syntheses attempted is given at the end of this chapter in *Table 2.10*.

Table 2.2 *Masses of reagents used in the preparation of $A_2O_2M_2OQ_2$ materials.*

Reagent		Mass (g)	Moles (mmol)
A_xO_y	La_2O_3	*0.4887*	*1.5*
	Pr_2O_3	*0.4947*	
	Nd_2O_3	*0.5047*	
	Sm_2O_3	*0.5231*	
	CeO_2	*0.5163*	*3.0*
M	Ti	*0.1436*	*3.0*
	Mn	*0.1648*	
	Fe	*0.1675*	
	Co	*0.1768*	
	Cu	*0.1906*	
	Zn	*0.1961*	
Q	S	*0.0962*	*3.0*
	Se	*0.2369*	
Al	*for A = Ce*	*0.0297*	*1.1*

Successfully prepared samples that contained small amounts of impurity phases were reground, pressed in a pellet, placed sealed in a quartz tube under vacuum and refired at 1000 ^{o}C for 12 h.

$A_2O_2(Mn_{0.5}Fe_{0.5})_2OSe_2$ (A = La, Pr, Nd, Sm)

The same procedure as outlined above was carried out, however a 1:1 mixture of Mn:Fe was prepared by grinding Fe (1.5 mmol, 0.0838 g) and Mn (1.5 mmol, 0.0843 g) together to give 3.0 mmol of *M* to use in the remainder of the synthesis.

$(La_{½}Nd_{½})_2O_2Mn_2OSe_2$

Again the same method was used, however a 2:1 ratio of La_2O_3 (1.0 mmol, 0.3258 g) and Nd_2O_3 (0.5 mmol, 0.1682 g) was ground together to give 1.5 mmol of A_2O_3 to use in the remainder of the synthesis.

2.2.3 Synthesis of $A_2O_2MSe_2$ materials

For La^{3+}, Pr^{3+}, Nd^{3+}, Sm^{3+} and Gd^{3+}-containing target materials, stoichiometric amounts of A_2O_3, *M* and *Q* powders were weighed out to within ±0.0001 g (*Table 2.2*), and ground together in an agate mortar and pestle. It was observed that these reactions worked equally well whether the reagents were pressed

into a pellet or left as a loose powder, and therefore the powder was loaded inside a 7 mm, high density, alumina crucible after grinding. The crucible was then placed inside an 11 mm (inner diameter) quartz tube alongside a crucible containing an Al getter to remove excess oxygen; again a 10 % stoichiometric excess of Al was used. This was then evacuated for ~10 min at ~0.1 mbar and flame sealed. The sealed tube was then placed in a furnace and heated as follows:

- Ramp at 1 ^{o}C.min^{-1} to 600 ^{o}C and dwell for 12 h
- Ramp at ½ ^{o}C.min^{-1} to 800 ^{o}C and dwell for 1 h
- Ramp at 1 ^{o}C.min^{-1} to 1100 ^{o}C and dwell for 12 h
- Cool to room temperature

The samples were removed at room temperature and the ampoules broken open, using a hammer, taking care not to spill any powder. The products of both crucibles were then individually ground, and analysed using XRPD. The equations for these reactions are shown below, and masses for reagents are given in *Table 2.3*.

$$A_2O_3 + M + 2Se \xrightarrow[-\frac{1}{3}Al_2O_3]{1000\,^{\circ}C,\ +\frac{2}{3}Al} A_2O_2MSe_2$$

$$2CeO_2 + M + 2Se \xrightarrow[-\frac{2}{3}Al_2O_3]{1000\,^{\circ}C,\ +\frac{4}{3}Al} Ce_2O_2MSe_2$$

Table 2.3 *Masses of reagents used in the preparation of $A_2O_2MQ_2$ materials.*

Reagent		Mass (g)	Moles (mmol)
A_xO_y	La_2O_3	*0.4887*	*1.5*
	Pr_2O_3	*0.4947*	
	Nd_2O_3	*0.5047*	
	Sm_2O_3	*0.5231*	
	Gd_2O_3	*0.5438*	
	CeO_2	*0.5163*	*3.0*
M	Mn	*0.0843*	*1.5*
	Fe	*0.0838*	
	Zn	*0.0981*	
Q	Se	*0.2369*	*3.0*
Al	*for A ≠ Ce*	*0.0297*	*1.1*
	for A = Ce	*0.0594*	*2.2*

A summary of all the syntheses attempted is given in *Table 2.10*. Note that several syntheses were repeated at 900 and 1000 °C, however it was found that purer samples were formed at 1100 °C.

2.2.4 Structure Analysis

All materials were analysed using X-ray powder diffraction, and the programs EVA and TOPAS Academic (TOtal Pattern Analysis Software, referred to throughout this work as TA) were used to identify and analyse the material(s) present.[4, 5] Structural information for the $La_2O_2Fe_2OSe_2$ and $CeOMn_{0.5}Se$ based syntheses was acquired from the ICSD using entry numbers 67657 and 97534, respectively.[6] Details of the measurements and sample preparation are discussed further on.

2.3 X-ray Powder Diffraction

Diffraction is one of the most important techniques employed in the characterisation of crystalline materials, as it gives potentially precise and accurate data on the positions of atoms within, and the dimensions of, a unit cell. This section will discuss the theory behind X-ray diffraction (XRD) and also the instrumentation and methods employed in analysis of samples and data.

2.3.1 Diffraction

Diffraction is an interference phenomenon caused when electromagnetic radiation interacts with a suitable grating. This grating causes the radiation passing through to act as if it were emanating from a series of point sources. These "new" electromagnetic waves then interfere with one another and the net result of this is that intense areas of light are observed when the light interferes constructively, *i.e.* when these waves are in-phase with each other. This interaction, shown in *Figure 2.2*, is described by *eqn 2.1*. This states, that in order to observe intensity in a diffraction pattern, the path difference, which is related to *a*sinθ, must be equal to the wavelength of light (λ) multiplied by an integer (*n*).

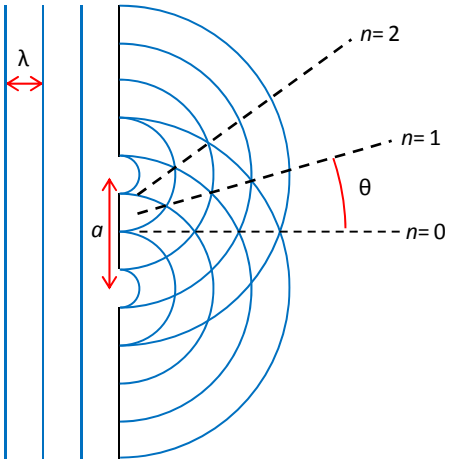

Figure 2.2 *Diffraction through a grating.*

$$n\lambda = a\sin\theta \qquad \textbf{eqn 2.1}$$

This phenomenon is also observed in crystalline materials, where the periodic arrangement of atoms can act as a diffraction grating. The repeating symmetry in a material is defined by its unit cell, which has dimensions *a*, *b* and *c* and internal angles of α, β and γ. As diffraction effects are maximised when the wavelength of the radiation is similar to the width of the grating, X-rays are used for these experiments, as they have wavelengths of the same order of magnitude as interatomic distances. Strictly speaking, it is the oscillation of electrons that interact with incident X-rays (X-rays approaching a sample) and act as emitters of scattered radiation. The re-radiated X-rays are then able to interfere with one another producing intense areas of electromagnetic radiation.

Bragg's law (*eqn 2.2* & *Figure 2.3*), which develops from *eqn 2.1*, describes the scattering of X-rays by crystallographic planes (the Miller planes). Here, X-rays are described as being reflected by adjacent planes, before interfering as seen earlier. Knowing the path difference between two beams of light (*A* & *B*) allows us to calculate the *d*-spacing, which is the distance between these planes. This is then related

the size of the unit cell by and equation like *eqn 2.3*, where *d* is *d*-spacing, *a*, *b* and *c* are the unit cell dimensions, and *h*, *k* and *l* are the Miller indices. Note that *eqn 2.3* is for an orthorhombic unit cell and the equation differs for higher and lower symmetry systems.

$$n\lambda = 2d_{hkl}\sin\theta \qquad \textbf{eqn 2.2}$$

$$\frac{1}{d^2} = \frac{h^2}{a^2} + \frac{k^2}{b^2} + \frac{l^2}{c^2} \qquad \textbf{eqn 2.3}$$

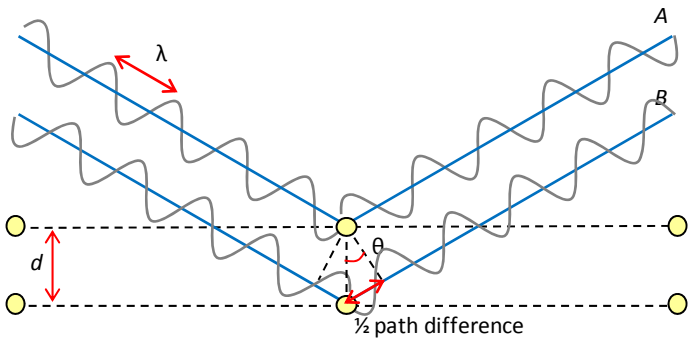

Figure 2.3 *Bragg's Law.*

The intensity of a specific reflection is related to the unit cell contents by the structure factor equation (*eqn 2.4*). The structure factor relates the positions of individual atoms (*xyz*), the Miller indices (*hkl*), and the scattering factor of the atoms to the observed intensities. Intensities are then recorded producing the diffraction pattern.

$$F_{hkl} = \sum_j f_j \exp\left[2\pi i\left(hx_j + ky_j + lz_j\right)\right] \qquad \textbf{eqn 2.4}$$

2.3.2 Powder Diffraction

The most powerful XRD technique is single crystal X-ray diffraction. This can be readily used to produce an accurate 3-dimensional description of electron density within a unit cell. Unfortunately, this technique is not always practical, for example if a material only forms small crystals (crystallites). In this case powder diffraction techniques can be implemented.

Unlike in single crystal diffraction, a powder consists of an infinite number of crystals, crystallites, arranged with random orientations. The result of this is that instead of observing spots of intensity we observe cones (*Figure 2.4*). Data is collected by intercepting these cones and measuring the intensity of a peak relative to the angle of the reflection (2θ). The result is a 1-dimensional pattern, which, due to peak overlap, contains far less information than single crystal data. Although it is possible to solve structures from powder data it is more common to use a starting model, and refine this relative to the data collected. This is called the Rietveld method and is discussed in section 2.5. On a basic level the positions of the peaks in a diffraction pattern tells us about the size/shape of the unit cell, and their intensities relate to the atomic positions within the cell. Also, information on the size of a crystallite, any strain it may experience and any short range ordering within a structure can be gathered from peak widths and background oscillations respectively.

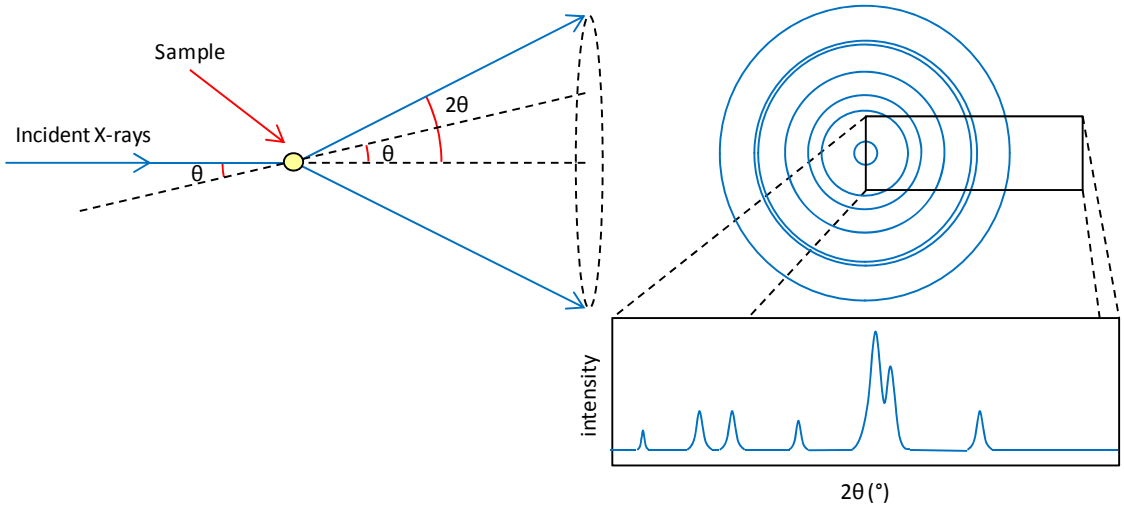

Figure 2.4 *Cones of intensity produced by powder X-ray diffraction.*

2.3.3 Instrumentation

Two diffractometers were used in this work. The Siemens d5000 ("d5") was used both for phase identification, and to record several high quality scans for full characterisation. Sample checks were also run on a Bruker Advance d8 ("d9") diffractometer in cases where swift data collection was required and this instrument was also used for the majority of the high quality X-ray diffraction data collected. Finally, variable temperature data were also collected on the d9 diffractometer, which was equipped with an Oxford Cryosystems PheniX closed circuit refrigerator (CCR) cryostat. These instruments will be discussed below, along with sample preparation methods and typical measurement parameters. Diffraction patterns recorded by these diffractometers were labelled as either *d5_xxxxx* or *d9_xxxxx*.

Siemens d5000

The Siemens d5000 diffractometer ("d5") uses a $CuK_{\alpha 1,2}$ X-ray source, with typical operating conditions of 40 kV and 40 mA in θ-2θ mode. This produces an X-ray beam that passes through a Soller slit and then through a 6 mm variable divergence slit (v6). The beam illuminates the sample and the resultant diffracted X-rays then pass through a second Soller slit and a graphite monochromator. The diffracted X-rays are then measured using an energy dispersive Sol-X detector. The slits reduce divergence of the beam, restricting it to illuminate the sample. The presence of a graphite (001) diffracted beam monochromator allows all wavelengths other than the $CuK_{\alpha 1,2}$ radiation to be filtered out. The instrumentation is controlled by the "Bruker AXS: XRD Commander" program.[7] *Table* 2.4 outlines the parameters used when performing routine sample analyses and high quality analyses.

Table 2.4 *Parameters used for typical d5 scans.*

Parameter	Routine Analysis	High Quality Analysis
2θ scan range (°)	*10–90*	*5–120*
Step size (°)	*0.020*	*0.020*
Time per step (s)	*1*	*7.5*
Scan time (min)	*65*	*718*

Bruker d8 Advance ("d9")

The d9 diffractometer was used for both routine sample analysis and high quality analysis of materials. This also uses a $CuK_{\alpha 1,2}$ radiation source, producing an X-ray beam that passes through a series of slits, including a 6 mm aperture slit, an anti-scatter slit, a Soller slit and a v6 variable divergence slit before illuminating the sample. The detector is a Lynx-Eye detector, which uses a series of 192 silicon strip detectors to produce a very high resolution diffraction pattern. The d9 is not fitted with a monochromator, however a Ni filter filters fluorescence and CuK_{β} radiation from the diffracted X-ray beam. Again, the d9 uses the 'Bruker AXS: XRD Commander' program to control the diffractometer.[7] *Table 2.5* outlines the parameters used for both routine and high quality data analyses.

Table 2.5 *Parameters used for typical d9 scans.*

Parameter	Routine Analysis	High Quality Analysis
2θ scan range (°)	*10–90*	*5–120*
Step size (°)	*0.021*	*0.021*
Time per step (s)	*0.5*	*8*
Scan time (min)	*30*	*750*

The d9 diffractometer was also used for variable temperature (VT) experiments, which were typically performed between 12 and 300 K. Sample temperature was controlled by an Oxford Cryosystems PheniX CCR cryostat (independent of the diffractometer control software) which allows cooling from 310 to 12 K.[8] This uses a liquid helium compressor to cool the base of the sample holder, which is surrounded by an inner heat shield assembly that reaches temperatures down to 50 K. Temperatures are logged by the CryoPad software at 60 s intervals and the average temperature for a pattern can be calculated using the local FORTRAN 77 routine *phenixlogfile*.[9] The parameters used for variable temperature diffraction experiments are outlined in *Table 2.6*. Again a v6 variable divergence slit was used. A consequence of the heating assembly is the presence of two amorphous humps in the diffraction pattern at ~18 and 20° 2θ, arising from the carbon windows; these are easily modelled in the refinement process as two unique peaks.

Table 2.6 *Parameters used for typical variable temperature d9 scans.*

Parameter	Value
2θ scan range (°)	*15–120*
Step size (°)	*0.010*
Time per step (s)	*0.12*
Scan time (min)	*20*
Temperature range (K)	*12–300*
Ramp rate (Kh^{-1})	*15*

2.3.4 Sample Preparation

Samples were prepared for XRPD on Si slides. These are specially cut along the (511) Si plane which is systematically absent in a diffraction pattern. The result is that there is "zero" background from the slide, although some amorphous contribution arising from Vaseline® can be observed.

A thin layer of Vaseline® was applied to the surface of the silicon slide. The sample was then placed on a 120 mesh sieve and sifted through onto the slide below. Once covered, the slide was then tapped gently on its side to ensure no loose powder remained on the surface. In the case of variable temperature diffraction the silicon wafer was adhered to the sample holder using heat conductive grease giving improved cooling of the silicon wafer with respect to an aluminium sample holder. Otherwise the wafer was adhered using Vaseline®.

2.4 Neutron Powder Diffraction

In a similar way to X-rays, neutrons can also be diffracted by crystalline materials, although they are scattered by atomic nuclei and not electrons. All of the neutron powder diffraction (NPD) data presented here were collected on the High Resolution Powder Diffractometer (HRPD) at the ISIS facility in the UK.[10] At ISIS, neutrons are produced by spallation, where a tungsten target is bombarded by pulses of high energy protons, and the pulses of neutrons resulting from the spallation process are then directed to a particular instrument. The high energy protons are produced from H^- ions which are stripped of their electrons on entry to a synchrotron ring and accelerated to ~2.5×10^8 ms^{-1}. Before travelling to an instrument the neutrons pass through moderators, which slow them down to appropriate speeds for diffraction.

Within each pulse of neutrons produced the energy of the individual neutrons will vary, and consequently so will the wavelength of each neutron, as shown by the de Broglie relationship given in *eqn 2.5*; where λ = wavelength, *h* is Planck's constant, *p* is momentum, *m* is mass, and *v* is velocity. By rewriting the Bragg equation (*eqn 2.6*), it can be seen that neutrons travelling at different speeds will interact differently with the crystal lattice. Consequently an energy-dispersive detector situated at a fixed angle to the sample will detect neutrons travelling at a range of velocities. This energy is measured as time-of-flight (TOF), which is the time it takes for a neutron to reach a detector from leaving the tungsten target.

$$\lambda = \frac{h}{p} \qquad \textbf{eqn 2.5}$$

where $p = mv$

$$n\frac{h}{mv} = 2d_{hkl}\sin\theta \qquad \textbf{eqn 2.6}$$

As neutrons are scattered by nuclei and not electrons, neutron diffraction has several advantages over X-ray diffraction. The main advantage is that neutron scattering lengths vary randomly across the periodic table. This means that, it general, it is possible to discern between ions with similar numbers of electrons. This would be more difficult in X-ray diffraction where the scattering power of an atom is proportional to its atomic number. Additionally, it is also easier to identify ions with low electron counts, such as H^+, which is effectively invisible to X-rays, or O^{2-} in the presence of high *Z* ions.

2.4.1 Magnetic Scattering

As neutrons have integer spin, and therefore have a magnetic moment, they are also scattered by magnetic moments arising from unpaired electrons. The result of this is that neutron diffraction also gives us information on the magnetic structure of a material. For example, if all of the moments in a material were arranged ferromagnetically (parallel, FM) one would observe increased intensity of those peaks produced by the magnetic ion. If the moments were arranged antiferromagnetically (anti-parallel, AFM) one would observe extra peaks arising from ordering of these spins in the diffraction pattern. If these extra peaks can be indexed to a unit cell with the same size and symmetry as the nuclear cell, then the materials is said to have a magnetic propagation vector of $\boldsymbol{k}$ = (000). If the peaks index to a larger unit cell however, for example $2a \times 2b \times c$, the propagation vector would be $\boldsymbol{k}$ = (½½0).

2.4.2 HRPD

As stated earlier all neutron data reported here were recorded on the HRPD at the ISIS facility in the UK.[10] We have discussed that pulses of neutrons are guided to an instrument, and that overall time it takes a neutron from leaving the target to reaching the detector is termed the time-of-flight. For HRPD these pulses of neutrons are first slowed by a liquid methane moderator, at 100 K, and then, typically, refined by choppers, rotating at 50/5 Hz, which remove neutrons such that only those within a TOF range of ~10–110 ms are used in the experiment. These choppers are vital as they ensure that slower neutrons, produced from one pulse, are not overtaken by faster neutrons from the next pulse. Detector banks are placed about the sample at fixed angles of 168° (back-scattering bank, bs), 90° and 30°, and the time-of-flight for each neutron hitting the detector is recorded; information from the HRPD manual on each data bank is given in *Table 2.7*. The resulting pattern produced for each bank can then be used in the analysis of the material. As the magnetic properties of the materials reported were of interest, a larger TOF window was used for these experiments of 10–210 or 30–230 ms, which was achieved by altering the chopper frequencies to 50/10 Hz. As measurements were required at a range of temperatures between 12 and 300 K, experiments were performed using the CCR 60 closed circuit refrigerator, which has a temperature range of 4–600 K. The typical parameters used in the collection of high quality neutron diffraction data and rapid variable temperature studies are given in *Table 2.8*.

Table 2.7 *HRPD detector bank details taken from the HRPD manual; based on a TOF window of 30–230 ms.*[10]

	bs	**90°**	**30°**
Detector specification	ZnS scintillator	ZnS scintillator	½" 10 atm He^3 glass tubes
Scattering angle (°)	*160–176*	*87–93*	*28–32*
Resolution ($\Delta d/d$)	*~4-5×10^{-4}*	*~2×10^{-3}*	*~2×10^{-2}*
d-spacing range (Å)	*~0.6–4.6*	*~0.9–6.6*	*~2.2–16.5*

The raw data produced by HRPD was processed using two techniques. Initially data were processed using Ariel and then split into **bs.xye*, **90.xye* and **30.xye* files using the local routine *splithrpdgsas2*, however more recently data processing has been performed using Mantid, which automatically produces individual **.dat* files for each bank of data.[11-13]

Table 2.8 *Parameters used for typical HRPD data collections.*

Parameter	High Quality Analysis	Rapid VT Analysis
TOF range (ms)	*10–210*	*10–210*
Current collected (μAh)	*66*	*2.5*
Temperature range (K)	-	*12–300*
Increments (K)	-	*6*

2.4.3 Sample Preparation

For all HRPD experiments ~4 g of powdered sample was placed into a 5 mm (depth) aluminium slab can with a vanadium window (*Figure 2.5*). This slab can was then sealed by addition of another vanadium window, which was bolted in place. This was then attached to a sample stick, with a thermocouple and heating element to allow direct control of the sample temperature. Sheets of gadolinium and cadmium metals, with holes to allow the beam to hit the sample, were then placed on the front of the can, relative to the beam, to reduce unwanted scattering from the assembly.

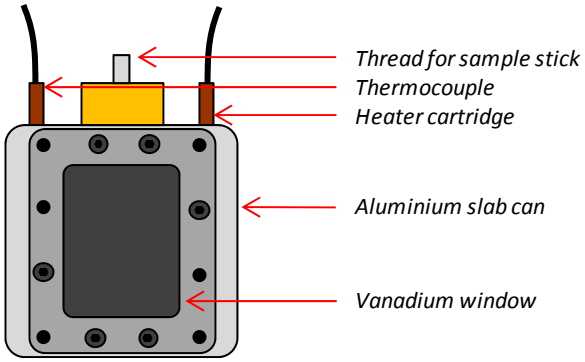

Figure 2.5 *A slab can for use on HRPD.*

2.5 Analysis of Diffraction Data

This section will discuss the analysis of both X-ray and neutron data collected. Particular attention will be paid to Rietveld refinement, which is a key tool for structural analysis from powder diffraction data. Indexing and Pawley refinements, as well as structure solution and magnetic structure determination methods will also be discussed.

2.5.1 Rietveld Refinement

For a given material with a known approximate crystal structure, Rietveld refinement can be performed on a starting model in order to derive parameters such as cell metrics and atomic positions.[14] The majority of the refinements in this work have been performed in TOPAS Academic (TA), and the remainder in GSAS (General Structure Analysis System).[5, 15, 16]

Rietveld refinement works by attempting to fit experimental intensities measured by a diffractometer, y_i values, using a non-linear least squares method. By minimising the difference between the mathematical model and the observed data, we can thus derive important structural information about a given material. In order for the least squares refinement to be successful a good starting model is required. This should include information on the unit cell such as space group, lattice parameters,

atomic coordinates, occupancies and a description of the peak shape. For this project the starting models were taken from crystallographic information files (**.cif*s) based on results published for $La_2O_2Fe_2OSe_2$ and $CeOMn_{0.5}Se$ by Mayer and Ijjaali, respectively, or from structures derived by direct methods or charge flipping (sections 2.5.5 & 2.5.6).[17, 18] The quantity minimised in the least squares refinement is termed S_y and is defined in *eqn 2.7*, where y_i is the observed intensity at 2θ point *i*, y_{ci} is the calculated intensity at point *i*, and w_i is the weighting factor.

$$S_y = \sum_i w_i (y_i - y_{ci})^2 \qquad \textit{eqn 2.7}$$

Many factors are considered when calculating the diffracted intensity at a given point. These include scale (*s*), Miller indices (*K*), *i.e. h*, *k* and *l*, Lorentz polarisation and multiplicity factors (L_K), reflection profile function (φ), preferred orientation (P_K), absorption (*A*), the structure factor (F_K) (defined in *eqn 2.4*) and background intensity (y_{bi}). These are combined as shown in *eqn 2.8*.

$$y_{ci} = s\sum_K L_K |F_K|^2 \varphi(2\theta_i - 2\theta_K) P_K A + y_{bi} \qquad \textit{eqn 2.8}$$

The quality of a refinement can be quantified by a number of residual factors (*R*-factors). The R_{wp} (weighted *R*-factor) is the most commonly quoted and mathematically robust *R*-factor as it relates directly to the quantity being minimised, S_y. R_{wp} tells us about the difference between the predicted pattern and the recorded data. It is defined (*eqn 2.9*) by y_i and y_{ci} and the weighting factor w_i.

$$R_{wp} = \sqrt{\frac{\sum_i w_i (y_i - y_{ic})^2}{\sum_i w_i (y_i)^2}} \qquad \textit{eqn 2.9}$$

Another commonly quoted *R*-factor is R_{Bragg}, which does not include background contribution, but takes into account multiplicity and structure factors. This is defined in *eqn 2.10*, where *N* is the number of observations and *P* is the number of refined parameters. Unlike the weighted *R*-factor however, it not based directly on the observed y_i values, but extracted peak intensities which are biased by the structural model. It is also common to quote the goodness-of-fit (*gof*) or χ^2 ($gof = \sqrt{\chi^2}$). This is derived from the ratio of R_{wp} to R_{exp}. Both χ^2 and R_{exp} are defined in *eqn 2.11*.

$$R_{Bragg} = \sqrt{\frac{\sum_i (N - P)}{\sum_i w_i (y_i)^2}} \qquad \textit{eqn 2.10}$$

$$\chi^2 = (R_{wp}/R_{\exp})^2 \qquad \textit{eqn 2.11}$$

$$\text{where} \quad R_{\exp} = \sqrt{\frac{N - P}{\sum_i w_i (y_i)^2}}$$

For a refinement using high quality data collected on the d9 diffractometer the following parameters were typically included to model the data: 12 terms to describe a Chebyshev background function, a term to describe sample height, a scale factor, a term to describe peak asymmetry and 4 terms of a

Thompson-Cox-Hastings pseudo-Voigt (TCHZ) peak shape function. Additionally, unit cell dimensions, atomic coordinates and anisotropic thermal displacement parameters were also refined. For refinements with neutron data the following were considered for each bank of data: 6 terms to describe a Chebyshev background function, 3 instrumental parameters to determine TOF *x*-axis calibration (*diffa*, *diffc* and *zero*), an absorption correction, 3 terms to describe peak shape (*lor*, *dsp* and *dspsq*) and a scale factor.

Throughout this report Rietveld plots will be formatted such that observed data are shown are blue, calculated data in red and the difference of these in grey.

2.5.2 Pawley Refinement

Pawley refinement proceeds in a similar way to Rietveld refinement, however information on cell contents is replaced by a list of the reflections allowed for the specified space group.[19] These reflections are then given an arbitrary intensity that is refined to fit the observed data. Unit cell dimensions and parameters such as peak shape, sample height and background are also included in the refinement. These refinements were also performed in TA.[5]

2.5.3 Analysis of Variable Temperature Data

Variable temperature X-ray diffraction produces several data sets at specific temperatures. It is therefore useful to be able to run multiple Rietveld refinements sequentially. In most cases reported here this was achieved using the local FORTRAN 77 routine *multitopas*, although the SEQGSAS function of GSAS was also implemented.[15, 20] *Multitopas* is designed to perform sequential Rietveld or Pawley refinements for all of the recorded data sets using a single input file (*seed.inp*). The input file is created by running a "normal" refinement for the initial data set in TA. A *multitopas* batch file is then produced including the filenames of the data to be used and other information such as temperatures for given data ranges. When the batch file is run each new refinement uses the results from the previous refinement (stored in the file *seed.out*) as a starting point. The input file can also be set up to output parameters, defined by the user, into a results file, *seed.res*. This file can then be read into a spreadsheet program to analyse the results.

SEQGSAS works similarly, although produces an individual input file for each refinement; where file names are altered sequentially. Data from these refinements can then be output from GSAS in ASCII format and read into a spreadsheet.

2.5.4 Indexing

We discussed earlier that peak positions give information on the size and shape of a unit cell, whilst the presence or absence of peaks tells us information on the symmetry of the unit cell. Indexing techniques inspect the peaks that are present in a diffraction pattern to produce a number of probable unit cells that could describe the pattern. TA has an automated indexing routine, which produces a list of

probable unit cells that describe the data.[5, 21] These results are given a goodness-of-fit value, where higher values are more likely solutions.

2.5.5 Charge-Flipping

Charge flipping is an *ab initio* structure solution technique implemented in TA, and works using X-ray powder diffraction data, and without any prior knowledge of unit cell contents or symmetry.[5, 22] The technique was developed by Oszlányi and Sütő in 2003, and works by attempting to produce physically meaningful electron density maps from the observed data. Electron density maps are produced by the inverse Fourier transform of a combination of structure factor amplitudes, extracted from the observed data, and a randomly selected phase set. All points in the resulting electron density map that are above a threshold, δ, are accepted, and those below the threshold are multiplied by a factor of -1 (hence "charge flipping"); note that the value of δ is a small proportion of a peak that would be observed for a light atom. The newly generated electron density map then undergoes a Fourier transform to give a set of temporary structure factors and phases. This phase set is then combined with observed structure factors and inverse Fourier transformed to give a new electron density map. This process is then repeated many times and the progression of the algorithm is monitored by an *R*-factor, which is minimised in the process. The results given from charge-flipping tell us about areas of electron density in real space, and if information on the unit cell contents is given atoms can be assigned to areas of electron density based on their atomic numbers.

2.5.6 EXPO

Another technique used in the solution of structures from powder diffraction data was direct methods, which were employed here using the program EXPO.[23, 24] Unlike the charge flipping algorithm, EXPO requires information on the unit cell dimensions, symmetry and contents in order to solve a structure. Structure factor amplitudes are obtained from the diffraction data using the Le Bail algorithm and the integrated intensities are processed by direct methods.

2.5.7 Magnetic Structure Determination

As discussed previously, neutron diffraction can give information on the magnetic structure of a material. Once a propagation vector (*k*-vector) has been determined from a diffraction pattern, further analysis can be performed to determine the arrangement of the moments within this unit cell. Examples of magnetic structure determination presented in this work used the program SARAh, interfaced with GSAS, or ISODISTORT interfaced with TA.[5, 15, 25, 26] The SARAh program is comprised of two sub-programs. The first, SARAh Representational Analysis, uses information given by the user on the nuclear symmetry, coordinates of the magnetic ions, and the *k*-vector to produce a list of possible irreducible representations (irreps) that describe the different arrangements of the magnetic moments possible for the enlarged unit cell with *P*1 symmetry; the reduction in symmetry to *P*1 means that the arrangement of the moments is not restricted by the nuclear symmetry. Note that, although extra atoms, produced by symmetry lowering and the enlargement of the unit cell, are automatically equated, the resulting cell

may contain unique sets of related atoms that are allowed to order differently to each other, and the irreps for each of these sites are listed by SARAh. Details from this analysis are then stored in a **.mat* file, which is then used by the second program, SARAh Refine, that allows investigation of these various irreps. Prior to this step a nuclear-only refinement is performed by the user in GSAS, and, once a global minimum as been found, the refined parameters are fixed. SARAh Refine then inserts a magnetic-only phase into this input file based on information in the **.mat* file and the user may choose from a list of possible basis vectors to investigate. SARAh Refine then feeds information on the chosen basis vector into the input file and GSAS refines atom occupancies within the magnetic phase to produce a value of χ^2 for that particular description. Inspection of χ^2 values produced from these investigations will then suggest which basis vector(s) are present and hence the magnetic symmetry. SARAh Refine also allows analysis using combinations of irreps, using reverse Monte Carlo cycles, allowing the investigation of an array of magnetic structures.

For SARAh refinements involving combinations of irreps, results were visualised as contour plots produced in gnuplot 4.0 using the *dgrid* and *pm3d* functions. The first command *dgrid* tells gnuplot to process the data to be plotted such that it is contained within a grid *x* columns wide by *y* rows high; where the limits for the grid are based on the range of values in the data file. A third parameter controls the weighting of each data point relative to its position on the grid, *i.e.* the closer a data point is to a point on the grid the more highly it is weighted, and vice versa. The *pm3d map* command then allows a coloured surface to be placed over the grid; note that these colours can be defined by the user. Finally the *splot* command was used to plot the data. A typical *gnuplot.commands* file used to produce the contour plots is given in the e-appendix. *Figure 2.6* shows representations of χ^2 versus basis vector plots produced in both Origin and gnuplot. The plot produced in Origin (*a*) shows the raw data output by SARAh with a plot of the same data from gnuplot (*b*) alongside. Whilst it may initially seem that the map produced in gnuplot has more data points, for example data are plotted at each corner, this is an artefact of the data processing; *i.e.* whilst values of $\Gamma_3 \approx 1$ and $\Gamma_1 \approx -1$ close the 'corners' of the plot were never sampled, plotted data have been extrapolated to these corners. The second comparison shows an *xyz (c)* and contour (*d*) plot for a case where the contribution of each basis vector plotted is linearly dependant on the other; *i.e.* $\Gamma_5 + \Gamma_6 = 1$ in all cases. The *xyz* plot (*c*) clearly shows the linear constraint between the magnitudes of each basis vector. When processed in gnuplot this appears as the map shown in (*d*). Whilst *a* and *c* are better representations of the data collected, their production is time consuming when there are multiple basis vectors to explore. The presentation used in *b* and *d* was therefore used throughout this report. Note that the conclusion as to the lowest χ^2 region (blue points) is the same from each presentation.

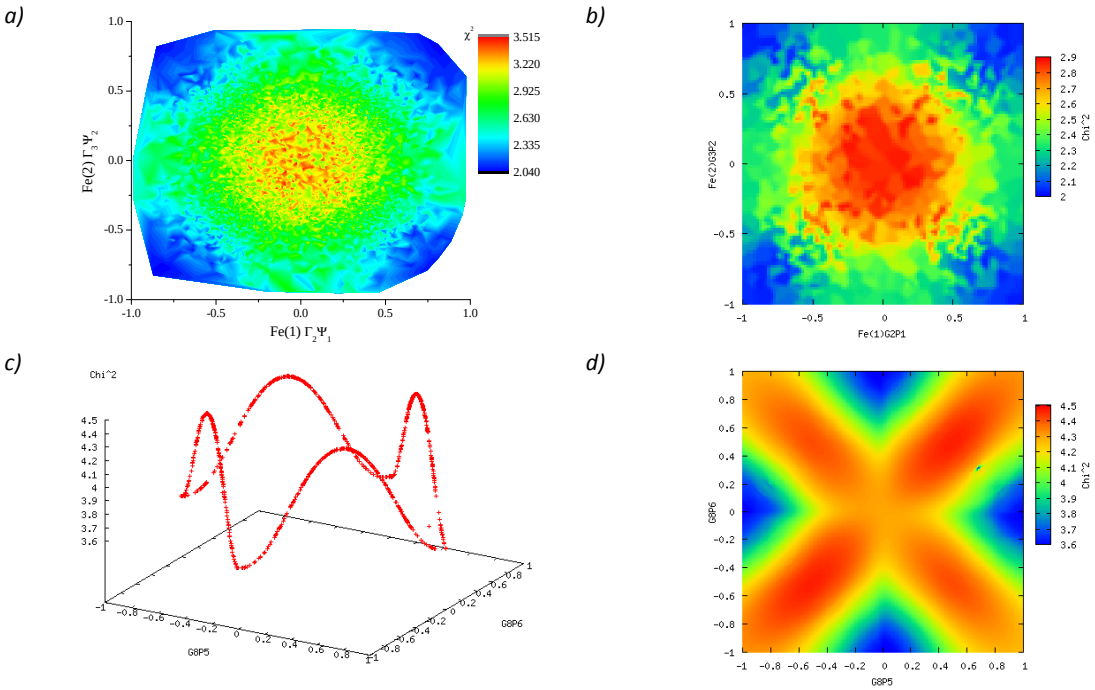

Figure 2.6 *A selection of contour and xyz plots produced using GNUPLOT and Origin, including (a&b) contour plots of data collected for $La_2O_2Fe_2OSe_2$ data produced in Origin and GNUPLOT, respectively, and (c&d) an xyz and contour plot of data collected for $La_2O_2Co_2OSe_2$ produced in GNUPLOT, respectively.*

The total diffraction pattern produced by both nuclear and magnetic scattering can be analysed using Rietveld refinement, with information added about both magnetic symmetry within the cell, and the magnitude and direction of the moments on the magnetic ions. As in a nuclear-only Rietveld refinement, the symmetry of a material is expressed using a space group, however due to the change in symmetry arising from the magnetic scattering, a Shubnikov group can be used to express the overall symmetry. In some cases, for example where the nuclear symmetry is much higher than the magnetic symmetry, individual nuclear and magnetic phases can be used in the Refinement process. Refinements were again performed using a combination of TA and GSAS.[5, 15, 16]

Whilst a Shubnikov group may be determined by hand it can also be determined via analysis in the web-based utility ISODISTORT.[26] Reproduction of the magnetic structure determined by SARAh Refine in an enlarged cell with *P*1 symmetry would give the user more information on the basis vectors active in the material, and, consequently, the Shubnikov groups that would allow this arrangement of moments. A **.cif* for the material in this Shubnikov group could then be produced, and used for Rietveld refinement in TA.[5]

2.6 SQUID Magnetometry

Magnetic properties of the materials were measured by a Quantum Design Magnetic Property Measurement System (MPMS), with a superconducting quantum interference device (SQUID). Here we will discuss the instrumentation and measurements used in this method.

2.6.1 Instrumentation

A SQUID magnetometer consists of three main parts, a superconducting magnet, a superconducting detection coil, and a SQUID, which is connected to the detection coil. The detection coil is a second order gradiometer which is placed in a uniform region of the magnetic field formed by a superconducting magnet. This detection coil couples inductively to a sample, and hence detects the magnetic properties of a material under various conditions. Any changes are transmitted to the SQUID as changes in current, and these are observed in the SQUID's output voltage. The principle part of the SQUID is the Josephson junction, which couples two superconductors via a small insulating gap, which superconducting electrons are able to tunnel through (*Figure 2.7*).[27-29]

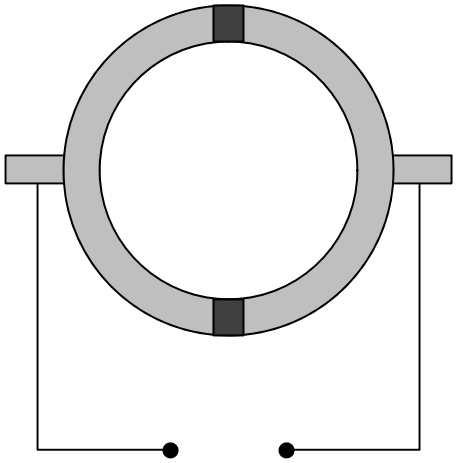

Figure 2.7 *A SQUID; the Josephson junctions are shown in dark grey and the superconductors are shown in light grey, the output is picked up between the two wire ends.*

The necessity of superconducting materials requires that the system is cooled to very low temperatures. In this case, liquid helium was used. The sensitivity of the SQUID is such that it even needs to be protected from the magnetic field of the earth in order to give accurate results.

2.6.2 Sample Preparation

Table 2.9 shows the amount of each sample used in each experiment which was loaded into the larger end of a gelatine capsule and compacted using the smaller end. A thin layer of varnish was then applied to the inside rim of the larger capsule and the smaller, upturned, end inserted (*Figure 2.8*). Another thin layer of varnish was then applied to the outside of the capsule and this was inserted inside a plastic straw. Note that as SQUID magnetometry is extremely sensitive it was imperative that the materials used for mounting the sample holder would only give a small diamagnetic contribution to the data collected. The varnish used was a mixture of "G" varnish and a 10:1 ethanol-toluene solution.

Table 2.9 *Masses of reagents used in SQUID magnetometry.*

Sample	Mass (g)
$La_2O_2Mn_2OSe_2$	*0.0642*
$Ce_2O_2Mn_2OSe_2$	*0.0433*
$Pr_2O_2Mn_2OSe_2$	*0.0867*
β-$La_2O_2MnSe_2$	*0.0370*

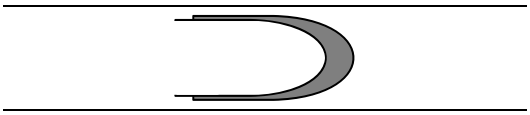

Figure 2.8 *Sample for SQUID magnetometry; the sample is shown in grey and is sandwiched between the two ends of a gelatine capsule.*

2.6.3 Sequence Programming

Sequences are programmed to measure the change in the magnetic moment of the material with respect to either temperature or field. Data here were typically collected on warming the material in the presence of an applied magnetic field, after cooling in either the presence or absence of a field, thus giving an idea of the behaviour of the moments. A typical sequence used in analysis of the materials reported here is outlined below.

- Check for paramagnetism at room temperature:
  - Measurement from 0 to 20000 Oe in 1000 Oe increments at 292 K
- Hysteresis measurements (with the initial three measurement steps repeated at the end to measure the final quadrant):
  - Sample cooled to temperature
  - Measurement from 0 to 200 Oe in 20 Oe increments
  - Measurement from 200 to 1000 Oe in 100 Oe increments
  - Measurement from 1000 to 20000 Oe in 1000 Oe increments
  - Measurement from 20000 to 1000 Oe in -1000 Oe increments
  - Measurement from 1000 to 200 Oe in -100 Oe increments
  - Measurement from 200 to 0 Oe in -20 Oe increments
  - Measurement from 0 to -200 Oe in -20 Oe increments
  - Measurement from -200 to -1000 Oe in -100 Oe increments
  - Measurement from -1000 to -20000 Oe in -1000 Oe increments
  - Measurement from -20000 to -1000 Oe in -1000 Oe increments
  - Measurement from -1000 to -200 Oe in -100 Oe increments
  - Measurement from -200 to 0 Oe in -20 Oe increments
- Field cooled (FC) measurement:
  - Sample cooled to 2 K with an applied field of 1000 Oe
  - Measurement from 2 to 292 K in 5 K increments with an applied field of 1000 Oe
- Zero-field cooled (ZFC) measurement:
  - Sample cooled to 2 K with an applied field of 0 Oe
  - Measurement from 2 to 292 K in 5 K increments with an applied field of 1000 Oe

2.6.4 Data Analysis

The output data can be analysed using a simple spreadsheet program, from the magnetic data recorded in the form of “Long moment”. These data can then be converted into molar susceptibility (χ_{mol}), which is a measure of how much a sample is attracted to a magnetic field, using the relationship given in *eqn*

2.12; where the "Long moment" (emu) and the field (Oe) are given in the data file, and RMM is the molecular mass of the material. Following this, data are then also corrected for diamagnetic contributions of the ions present using tabulated values, and also for any contribution from the sample holder.[30] Magnetic moments, μ_{eff}, were typically calculated from the collected data in two ways. Firstly the calculated gradient (*g*) from a plot of applied field (Oe) against magnetisation (emu.mol^{-1}) can be used to calculate the observed moment as given in *eqn 2.13*, where *T* is temperature. Secondly, for a material that exhibits paramagnetic Curie-Weiss behaviour, the Curie constant (*C*) can be determined by taking the reciprocal of the gradient for a linear plot of χ_{mol}^{-1} versus temperature (*T*). This can be used to calculate the moment as shown by *eqn 2.14*.

$$\chi_{mol} = \frac{Long\ momen\ t}{(mass/RMM) \times field} \qquad \textbf{eqn 2.12}$$

$$\mu_{eff} = 2.828\sqrt{gT} \qquad \textbf{eqn 2.13}$$

$$\mu_{eff} = 2.828\sqrt{C} \qquad \textbf{eqn 2.14}$$

Table 2.10 *Summary of the successful and unsuccessful syntheses reported in this thesis.*

Code	Target Phase	Method	Comments
DGF031	$Pr_2O_2Fe_2OSe_2$	2.2.2	Synthesis of 0.5g of product, used for XRPD experiments.
DGF104_6b	$Pr_2O_2Mn_2OSe_2$	2.2.2	Synthesis of 0.5g of product, used for XRPD and VT experiments.
DGF109	$La_2O_2Mn_2OSe_2$	2.2.2	Synthesis of several 0.5g samples that were combined and refired as a bulk 3g powder for NPD and SQUID magnetometry.
DGF110	$Pr_2O_2Mn_2OSe_2$	2.2.2	Synthesis of several 0.5g samples that were combined and refired as a bulk 3g powder for NPD and SQUID magnetometry.
DGF111	$La_2O_2Cu_2OSe_2$	2.2.2	Synthesis of 0.5g of product, used for XRPD experiments.
DGF112	$Pr_2O_2Cu_2OSe_2$	2.2.2	Synthesis of 0.5g of product, used for XRPD experiments.
DGF113	$La_2O_2Zn_2OSe_2$	2.2.2	Synthesis of 0.5g of product, used for XRPD experiments.
DGF114	$La_2O_2Ti_2OSe_2$	2.2.2	Synthesis of 0.5g of product, used for XRPD experiments.
DGF118a	$La_2O_2(Mn_{0.5}Fe_{0.5})_2OSe_2$	2.2.2	Synthesis of 0.5g of product, used for XRPD experiments.
DGF118b	$Pr_2O_2(Mn_{0.5}Fe_{0.5})_2OSe_2$	2.2.2	Synthesis of 0.5g of product, used for XRPD experiments.
DGF118c	$Nd_2O_2(Mn_{0.5}Fe_{0.5})_2OSe_2$	2.2.2	Synthesis of 0.5g of product, used for XRPD experiments.
DGF120	$Sm_2O_2(Mn_{0.5}Fe_{0.5})_2OSe_2$	2.2.2	Synthesis of 0.5g of product, used for XRPD experiments.
DGF122	$Ce_2O_2Fe_2OSe_2$	2.2.2	Synthesis of 0.3g of product using Al crucible method. After initial synthesis sample was refired with fresh Al powder at 1000 °C for 12 h.
DGF124	$Ce_2O_2Co_2OSe_2$	2.2.2	Synthesis of 0.5g of product, used for XRPD experiments.
DGF136	$Ce_2O_2Mn_2OSe_2$	2.2.2	Synthesis of several 0.5g gram samples that were combined and refired as a bulk 3g powder for NPD and SQUID magnetometry.
DGF210	β-$La_2O_2MnSe_2$	2.2.3	Initial synthesis of 0.5g of product, used for XRPD experiments, VT measurements, structure solution.
DGF210ii	β-$La_2O_2MnSe_2$	2.2.3	Synthesis of 0.5g used for SQUID magnetometry experiments.
DGF212	$Nd_2O_2MnSe_2$	2.2.3	Synthesis of 0.5g of product, used for XRPD experiments.
DGF213	$La_2O_2Fe_2OSe_2$	2.2.2	Synthesis of several 0.5g gram samples that were combined and refired as a bulk 3g powder for , XRPD and VT measurements. Due to
DGF217	$La_2O_2ZnSe_2$	2.2.3	Synthesis of 0.5g of product, used for XRPD experiments.
DGF220	$Ce_2O_2FeSe_2$	2.2.3	Synthesis of 0.5g of product, used for XRPD experiments, and structure solution.
DGF221	$Nd_2O_2FeSe_2$	2.2.3	Synthesis of 0.5g of product, used for XRPD experiments.
DGF222	$Ce_2O_2ZnSe_2$	2.2.3	Synthesis of 0.5g of product, used for XRPD experiments.
DGF223	$Gd_2O_2MnSe_2$	2.2.3	Synthesis of 0.5g of product, used for XRPD experiments.
DGF225	$Pr_2O_2MnSe_2$	2.2.3	Synthesis of 0.5g of product, used for XRPD experiments.
DGF226	$Sm_2O_2MnSe_2$	2.2.3	Synthesis of 0.5g of product, used for XRPD experiments.
DGF227	$Pr_2O_2FeSe_2$	2.2.3	Synthesis of 0.5g of product, used for XRPD experiments.
DGF242	β-$La_2O_2MnSe_2$	2.2.3	Combination of several 0.5g syntheses to produce 3g of sample for NPD.
DGF306	$La_2O_2Fe_2OS_2$	2.2.2	Synthesis of several 0.5g gram samples that were combined and refired as a bulk 3g powder for , XRPD and VT measurements. Due to
DGF325	$(La_{⅔}Nd_{⅓})_2O_2Mn_2OSe_2$	2.2.2	Synthesis of 0.5g of product, used for XRPD experiments.
EEM205	$Ce_2O_2FeSe_2$	2.2.3	Combination of several 0.5g syntheses to produce 3g of sample for NPD.

2.7 References

1. P. A. Faeth and A. F. Clifford, *Proceedings of the 3rd Conference on Rare Earth Research*, 1963.
2. S. Rabideau and G. Glocker, *J. Am. Chem. Soc.*, 1951, **73**, 488-488.
3. J. K. Marsh, *J. Chem. Soc.*, 1946, 15-17.
4. Bruker AXS, *Diffrac^plus Basic Evaluation Package: EVA 10.0*, Karlsruhe, 2004.
5. A. A. Coelho, *TOPAS Academic: General profile and Structure Analysis Software for Powder Diffraction Data*, Bruker AXS, Karlsruhe, 2010.
6. http://cds.dl.ac.uk/icsd/.
7. Bruker AXS, *Diffrac^plus XRD Commander v2.3: Software for Controlling Bruker Diffractometers*, Karlsruhe, 2000.
8. Oxford Cryosystems, *Cryopad v1.484*, 2007.
9. J. S. O. Evans, *phenixlogfile, FORTRAN 77 routine*, University of Durham, 2000.
10. R. Ibberson, W. I. F. David and K. S. Knight, *The High Resolution Neutron Powder Diffractometer (HRPD) at ISIS - A User Guide*, ISIS Crystallography, Didcot, 1992.
11. J. S. O. Evans, *splithrpdgsas2*, Durham, 2007.
12. P. G. Radielli, T. Proffen and L. C. Chapon, *Ariel 4.0*, ISIS Facility, Didcot, UK, 2008.
13. www.mantidproject.org.
14. H. M. Rietveld, *J. Appl. Cryst.*, 1969, **2**, 65-71.
15. A. C. Larson and R. B. Von Dreele, *The General Structure Analysis System (GSAS)*, Los Alamos National Laboratory: Los Alamos, 2004.
16. B. H. Toby, *J. Appl. Cryst.*, 2001, **34**, 210-221.
17. J. M. Mayer, L. F. Schneemeyer, T. Siegrist, J. V. Waszczak and B. v. Dover, *Angew. Chem. Int. Ed. Engl.*, 1992, **31**, 1645-1647.
18. I. Ijjaali, K. Mitchell, C. L. Haynes, A. D. McFarland, R. P. van Duyne and J. A. Ibers, *J. Solid State Chem.*, 2003, **176**, 170-174.
19. G. S. Pawley, *J. Appl. Cryst.*, 1981, **14**, 357-361.
20. J. S. O. Evans, *multitopas, FORTRAN 77 routine*, University of Durham, 1999.
21. A. A. Coelho, *J. Appl. Cryst.*, 2003, **36**, 86-95.
22. G. Oszlanyi and A. Suto, *Acta Cryst.*, 2004, **A60**, 134-141.
23. A. Altomare, G. Cascarano, C. Giacovazzo, A. Guagliardi, M. C. Burla, G. Polidori and M. Camalli, *J. Appl. Cryst.*, 1994, **27**, 435-436.
24. A. Altomare, M. C. Burla, G. Cascarano, C. Giacovazzo, A. Guagliardi, A. G. G. Moliterni and G. Polidori, *J. Appl. Cryst.*, 1995, **28**, 842-846.
25. A. S. Wills, *Physica B*, 2000, **276-278**, 680-681.
26. B. J. Campbell, H. T. Stokes, D. E. Tanner and D. M. Hatch, *J. Appl. Cryst.*, 2006, **39**, 607-614.
27. W. G. Jenks, I. M. Thomas and J. P. Wikswo, *Encyclopedia of Applied Physics, "SQUIDs"*, VCH, 1997.
28. S. Blundell, *Magnetism in Condensed Matter*, Oxford University Press, Oxford, 2007.
29. N. Spaldin, *Magnetic Materials - Fundamentals and Device Applications*, Cambridge University Press, Cambridge, 2003.
30. G. A. Bain and J. F. Berry, *J. Chem. Ed.*, 2008, **85**, 532-536.

Structural and Magnetic Properties of $A_2O_2Mn_2OSe_2$ Materials (*A* = La–Pr)

3.1 Introduction

$La_2O_2Mn_2OSe_2$ (*Figure 3.1*) was originally reported by Withers a former student in the group, and was found to be isostructural with $La_2O_2Fe_2OSe_2$ (atomic coordinates are given in *Table 3.1*).[1, 2] Masters thesis work by this author showed that $Pr_2O_2Mn_2OSe_2$ could also be prepared, however the synthesis of materials with smaller lanthanide ions was not possible.[3] Both of these materials have been demonstrated to undergo phase transitions on cooling, evidenced by a change in the thermal expansion of the *c* cell parameter. Studies by Withers suggested that this transition was coincident with an increase in the thermal displacement of the O(2) site, which is that in the $[Mn_2O]^{2+}$ layers. This displacement is most prominent in the *z* direction, suggesting that the oxide ions become statically displaced above and below the manganese layers on cooling. Furthermore, investigation of X-ray data collected for $Pr_2O_2Mn_2OSe_2$ at 12 K, showed evidence of peak splitting, particularly of the {200} reflection of the tetragonal unit cell. It was found that this peak splitting could be explained by a reduction in the symmetry of the unit cell from tetragonal (*I*4/*mmm*) to orthorhombic (*Immm*); allowing the {200} reflection to split into the constituent (200) and (020) reflections.

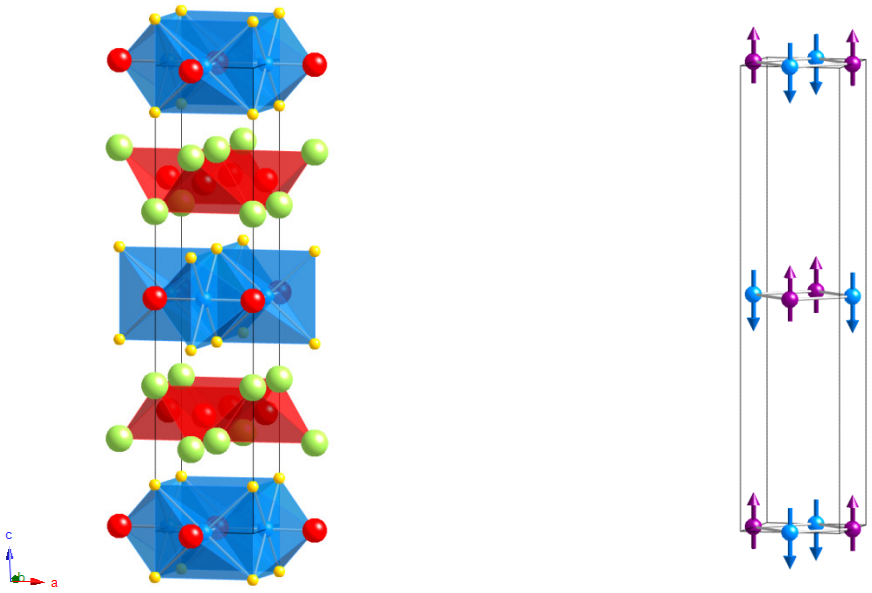

Figure 3.1 *Nuclear (left) and proposed magnetic (right) structure of $La_2O_2Mn_2OSe_2$; Mn = blue/purple, La = green, O = red, Se = yellow, the unit cell is outlined; the blue/purple colour of the Mn^{2+} ions relates similarly orientated moments.*

Table 3.1 *Cell coordinates and site occupancies (Occ.) for $A_2O_2Mn_2OSe_2$ materials.*

	Wyckoff site	*x* (*a*)	*y* (*b*)	*z* (c)	*Occ.*
A	*4e*	*0.5*	*0.5*	*~0.19*	*1*
Mn	*4c*	*0.5*	*0*	*0*	*1*
Se	*4e*	*0*	*0*	*~0.10*	*1*
O(1)	*4d*	*0.5*	*0*	*0.25*	*1*
O(2)	*2b*	*0.5*	*0.5*	*0*	*1*

Neutron diffraction data, collected for $La_2O_2Mn_2OSe_2$, have shown that the manganese ions in the material order antiferromagnetically below 200 K (*Figure 3.1*).[1] The arrangement of these moments can

be described by the Shubnikov symmetry *I*4'/*mm*'*m*. *Figure 3.2* shows that, within the layers, the nearest neighbour (n.n.) interactions (J_1) are antiferromagnetic, and the ~90° Mn-Se-Mn (J_2) and 180° Mn-O-Mn (J_2') interactions are ferromagnetic. The first of these observations can be justified by Goodenough's rules, which state that the 90° interaction of two d^5 ions will be antiferromagnetic due to direct orbital overlap.[4] Goodenough's rules are not obeyed for the 180° interactions however, which are predicted to be strongly antiferromagnetic. As discussed in chapter 1, theoretical studies have calculated this as one of the possible arrangements for $La_2O_2Fe_2OSe_2$ and $B_2F_2Fe_2OQ_2$ (*B* = Sr, Ba; *Q* = S, Se) materials, demonstrating how the frustration of the J_2 and J_2' interactions is compensated for by the larger magnitude of the J_1 interaction. [iii, 5, 6] In accordance with these works, and others, this arrangement is labelled AFM1. Susceptibility data collected for $La_2O_2Mn_2OSe_2$ and $Pr_2O_2Mn_2OSe_2$ confirm the observation of antiferromagnetic ordering in these materials.

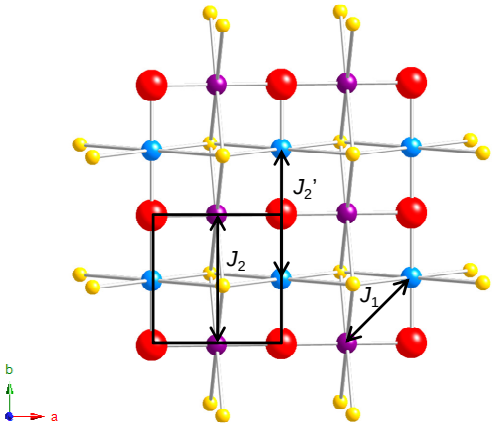

Figure 3.2 *Magnetic coupling interactions in $A_2O_2Mn_2OSe_2$; Mn = blue/purple, O = red, Se = yellow.*

This chapter reports a detailed investigation of the structural and magnetic properties of $La_2O_2Mn_2OSe_2$ and $Pr_2O_2Mn_2OSe_2$, via a combination of high resolution X-ray and neutron diffraction studies. In addition to these, studies of $Ce_2O_2Mn_2OSe_2$ are reported.

3.2 Room Temperature Structures

These materials were synthesised using the methods described in section 2.2.2. The room temperature structures of each material were then refined from X-ray data collected on a Bruker d8 diffractometer (the "d9") and neutron data collected from each of the backscattering (bs) and 90° banks of HRPD at ISIS.[7] Specific details of these experiments can be found in sections 2.3.3 and 2.4.2. Refinements were performed in TOPAS Academic (TA), and included variables to describe both structural and instrumental parameters.[8] The variables used to model the data include those listed in *Table 3.2*, as well as parameters to model background, TOF *x*-axis calibration, absorption, 2θ zero error, scale factors and profile coefficients. The overall number of variables refined for each material is given in *Table 3.2*, and includes variables used to describe impurity phases present. Whilst no impurity phases were observed in $La_2O_2Mn_2OSe_2$ by X-ray and neutron diffraction, there were trace amounts of MnSe present in the

[iii] Note that Kabbour *et al.* define the J_1, J_2 and J_2' interactions as J_3, J_2 and J_1, respectively.

$Pr_2O_2Mn_2OSe_2$ sample. The sample of $Ce_2O_2Mn_2OSe_2$ contained a larger number of impurities, including MnSe, $CeOMn_{0.5}Se$ and another "unknown" phase; these will be discussed in section 3.5. Rietveld plots for $La_2O_2Mn_2OSe_2$ are given in *Figure 3.3*, and those for $Ce_2O_2Mn_2OSe_2$ and $Pr_2O_2Mn_2OSe_2$ are given in appendices II and III. Note that extra peaks were observed at 1.23 and 2.13 Å in the neutron data not evident in the X-ray data. These were therefore assumed to arise from the sample can / environment and were excluded from the refinements. A selection of bond lengths and angles for all three materials at room temperature is given in *Table 3.3*.

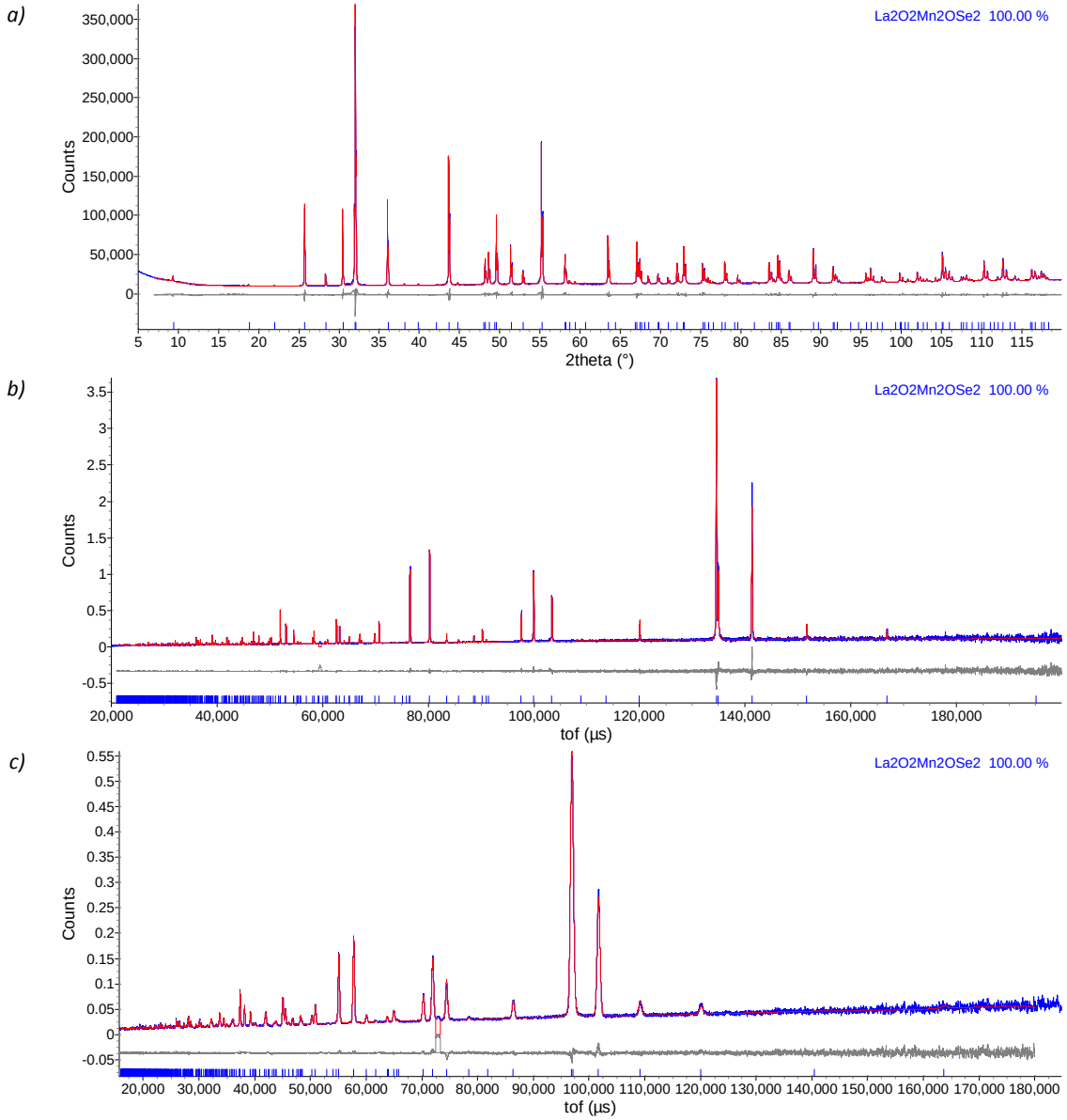

Figure 3.3 *Rietveld plots for $La_2O_2Mn_2OSe_2$ at room temperature using (a) X-ray, (b) HRPD bs and (c) 90° bank data; observed = blue, calculated = red, difference = grey. DGF109, d9_03034, hrp39877.*

Table 3.2 *Results from combined X-ray / neutron Rietveld refinements of $A_2O_2Mn_2OSe_2$ materials at room temperature.*

	$La_2O_2Mn_2OSe_2$	$Ce_2O_2Mn_2OSe_2$	$Pr_2O_2Mn_2OSe_2$
Nuclear symmetry	*I*4/*mmm*	*I*4/*mmm*	*I*4/*mmm*
a (Å)	*4.138921(4)*	*4.11304(2)*	*4.09739(2)*
c (Å)	*18.84990(3)*	*18.7410(9)*	*18.69481(9)*
V (Å^3)	*322.911(1)*	*317.043(3)*	*313.859(3)*
A z (*c*)	*0.18668(1)*	*0.18725(3)*	*0.18843(2)*
Se *z* (*c*)	*0.09994(2)*	*0.10118(3)*	*0.10164(3)*
A U_{eq} (100×Å^2)	*1.007(8)*	*0.84(2)*	*1.00(2)*
Mn U_{eq} (100×Å^2)	*1.63(2)*	*1.39(3)*	*1.58(2)*
Se U_{eq} (100×Å^2)	*1.24(1)*	*1.13(1)*	*1.30(1)*
O(1) U_{eq} (100×Å^2)	*1.01(2)*	*0.92(2)*	*0.94(1)*
O(2) U_{eq} (100×Å^2)	*3.07(3)*	*3.37(4)*	*3.71(3)*
N^o. variables	*70*	*91*	*68*
R_{wp} (%)	*3.52*	*3.58*	*3.37*
χ^2	*4.51*	*3.67*	*3.07*

U_{ij} values, statistics for specific banks of data and other information can be found in appendices I–III.

Table 3.3 *Selected inter-atomic distances and bond angles for $A_2O_2Mn_2OSe_2$ materials at room temperature.*

		$La_2O_2Mn_2OSe_2$	$Ce_2O_2Mn_2OSe_2$	$Pr_2O_2Mn_2OSe_2$
Bond lengths (Å)	$d_{M\text{-}M}$	*2.92666(1)*	*2.90836(1)*	*2.89729(1)*
	$d_{M\text{-}O}$	*2.06946(1)*	*2.05652(1)*	*2.04869(1)*
	$d_{M\text{-}Se}$	*2.7985(2)*	*2.7973(4)*	*2.7942(3)*
	$d_{A\text{-}O}$	*2.3890(1)*	*2.3690(2)*	*2.3499(2)*
	$d_{A\text{-}Se}$	*3.3524(2)*	*3.3257(4)*	*3.3207(3)*
Bond angles (°)	*M*-Se-*M* (1)	*63.054(6)*	*62.644(9)*	*62.456(8)*
	M-Se-*M* (2)	*95.38(1)*	*94.65(2)*	*94.31(1)*
	Se-*M*-Se	*84.62(1)*	*85.36(2)*	*85.69(1)*
	A-O-*A* (1)	*104.455(4)*	*104.267(9)*	*103.881(9)*
	A-O-*A* (2)	*120.05(1)*	*120.47(2)*	*121.35(2)*

Refinement of the occupancies on individual atom sites, with *A* site occupancies fixed at 1 to provide an overall scale, confirmed that both the lanthanum and praseodymium-containing materials were stoichiometric, within three standard uncertainties, with refined formulae of $La_2O_{1.988(4)}Mn_{2.001(4)}O_{0.993(4)}Se_{2.009(3)}$, and $Pr_2O_{2.006(5)}Mn_{2.000(6)}O_{1.003(4)}Se_{2.006(5)}$. Similar refinements for the cerium-containing material gave a formula of $Ce_2O_{2.030(6)}Mn_{1.994(6)}O_{1.040(5)}Se_{1.993(5)}$, though the quality of data was lower than that for the other two materials. Whilst this is close to the excepted stoichiometry for Ce^{3+} and Mn^{2+} ions, the partial oxidation of cerium cannot be ruled out. As in work by Withers, we observe a large thermal displacement of the O(2) site, relative to the other atoms present. Anisotropic displacement parameters (ADPs) suggest that this is due to a larger U_{33} contribution, suggesting that the oxide ions are displaced above and below the $[Mn_2O]^{2+}$ planes. Refined ADPs are given in appendices I–III. For $La_2O_2Mn_2OSe_2$, refinement with isotropic thermal displacement parameters gave R_{wp} and χ^2 values of 3.99 % and 5.80, respectively, justifying the use of anisotropic thermal displacement parameters in the final refinements; where refined values are 3.52 and 4.51 for R_{wp} and χ^2, respectively (*Table 3.2*).

3.3 Variable Temperature Studies

Variable temperature data were collected on the d9 diffractometer and on HRPD at ISIS in order to investigate structural distortions as a function of temperature and low temperature magnetic order.[7] These experiments were performed as described in sections 2.3.3 and 2.3.4, and the data were analysed using the local FORTRAN routine *multitopas*.[9]

Figure 3.4a shows the change in the *a* cell parameters as a function of temperature for each material, normalised relative to parameters at 300 K; un-normalised data are given in appendices I–III. Note that although $Pr_2O_2Mn_2OSe_2$ is orthorhombic at low temperatures, the data presented here are from the refinement of a tetragonal unit cell; the orthorhombic model will be discussed in section 3.3.3. The cell parameters exhibit a continuous thermal expansion and whilst there is no apparent trend in the magnitude of the thermal expansion observed for each material, the limited contraction observed for $Pr_2O_2Mn_2OSe_2$, relative to $La_2O_2Mn_2OSe_2$ and $Ce_2O_2Mn_2OSe_2$, could be explained by the smaller size of the Pr^{3+} ion, limiting the contraction of the $[Pr_2O_2]^{2+}$ layers, and hence the *a* cell parameter.

Figure 3.4b shows the temperature dependence of the *c* cell parameter for each material. There is a marked change in thermal expansion in this direction for each material at ~115, 90 and 180 K, for $La_2O_2Mn_2OSe_2$, $Ce_2O_2Mn_2OSe_2$ and $Pr_2O_2Mn_2OSe_2$, respectively. Again, data have been normalised relative to the lattice parameters at 300 K for ease of comparison and un-normalised data are given in appendices I–III. This change in thermal expansion consistent with a phase transition on cooling and data clearly show that the transition in the Pr-containing material is more marked than that in the La-containing material. It was therefore originally thought that the transition was related to the size of the lanthanide ion. Data collected for the Ce-containing material, however, show a smaller transition than those observed for $La_2O_2Mn_2OSe_2$ and $Pr_2O_2Mn_2OSe_2$. This behaviour could be explained by variation of the cerium oxidation state from Ce^{3+} to Ce^{4+}, as has been observed in CeOCuS, however, the occupancies refined at room temperature suggest that the material is approximately stoichiometric.[10-12] The change in the cell volume, and *c*/*a* ratio, as a function of temperature are shown in *Figure 3.4c*. X-ray powder diffraction data collected for each material on warming and cooling confirmed that the transitions discussed are fully reversible.

In order to clarify the trends observed in the thermal expansions of these three materials $(La_{⅔}Nd_{⅓})_2O_2Mn_2OSe_2$ was prepared; where the average radius of the *A* site was equal to that of Ce^{3+}. Analysis of the room temperature and 12 K unit cells for this material gave a/a_{300}, c/c_{300} and V/V_{300} ratios of 0.99759(4), 0.99603(6) and 0.99124(8), respectively. Comparison of these values with those in *Figure 3.4* suggests that this material undergoes a similar thermal expansion to $La_2O_2Mn_2OSe_2$, and therefore suggests that the behaviour of $Ce_2O_2Mn_2OSe_2$ is anomalous. Results from Rietveld refinement of the room temperature and low temperature structures of $(La_{⅔}Nd_{⅓})_2O_2Mn_2OSe_2$ from X-ray data are given in appendix IV.

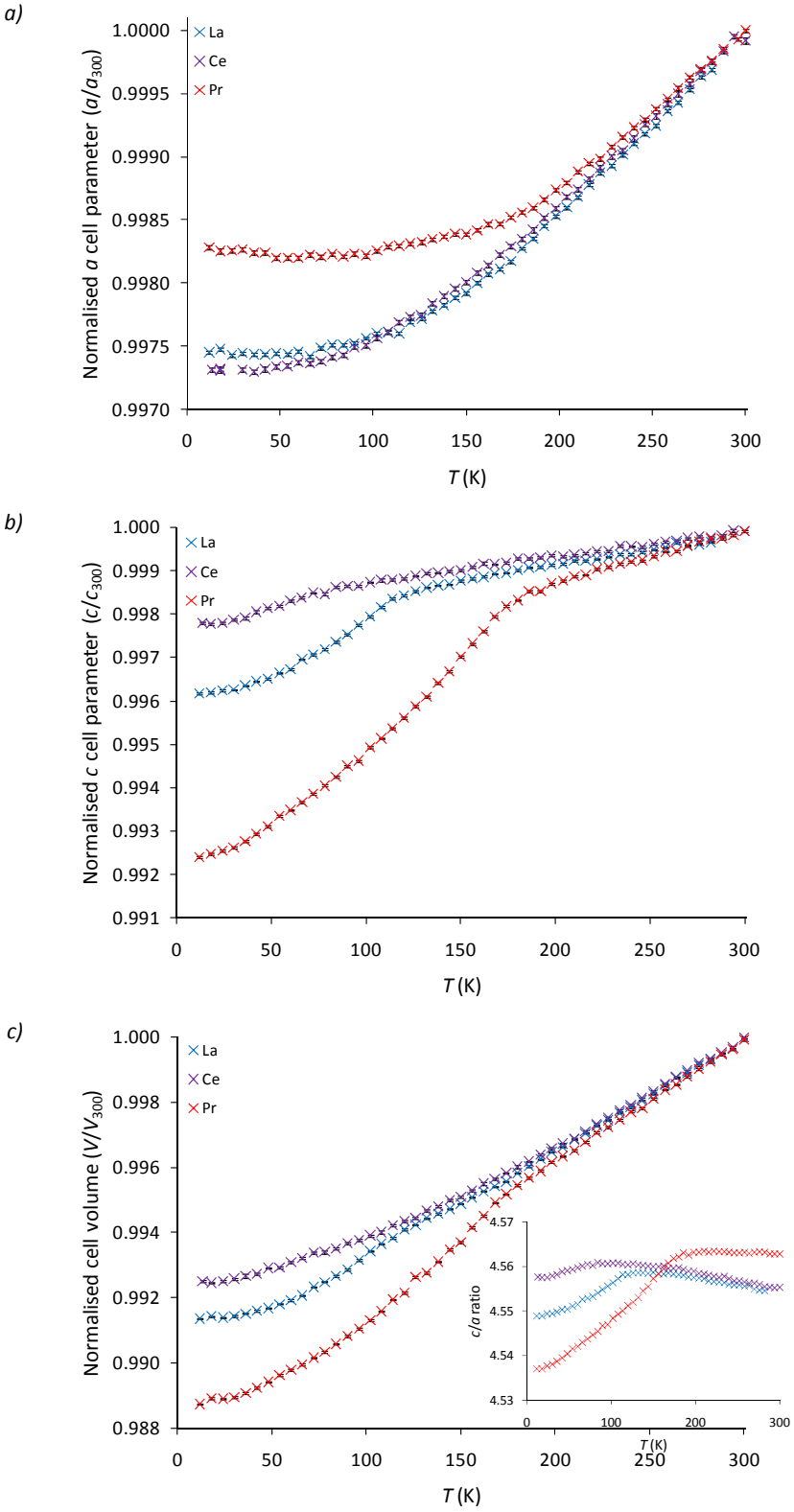

Figure 3.4 *Normalised (a) a & (b) c cell parameters and (c) cell volume for $A_2O_2Mn_2OSe_2$ materials as function of temperature with c/a ratio inset in (c); La = blue, Ce = purple, Pr = red.*

In each material the thermal expansion of the *a* and *c* cell parameters was modelled using an Einstein-type function, *eqn 3.1*; where a_0 is the lattice parameter at 0 K, θ is the Einstein temperature, and *C* is a refinable coefficient.[13] Note that these models are not included in *Figure 3.4* for ease of inspection, but are included in cell parameter plots in the appendix. It was found that the thermal

expansion observed in *a* could be adequately described by a single Einstein-coefficient. The thermal expansion observed in *c* was only modelled below the structural transition temperature. Whilst data for $La_2O_2Mn_2OSe_2$ and $Ce_2O_2Mn_2OSe_2$ were modelled using one Einstein-coefficient, modelling of the thermal expansion of $Pr_2O_2Mn_2OSe_2$ required two. Refined parameters for these models are given in *Table 3.4*.

$$\ln\left(\frac{a}{a_0}\right) = \sum_i \frac{C_i}{\exp\left(\frac{\theta_i}{T}\right) - 1} \qquad \textit{eqn 3.1}$$

Table 3.4 *Refined parameters for models of thermal expansion for $A_2O_2Mn_2OSe_2$ materials; values for $Pr_2O_2Mn_2OSe_2$ are taken from refinements in I4/mmm.*

		$La_2O_2Mn_2OSe_2$	$Ce_2O_2Mn_2OSe_2$	$Pr_2O_2Mn_2OSe_2$
	a_0 (Å)	*4.12897(2)*	*4.10270(2)*	*4.09061(3)*
a	C_i (10^{-6})	*18.0(3)*	*15.8(1)*	*20.3(6)*
	θ_i (K)	*404(6)*	*313(4)*	*616(12)*
	c_0 (Å)	*18.7825(2)*	*18.7016(4)*	*18.5597(4)*
	C_1 (10^{-6})	*35(1)*	*16(1)*	*36(1)*
c	θ_1 (K)	*135(5)*	*63(10)*	*82(5)*
	C_2 (10^{-6})	-	-	*74(22)*
	θ_2 (K)	-	-	*688(87)*

Figure 3.5 shows the variation in U_{33} parameters for the atom sites in each material. The data for $La_2O_2Mn_2OSe_2$ and $Pr_2O_2Mn_2OSe_2$ clearly show that the U_{33} parameter for the O(2) ion increases on cooling below the transition temperature obtained from the *c* cell parameter. The effect is most pronounced in the Pr^{3+} material, and is not observed, or is least pronounced, in $Ce_2O_2Mn_2OSe_2$. This reflects the magnitude of the *c*-axis transitions observed previously. This behaviour will be discussed in more detail in sections 3.3.1 and 3.3.2.

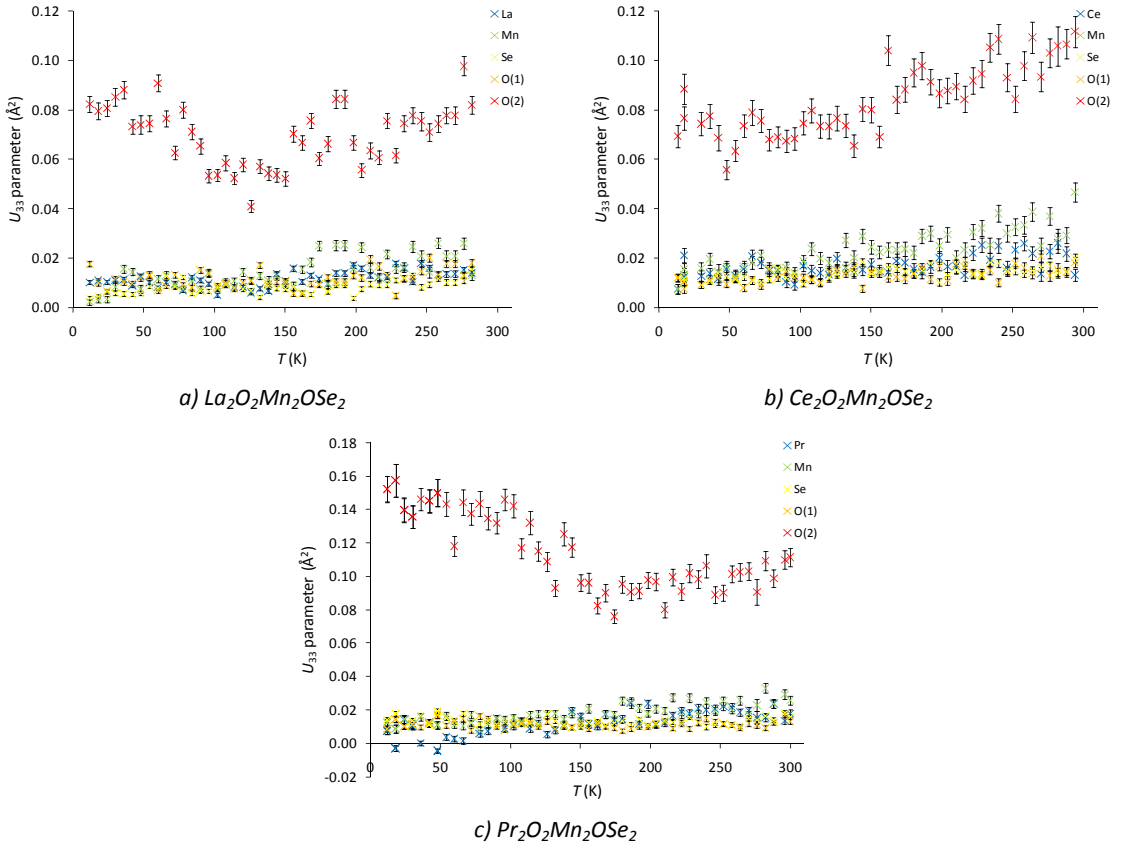

Figure 3.5 *The U_{33} parameters for a) $La_2O_2Mn_2OSe_2$, b) $Ce_2O_2Mn_2OSe_2$ and c) $Pr_2O_2Mn_2OSe_2$ as a function of temperature; A = blue, Mn = green, Se = yellow, O(1) = orange, O(2) = red.*

3.3.1 Displacement of the O(2) Ion

As discussed, the large U_{33} parameter observed for the O(2) atom site at both high and low temperatures, suggests that the O(2) ions are displaced above and below the layers. *Figure 3.6* shows Fourier difference plots, calculated in TA, for $Pr_2O_2Mn_2OSe_2$ neutron data collected at both 12 and 300 K, where the O(2) site has been removed prior to calculation. These results suggest that at room temperature nuclear density appears smeared over a range of *z* coordinates, whereas at 12 K it seems to be localising into values above and below the *z* = 0.5 plane. Whilst these displacements have not been found to be ordered, the behaviour of the ions can be modelled using two O(2) sites, displaced above and below the metal-oxide layer, both with occupancies of 0.5. This model sees a reduction in R_{wp} from 5.19 to 4.93 % for $Pr_2O_2Mn_2OSe_2$ data collected at 12 K. *Figure 3.7a* shows how the coordinate changes as a function of temperature, with the newly refined values for U_{33} inset. This clearly shows that the *z* coordinate follows the same behaviour as that seen for the original U_{33} parameter (*Figure 3.5*) and the U_{33} values then follow a trend more similar to that of the other atom sites present. *Figure 3.7b* is a plot of the associated Mn-O-Mn bond angle as a function of temperature, and clearly shows that the Mn-O-Mn bond is bent at room temperature, ~168°, and bends further on cooling below ~150 K to a minimum value of ~163°. We presume that the disorder / bending is static at low temperature and dynamic at high. Note that the input files used to produce the Fourier plots are given in the e-appendix.

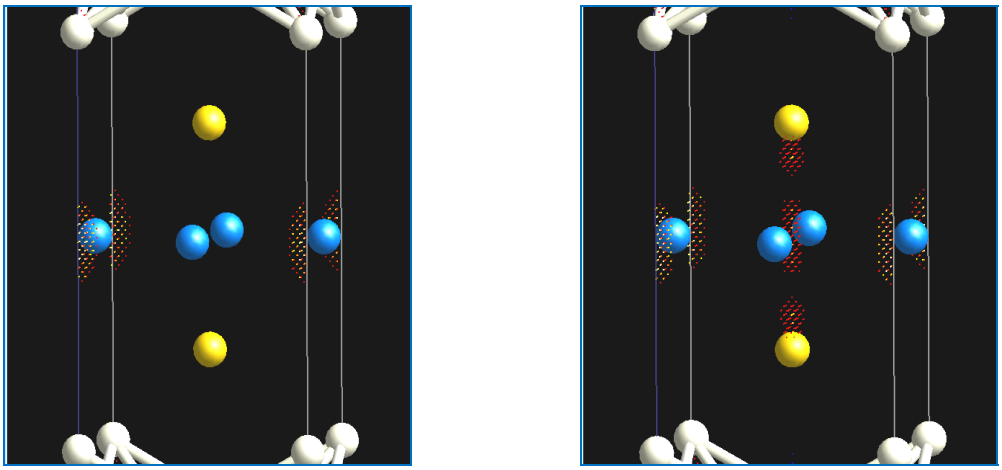

a) 295 K b) 12 K

Figure 3.6 *Fourier difference plots showing the elongated nuclear density left by removal of the O(2) site, at (a) room temperature and (b) 12 K; Pr = white, Mn = blue, Se = yellow; negative difference is shown in blue, positive differences range from red-yellow-white, with white corresponding to larger values. DGF110, hrp39783 & hrp39824, respectively.*

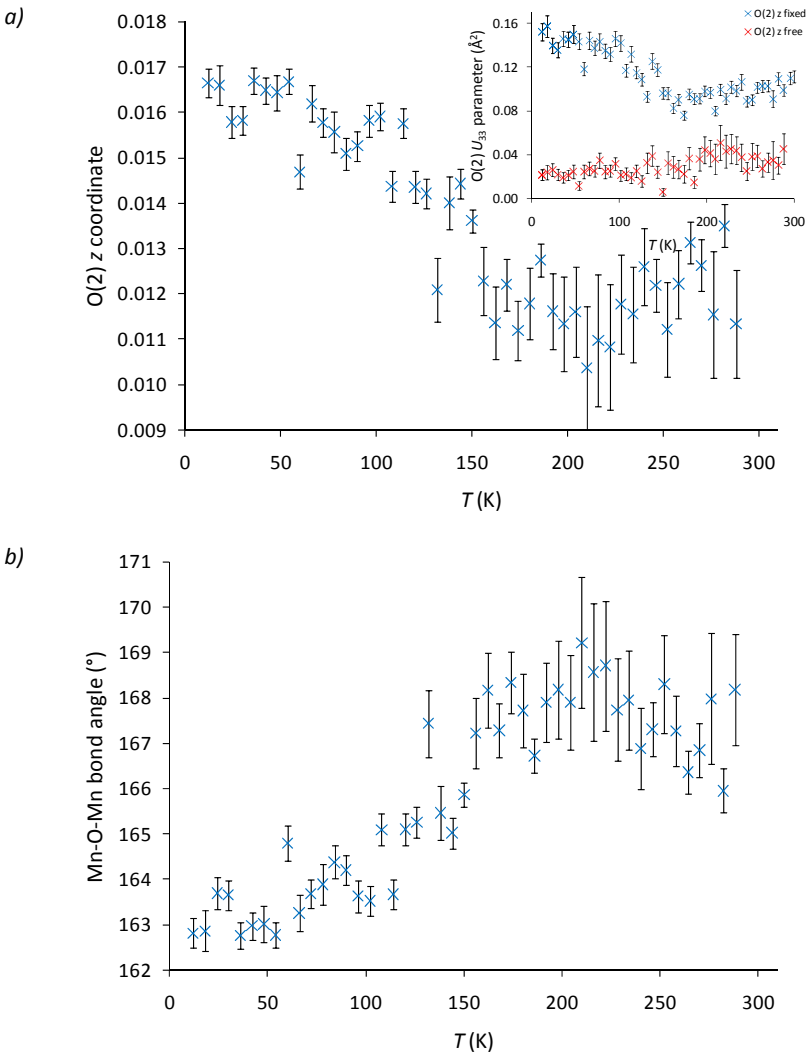

Figure 3.7 *The (a) O(2) z coordinate and (b) Mn-O-Mn bond angle in $Pr_2O_2Mn_2OSe_2$ as a function of temperature, with O(2) U_{33} values inset in (a).*

3.3.2 Non-magnetic Superstructure Peaks

Close inspection of high quality neutron and X-ray data collected at 12 K for $La_2O_2Mn_2OSe_2$ showed the presence of two small superstructure peaks at 1.68 and 1.70 Å, shown in *Figure 3.8*. The intensity of these peaks is relatively small, 0.4 % of the most intense reflection from neutron data (the {015} at 2.78 Å); similarly the intensity of these peaks is roughly 0.6 % of the most intense reflection from the X-ray data (again the {015}). These peaks were visible in both neutron and X-ray data, suggesting that they are structural in nature. In order to further investigate these peaks, longer X-ray data collections were performed over the range 53.5–55.0 2θ (*d* = 1.67–1.71 Å) between 12 and 300 K. *Figure 3.9* shows how the intensity of these peaks varies as a function of temperature, with the data modelled by *eqn 3.2*, where I_0 is the peak intensity at 0 K, T is temperature, T_c^{peaks} is the temperature at which the peaks appear, and β is the critical exponent. The peaks clearly appear with T_c^{peaks} of 106 K; a film plot of the data is given in appendix I. Whilst the appearance of these peaks is not exactly coincident with the transitions observed for the *c* cell parameter (~115 K) and U_{33} (~100 K, *Figure 3.5*), it is presumed they are indicative of ordering of the O(2) ions; any discrepancy in the temperatures could arise from the relatively small intensity of the peaks in question. Indexing of these peaks was attempted using both the *k_search* routine in the FullProf program suite, and the indexing routine in TA, however no sensible commensurate cell was obtained.[8, 14, 15] *Figure 3.9* also shows the background of the X-ray scans as a function of temperature, and is seen to decrease with decreasing temperature, particularly below ~106 K. This was modelled in TA using a single value to describe a straight line with equal intensity for all values of 2θ. A transition from either disordering, or only short range ordering, of the O(2) ions to longer range ordering could lead to both a reduction in background intensity and the appearance of new Bragg reflections.

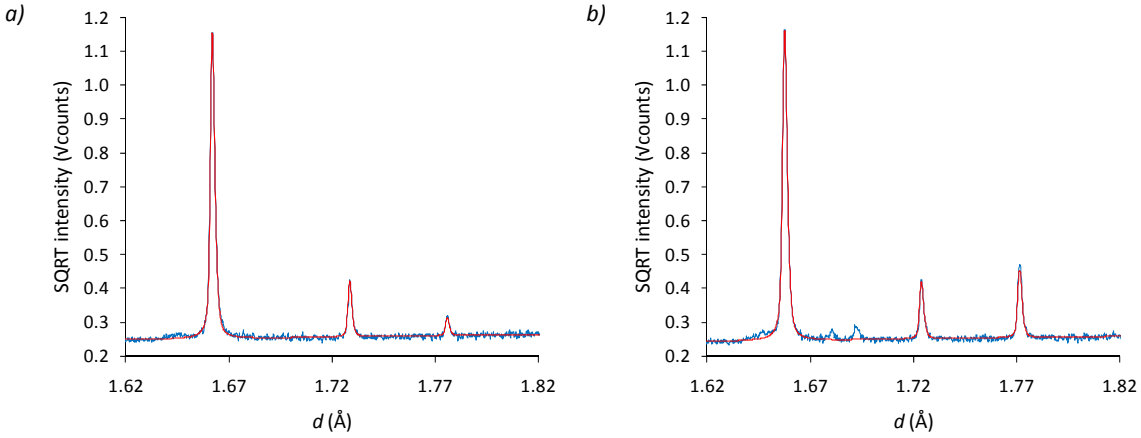

Figure 3.8 *Rietveld plots at (a) 295 and (b) 12 K highlighting the appearance of peaks at 1.68 and 1.70 Å for $La_2O_2Mn_2OSe_2$. DGF109, hrp39877 & hrp39916, respectively.*

$$I_{calc} = I_0 \times (1 - (T / T_c^{peaks}))^{\beta} \qquad \textbf{eqn 3.2}$$

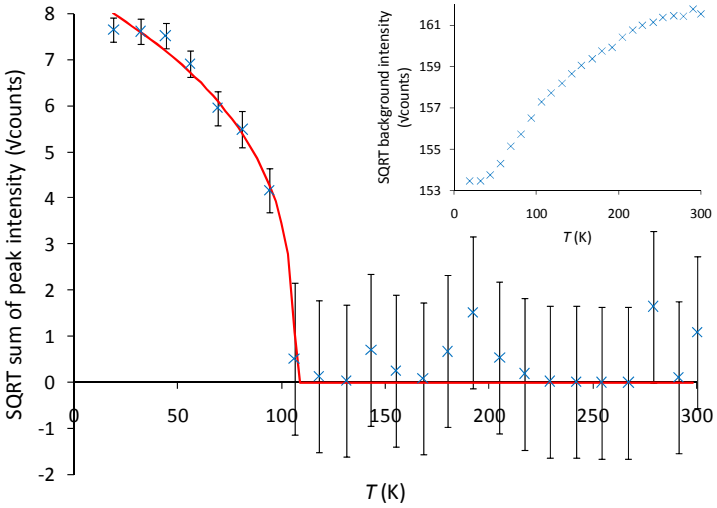

Figure 3.9 *The square root of the sum of the intensity of the peaks observed at 1.68 and 1.70 Å as a function of temperature for $La_2O_2Mn_2OSe_2$, with background intensity inset.*

Similar peaks are also observed in $Pr_2O_2Mn_2OSe_2$, with T_c^{peaks} = 170 K, *Figure 3.10* and *Figure 3.11*, however due to the peak broadening in $Pr_2O_2Mn_2OSe_2$, and furthermore peak splitting below 36 K, these peaks appear as one broad reflection at 12 K; again a film plot of the data can be found in appendix III. The transitions observed in the *c*-axis and U_{33} parameter occur at ~185 and 150 K, respectively. As in $La_2OMn_2OSe_2$, a change in the behaviour of the background intensity is seen at the same temperature. Studies of $Ba_2ZnO_2Ag_2Se_2$, by Clarke *et al*., showed the presence of superstructure peaks associated with ordering of the oxide ions within square-planar [ZnO_2] layers to produce discrete ZnO_2 units; however evidence suggests that in $La_2O_2Mn_2OSe_2$ and $Pr_2O_2Mn_2OSe_2$ this displacement is out of the plane.[16] Peaks are not observed in $Ce_2O_2Mn_2OSe_2$ (appendix II), again suggesting their presence is related to an increase in U_{33} of the O(2) site.

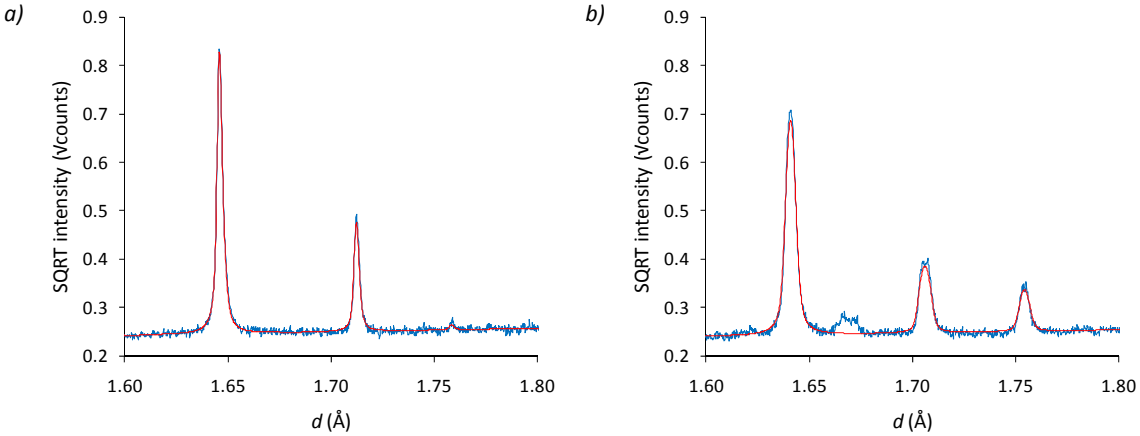

Figure 3.10 *Rietveld plots at (a) 295 and (b) 12 K highlighting the appearance of peak observed at ~1.67 Å for $Pr_2O_2Mn_2OSe_2$. DGF110, hrp39783 & hrp39824, respectively.*

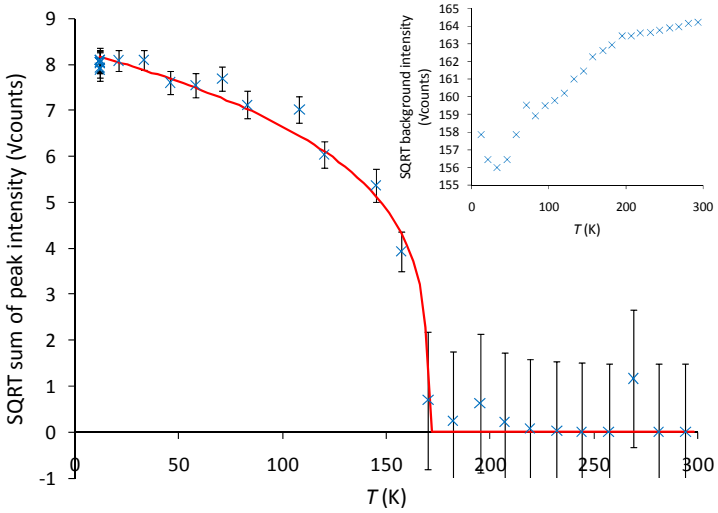

Figure 3.11 *The square root of the sum of the intensity of the peaks observed at ~1.67 Å as a function of temperature for $Pr_2O_2Mn_2OSe_2$ with background intensity inset.*

In an attempt to further understand the nature of these peaks, the peak position as a function of temperature was investigated for $Pr_2O_2Mn_2OSe_2$. This was then compared with the anisotropic expansion of the unit cell in order to try and understand what *hkl* values would explain the observed 2θ temperature dependence. *Figure 3.12* shows a comparison of the observed peak position and 2θ values calculated by least squares fitting. Least squares fitting was achieved by calculating peak positions from the Bragg equation (chapter 2) using lattice parameters obtained from variable temperature neutron studies, and *h*, *k* and *l* indices which were allowed to refine. As the peak intensity below 170 K was initially very weak, only the data below 160 K were modelled. The results suggest that the behaviour of the reflection would be consistent with *h*, *k* and *l* values of approximately 0, 1.25 and 9.5, respectively. This shows that the peaks have a 2θ temperature dependence consistent with that of $Pr_2O_2Mn_2OSe_2$. Whilst this examination is not entirely quantitative, the refined indices could suggest a cell with dimensions *a*×4*b*×2*c*. Further investigation of a *a*×4*b*×2*c* unit cell, with *P*1 symmetry, using ISODISTORT did not suggest that any of the active distortion modes for the O(2) site would give the intensities observed in the diffraction patterns.[17] Plots comparing behaviour of the (100), (010) and (001) reflections with the observed peak position are given in appendix III.

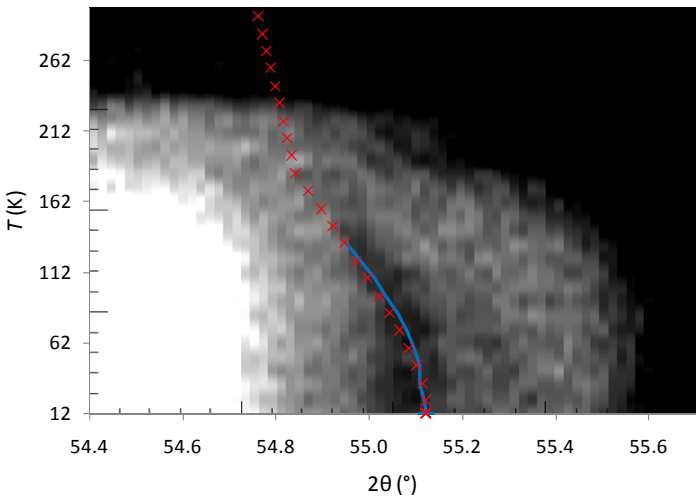

Figure 3.12 *Modelled (red) and observed (blue) position of a (0 1.25 0.95) superstructure peak in $Pr_2O_2Mn_2OSe_2$; a pseudo film plot of the data collected is given in the background. DGF110, d9_03001.*

3.3.3 Peak Splitting in $Pr_2O_2Mn_2OSe_2$

As discussed earlier, preliminary work suggested that $Pr_2O_2Mn_2OSe_2$ undergoes a further phase transition to on cooling below ~170 K.[3] Inspection of high quality X-ray powder diffraction data collected at 12 K suggested that this was associated with a decrease in symmetry of the unit cell from tetragonal (*I*4/*mmm*) to orthorhombic (*Immm*). This was particularly visible in splitting of the {200} reflection into the constituent (020) and (200) reflections. As this transition had not been observed in any other $La_2O_2Fe_2OSe_2$-type materials, it was investigated further with the aid of HRPD neutron data. *Figure 3.13* shows a film-plot of the data collected for the HRPD bs bank between 1.9 and 2.2 Å, with the {200} reflection at ~2.05 Å. Contrary to previous results, these data clearly suggest that peak splitting, and hence symmetry lowering, is only observed below 36 K (the blue region in *Figure 3.13* and *Figure 3.14*). Subsequent modelling of the data, shown in *Figure 3.14a*, confirmed this, with the *a* and *b* parameters of the unit cell diverging below 36 K.

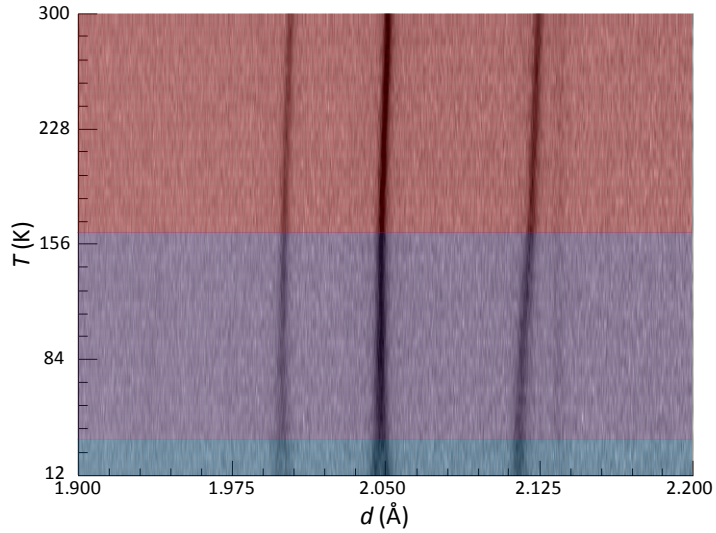

Figure 3.13 *Psuedo-film plot showing the splitting of the {200} reflection at ~2.05 Å as a function of temperature; red = tetragonal, purple = peak broadening, blue = orthorhombic region; plot shows the 1.9–2.2 Å (91–106 ms) region of the HRPD bs bank data.*

Close inspection of the backscattering bank neutron data also suggested that the diffraction peaks were broader at 12 K. This was modelled by refinement of the *dsp* term, given in *eqn 3.3*, used to describe the strain contribution to the full width half maximum of a pseudo-Voigt peak shape.[8] The results from this modelling are shown in *Figure 3.14b* and suggest that diffraction peaks begin to broaden below 180 K, until peak splitting occurs at 36 K, below which the strain broadening contribution remains constant. This broadening regime is shown in purple in *Figure 3.13* and *Figure 3.14*. *Figure 3.15* shows a comparison of the {200} reflections, modelled using both *I*4/*mmm* and *Immm* symmetry, at 300 and 12 K. X-ray and neutron data collected at 72 K also confirm that peak splitting does not occur until lower temperatures, and these are included in *Figure 3.15*. Note that in each of these refinements the peak shape used is derived from the whole data set. The refined parameters for the 72 K model are given in appendix III.

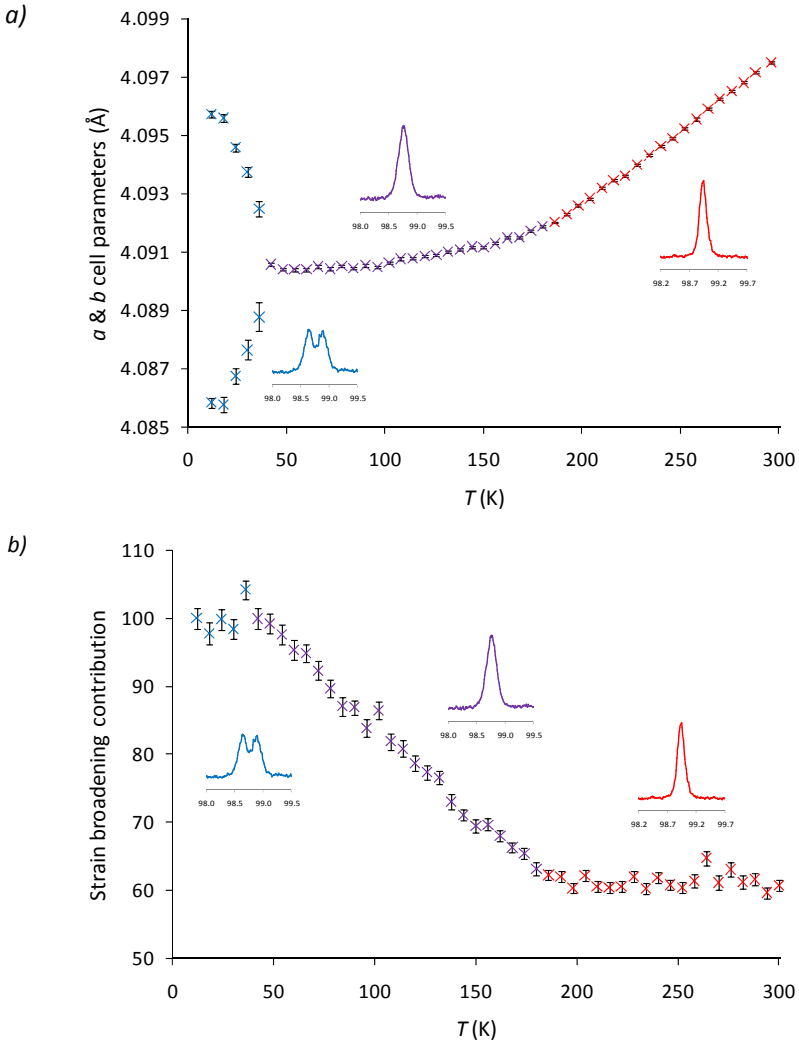

Figure 3.14 *The (a) a & b cell parameters and (b) strain broadening observed in $Pr_2O_2Mn_2OSe_2$ as a function of temperature; the {200} reflection is inset; red = tetragonal, purple = peak broadening, blue = orthorhombic region.*

$$pv\_fwhm = (dsp \times D\_spacing) + (dspsq \times D\_spacing^2) \qquad \textbf{eqn 3.3}$$

Whilst peak splitting was not observed in $La_2O_2Mn_2OSe_2$ or $Ce_2O_2Mn_2OSe_2$ there was a suggestion of peak broadening, although this was gradual and much less pronounced; plots of strain broadening parameter against temperature for these materials are given in appendices I and II.

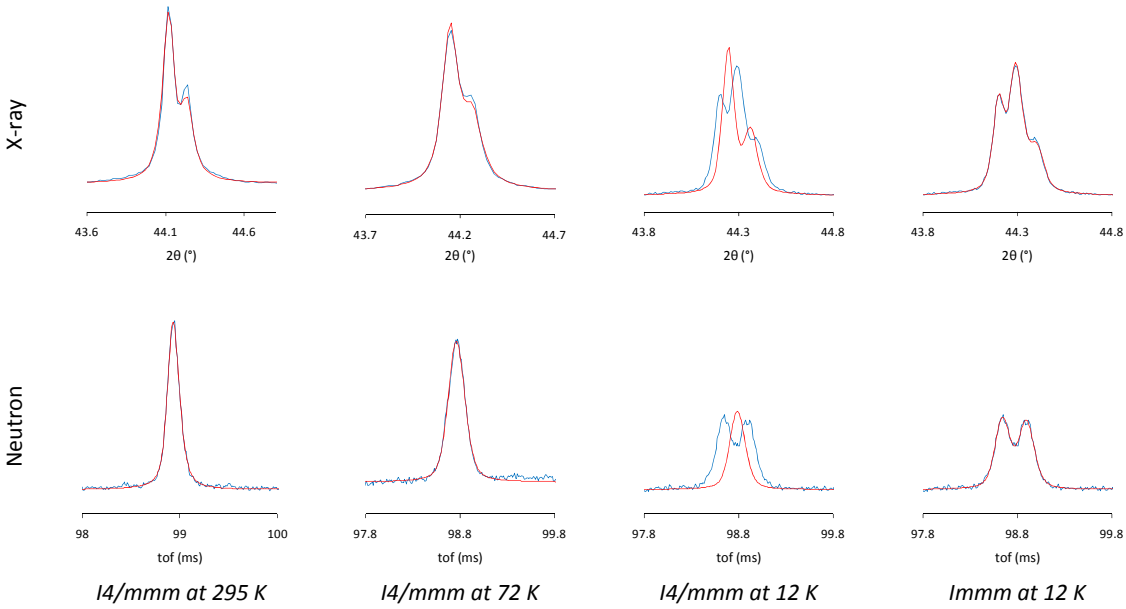

Figure 3.15 *The Pawley fit of the {200} reflection for $Pr_2O_2Mn_2OSe_2$ at 295 and 12 K using both I4/mmm and Immm symmetry; observed = blue, calculated = red, X-ray data have a Cu $K_{\alpha1,2}$ doublet.*

This transition is similar to that observed in ZrCuSiAs-type PrOMnSb, which undergoes a transition from tetragonal (*P*4/*nmm*) to orthorhombic (*Pmmn*) symmetry below 35 K, with an *a*/*b* ratio of 0.99660(1) at 20 K (*Figure 3.16*); the *a*/*b* ratio for $Pr_2O_2Mn_2OSe_2$ at 12 K is 0.99804(1).[18] This transition is thought to be driven by local distortion of the Pr^{3+} ion symmetry, and involves a reduction in point symmetry of the Pr^{3+} site from 4*mm* to *mm*2; this also occurs in $Pr_2O_2Mn_2OSe_2$. Interestingly, this behaviour has not been observed in related materials, such as $La_2O_2Mn_2OSe_2$, $Pr_2O_2Fe_2OSe_2$ (chapter 5) or PrOCuSe, suggesting that it may be driven by a complementarity, or mis-match, of the size of the Pr^{3+} and Mn^{2+} ion.[19]

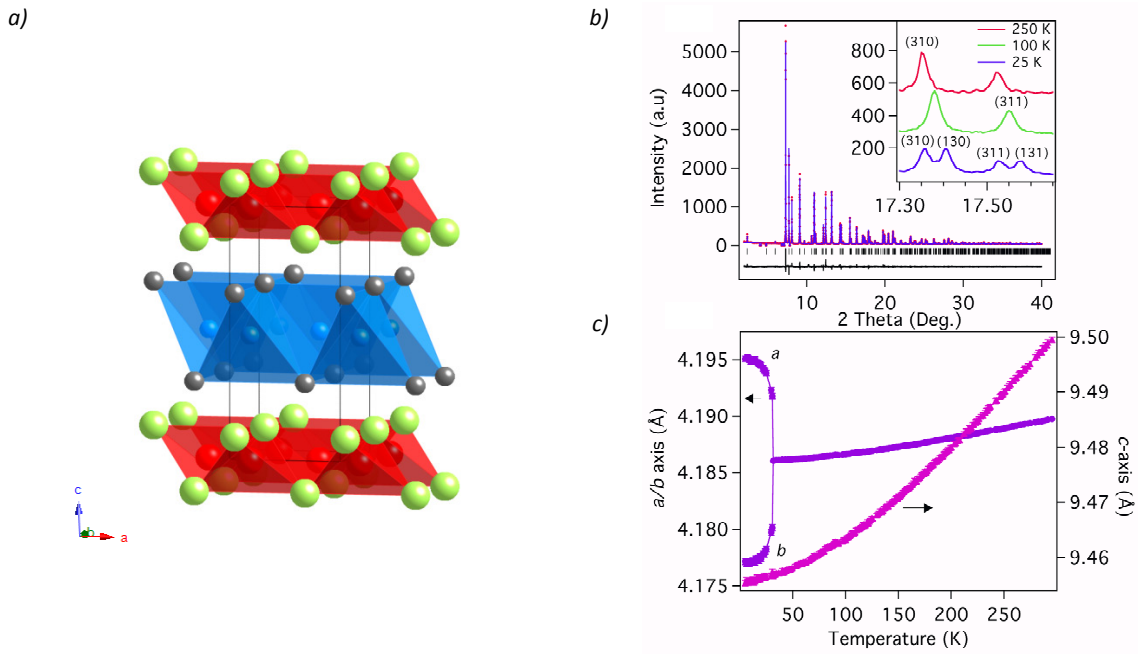

Figure 3.16 *The (a) structure of PrOMnSb and (b & c) figures taken from Kimber et al.[iv] with (b) the peak splitting and (c) cell parameters observed for PrOMnSb as a function of temperature; La = green, Mn = blue, O = red, Sb = grey, the unit cell is outlined, in (b) observed = red, calculated = blue, difference = black.*

Although there are no obvious indications that the symmetry is lower than orthorhombic at 12 K, the validity of an orthorhombic model was scrutinised using the Stephens model of anisotropic peak broadening.[20] This works by applying broadening (strain related) terms to different *hkl* reflections as given in *eqn 2.1*. The calculated term S^2 is then applied to both Gaussian and Lorentzian components of the peak shape by *eqn 3.5* and *eqn 3.6*, where the ε parameter determines the contribution of the Gaussian and Lorentzian terms. Application of this model to the orthorhombic cell might uncover any *hkl* dependant peak broadening, and therefore indicate if the symmetry needed lowering further. HRPD backscattering neutron data were used in the refinement due to the high resolution of the data collected. Refinement statistics showed an improvement with R_{wp} decreasing from 6.13 to 5.56 %. The refined coefficients from this fit are shown in *Table 3.5*. The only values greater than 3 standard uncertainties from 0 related to a broadening of 00*l* reflections relative to others, as is commonly observed for layered structures. There is therefore no strong evidence to suggest a further lowering of metric symmetry.

$$S^2 = S_{400}(h^4) + S_{040}(k^4) + S_{004}(l^4) + S_{220}(h^2k^2) + S_{202}(h^2l^2) + S_{022}(k^2l^2) \qquad \textit{eqn 3.4}$$

$$gauss\_fwhm = \left(\left(\frac{1.8}{\pi}\right) \times \left(\frac{d_{hkl}^2 + \sqrt{\max(S^2,0)}}{1000}\right) \times (1-\varepsilon) \times d_{hkl}\right) + 0.0001 \qquad \textit{eqn 3.5}$$

$$lor\_fwhm = \left(\left(\frac{1.8}{\pi}\right) \times \left(\frac{d_{hkl}^2 + \sqrt{\max(S^2,0)}}{1000}\right) \times \varepsilon \times d_{hkl}\right) + 0.0001 \qquad \textit{eqn 3.6}$$

[iv] Reprinted Figure 2 with permission from S. A. J. Kimber *et al.*, *Phys. Rev. B*, 2010, **82**, 100412. Copyright 2010 by the American Physical Society.

Table 3.5 *Refined parameters for the Stephens model of anisotropic peak broadening for $Pr_2O_2Mn_2OSe_2$ at 12 K.*

Parameter	Value
S_{400} (×10^6)	*-61(31)*
S_{040} (×10^6)	*-1(3)*
S_{004} (×10^6)	*0.52(2)*
S_{220} (×10^6)	*62(15)*
S_{202} (×10^6)	*-5(1)*
S_{002} (×10^6)	*-3.0(4)*
ε	*0.22(2)*

3.4 Magnetic Structure Determination

Previous studies of $La_2O_2Mn_2OSe_2$ at a limited number of temperatures and with low resolution data suggested an AFM1 structure is adopted on cooling (*Figure 3.1* and *Figure 3.2*), which was thought to be coincident with the phase transition observed in the *c* cell parameter.[1] In this section the ordering observed in $La_2O_2Mn_2OSe_2$ is reinvestigated, alongside that in $Ce_2O_2Mn_2OSe_2$ and $Pr_2O_2Mn_2OSe_2$, by a combination of diffraction, using both X-ray and HRPD data, and SQUID magnetometry. The ordering temperatures for these materials will also be investigated using rapid variable temperature data collected on HRPD.

3.4.1 Neutron Diffraction

On cooling $La_2O_2Mn_2OSe_2$ below ~165 K, strong new peaks became present in the neutron data at 1.84 and 4.03 Å and the intensity of the peaks at 1.77 and 3.45 Å was seen to increase significantly. *Figure 3.17* shows a film plot of the 90° bank neutron data, plotted from 12 to 300 K, and between 2.6 and 4.2 Å. These peaks were found to be consistent with antiferromagnetic ordering within the material with a *k*-vector of $\boldsymbol{k}$ = (000); this was confirmed though Pawley refinements in TA.[8, 21] Subsequent analysis of the data was performed using the program SARAh Refine, interfaced with the GSAS program suite.[22, 23] Representational analysis in SARAh uses a set of basis vectors to describe the symmetry of a system, and hence reduces the space group, of a purely magnetic model, to *P*1, where the magnetic cell dimensions are determined by the *k*-vector. For *I*4/*mmm* parent symmetry, with a propagation vector of (000), the allowed irreducible representations (irreps) are labelled by SARAh as Γ_3, Γ_7, and Γ_9, where Γ_9 has four basis vectors (Ψ_3, Ψ_4, Ψ_5, Ψ_6). Γ_3 produces a ferromagnetic arrangement (moments along *z*), Γ_7 produces an antiferromagnetic arrangement (again with the moments directed along *z*), and the four Γ_9 coefficients describe orientations of the moments in the *ab* plane. Refinement in GSAS, using the SARAh Refine interface, suggested that the antiferromagnetic, Γ_7, arrangement was sufficient to model the data collected (*Figure 3.1* and *Figure 3.2*). *Figure 3.18* shows a selection of contour plots produced from refinements using varying combinations of all of the Γ_3, Γ_7, and Γ_9 irreps to investigate the possibility of canting of the moments; note that these plots show varying combinations of the Γ_3 and Γ_9 irreps versus the Γ_7 irrep and a complete set of plots is given in appendix I. Results from these calculations showed that global minima in χ^2 for these refinements were obtained when the contribution of Γ_7 was at a maximum and other contributions were at a minimum. It is therefore reasonable to assume the

co-linear antiferromagnetic arrangement is the most suitable. These observations supported Withers' model, and consequently the Shubnikov space group *I*4'/*mm*'*m* (space group number 139.534 in TA / ISODISTORT) was used to describe the system.[8, 17] Details of the $La_2O_2Mn_2OSe_2$ 12 K refinement, performed in TA, are given in *Table 3.6*.

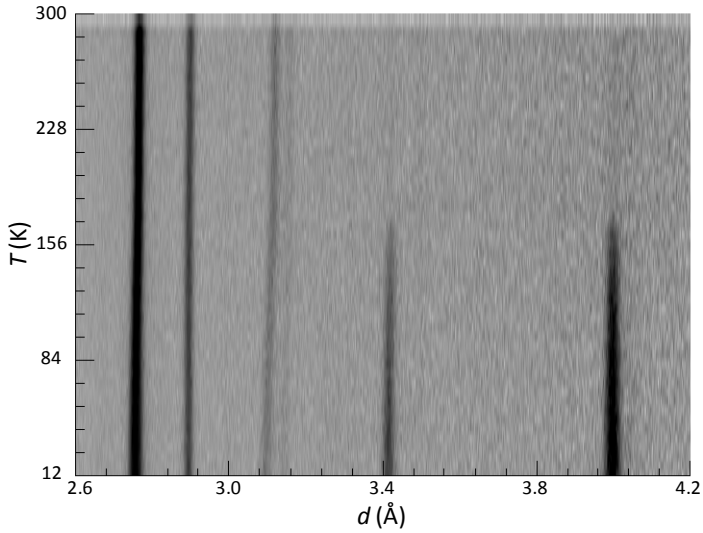

Figure 3.17 *Psuedo-film plot showing the evolution of the observed magnetic peaks at 3.45 and 4.03 Å as a function of temperature in $La_2O_2Mn_2OSe_2$; plot shows the 2.6-4.2 Å (90-146 ms) region of the 90° HRPD bank.*

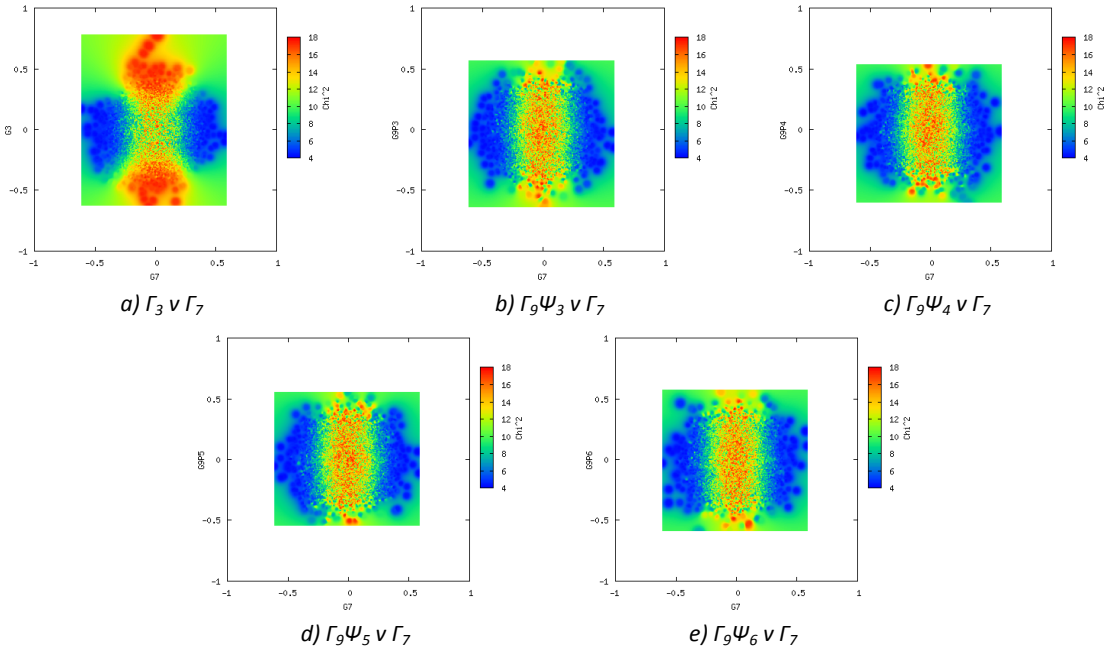

Figure 3.18 *Contour plots showing the change in χ^2 with varying contributions of the (a) Γ_3, (b) $\Gamma_9\Psi_3$, (c) $\Gamma_9\Psi_4$, (d) $\Gamma_9\Psi_5$ and (e) $\Gamma_9\Psi_6$ basis vectors versus the Γ_7 irrep; low values of χ^2 are shown in blue and large values in red.*

Similar peaks were also observed in neutron data collected for $Ce_2O_2Mn_2OSe_2$ and $Pr_2O_2Mn_2OSe_2$, and were also successfully modelled using an AFM1 arrangement of moments (*Figure 3.1* and *Figure 3.2*). The breaking of the tetragonal symmetry in $Pr_2O_2Mn_2OSe_2$ produces two independent Mn^{2+} sites which can therefore have different moments. Refinements were therefore performed in *Im*'*m*'*m* and, in order

to keep the AFM arrangement of the ions well defined, the moment on Mn(2) was constrained to be the equal and opposite to that on Mn(1). Allowing the magnitudes to differ resulted in divergence of the refinement. Unlike in other mixed-anion materials, *e.g.* CeOFeAs, there is no evidence of ordering of the rare-earth ions down to 12 K from neutron data, or from susceptibility data discussed in section 3.4.2.[24] The final refinements for each material, at 12 K, are given in *Table 3.6* and Rietveld plots for $La_2O_2Mn_2OSe_2$ are shown in *Figure 3.19*; plots for *A* = Ce and Pr are given in appendices II and III. Similar to the room temperature refinements, the peaks in the neutron data at 1.23 and 2.13 Å were excluded. Selected inter-atomic distances and bond angles for each material are given in *Table 3.7*.

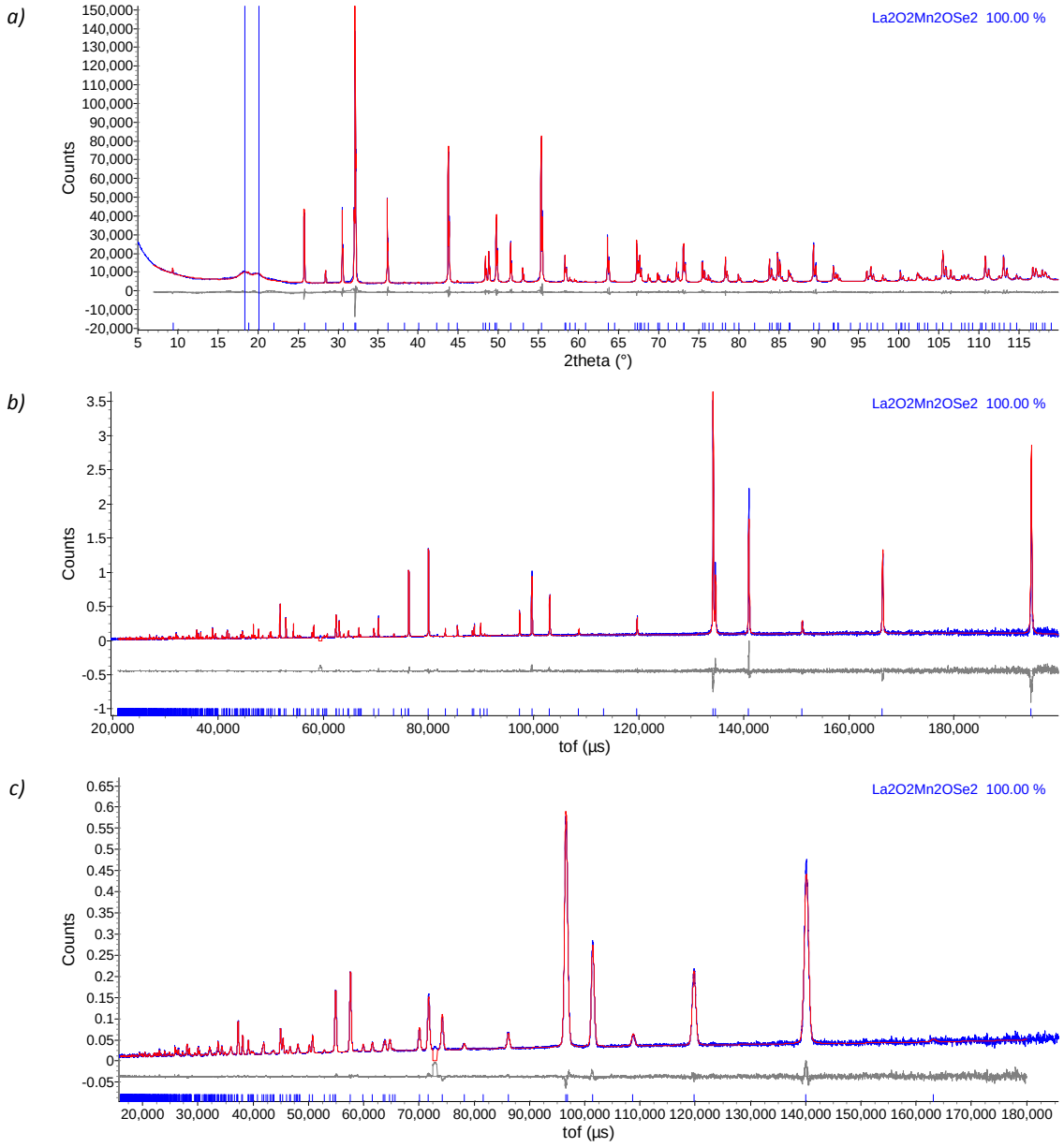

Figure 3.19 *Rietveld plots for $La_2O_2Mn_2OSe_2$ at 12 K using (a) X-ray, (b) HRPD bs and (c) 90° bank data; observed = blue, calculated = red, difference = grey. These plots can be compared with those in Figure 3.3. DGF109, d9_03049, hrp39916.*

Table 3.6 *Results from combined X-ray / neutron Rietveld refinements of $A_2O_2Mn_2OSe_2$ materials at 12 K.*

	$La_2O_2Mn_2OSe_2$	$Ce_2O_2Mn_2OSe_2$	$Pr_2O_2Mn_2OSe_2$
Nuclear symmetry	*I4/mmm*	*I4/mmm*	*Immm*
Magnetic symmetry	*I4'/mm'm*	*I4'/mm'm*	*Im'm'm*
a (Å)	*4.12870(1)*	*4.10247(1)*	*4.08616(3)*
b (Å)	*= a*	*= a*	*4.09417(4)*
c (Å)	*18.78115(5)*	*18.70183(8)*	*18.5539(1)*
V (Å^3)	*320.146(1)*	*314.757(2)*	*309.789(6)*
A z (*c*)	*0.18644(1)*	*0.18700(2)*	*0.18826(3)*
Se *z* (*c*)	*0.09999(2)*	*0.10089(3)*	*0.10167(3)*
O(1) *z* (*c*)	*0.25*	*0.25*	*0.2512(2)*
A U_{eq} (100×Å^2)	*0.51(1)*	*0.49(2)*	*0.71(3)*
Mn(1) U_{eq} (100×Å^2)	*0.63(2)*	*0.63(2)*	*0.28(7)*
Mn(2) U_{eq} (100×Å^2)	*= Mn(1)*	*= Mn(1)*	*2.1(1)*
Se U_{eq} (100×Å^2)	*0.68(1)*	*0.70(1)*	*1.34(3)*
O(1) U_{eq} (100×Å^2)	*0.58(1)*	*0.68(2)*	*0.90(3)*
O(2) U_{eq} (100×Å^2)	*2.82(3)*	*2.49(3)*	*5.35(7)*
Mn^{2+} M_z (μ_B)	*4.223(7)*	*4.023(7)*	*4.219(8)*
N^o. variables	*70*	*91*	*78*
R_{wp} (%)	*4.11*	*3.93*	*4.94*
χ^2	*4.52*	*4.38*	*4.61*

U_{ij} values, statistics for specific banks of data and other information can be found in appendices I–III.

Table 3.7 *Selected inter-atomic distances and bond angles for $A_2O_2Mn_2OSe_2$ materials at 12 K.*

		$La_2O_2Mn_2OSe_2$	$Ce_2O_2Mn_2OSe_2$	$Pr_2O_2Mn_2OSe_2$
Bond lengths (Å)	$d_{M\text{-}M}$	*2.91943(1)*	*2.90089(1)*	*2.89219(1)*
	$d_{M\text{-}O}$	*2.06435(1)*	*2.05124(1)*	*2.04709(1)*
				2.04308(1)
	$d_{M\text{-}Se}$	*2.7908(2)*	*2.7871(3)*	*2.7807(4)*
				2.7837(4)
	$d_{A\text{-}O}$	*2.3846(1)*	*2.3655(2)*	*2.331(2)*
				2.357(2)
	$d_{A\text{-}Se}$	*3.3406(2)*	*3.3179(3)*	*3.3084(4)*
Bond angles (°)	*M*-Se-*M* (1)	*63.074(6)*	*62.720(8)*	*62.63(1)*
	M-Se-*M* (2)	*95.41(1)*	*94.78(1)*	*94.57(2)*
				94.68(2)
	Se-*M*-Se	*84.59(1)*	*85.22(1)*	*85.43(2)*
				85.32(2)
	A-O-*A* (1)	*104.511(5)*	*104.362(8)*	*103.81(1)*
	A-O-*A* (2)	*119.93(1)*	*120.26(2)*	*122.4(1)*
				120.6(1)

At 12 K, the refined moments on the Mn^{2+} ions in $La_2O_2Mn_2OSe_2$, $Ce_2O_2Mn_2OSe_2$ and $Pr_2O_2Mn_2OSe_2$ are 4.223(7), 4.023(7) and 4.219(8) μ_B, respectively. These values are comparable to Mn^{2+} moments in materials such as MnO (4.892 μ_B at 10 K) and Mn_2SiSe_4 (4.36(7) μ_B at 12 K). Theoretically one would expect a Mn^{2+} moment of 5 μ_B, however this is probably reduced by covalency within the materials. The magnetic ordering observed is similar to that in PrOMnSb, which is seen to order with an AFM1 arrangement below 230 K, and has a Mn^{2+} moment of 3.69(3) μ_B at 4 K.[18] On cooling below 100 K, however, these Mn^{2+} moments are observed to "flop" into the *ab* plane, and furthermore the Pr^{3+} moments are seen to order below 35 K, suggesting a correlation with the onset of orthorhombic symmetry. Note that comparisons of the ordering observed here with those observed for other $La_2O_2Fe_2OSe_2$-type materials will be made in chapter 5.

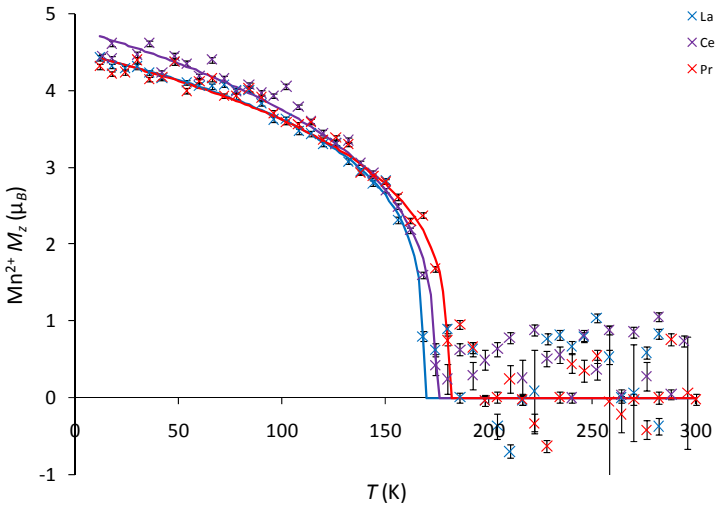

Figure 3.20 *Magnetic moment of Mn^{2+} for $A_2O_2Mn_2OSe_2$ materials as a function of temperature; La = blue, Ce = purple, Pr = red.*

Figure 3.20 shows the change in the magnitude of the Mn^{2+} moments, derived from variable temperature neutron data, collected for each material. The behaviour of these moments has been modelled using *eqn 3.7*, and the Néel temperatures extracted for each material were 168.1(4), 174.1(2) and 180.3(4) K, respectively; other refined parameters are included in *Table 3.8*. The difference between these temperatures and the phase transition observed in the *c* parameter in section 3.3, suggests that the two transitions are not fully correlated, as has been suggested by Withers.[1] The observed increase in T_N with decreasing rare-earth radii, reflects the decrease in cell parameters and hence an increase in orbital overlap. Refined β values of 0.24(7), 0.29(7) and 0.27(4) for $La_2O_2Mn_2OSe_2$, $Ce_2O_2Mn_2OSe_2$ and $Pr_2O_2Mn_2OSe_2$, respectively, are similar to that reported for the *S* = 5/2 material $CsMnBr_3$ of 0.25(2).[25]

$$M_{calc} = M_0 \times (1 - (T / T_N))^{\beta} \qquad \textbf{eqn 3.7}$$

Table 3.8 *Refined parameters for models of magnetic ordering of Mn^{2+} ions as a function of temperature in $A_2O_2Mn_2OSe_2$.*

		$La_2O_2Mn_2OSe_2$	$Ce_2O_2Mn_2OSe_2$	$Pr_2O_2Mn_2OSe_2$
Mn^{2+} M_z	M_0 (μ_B)	*4.5(3)*	*4.8(3)*	*4.5(1)*
	T_N (K)	*168.1(4)*	*174.1(2)*	*180.3(4)*
	β	*0.24(7)*	*0.29(7)*	*0.27(4)*

3.4.2 SQUID Magnetometry

Interpretation of magnetic data on all of these systems is significantly complicated by the presence of minor amounts of magnetic impurities and conclusions should be treated with care. The problems of minor ferro- or ferri-magnetic impurities in magnetic measurements of other Mn-containing systems has been highlighted in the literature.[26]

The field-cooled (FC) and zero-field-cooled (ZFC) molar susceptibilities of $La_2O_2Mn_2OSe_2$, measured with an applied field of 1000 Oe, are shown in *Figure 3.21*. There are several features observed in the data collected on warming, particularly a marked difference between FC and ZFC magnetisation at all temperatures below 167 K. The FC warming data can be split into three main regions. Firstly there is a

marked reduction in susceptibility at ~40 K. This is followed by a second reduction in susceptibility around 140 K. Finally FC and ZFC data meet around 167 K (this is best observed in the plot of $1/\chi_{mol}$ versus *T* inset in *Figure 3.21*). This temperature is similar to the T_N value observed in the neutron diffraction experiments (168 K) and presumably represents the Néel ordering temperature. Above 167 K, the gradient of the lines plotted for both FC and ZFC experiments is positive, *i.e.* the $1/\chi_{mol}$ versus *T* plot has a negative gradient. This behaviour is non-Curie-Weiss, although similar to that observed in chromium metal, $Na_{0.51}CoO_2$ and $LaO_{1-x}F_xFeAs$.[27-29] This increase in susceptibility with temperature presumably reflects the persistence of strong short-range AFM interactions above T_N in this frustrated system, as seen, for example, in related cobalt-containing materials.[30] The data reported by Withers show similar behaviour, although the low temperature discontinuities observed were smaller.[1]

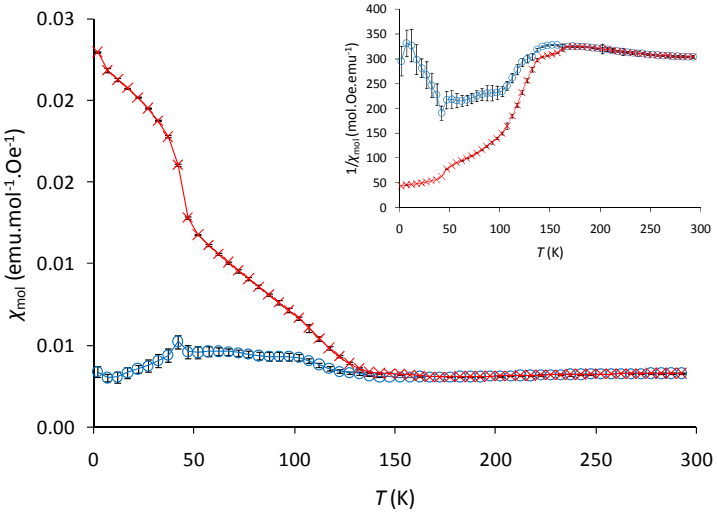

Figure 3.21 *Magnetic susceptibility as a function of temperature for both FC and ZFC experiments on $La_2O_2Mn_2OSe_2$ recorded with an applied field of 1000 Oe; FC = red, ZFC = blue; inset shows inverse susceptibility. DGF109.*

The appearance of portions of the FC and ZFC data near the low temperature discontinuities is reminiscent of spin glass or superparamagnetic behaviour. We note that no significant features were seen in the neutron data at these temperatures. We therefore believe the effects below 45 K are from a small of amount of ferrimagnetic Mn_3O_4 impurity, not observed in the diffraction data, which have been previously demonstrated to swamp sample signals at <1 % by weight.[26, 31] Work on Mn_3O_4 nanoparticles has demonstrated superparamagnetic behaviour, with blocking temperatures (T_b) dependant on particle size; T_C is reported as 42 K and T_b values are reported as 36, 40 and 41 K for 6, 10 and 15 nm particles, respectively.[32, 33] Based on these reports, and a magnetisation of ~10 emu.g^{-1} for Mn_3O_4 at 1000 Oe for a particle size of ~15 nm, one can estimate that a contribution of ~0.5 % by weight of impurity would give rise to the magnetisation observed below 45 K in *Figure 3.21*. Such nanoparticles with their broad diffraction profiles would be hard to observe in the powder diffraction data. The 140 K discontinuity could arise from small amounts of $LaMnO_3$, which has been reported to order ferromagnetically below 140 K.[34, 35] FC / ZFC divergence similar to that observed has been reported and attributed to a cluster-glass state. Small amounts of perovskite impurities $LaFeO_3$ and $LaCoO_3$ have been observed in the synthesis of the iron and cobalt-containing analogues of these phases.

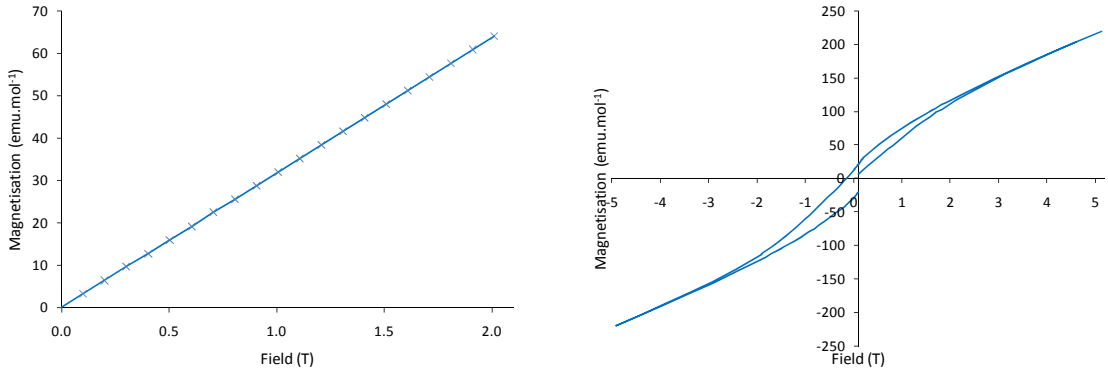

a) 292 K *b) 2 K*

Figure 3.22 *Magnetisation as a function of applied magnetic field at (a) 292 K and (b) 2 K for $La_2O_2Mn_2OSe_2$. DGF109.*

Figure 3.22 shows the variation in magnetization as a function of applied field at 292 and 2 K. Data collected at 292 K indicate the material is paramagnetic at room temperature, whilst those collected at 2 K show a weak hysteresis, with a coercive field of 2050 Oe, characteristic of ferromagnetic ordering within the material. This, again, is possibly the result of minor impurities in the sample. Mn_3O_4 has a reported coercive field in the bulk of 4600 Oe at 4.2 K.[31] The lower coercive field could be caused by nanosizing of the impurity. In order to investigate the discontinuity observed at 45 K, measurements were also taken at 12, 100 and 160 K; plots for these data are given in appendix I. *Table 3.9* shows the coercive fields calculated at each temperature from these measurements, and shows a decrease with increasing temperature consistent with superparamagnetic particles as T_b is approached. As expected from the data presented in *Figure 3.21*, calculation of the Mn^{2+} magnetic moment from the room temperature data gives a value of ~2.7 μ_B, which is considerably lower than the expected value for high spin Mn^{2+} of 5.9 μ_B.

Table 3.9 *Calculated coercive fields at selected temperatures for the $La_2O_2Mn_2OSe_2$ sample.*

	2 K	12 K	100 K	160 K	292 K
Coercive field (Oe)	*2050*	*1550*	*400*	*30*	*0*

Susceptibility data collected for $Ce_2O_2Mn_2OSe_2$ and $Pr_2O_2Mn_2OSe_2$, *Figure 3.23*, are dominated by the paramagnetic Ce^{3+} and Pr^{3+} ions; although deviations between FC and ZFC data are seen in the Curie plot for $Pr_2O_2Mn_2OSe_2$ at ~180 K, which is consistent with the observed T_N from the neutron data. Both of these materials also exhibit hysteresis at low temperatures, although this effect is less pronounced (*Figure 3.24*), with 12 K coercive fields for these samples of 450 Oe and 120 Oe, respectively. This may again be due to minor manganese-containing impurities. From the magnetisation versus applied field plot (*Figure 3.24*) at room temperature the μ_{eff} for $Pr_2O_2Mn_2OSe_2$ is calculated as 4.38 μ_B, corresponding to an Mn^{2+} contribution of 2.53 μ_B. In order to investigate the divergence observed in $Pr_2O_2Mn_2OSe_2$, FC and ZFC data were also collected with an applied field of 50 Oe, to minimise the contribution of the paramagnetic Pr^{3+} ions. These results are shown in *Figure 3.25*, and clearly show the FC and ZFC data diverging below 180 K, although other discontinuities, thought to originate from impurities in the sample, can also be seen. The moment calculated from the approximately linear region 200–300 K of the

Curie-Weiss plot is 5.97 μ_B with a Curie constant of -179 K, 4.79 μ_B after removal of the Pr^{3+} contribution. These compare with values from *Figure 3.24* of 5.75 μ_B with a Curie constant of -197 K, 4.49 μ_B after removal of the Pr^{3+} contribution.

The Ce^{3+} containing sample contains, as discussed below, significant unknown impurity phases. Whilst values should be treated with caution we extract μ_{eff} values of 5.98 μ_B (with a Curie constant of -485 K) and 3.60 μ_B from the Curie-Weiss plot in *Figure 3.23* between 200 and 300 K, and the magnetisation versus field plot in *Figure 3.24*, respectively. Assuming paramagnetic Ce^{3+} with μ_{eff} = 2.54, the Mn^{2+} contributions are 5.42 and 2.50 μ_B, respectively. The apparent room temperature moment of Mn^{2+} in each system is similar, suggesting similar short-range interactions are present.

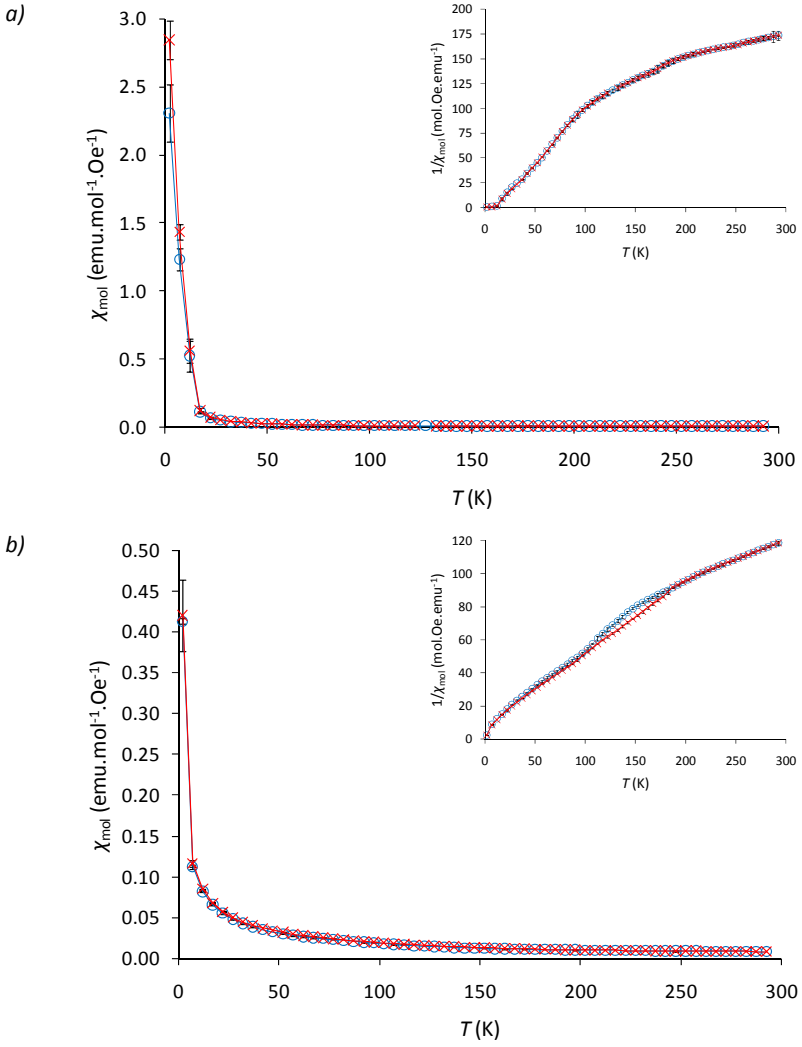

Figure 3.23 *Magnetic susceptibility as a function of temperature for FC and ZFC experiments on (a) $Ce_2O_2Mn_2OSe_2$ and (b) $Pr_2O_2Mn_2OSe_2$ data measured with a field of 1000 Oe; FC = red, ZFC = blue; inset shows inverse susceptibility. DGF136 & DGF110, respectively.*

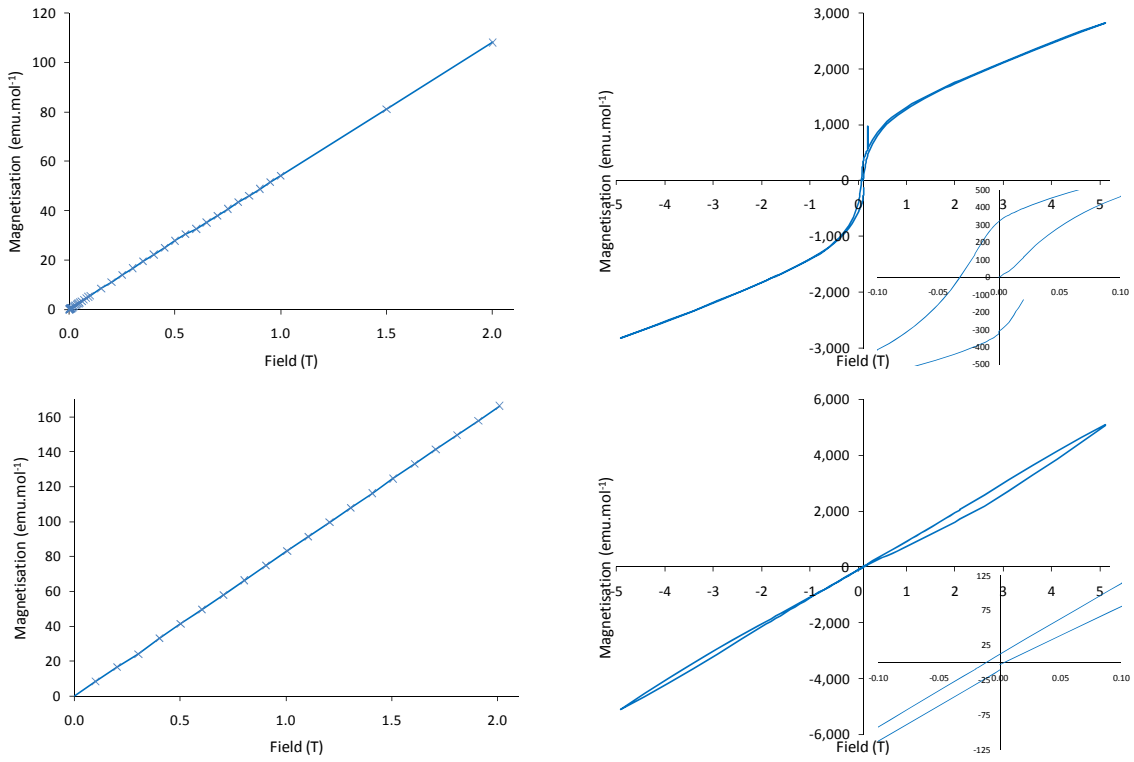

a) 292 K *b) 2 K*

Figure 3.24 *Magnetisation as a function of applied magnetic field at (a) 292 K and (b) 12 K for (top) $Ce_2O_2Mn_2OSe_2$ and (bottom) $Pr_2O_2Mn_2OSe_2$; zoomed in regions are inset to highlight hysteresis. DGF136 & DGF110, respectively.*

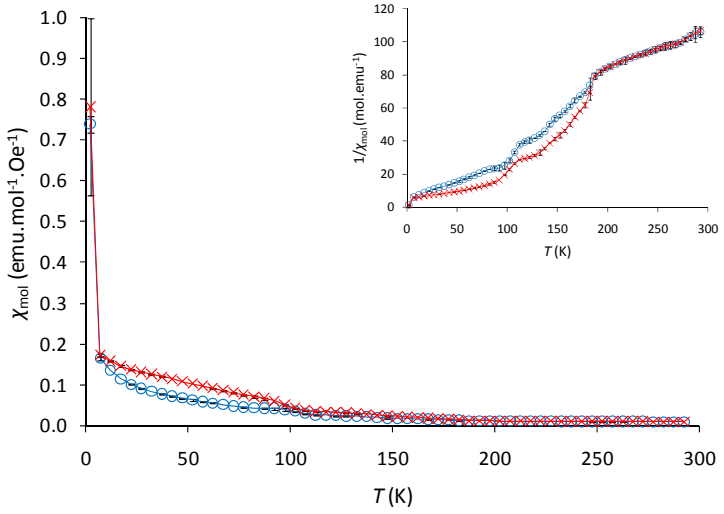

Figure 3.25 *Magnetic susceptibility as a function of temperature for both FC and ZFC experiments on $Pr_2O_2Mn_2OSe_2$ with an applied field of 50 Oe; FC = red, ZFC = blue; inset shows inverse susceptibility. DGF110.*

3.5 Impurity Phases in $Ce_2O_2Mn_2OSe_2$

As discussed in section 3.2, the $Ce_2O_2Mn_2OSe_2$ sample contained several phases in addition to the target phase, comprising approximately 20 % by weight. These have been found to be $CeOMn_{0.5}Se$, MnSe, CeO_2 and one other "unknown" phase. $CeOMn_{0.5}Se$ has a ZrCuSiAs-type structure with Mn^{2+} sites half-occupied and cell parameters of a = 4.0260(7) and c = 9.107(2) Å.[36] These two phases are related by

formal loss of "MnO" from the $[Mn_2O]^{2+}$ layer of $Ce_2O_2Mn_2OSe_2$ followed by a translation of the "$Ce_2O_2Se_2$" layers to accommodate tetrahedral coordination of the, now half occupied, Mn sites. *Figure 3.26* shows a comparison of the two models. In order to investigate this phase more thoroughly a pure sample would be required, however preparation of this has proven difficult. The contribution of $CeOMn_{0.5}Se$ to the X-ray data can be seen in *Figure 3.27*, alongside the other phases present.

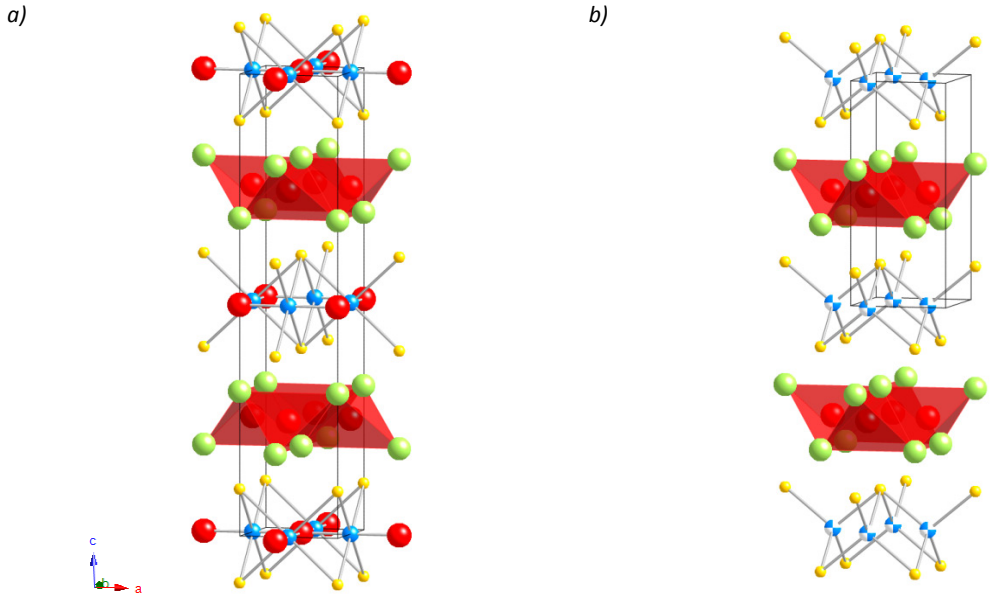

Figure 3.26 *Comparison of the nuclear structures of (a) $Ce_2O_2Mn_2OSe_2$ and (b) $CeOMn_{0.5}Se$; Ce = green, Mn = blue, O = red, Se = yellow, unit cells are outlined.*

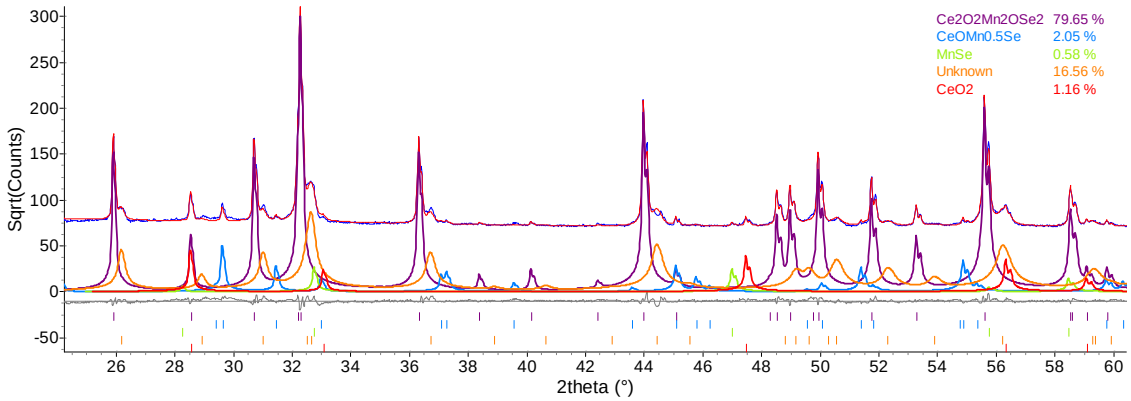

Figure 3.27 *The contribution the different phases to the X-ray diffraction pattern of $Ce_2O_2Mn_2OSe_2$; observed = blue, calculated = red. DGF136, d9_03354.*

Another major phase present, estimated to be *ca.* 9.6 % by weight from Rietveld refinement of both X-ray and neutron data (*Table 3.10*), was the "unknown" phase. This was observed as small, broad peaks alongside each of the peaks of the main phase (*Figure 3.27*). Due to the small and broad nature of these peaks they have been difficult to analyse. Their systematic appearance beside each of the main peaks, however, suggests that the "unknown" phase shares a similar structure to $Ce_2O_2Mn_2OSe_2$, but with slightly smaller cell parameters. Due to the similarity in structure discussed, between $Ce_2O_2Mn_2OSe_2$ and $CeOMn_{0.5}Se$, one possible model could be that of a material with intergrowths of octahedral and tetrahedral transition metal layers, or similarly the presence of oxygen or manganese vacancies in the $[Mn_2O]^{2+}$ layers. In order to model this phase a second $Ce_2O_2Mn_2OSe_2$-related phase was included,

however with smaller lattice parameters. Comparison of peak intensities for both $Ce_2O_2Mn_2OSe_2$ and the unknown phase suggested that these phases must have closely related structures, however, the relatively weak intensity of the peaks for the unknown phase meant that this analysis was limited. *Figure 3.28* shows a comparison of the thermal expansion of both $Ce_2O_2Mn_2OSe_2$-type phases calculated from Rietveld refinement using variable temperature neutron data. Whilst the overall degree of thermal expansion observed is larger for the unknown phase, the trends on cooling are similar, suggesting, again, that these phases are closely related. Similar trends are observed for individual *a* and *c* cell parameters, which are given in appendix II.

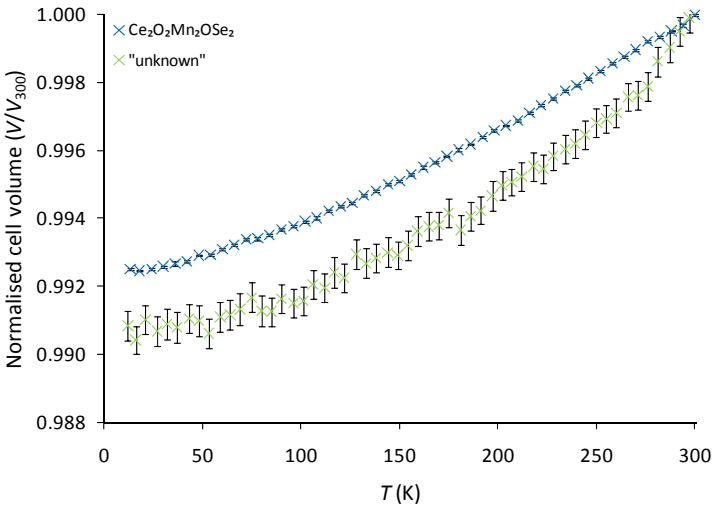

Figure 3.28 *Cell volume for $Ce_2O_2Mn_2OSe_2$ and the "unknown" phase as a function of temperature; $Ce_2O_2Mn_2OSe_2$ = blue, "unknown" = green.*

The room temperature Rietveld refinement discussed earlier included models for each of these impurities, and the weight percentages calculated for each phase are given in *Table 3.10*. It should be noted that weight percentages were refined individually for the X-ray and neutron data collected; percentages for individual neutron banks were equated. From these it would be easy to dismiss the presence of CeO_2 and MnSe in the sample, however, X-ray data collected clearly show the presence of peaks arising from these phases, and refinement statistics are improved on their inclusion.

Table 3.10 *Weight percentages for phases present in $Ce_2O_2Mn_2OSe_2$ at room temperature, for X-ray, HRPD bs and 90° neutron data banks.*

Phase	X-ray	Neutron	Average
$Ce_2O_2Mn_2OSe_2$	80.7	89.4	85.1
"unknown"	15.8	7.0	11.4
$CeOMn_{0.5}Se$	1.88	1.51	1.70
MnSe	0.53	1.23	0.88
CeO_2	1.03	0.90	0.97

3.6 Conclusions

In conclusion, two new members of the $A_2O_2Mn_2OSe_2$ family has been successfully prepared: $Ce_2O_2Mn_2OSe_2$ and $(La_{½}Nd_{½})_2O_2Mn_2OSe_2$. The structure of these and those of $La_2O_2Mn_2OSe_2$ and

$Pr_2O_2Mn_2OSe_2$ at both room temperature and 12 K have been reported. Variable temperature studies have shown that each material undergoes a phase transition, revealed by a change in the thermal expansion of the *c* cell parameter, at 115, 90 and 180 K, for $La_2O_2Mn_2OSe_2$, $Ce_2O_2Mn_2OSe_2$ and $Pr_2O_2Mn_2OSe_2$, respectively. This transition is accompanied by an increase in the thermal displacement of the O(2) site in the *z* direction, which can be modelled by a distortion of the Mn-O-Mn bond angle away from 180°. These effects are most pronounced in the praseodymium-containing material, which is also seen to undergo a further transition to an orthorhombic cell on cooling below 36 K; similar to that observed in PrOMnSb.[18] This is contrary to previous work, that suggested peak splitting occurred from 170 K. Close inspection of HRPD neutron data, however, suggested that significant peak broadening occurs between 180 and 36 K. Peak broadening is then seen to remain constant below the phase transition.

Neutron diffraction studies have confirmed that all three materials adopt the AFM1 structure at low temperature, as originally reported by Withers for $La_2O_2Mn_2OSe_2$.[1] The moments in these materials are seen to order at 168, 174 and 180 K, respectively, reflecting increasing orbital overlap with decrease lanthanide ion radius. Investigation of neutron and magnetic susceptibility data collected for $Ce_2O_2Mn_2OSe_2$ and $Pr_2O_2Mn_2OSe_2$ suggests that magnetic ordering of the rare-earth ions does not occur, unlike in PrOMnSb.

3.7 References

1. N. D. Withers, *Synthesis and Characterisation of New Layered Oxychalcogenide Materials*, Durham University, *Ph.D.*, Durham, 2005.
2. J. M. Mayer, L. F. Schneemeyer, T. Siegrist, J. V. Waszczak and B. v. Dover, *Angew. Chem. Int. Ed. Engl.*, 1992, **31**, 1645-1647.
3. D. G. Free, *Synthesis and Chemistry of New Layered Oxychalcogenides*, Durham University, *M.Chem.*, Durham, 2007.
4. J. B. Goodenough, *Magnetism and the Chemical Bond*, John Wiley & Sons, New York - London, 1963.
5. H. Kabbour, E. Janod, B. Corraze, M. Danot, C. Lee, M.-H. Whangbo and L. Cario, *J. Am. Chem. Soc.*, 2008, **130**, 8261-8270.
6. J. X. Zhu, R. Yu, H. Wang, L. L. Zhao, M. D. Jones, J. Dai, E. Abrahams, E. Morosan, M. Fang and Q. Si, *Phys. Rev. Lett.*, 2010, **104**, 216405.
7. R. Ibberson, W. I. F. David and K. S. Knight, *The High Resolution Neutron Powder Diffractometer (HRPD) at ISIS - A User Guide*, ISIS Crystallography, Didcot, 1992.
8. A. A. Coelho, *TOPAS Academic: General profile and Structure Analysis Software for Powder Diffraction Data*, Bruker AXS, Karlsruhe, 2010.
9. J. S. O. Evans, *multitopas, FORTRAN 77 routine*, University of Durham, 1999.
10. M. J. Pitcher, C. F. Smura and S. J. Clarke, *Inorg. Chem.*, 2009, **48**, 9054-9056.
11. G. H. Chan, B. Deng, M. I. Bertoni, J. R. Ireland, M. C. Hersam, T. O. Mason, R. P. v. Duyne and J. A. Ibers, *Inorg. Chem.*, 2006, **45**, 8264-8272.
12. K. Ueda, K. Takafuji and H. Hosono, *J. Solid State Chem.*, 2003, **170**, 182-187.
13. K. Wang and R. R. Reeber, *Appl. Phys. Lett.*, 2000, **76**, 2203-2204.
14. T. Roisnel and J. Rodríguez-Carvajal, *Proceedings of the Seventh European Powder Diffraction Conference (EPDIC 7)*, 2000, 118-123.
15. A. A. Coelho, *J. Appl. Cryst.*, 2003, **36**, 86-95.
16. S. J. C. Herkelrath, I. Saratovsky, J. Haderman and S. J. Clarke, *J. Am. Chem. Soc.*, 2008, **130**, 14426-14427.

17. B. J. Campbell, H. T. Stokes, D. E. Tanner and D. M. Hatch, *J. Appl. Cryst.*, 2006, **39**, 607-614.
18. S. A. J. Kimber, A. H. Hill, Y. Zhong-Zhang, H. O. Jeschke, R. Valenti, C. Ritter, I. Schellenberg, W. Hermes, R. Pottgen and D. N. Argyriou, *Phys. Rev. B*, 2010, **82**, 100412.
19. A. Tuxworth, *Synthesis and Characterisation of Layered Oxychalcogenides*, Durham University, *M.Chem.*, Durham, 2010.
20. P. W. Stephens, *J. Appl. Cryst.*, 1999, **32**, 281-289.
21. G. S. Pawley, *J. Appl. Cryst.*, 1981, **14**, 357-361.
22. A. S. Wills, *Physica B*, 2000, **276-278**, 680-681.
23. A. C. Larson and R. B. Von Dreele, *The General Structure Analysis System (GSAS)*, Los Alamos National Laboratory: Los Alamos, 2004.
24. J. Zhao, Q. Huang, C. de la Cruz, S. Li, J. W. Lynn, Y. Chen, M. A. Green, G. F. Chen, G. Li, Z. Li, J. L. Luo, N. L. Wang and P. Dai, *Nature Mater.*, 2008, **7**, 953-959.
25. Y. Ajiro, T. Nakashima, Y. Unno, H. Kadowaki, M. Mekata and N. Achiwa, *J. Phys. Soc. Jap.*, 1988, **57**, 2648-2650.
26. R. J. Goff, A. J. Williams and J. P. Attfield, *Phys. Rev. B*, 2004, **70**, 014426.
27. A. R. Pepper and R. Street, *Proc. Phys. Soc.*, 1966, **87**, 971-973.
28. L. Viciu, J. W. G. Bos, H. W. Zandbergen, Q. Huang, M. L. Foo, S. Ishiwata, A. P. Ramierz, M. Lee, N. P. Ong and R. J. Cava, *Phys. Rev. B*, 2006, **73**, 174104.
29. R. Klingeler, N. Leps, I. Hellmann, A. Popa, U. Stockert, C. Hess, V. Kataev, H. J. Grafe, F. Hammerath, G. Lang, S. Wurmehl, G. Behr, L. Harnagea, S. Singh and B. Büchner, *Phys. Rev. B*, 2010, **81**, 024506.
30. H. Wu, *Phys. Rev. B*, 2010, **82**, 020410.
31. K. Dwight and N. Menyuk, *Phys. Rev.*, 1960, **119**, 1470-1479.
32. W. S. Seo, H. H. Jo, K. Lee, B. Kim, S. J. Oh and J. T. Park, *Angew. Chem. Int. Ed. Engl.*, 2004, **43**, 1115-1117.
33. R. Regmi, R. Tackett and G. Lawes, *J. Magnetism and Magnet. Mater.*, 2009, **321**, 2296-2299.
34. Q. Huang, A. Santoro, J. W. Lynn, R. W. Erwin, J. A. Borchers, J. L. Peng and R. L. Greene, *Phys. Rev. B*, 1997, **55**, 14987-14999.
35. L. Ghivelder, I. Abrego Castillo, Gusm, atilde, M. A. o, J. A. Alonso and L. F. Cohen, *Phys. Rev. B*, 1999, **60**, 12184.
36. I. Ijjaali, K. Mitchell, C. L. Haynes, A. D. McFarland, R. P. van Duyne and J. A. Ibers, *J. Solid State Chem.*, 2003, **176**, 170-174.

Structural and Magnetic Properties of $La_2O_2Fe_2OQ_2$ (*Q* = S, Se) Materials

4.1 Introduction

The synthesis of $La_2O_2Fe_2OSe_2$ and $La_2O_2Fe_2OS_2$ were originally reported by Mayer *et al.* and their structures determined from single crystal studies.[1] As has been discussed in previous chapters, the structure is best described as containing PbO-type $[La_2O_2]^{2+}$ layers, separated from anti-CuO_2-type $[Fe_2O]^{2+}$ layers by a layer of Se^{2-} ions (*Figure 4.1*) (atomic coordinates are given in *Table 4.1*). Physical property measurements reported in this paper suggested that both materials order antiferromagnetically on cooling below ~100 K, and can be described as Mott insulators; resistivities of 200 and 10^3 Ωm were reported for the oxysulphide and oxyselenide, respectively. Whilst low temperature neutron studies have not been reported, theoretical studies of this material by Zhu *et al.* have suggested possible models for magnetic ordering. These suggest that the material will order with an AFM1 or AFM6 arrangement, *Figure 4.1*, depending on the magnitude of the Mott-Hubbard interaction energy (*U*).[2] These conclusions are similar to those published for the $B_2F_2Fe_2OQ_2$ (*B* = Sr, Ba; *Q* = S, Se) family, although neutron data reported for $Ba_2F_2Fe_2OSe_2$ suggest incommensurate magnetic ordering.[3] As seen in chapter 3, the AFM1 structure is observed in the $A_2O_2Mn_2OSe_2$ family (*A* = La–Pr). Recent results published by Fuwa *et al.* for $Nd_2O_2Fe_2OSe_2$ suggest Fe^{2+} moments lie in the *ab* plane, and two further models are predicted, similar to that observed by Withers for $La_2O_2Co_2OSe_2$.[4, 5] Here we report the structural and magnetic properties of $La_2O_2Fe_2OS_2$ and $La_2O_2Fe_2OSe_2$, which have been studied using a combination of X-ray and neutron powder diffraction. Note that data presented here for $La_2O_2Fe_2OSe_2$ have been published.[6]

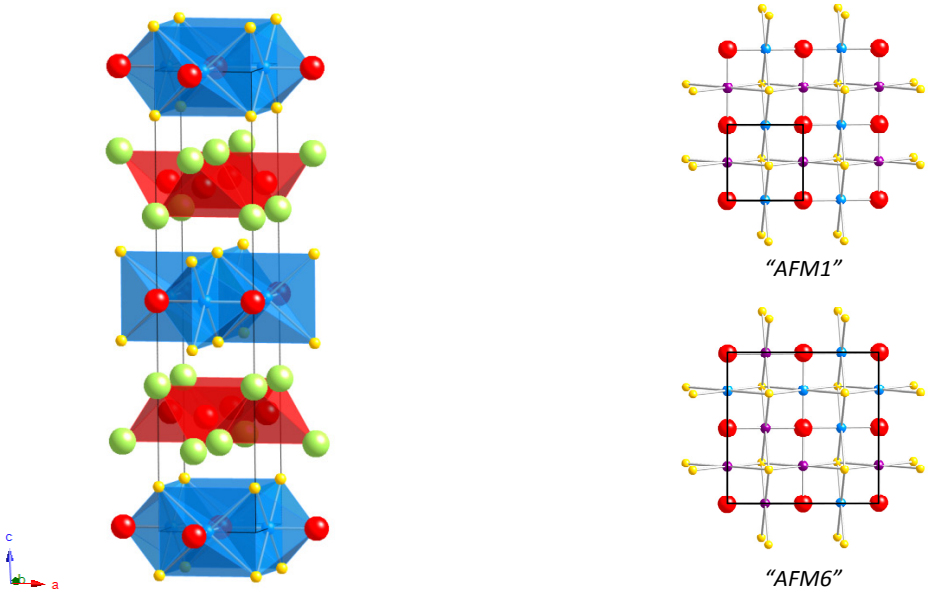

Figure 4.1 *Nuclear structure of $La_2O_2Fe_2OSe_2$ (left) and theoretically proposed arrangement of the moments in the $[Fe_2O]^{2+}$ layers (right); Fe = blue, La = green, O = red, Se = yellow, nuclear and magnetic unit cells are outlined in black.*

Table 4.1 *Cell coordinates and site occupancies (Occ.) for $La_2O_2Fe_2OQ_2$ materials.*

	Wyckoff site	*x* (*a*)	*y* (*b*)	*z* (c)	*Occ.*
La	*4e*	*0.5*	*0.5*	*~0.18*	*1*
Fe	*4c*	*0.5*	*0*	*0*	*1*
Q	*4e*	*0*	*0*	*~0.09*	*1*
O(1)	*4d*	*0.5*	*0*	*0.25*	*1*
O(2)	*2b*	*0.5*	*0.5*	*0*	*1*

4.2 Room Temperature Structures

$La_2O_2Fe_2OSe_2$ and $La_2O_2Fe_2OS_2$ were synthesised using the method discussed in section 2.2.2, and their room temperature structures were confirmed from X-ray powder diffraction data to be similar to those published.[1] Rietveld refinements were performed using TOPAS Academic (TA), and included variables to describe both structural and instrumental parameters. The variables used to model the data include those listed in *Table 4.2*, as well as parameters to model background, TOF *x*-axis calibration, absorption, 2θ zero errors, scale factors and profile coefficients. In addition to the formation of $La_2O_2Fe_2OQ_2$, a small amount of $LaFeO_3$ impurity was also observed in each material. The results of the Rietveld analysis are summarised in *Table 4.2*, with parameters originally reported from single crystal data alongside. Selected bond distances and angles are given in *Table 4.3*.

Table 4.2 *Results from combined X-ray / neutron Rietveld refinements of $La_2O_2Fe_2OS_2$ and $La_2O_2Fe_2OSe_2$ at room temperature, with single crystal values from the literature for comparison.*

	$La_2O_2Fe_2OS_2$	Reported	$La_2O_2Fe_2OSe_2$	Reported
Nuclear symmetry	*I4/mmm*	*I4/mmm*	*I4/mmm*	*I4/mmm*
a (Å)	*4.04042(5)*	*4.0408(1)*	*4.08475(1)*	*4.0788(2)*
c (Å)	*17.8803(2)*	*17.8985(6)*	*18.59736(9)*	*18.648(2)*
V (Å^3)	*291.895(8)*	*292.25(1)*	*310.301(3)*	*310.24(4)*
La *z* (*c*)	*0.18075(3)*	-	*0.18436(3)*	*0.18445*
Q z (*c*)	*0.0936(1)*	-	*0.09637(4)*	*0.9669*
La U_{iso} (100×Å^2)	*0.48(3)*	-	*0.35(2)*	*0.68(4)*
Fe U_{iso} (100×Å^2)	*1.01(3)*	-	*0.69(3)*	*2.0(2)*
Q U_{iso} (100×Å^2)	*1.01(6)*	-	*0.54(3)*	*1.06(6)*
O(1) U_{iso} (100×Å^2)	*0.55(4)*	-	*0.47(4)*	*1.0(4)*
O(2) U_{iso} (100×Å^2)	*1.38(6)*	-	*1.17(6)*	*1.3(8)*
N^o. variables	*96*	-	*88*	-
R_{wp} (%)	*3.49*	-	*3.29*	-
χ^2	*3.46*	-	*2.88*	-

U_{ij} values, statistics for specific banks of data and other information are given in appendices V and VI. U_{iso} values for reported work were calculated from original B_{iso} values.

Table 4.3 *Selected interatomic distances and bond angles for $La_2O_2Fe_2OQ_2$ materials at room temperature.*

		$La_2O_2Fe_2OS_2$	$La_2O_2Fe_2OSe_2$
Bond lengths (Å)	$d_{F\text{-}M}$	*2.85701(1)*	*2.88836(1)*
	$d_{M\text{-}O}$	*2.02021(1)*	*2.04238(1)*
	$d_{M\text{-}Q}$	*2.623(1)*	*2.7172(5)*
	$d_{A\text{-}O}$	*2.3695(3)*	*2.3794(2)*
	$d_{A\text{-}Q}$	*3.2545(9)*	*3.3197(4)*
Bond angles (°)	*M*-Q-*M*(1)	*65.99(3)*	*64.21(1)*
	M-Q-*M*(2)	*100.74(6)*	*97.46(2)*
	Q-*M*-Q	*79.27(6)*	*82.54(2)*
	A-O-*A* (1)	*105.85(1)*	*105.260(9)*
	A-O-*A* (2)	*116.99(3)*	*118.27(2)*

Refinement of the occupancies on individual atom sites confirmed both materials were stoichiometric within the precision of the diffraction data. Fixing the La occupancy at 1 and allowing other the site occupancies to refine gave the formulae $La_2O_{2.02(1)}Fe_{1.99(1)}O_{0.98(1)}S_{1.96(3)}$ and $La_2O_{1.970(4)}Fe_{1.990(2)}O_{0.999(4)}Se_{1.980(4)}$. Whilst the general agreement between the data reported here and those data originally published is good, we note that our results suggest a significantly larger thermal displacement of the O(2) site relative to the other atoms. Refinement of the data using anisotropic thermal displacement parameters (ADPs) suggests that this is due to a large U_{33} contribution, perpendicular to the $[Fe_2O]^{2+}$ layers; refined ADP values for all atoms are given in appendices V and VI. This is similar to the disorder observed in the $A_2O_2Mn_2OSe_2$ family, where a large U_{33} parameter for O(2) was attributed to local distortion of the *M*-O-*M* bonds, with the O(2) atoms lying above and below the metal layers. Similar to these materials, there is no evidence for long-range ordering of these ions at room temperature, and no further data to suggest ordering at 12 K.

Rietveld plots for $La_2O_2Fe_2OSe_2$ and $La_2O_2Fe_2OS_2$ are presented in *Figure 4.2* and *Figure 4.3*. The overall quality of these fits is good, though we note that calculated intensity for the (004) reflection of $La_2O_2Fe_2OSe_2$ at ~162000 µs (4.65 Å) in the 90° neutron bank is low, despite the correct intensity being calculated for the same reflection in the 30° bank at ~59500 µs. Note that data were collected with a larger than standard time-of-flight (TOF) window, and therefore reasons for the difference in intensity could include calibration errors over the larger window and problems with sample can absorption. It is also worth noting that there are no high TOF reflections expected in the backscattering (bs) or 30° data banks to allow for further comparison. Weak peaks were also observed in the neutron data at 2.13 Å, however as they were not observed in the X-ray data it was assumed that these were a result of scattering from the sample environment, and were therefore excluded from the refinement. The low angle "humps" in the X-ray data are due to the carbon fibre windows of the cryostat and have been modelled using two additional peaks.

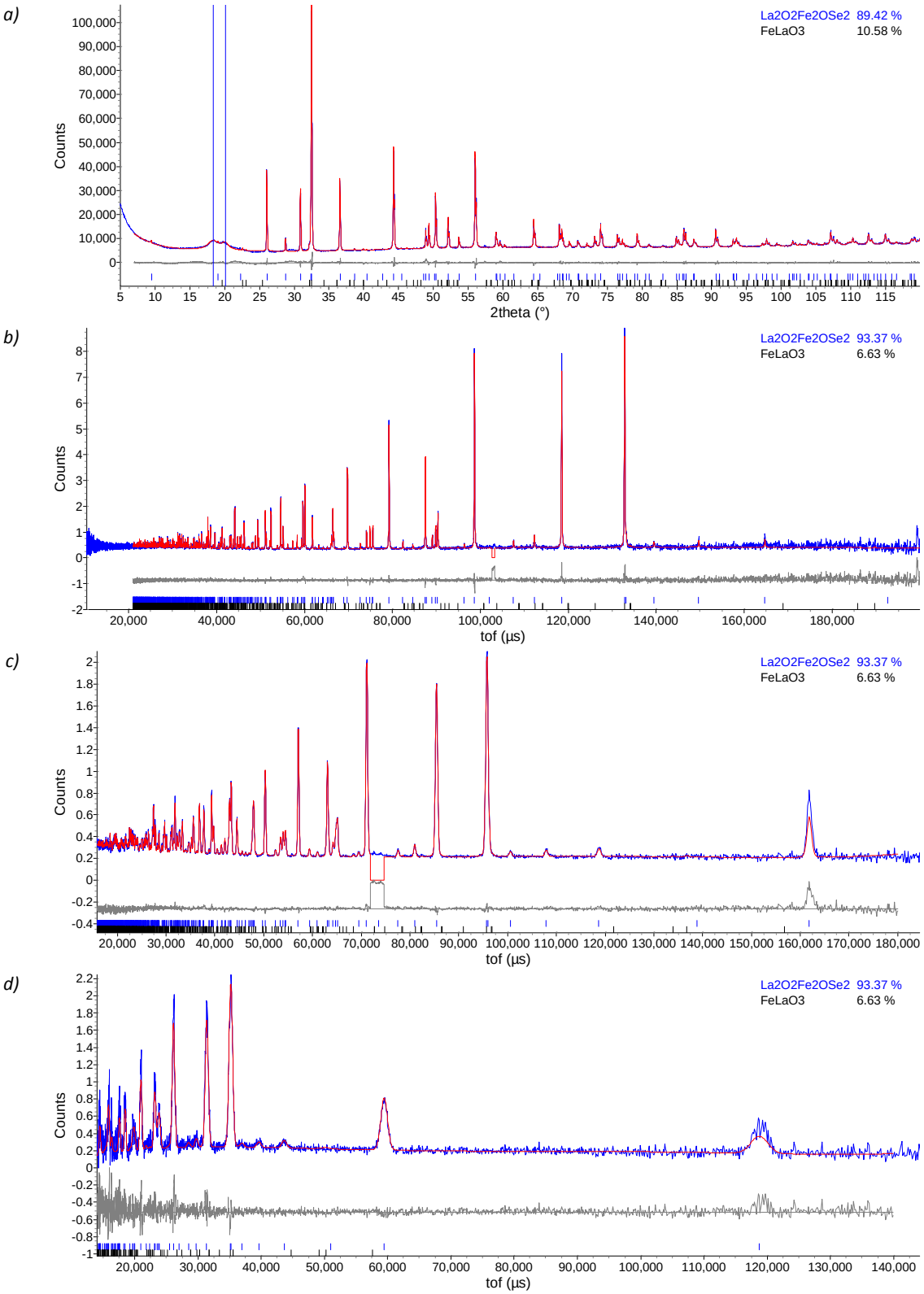

Figure 4.2 *Rietveld plots for $La_2O_2Fe_2OSe_2$ at room temperature for (a) X-ray, (b) HRPD bs, (c) 90° and (d) 30° bank data; observed = blue, calculated = red, difference = grey. DGF213, d9_04096, hrp45577.*

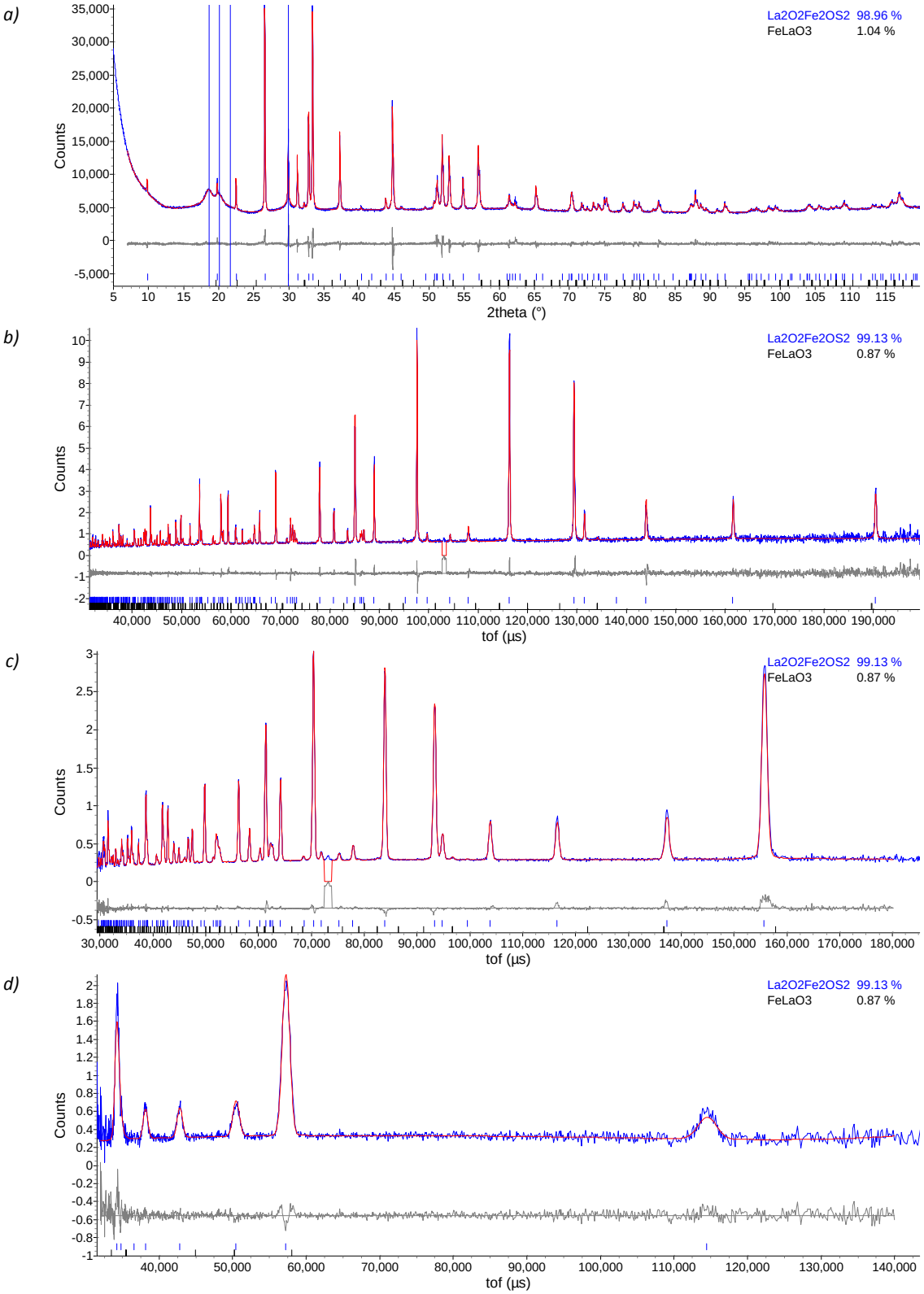

Figure 4.3 *Rietveld plots for $La_2O_2Fe_2OS_2$ at room temperature for (a) X-ray, (b) HRPD bs, (c) 90° and (d) 30° bank data; observed = blue, calculated = red, difference = grey. DGF306, d9_04634, hrp46778.*

4.3 Variable Temperature Structural Studies

Variable temperature X-ray and neutron data were collected for both materials between 12 and 300 K. These experiments were performed according to the parameters defined in sections 2.3.3 and 2.4.2, and

data were analysed using both the *multitopas* method, and by the SEQGSAS routine in GSAS.[7-9] *Figure 4.4* shows the variation of the *a* cell parameter as a function of temperature. In both materials the *a* cell parameter is seen to decrease steadily as a function of temperature, with perhaps a hint of a discontinuity in the thermal expansion at approximately 110 and 90 K for $La_2O_2Fe_2OS_2$ and $La_2O_2Fe_2OSe_2$, respectively. As in chapter 3, the thermal expansion of the *a* cell parameters was modelled using an Einstein model of thermal expansion.[10] Refined parameters from this model are given in *Table 4.4*. Closer inspection of the data suggested that the thermal expansion could be fitted better using two Einstein models, above and below the observed discontinuities. Plots including both functions are given in appendices V and VI.

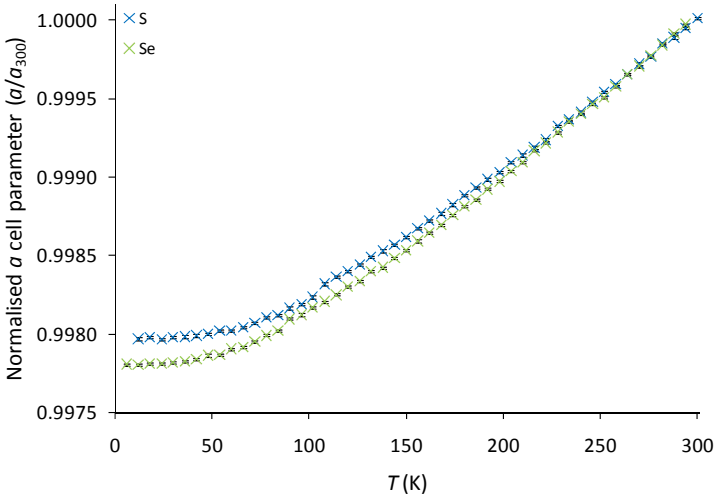

Figure 4.4 *The a cell parameters for $La_2O_2Fe_2OQ_2$ materials as a function of temperature; S = blue, Se = green.*

Table 4.4 *Refined parameters for models of thermal expansion for $La_2O_2Fe_2OQ_2$ materials.*

		$La_2O_2Fe_2OS_2$	$La_2O_2Fe_2OSe_2$
	a_0 (Å)	*4.03847(2)*	*4.08034(2)*
a	C_i (10^{-6})	*10.15(7)*	*10.45(7)*
	θ_i (K)	*230(3)*	*205(4)*

Similar plots of the *c* cell parameter, *Figure 4.5*, show a change in the rate of thermal expansion of $La_2O_2Fe_2OSe_2$ at ~150 K; this is emphasised in the *c*/*a* ratio temperature dependence, which is inset. This change in thermal expansion is similar to that observed in $La_2O_2Mn_2OSe_2$ and $Pr_2O_2Mn_2OSe_2$, where much larger changes in thermal expansion are observed at 115 and 180 K, respectively. There are, however, no extra reflections observed or peak splitting to suggest a reduction in symmetry. The data for $La_2O_2Fe_2OS_2$ also show a discontinuity in the thermal expansion at ~150 K. Warming data collected suggest that these transitions are fully reversible.

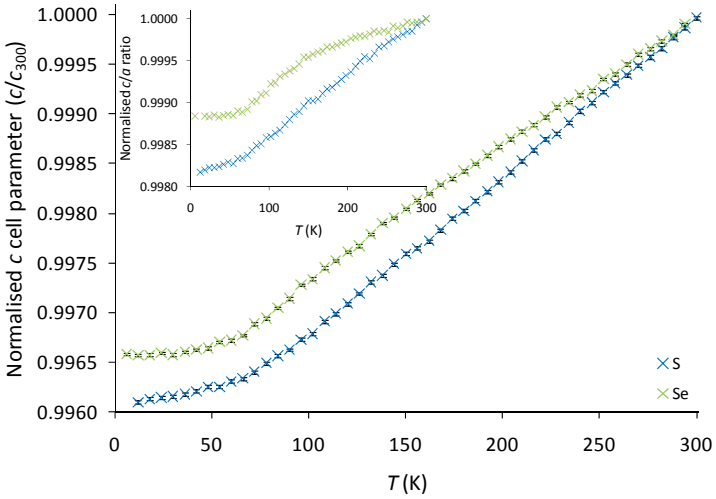

Figure 4.5 *The c cell parameters of $La_2O_2Fe_2OQ_2$ materials as a function of temperature, with the c/a ratio inset (where c/a has also been normalised against the values at 300 K); S = blue, Se = green.*

Figure 4.6 shows the variation in the U_{33} parameters refined for each atom site, as a function of temperature. It can be seen that in both materials, at room temperature, the thermal displacement of the O(2) ion is larger than that of the other atoms present. The O(2) U_{33} parameters are, however, seen to decrease steadily on cooling, until, at low temperature, they appear more comparable to those of the other sites. Close inspection suggests a possible subtle change in the behaviour of the O(2) U_{33} parameter for both materials below 150 K (*i.e.* where the discontinuity is observed in the *c* parameter). For the sulphide-containing material this is seen as a change in the slope of U_{33} versus temperature, and for the selenide material by a discontinuity. These behaviours differ from the manganese containing materials, in which the U_{33} parameters are seen to increase on cooling below the transition observed in *c*. There is some evidence to suggest that, for $La_2O_2Fe_2OS_2$, the U_{33} parameter of the O(2) site decreases at a greater rate below ~150 K, which is coincident with the discontinuity observed in the thermal expansion of the *c* cell parameter.

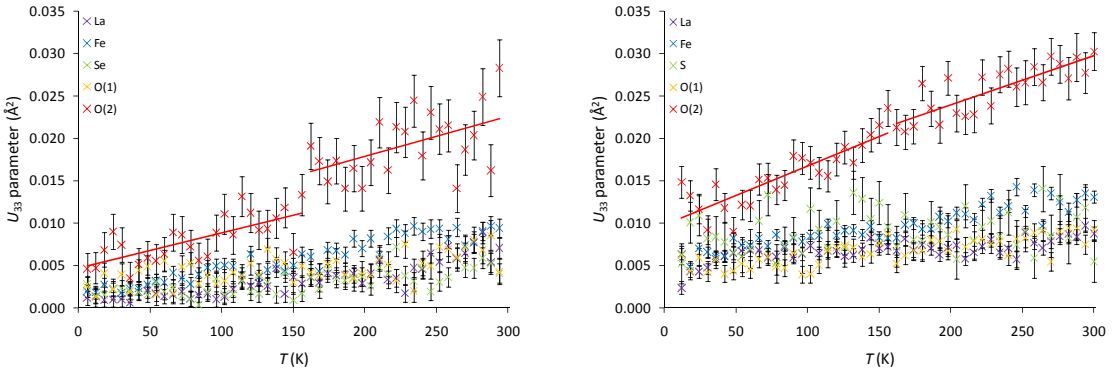

a) $La_2O_2Fe_2OSe_2$ *b) $La_2O_2Fe_2OS_2$*

Figure 4.6 *U_{33} parameters for (a) $La_2O_2Fe_2OSe_2$ and (b) $La_2O_2Fe_2OS_2$ as a function of temperature; La = purple, Fe = blue, Q = green, O(1) = yellow, O(2) = red; the red lines are linear fits to the data intended as guides to the eye.*

Figure 4.7 shows the effect of temperature on the strain broadening contribution to the peak shapes derived from the HRPD bs neutron bank. For $La_2O_2Fe_2OSe_2$ we observe an increase in the peak width

below 90 K, *i.e.* coincident with the discontinuities observed in the *a* cell parameter. Whilst for $La_2O_2Fe_2OS_2$ this broadening is observed below 80 K. Although an increase in peak width is observed for both materials, there is no clear evidence of peak splitting that would suggest a lowering of symmetry, despite the use of high-resolution neutron and X-ray data.[v] Also, the broadening observed is still relatively small, and corresponds to a change in peak full width half maximum of the {200} reflection of only ~4 %. Any lowering in symmetry is therefore very subtle. As in the example of $Pr_2O_2Mn_2OSe_2$ in chapter 3, this was modelled by the *dsp* contribution to the Lorentzian full width half maximum of the peak shape.

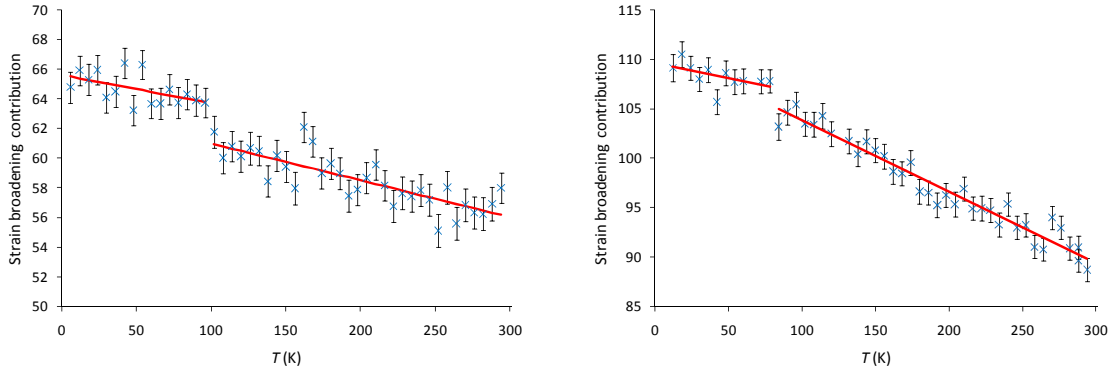

a) $La_2O_2Fe_2OSe_2$ *b) $La_2O_2Fe_2OS_2$*

Figure 4.7 *Strain broadening parameters for (a) $La_2O_2Fe_2OSe_2$ and (b) $La_2O_2Fe_2OS_2$ as a function of temperature.*

In summary, there is evidence from cell parameters, thermal displacement parameters and peak broadening that each material undergoes subtle transitions at varying temperatures. In $La_2O_2Fe_2OSe_2$ these transitions appear linked, *i.e.* the transition observed in the *a* cell parameter is coincident with the observation of peak broadening (90 K), and the transition observed in the *c* cell parameter is coincident with a change in the thermal displacement of the O(2) ion (150 K). For $La_2O_2Fe_2OS_2$, whilst changes in the *c* cell parameter and thermal displacement of O(2) both occur at 150 K, the transitions observed in the *a* cell parameter (110 K) and peak broadening (80 K) are less closely related. It is also worth noting that the transitions observed in the *c* cell parameter and the U_{33} parameters for O(2) occur in both materials at ~150 K. We will see later that the $La_2O_2Fe_2OSe_2$ 90 K transitions and $La_2O_2Fe_2OS_2$ 110 K transitions are associated with magnetic ordering of the Fe^{2+} ions.

4.4 Magnetic Structure Determination of $La_2O_2Fe_2OSe_2$

On cooling $La_2O_2Fe_2OSe_2$ below 90 K, new peaks became visible in all three banks of neutron data, at *d*-spacings of 3.01, 3.27, 3.50, 3.62, 4.44, 5.48 and 6.78 Å, that were not present in the X-ray data (*Figure 4.8* & *Figure 4.9*). These were found to be consistent with antiferromagnetic ordering of the Fe^{2+} ions, and could be indexed with an enlarged unit cell of $2a \times b \times 2c$, *i.e.* a propagation vector of $\boldsymbol{k}$ = (½0½).

[v] HRPD instrumental resolution $\Delta d/d \approx 10^{-4}$ Å

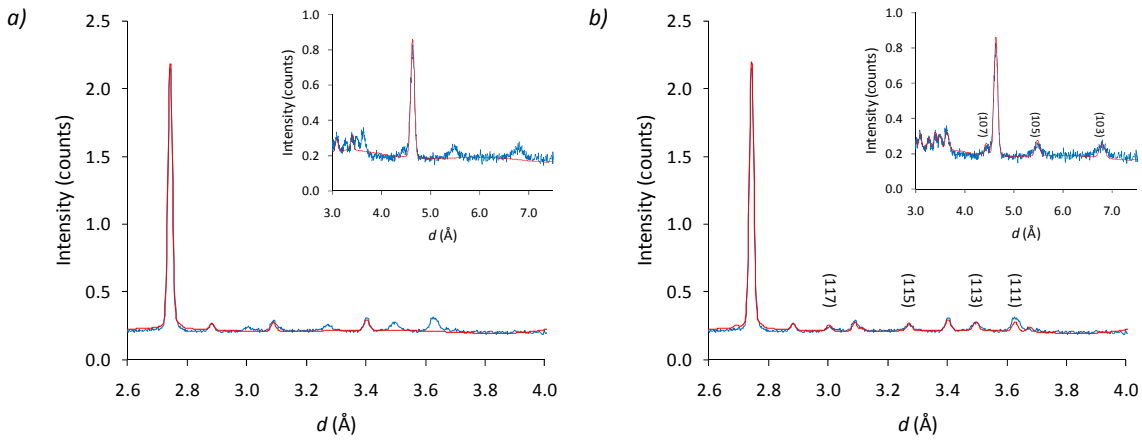

Figure 4.8 *Rietveld plots highlighting the magnetic peaks observed in $La_2O_2Fe_2OSe_2$ for the 2.6-4.0 Å region of the 90° neutron data bank, with the 3.0-7.0 Å region of the 30° neutron data bank inset; observed = blue, calculated = red. DGF213, hrp45526.*

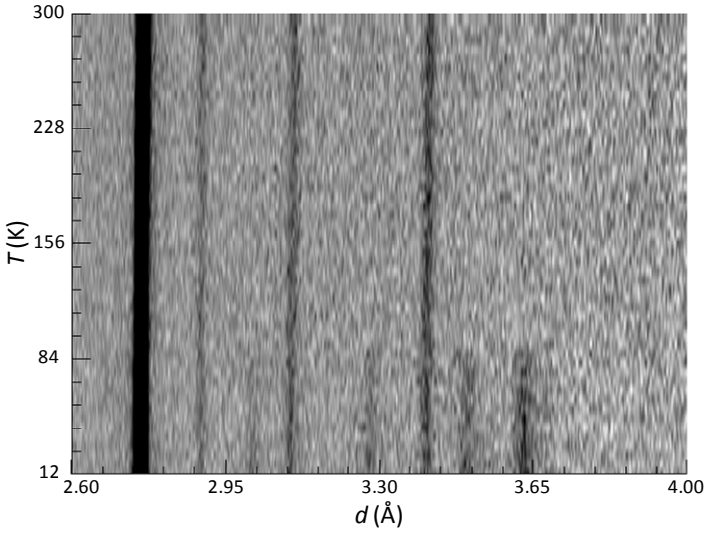

Figure 4.9 *Film plot showing the evolution of the observed magnetic peaks in $La_2O_2Fe_2OSe_2$; plot shows the 2.6–4.0 Å (90–140 ms) region of the 90° HRPD bank.*

Possible magnetic structures were investigated using SARAh Refine interfaced with the GSAS software suite.[8, 11] Due to the weak intensity of the observed peaks, refinements were performed with 90° and 30° bank data only, over the data ranges 98–158 ms (2.8–4.5 Å) and 36–116 ms (2.8–9.1 Å), respectively, to ensure significant contribution of magnetic scattering to the overall χ^2. For *I*4/*mmm* symmetry, with ***k*** = (½0½), SARAh produces two independent metal sites (Fe(1) and Fe(2) in *Figure 4.11*), with three basis vectors allowed per site; labelled Fe(1)$\Gamma_2\Psi_1$, Fe(1)$\Gamma_2\Psi_2$, Fe(1)$\Gamma_4\Psi_3$, Fe(2)$\Gamma_1\Psi_1$, Fe(2)$\Gamma_3\Psi_2$, and Fe(2)$\Gamma_3\Psi_3$. The Fe(1)$\Gamma_2\Psi_1$ and Fe(2)$\Gamma_3\Psi_2$ basis vectors describe moments aligned along the *a* axis, coupled antiferromagnetically (AFM) along *a* and ferromagnetically (FM) along *b*, Fe(1)$\Gamma_2\Psi_2$ and Fe(2)$\Gamma_3\Psi_3$ describe a similar arrangement, however with moments aligned along *c*, and Fe(1)$\Gamma_4\Psi_3$ and Fe(2)$\Gamma_1\Psi_1$ have moments aligned along *b*. Initially mixing of all six basis vectors was allowed to try and fit the observed magnetic scattering, however results showed that values of χ^2 were consistently higher for larger contributions of Fe(1)$\Gamma_4\Psi_3$ and Fe(2)$\Gamma_1\Psi_1$. Similar analysis was therefore performed with these basis vectors excluded and results suggested that χ^2 was lowest with a combination of the Fe(1)$\Gamma_2\Psi_1$ and

Fe(2)$\Gamma_3\Psi_2$ basis vectors mixing. *Figure 4.10* contains contour plots of χ^2 as a function of the four basis vectors used in the final analysis, and clearly shows that smaller values of χ^2 are consistently achieved with the Fe(1)$\Gamma_2\Psi_1$ and Fe(2)$\Gamma_3\Psi_2$ basis vectors. This is perhaps most clearly visible in the plot of Fe(2)$\Gamma_3\Psi_2$ against Fe(1)$\Gamma_2\Psi_1$ (*Figure 4.10b*) where blue low χ^2 regions are seen at the corner of the figure where both basis vectors are ±1. Contour plots for analysis using all six basis vectors can be found in appendix VI.

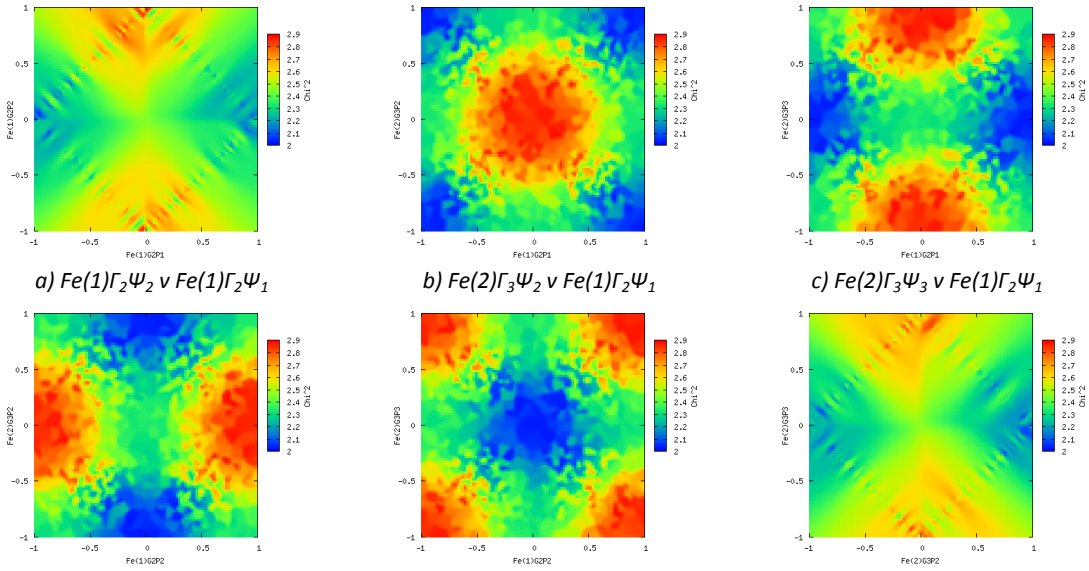

a) Fe(1)$\Gamma_2\Psi_2$ v Fe(1)$\Gamma_2\Psi_1$ *b) Fe(2)$\Gamma_3\Psi_2$ v Fe(1)$\Gamma_2\Psi_1$* *c) Fe(2)$\Gamma_3\Psi_3$ v Fe(1)$\Gamma_2\Psi_1$*

d) Fe(2)$\Gamma_3\Psi_2$ v Fe(1)$\Gamma_2\Psi_2$ *e) Fe(2)$\Gamma_3\Psi_3$ v Fe(1)$\Gamma_2\Psi_2$* *f) Fe(2)$\Gamma_3\Psi_3$ v Fe(2)$\Gamma_3\Psi_2$*

Figure 4.10 *Contour plots (a-f) showing the change in χ^2 with varying contributions of Fe(1)$\Gamma_2\Psi_1$, Fe(1)$\Gamma_2\Psi_2$, Fe(2)$\Gamma_3\Psi_2$, and Fe(2)$\Gamma_3\Psi_3$ basis vectors; low values of χ^2 are shown in blue and large values in red.*

Figure 4.11 shows the resulting arrangement of moments, which is the AFM3 arrangement shown in *Figure 4.12*. This is best described as two interpenetrating lattices composed of Fe(1) and Fe(2) ions, respectively, in which the moments are coupled AFM along *a* and FM along *b*. These lattices then interact such that each ion has an equal number of AFM and FM nearest-neighbour interactions. The results observed in *Figure 4.10* show that the two basis vectors can be present with either equal or opposite sign, with no increase in χ^2, showing that powder data collected are not sufficient to describe the relative orientations of the two lattices; *i.e.* in *Figure 4.11* if one flips the direction of all Fe(2) sites, one obtains an equivalent magnetic structure. The observation of AFM ordering supports Mayer's earlier magnetic susceptibility measurements.[1]

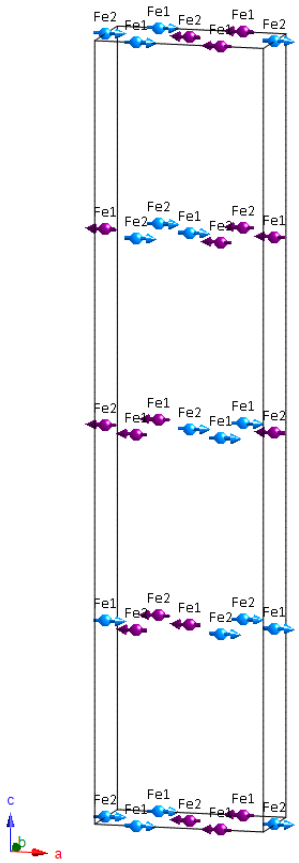

Figure 4.11 *Magnetic structure of $La_2O_2Fe_2OSe_2$; Fe = blue/purple relating similarly orientated spins, the magnetic unit cell is outlined.*

Subsequent to this, analysis of possible canting of the moments from the *ab* plane was investigated, with refinements suggesting a small contribution of the moment in the *z* direction, 0.23(5) μ_B. However the improvement in the statistics of the fit was minimal, suggesting that no significant degree of canting can be concluded from the current data. In order to investigate this possibility, higher quality data would be required.

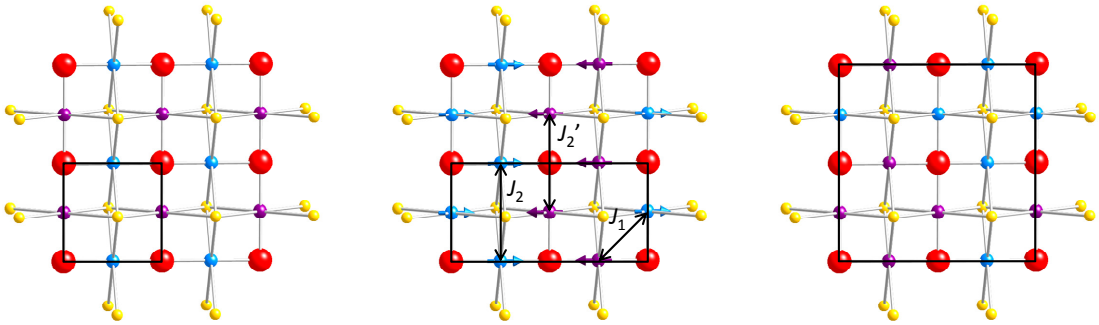

a) "AFM1" *b) "AFM3"* *c) "AFM6"*

Figure 4.12 *Theoretical and experimental magnetic structures (a) AFM1, (b) AFM3 and (c) AFM6 for $La_2O_2Fe_2OQ_2$; Fe = blue/purple, O = red, Q = yellow; magnetic cells are outlined in black.*

Independent density functional theory (DFT) studies by Kabbour *et al*. and Zhu *et al.*, originally suggested that the AFM1 and AFM6 arrangements were most likely for $La_2O_2Fe_2OSe_2$-type materials.[2, 3] As in $La_2O_2Mn_2OSe_2$ there are three important coupling interactions; the nearest-neighbour interactions (J_1), the edge-sharing, ~98°, Fe-Se-Fe interaction (J_2), and the 180° Fe-O-Fe interactions (J_2'), shown again

here in *Figure 4.12*. Both theoretical studies predict J_2' as AFM, J_2 as FM and J_1 as AFM; predictions for J_2 and J_2' are in line with simple predictions from Goodenough-Kanamori rules.[12, 13] In the AFM1 arrangement, adopted by $La_2O_2Mn_2OSe_2$, J_2' interactions are frustrated, but J_2 and J_1 are satisfied, whereas in the AFM6 arrangement half of the J_1 interactions are frustrated. In the AFM3 structure Fe-O-Fe interactions are satisfied along the longer *a* axis, but frustrated along *b*, whilst J_2 interactions are satisfied along *b* but not *a*. The magnetic structure is discussed more fully alongside those of $La_2O_2Mn_2OSe_2$ and $La_2O_2Co_2OSe_2$ in chapter 5.

Whilst the analysis of *Figure 4.10* suggested that the AFM3 structure was adopted, for completeness refinements using AFM1 and AFM6 structures were also performed and gave χ^2 values of 3.9 and 2.8, respectively. These values of χ^2 are significantly higher than those for the AFM3 model and are either equal to, or higher than, the top (red) values plotted in *Figure 4.10*. The R_{wp} values obtained for the 30° data bank for the various models are given in *Table 4.5*.

Table 4.5 *R_{wp} values for 30° bank neutron data following refinement with various magnetic models.*

Model	R_{wp} (%)
Nuclear only	*11.85*
AFM1	*11.87*
AFM3	*8.90*
AFM6	*10.48*

Once the magnetic structure had been determined, final structural refinements were performed in TA. Analysis of the AFM3 model in the web-based resource ISODISTORT showed that structure could be described using P_s1 Shubnikov symmetry (labelled space group number 1.3 in ISODISTORT and TA) with the basis vector (1,1,-1)(0,2,0)(2,2,0). Final refinements in TA, however, were performed in P_s1 (again 1.3) with basis vector (2,0,0)(0,1,0)(0,0,2), as this setting makes it easier to restrain nuclear properties such as atomic coordinates. Final results from Rietveld analysis can be found in *Table 4.6*, and Rietveld plots are shown in *Figure 4.13*.[14] Selected bond lengths and angles are given in *Table 4.7*. As in the room temperature refinements, the calculated intensity for the (004) reflection appears lower than that observed. We note again, however, that the correct intensity is calculated for this peak in the 30° bank, and also that it is a nuclear peak, and therefore would not have influenced the determination of the magnetic structure. From the data collected at 12 K, the refined magnetic moment of Fe^{2+} was 2.69(4) μ_B, which compares with reported values of 2.25(8) μ_B for $Fe_{1.086}Te$ at 67 K, 0.36(5) μ_B for LaOFeAs at 8 K and 3.32 μ_B for FeO at 77 K.[15-17]

Table 4.6 *Results from combined X-ray / neutron Rietveld refinements of $La_2O_2Fe_2OS_2$ and $La_2O_2Fe_2OSe_2$ at 12 K.*

	$La_2O_2Fe_2OS_2$	**$La_2O_2Fe_2OSe_2$**
Nuclear symmetry	*I4/mmm*	*I4/mmm*
Magnetic symmetry	P_s1	P_s1
a (Å)	*4.03287(4)*	*4.07645(1)*
c (Å)	*17.8140(2)*	*18.53854(8)*
V (Å^3)	*289.727(6)*	*308.063(2)*
La *z* (*c*)	*0.18054(3)*	*0.18415(2)*
Q z (*c*)	*0.0937(1)*	*0.09618(3)*
La U_{iso} (100×Å^2)	*0.84(2)*	*0.73(1)*
Fe U_{iso} (100×Å^2)	*1.11(2)*	*0.91(1)*
Q U_{iso} (100×Å^2)	*1.23(5)*	*0.81(2)*
O(1) U_{iso} (100×Å^2)	*0.90(3)*	*0.95(2)*
O(2) U_{iso} (100×Å^2)	*1.15(5)*	*1.04(3)*
Fe^{2+} M_x (μ_B)	*2.60(3)*	*2.69(4)*
N°. variables	*96*	*88*
R_{wp} (%)	*3.99*	*3.40*
χ^2	*5.49*	*4.06*

U_{ij} values, statistics for specific banks of data and other information can be found in appendices V and VI.

Table 4.7 *Selected interatomic distances and bond angles for $La_2O_2Fe_2OQ_2$ materials at 12 K.*

		$La_2O_2Fe_2OS_2$	$La_2O_2Fe_2OSe_2$
Bond lengths (Å)	$d_{M\text{-}M}$	*2.85167(1)*	*2.88249(1)*
	$d_{M\text{-}O}$	*2.01644(1)*	*2.03823(1)*
	$d_{M\text{-}Q}$	*2.618(1)*	*2.7080(3)*
	$d_{A\text{-}O}$	*2.3658(3)*	*2.3758(2)*
	$d_{A\text{-}Q}$	*3.2443(9)*	*3.3119(3)*
Bond angles (°)	*M*-*Q*-*M*(1)	*66.01(3)*	*64.310(9)*
	M-*Q*-*M*(2)	*100.77(6)*	*97.64(2)*
	Q-*M*-*Q*	*79.23(6)*	*82.36(2)*
	A-O-*A* (1)	*105.88(1)*	*105.308(8)*
	A-O-*A* (2)	*116.93(2)*	*118.16(2)*

Analysis of neutron data collected at 12 K for $La_2O_2Fe_2OS_2$ showed that it also orders with an AFM3 structure, and a film plot showing the evolution of magnetic peaks is given in *Figure 4.15*. Details from the final refinement of this material at 12 K are given in *Table 4.6* and Rietveld plots are shown in *Figure 4.14*. Selected bond lengths and angles are, again, given in *Table 4.7*. The refined Fe^{2+} moment of 2.60(3) μ_B is similar to that observed for $La_2O_2Fe_2OSe_2$.

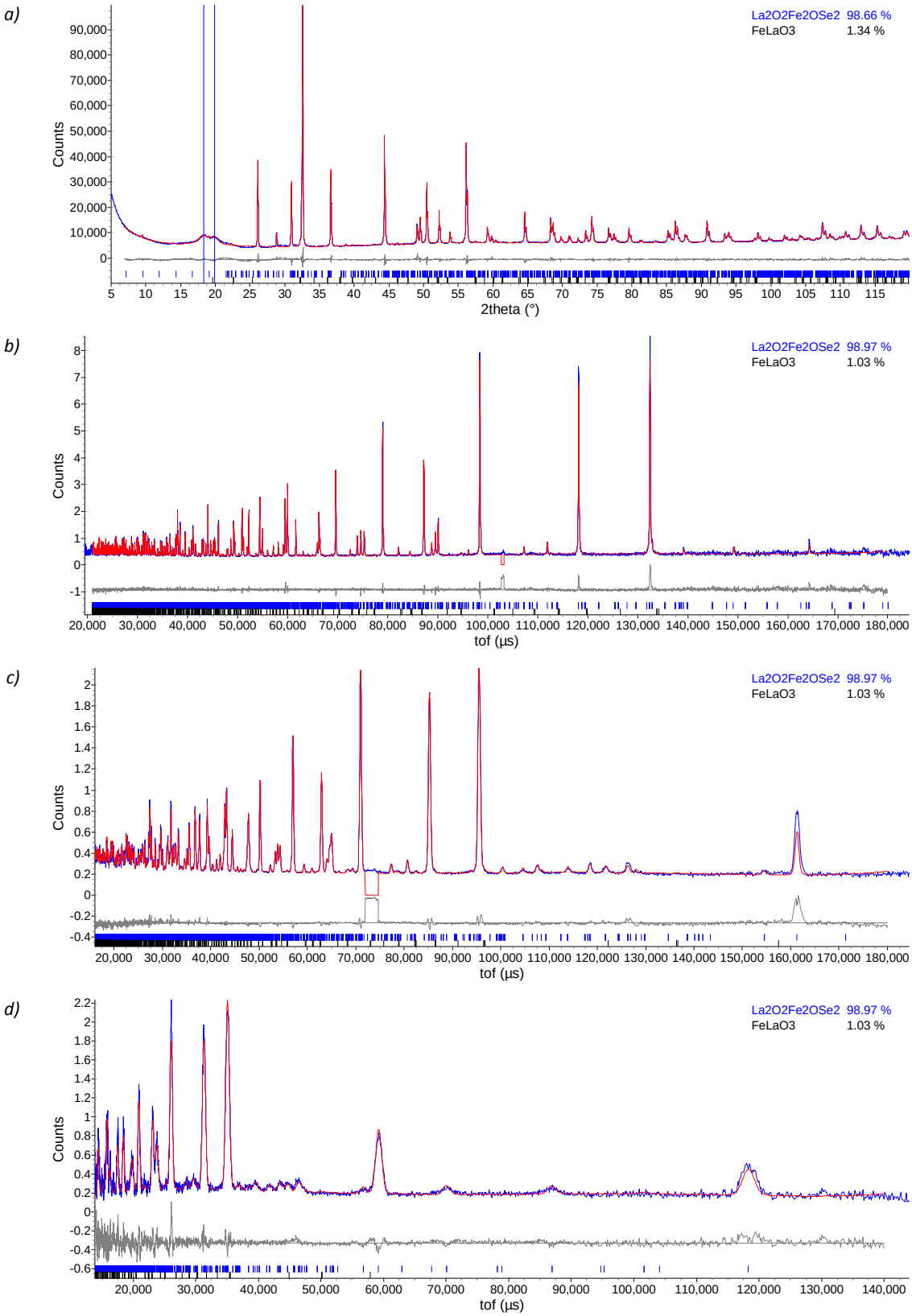

Figure 4.13 *Rietveld plots for $La_2O_2Fe_2OSe_2$ at 12 K using (a) X-ray, (b) HRPD bs, (c) 90° and (d) 30° bank data; observed = blue, calculated = red, difference = grey. DGF213, d9_04095, hrp45526.*

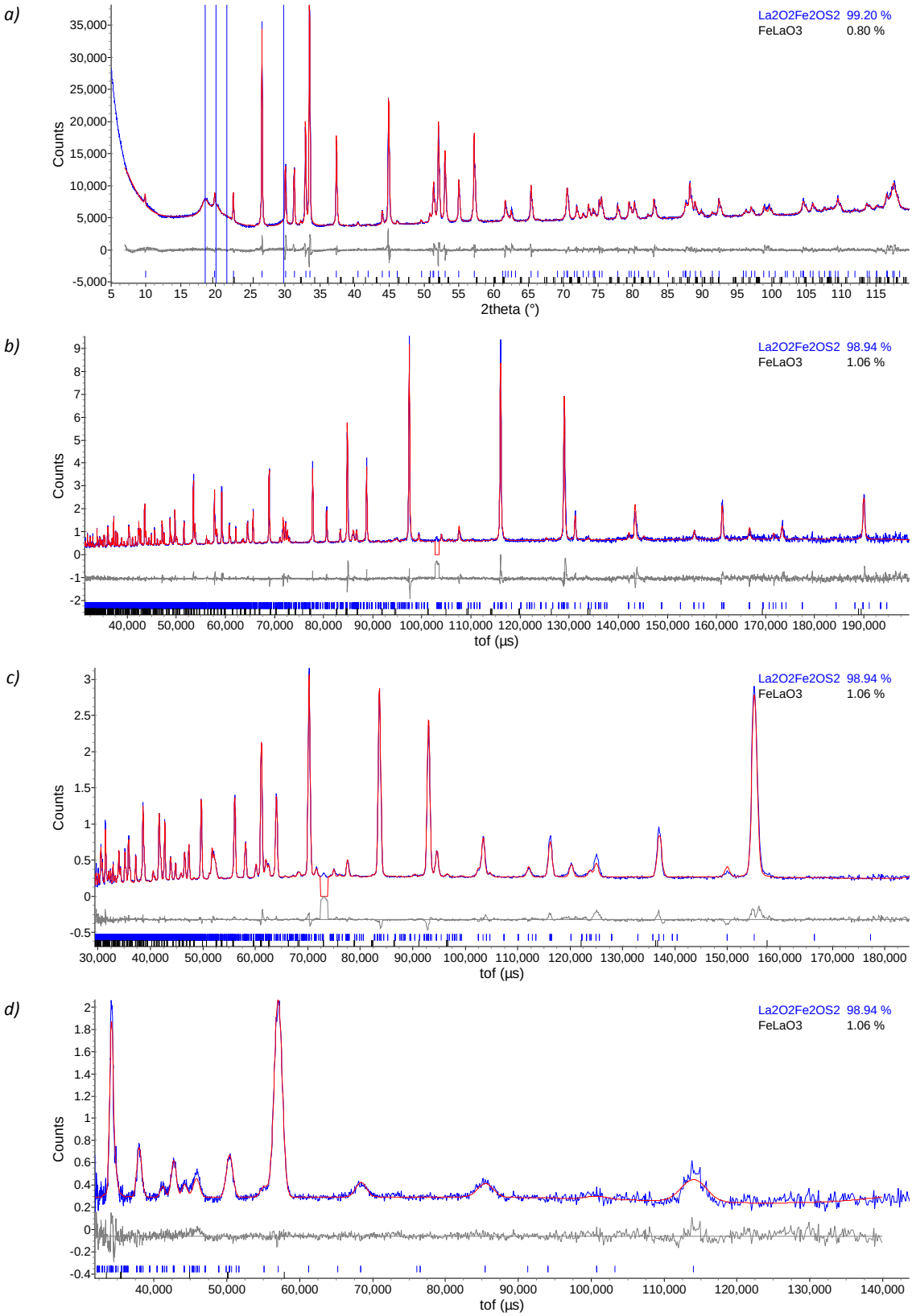

Figure 4.14 *Rietveld plots for $La_2O_2Fe_2OS_2$ at 12 K using (a) X-ray, (b) HRPD bs, (c) 90° and (d) 30° bank data; observed = blue, calculated = red, difference = grey. DGF306, d9_04646, hrp46728.*

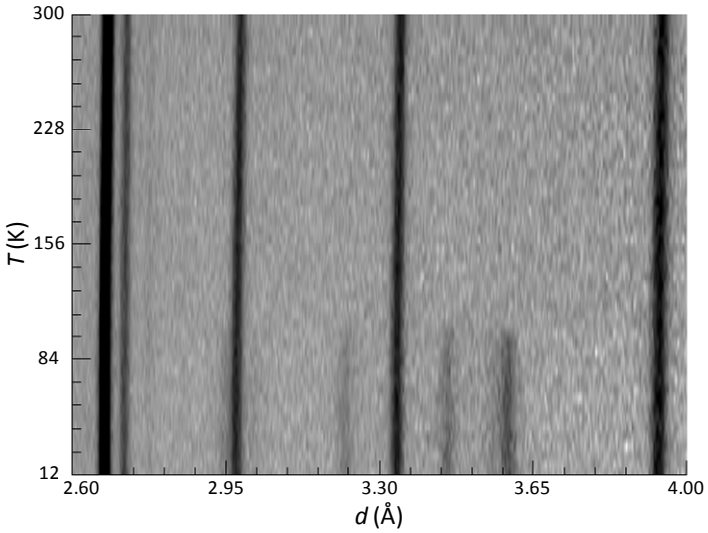

Figure 4.15 *Film plot showing the evolution of the observed magnetic peaks in $La_2O_2Fe_2OS_2$; plot shows the 2.6–4.0 Å (90–140 ms) region of the 90° HRPD bank.*

Whilst the magnetic structure obtained is different to those predicted from DFT studies, it is similar to that that observed for $Fe_{1+x}Te$, with $x < 0.1$, which has the same propagation vector, $\boldsymbol{k}$ = (½0½), and has moments directed along the *b* axis (*Figure 4.16*).[16, 18-20] As discussed in the introduction, $Fe_{1+x}Te$ shares the anti-fluorite structure adopted by FeSe, with excess Fe^{2+} ions located between layers. In this material the magnetic transition is accompanied by a clear phase transition to a monoclinic, $P2_1/m$ cell, with a/b = 1.01 and β = 89.2°, which then allows the observed magnetic ordering to be described by a single irreducible representation, rather than the two (Γ_2 and Γ_3) required here. This lowering in symmetry is shown in *Figure 4.17* by splitting of the (112) and (11-2) peaks, and naturally leads to exchange interactions that can differ in different directions, *i.e.* J_1 splits into J_{1a} and J_{1b}, and J_2 splits into J_{2a} and J_{2b}, as shown in *Figure 4.16*. This then leads to a region of the magnetic phase diagram in which the AFM3 structure is stable, as discussed by Fang *et al.*.[20] Whilst there is no clear evidence for peak splitting in the $La_2O_2Fe_2OQ_2$ phases at low temperature, the discontinuity observed in the thermal expansion of the *a* cell parameter, and the coincident peak broadening in $La_2O_2Fe_2OSe_2$, could indicate a subtle lowering in symmetry allowing the J_1, J_2 and J_2' interactions to differ. This decrease in symmetry would again allow the AFM3 arrangement to be explained by a single irreducible representation. One could also imagine that if the doubled *a* axis in $La_2O_2Fe_2OQ_2$ was slightly smaller than twice the *b* axis, then the resulting J_{2a}' interaction would be slightly larger than the J_{2b}' interaction, and hence AFM coupling would be observed along *a* and frustrated FM coupling observed along *b*. As discussed in chapter 5, however, it is surprising that these subtle changes in symmetry could lead to such large changes in interactions, and that an inherently frustrated system orders at such a high temperature. In the $Fe_{1+y}Te$ systems this may be a result of the effects of itinerant electrons and orbital ordering. In these insulating systems the anisotropy could be caused by local ordering of the O(2) sites above and below the $[Fe_2O]^{2+}$ layers.

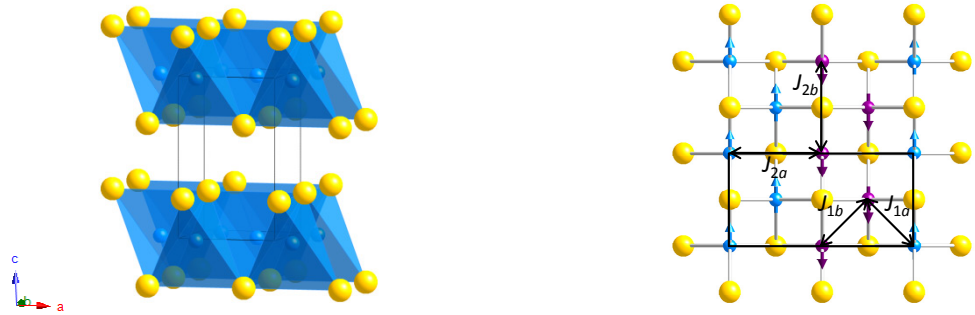

Figure 4.16 *Nuclear and magnetic structures of $Fe_{1.086}Te$; Fe = blue/purple, Te = yellow; the magnetic cell is outlined in black.*

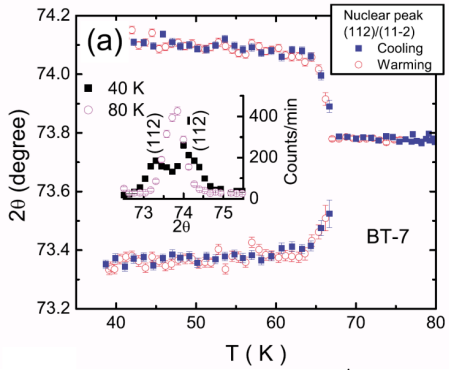

Figure 4.17 *Peak splitting observed in $Fe_{1.086}Te$ taken from Li et al..*[vi]

4.5 Variable Temperature Magnetic Data

In addition to high quality 12 K data sets, variable temperature neutron data were also collected, according to the parameters outlined in section 2.4.2 (*Figure 4.9* and *Figure 4.15*). Although individual data sets are relatively noisy, the data clearly show that the Fe^{2+} moments for the materials order below 110 and 90 K, for $La_2O_2Fe_2OS_2$ and $La_2O_2Fe_2OSe_2$, respectively; coincident with the discontinuities observed in the *a* cell parameters for both materials. *Figure 4.18* shows the results from the refinement of these data for both materials. The ordering of these moments was described using the function given in *eqn 3.7* and refined parameters are given in *Table 4.8*. Refined values of 0.10 for β, in both materials, are close to the expected value of 0.125 expected for a 2d-Ising system.[21] Note that the fits reported were performed using a bootstrap error analysis method in TA, due to large correlation of the β and T_N parameters.[22] The larger value of T_N for the sulphide system reflects the smaller unit cell, which consequently has increased orbital overlap, and hence stronger coupling. The large scatter observed above T_N for both materials in *Figure 4.18* is evidence that the moment is no longer present, and the parameter included in the refinement to model this is ill defined.

[vi] Reprinted Figure 2a with permission from S. Li *et al.*, *Phys. Rev. B*, 2009, **79**, 054503. Copyright 2009 by the American Physical Society.

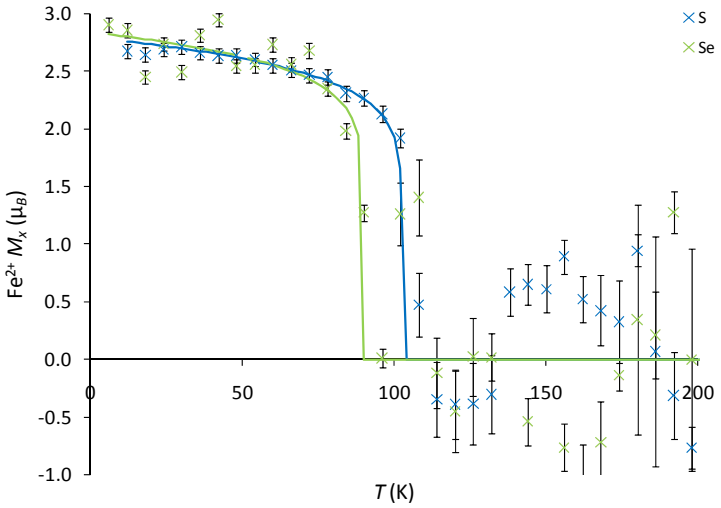

Figure 4.18 *Magnetic moment of Fe^{2+} for $La_2O_2Fe_2OQ_2$ materials as a function of temperature; S = blue, Se = green.*

Table 4.8 *Refined parameters for models of magnetic ordering of Fe^{2+} ions as a function of temperature in $La_2O_2Fe_2OQ_2$.*

		$La_2O_2Fe_2OS_2$	$La_2O_2Fe_2OSe_2$
Fe^{2+} M_x	M_0 (μ_B)	*2.8(2)*	*2.84(6)*
	T_N (K)	*103(5)*	*89(1)*
	β	*0.10(7)*	*0.10(2)*

4.6 Conclusions

In conclusion, we have demonstrated that both $La_2O_2Fe_2OS_2$ and $La_2O_2Fe_2OSe_2$ order antiferromagnetically on cooling, with the propagation vector ***k*** = (½0½). This observation is consistent with susceptibility data published by Mayer, however the adopted magnetic structure is contrary to those predicted from theoretical calculations.[1] The AFM3 structure adopted consists of moments that are directed along the doubled *a* axis, coupled AFM along *a* and FM along *b*. The moments are observed to order below 110 and 90 K for the sulphide and selenide samples, respectively, which is consistent with discontinuities observed in the thermal expansion of *a* and peak width in $La_2O_2Fe_2OSe_2$. These observations suggest that a subtle structural transition may accompany magnetic ordering, as observed in $Fe_{1.086}Te$, which also orders with the AFM3 structure.

Other structural observations are similar to those observed in $A_2O_2Mn_2OSe_2$ materials, with a change in thermal expansion of *c* on cooling, and large thermal displacement of the O(2) anion site at room temperature. Unlike in the manganese series, however, these effects are much less pronounced, and also are not accompanied by the appearance of any super structure peaks that may indicate ordering of the O(2) ions.

4.7 References

1. J. M. Mayer, L. F. Schneemeyer, T. Siegrist, J. V. Waszczak and B. v. Dover, *Angew. Chem. Int. Ed. Engl.*, 1992, **31**, 1645-1647.
2. J. X. Zhu, R. Yu, H. Wang, L. L. Zhao, M. D. Jones, J. Dai, E. Abrahams, E. Morosan, M. Fang and Q. Si, *Phys. Rev. Lett.*, 2010, **104**, 216405.
3. H. Kabbour, E. Janod, B. Corraze, M. Danot, C. Lee, M.-H. Whangbo and L. Cario, *J. Am. Chem. Soc.*, 2008, **130**, 8261-8270.
4. Y. Fuwa and et al., *J. Phys.: Condens. Matter*, 2010, **22**, 346003.
5. N. D. Withers, *Synthesis and Characterisation of New Layered Oxychalcogenide Materials*, Durham University, *Ph.D.*, Durham, 2005.
6. D. G. Free and J. S. O. Evans, *Phys. Rev. B*, 2010, **81**, 214433.
7. J. S. O. Evans, *multitopas, FORTRAN 77 routine*, University of Durham, 1999.
8. A. C. Larson and R. B. Von Dreele, *The General Structure Analysis System (GSAS)*, Los Alamos National Laboratory: Los Alamos, 2004.
9. B. H. Toby, *J. Appl. Cryst.*, 2001, **34**, 210-221.
10. K. Wang and R. R. Reeber, *Appl. Phys. Lett.*, 2000, **76**, 2203-2204.
11. A. S. Wills, *Physica B*, 2000, **276-278**, 680-681.
12. J. B. Goodenough, *Magnetism and the Chemical Bond*, John Wiley & Sons, New York - London, 1963.
13. J. Kanamori, *J. Phys. Chem. Solids*, 1959, **10**, 87-98.
14. B. J. Campbell, H. T. Stokes, D. E. Tanner and D. M. Hatch, *J. Appl. Cryst.*, 2006, **39**, 607-614.
15. C. de la Cruz, Q. Huang, J. W. Lynn, J. Li, W. Ratcliff II, J. L. Zarestky, H. A. Mook, G. F. Chen, J. L. Luo, N. L. Wang and P. Dai, *Nature*, 2008, **453**, 899-902.
16. S. Li, C. de la Cruz, F. Q. Huang, Y. Chen, J. W. Lynn, J. Hu, Y. L. Huang, F. C. Hsu, K. W. Yeh, M. K. Wu and P. Dai, *Phys. Rev. B*, 2009, **79**, 054503.
17. W. L. Roth, *Phys. Rev.*, 1958, **110**, 1333-1341.
18. D. Fruchart, P. Convert, P. Wolfers, R. Madar, J. P. Senateur and R. Fruchart, *Mater. Res. Bull.*, 1975, **10**, 169-174.
19. W. Bao, Y. Qui, Q. Huang, M. A. Green, P. Zajdel, M. R. Fitzsimmons, M. Zhernenkov, S. Chang, M. Fang, B. Qian, E. K. Vehstedt, J. Yang, H. M. Pham, L. Spinu and Z. Q. Mao, *Phys. Rev. Lett.*, 2009, **102**, 241001.
20. C. Fang, B. A. Bernevig and J. Hu, *Europhys. Lett.*, 2009, **86**, 67005.
21. L. Onsager, *Phys. Rev.*, 1944, **65**, 117-149.
22. B. Efron and R. Tibshirani, *Stat. Sci.*, 1986, **1**, 54-77.

Structural and Magnetic Comparisons of $A_2O_2M_2OSe_2$-type Materials

5.1 Introduction

Chapters 3 and 4 discussed the structural and magnetic properties of $A_2O_2Mn_2OSe_2$ (A = La–Pr) and $La_2O_2Fe_2OQ_2$ (Q = S, Se) (*Figure 5.1*); atomic coordinates are given in *Table 5.1*. In this chapter the synthesis and characterisation of other $La_2O_2Fe_2OSe_2$-type materials, including $Ce_2O_2Fe_2OSe_2$, $Pr_2O_2Fe_2OSe_2$ and a series of manganese-iron materials with the formula $A_2O_2(Mn_{0.5}Fe_{0.5})_2OSe_2$ are described. In addition to this the magnetic structure of $La_2O_2Co_2OSe_2$ is discussed following reinvestigation of neutron data originally recorded by Withers, and comparisons drawn with $La_2O_2Fe_2OSe_2$ and $La_2O_2Mn_2OSe_2$.[1] The structural and physical trends observed on variation of rare-earth and transition metal ions over the range of known $A_2O_2M_2OSe_2$ materials will also be discussed.

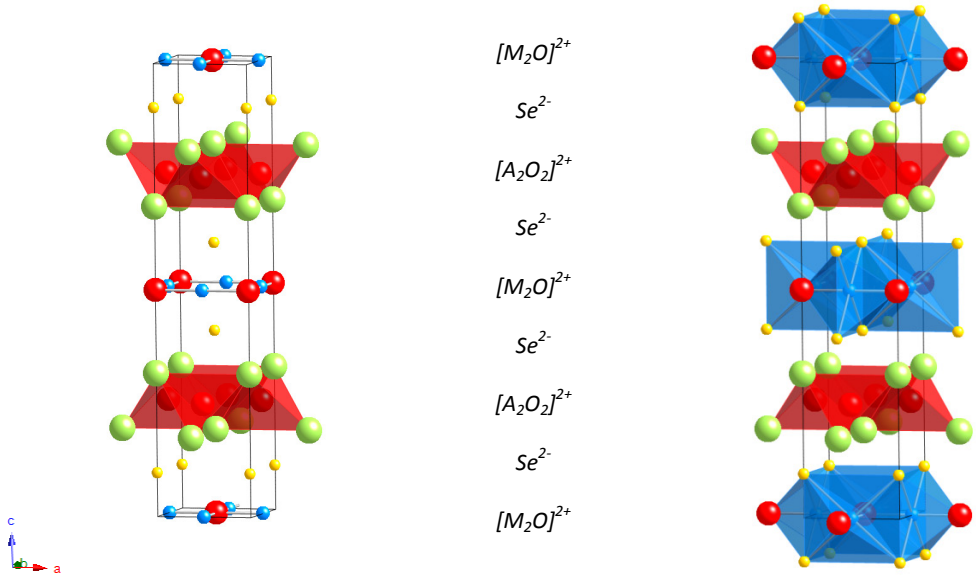

Figure 5.1 *Structure of $A_2O_2M_2OSe_2$ with different transition metal coordination geometries depicted; A = green, M = blue, O = red, Se = yellow, the unit cell is outlined.*

Table 5.1 *Cell coordinates and site occupancies (Occ.) for $A_2O_2M_2OSe_2$ materials.*

	Wyckoff site	*x* (*a*)	*y* (*b*)	*z* (c)	*Occ.*
A	*4e*	*0.5*	*0.5*	*~0.19*	*1*
M	*4c*	*0.5*	*0*	*0*	*1*
Se	*4e*	*0*	*0*	*~0.10*	*1*
O(1)	*4d*	*0.5*	*0*	*0.25*	*1*
O(2)	*2b*	*0.5*	*0.5*	*0*	*1*

5.2 Iron-containing Materials

Work in the group has expanded the $A_2O_2Fe_2OQ_2$ family to include a variety of sulphur and selenium containing materials: $Pr_2O_2Fe_2OSe_2$, $Nd_2O_2Fe_2OSe_2$, $Sm_2O_2Fe_2OSe_2$, and $Nd_2O_2Fe_2OS_2$.[1-3] Following the successful synthesis of $Ce_2O_2Mn_2OSe_2$, as discussed previously, $Ce_2O_2Fe_2OSe_2$ was also prepared. In addition to this, variable temperature studies of $Pr_2O_2Fe_2OSe_2$ were performed to investigate the

possibility of symmetry-lowering as had been observed in $Pr_2O_2Mn_2OSe_2$. Here we will discuss both of these materials and compare their properties with those of $La_2O_2Fe_2OSe_2$.

5.2.1 $Ce_2O_2Fe_2OSe_2$

The synthesis of $Ce_2O_2Fe_2OSe_2$ was achieved using similar techniques to $Ce_2O_2Mn_2OSe_2$. Subsequent characterisation of the product using powder X-ray diffraction indicated that the target phase was isostructural with $La_2O_2Fe_2OSe_2$, and Rietveld refinement was performed in TOPAS Academic (TA).[4] The only impurity observed was a small amount, ~6.6 % by weight, of CeO_2. Results from Rietveld refinement are given in *Table 5.2*, and a Rietveld plot in *Figure 5.2*. The variables used in the refinement included those listed in *Table 5.2*, as well as parameters to model background, peak shape, peak asymmetry, sample height, scale, and parameters to model the CeO_2 impurity. Again, as in other $A_2O_2M_2O_2Se_2$ materials, a large thermal displacement was observed for the O(2) site.

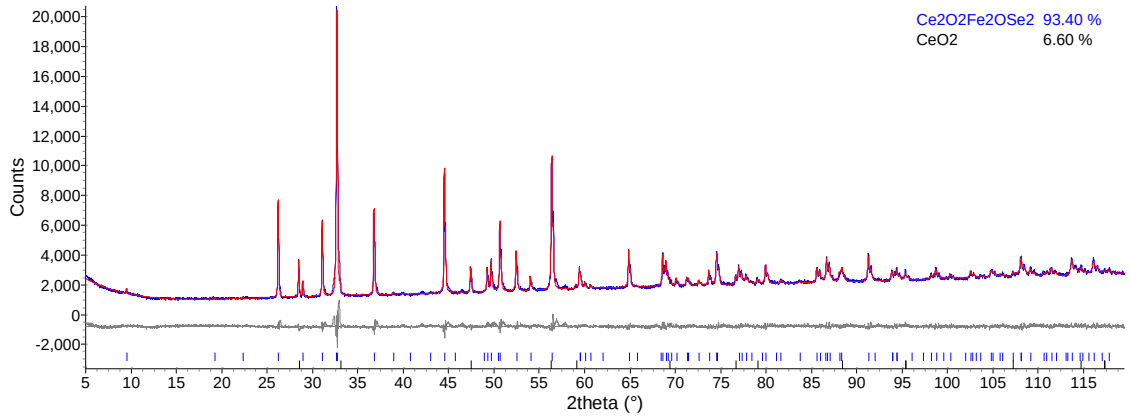

Figure 5.2 *Rietveld plot for $Ce_2O_2Fe_2OSe_2$ at room temperature using X-ray data; observed = blue, calculated = red, difference = grey. DGF122, d9_03016.*

Table 5.2 *Results from X-ray Rietveld refinements of $Ce_2O_2Fe_2OSe_2$ and $Pr_2O_2Fe_2OSe_2$ at room temperature and 12 K.*

	$Ce_2O_2Fe_2OSe_2$	**$Pr_2O_2Fe_2OSe_2$**	
Temperature	*295 K*	*12 K*	*295 K*
Space group	*I4/mmm*	*I4/mmm*	*I4/mmm*
a (Å)	*4.05928(9)*	*4.03756(4)*	*4.04351(4)*
c (Å)	*18.4638(5)*	*18.3837(3)*	*18.4476(3)*
V (Å^3)	*304.24(2)*	*299.689(7)*	*301.618(7)*
A z (*c*)	*0.18471(8)*	*0.18581(6)*	*0.18593(6)*
Se *z* (*c*)	*0.0975(2)*	*0.0983(1)*	*0.0985(1)*
A U_{iso} (100×Å^2)	*0.48(5)*	*-0.03(3)*	*0.29(3)*
Fe U_{iso} (100×Å^2)	*0.9(1)*	*0.18(7)*	*0.67(7)*
Se U_{iso} (100×Å^2)	*0.77(8)*	*0.28(5)*	*0.77(6)*
O(1) U_{iso} (100×Å^2)	*1.6(4)*	*0.4(3)*	*0.6(3)*
O(2) U_{iso} (100×Å^2)	*2.9(8)*	*-0.3(4)*	*0.4(4)*
N°. variables	*28*	*26*	*26*
R_{wp} (%)	*4.34*	*4.81*	*4.70*
χ^2	*3.94*	*1.69*	*1.68*

Further details are given in appendices VII and VIII.

5.2.2 $Pr_2O_2Fe_2OSe_2$

The synthesis of $Pr_2O_2Fe_2OSe_2$ was originally reported in previous work.[2] Structural information determined from X-ray diffraction is given in *Table 5.2*, and a Rietveld plot in *Figure 5.3*; a Rietveld plot for refinement with data collected at 12 K is given in appendix VIII. This material was investigated as $Pr_2O_2Mn_2OSe_2$ was shown to undergo a reduction from tetragonal to orthorhombic symmetry at low temperatures. As this phase transition has not been observed in other $A_2O_2Mn_2OSe_2$ materials, it was postulated that the origin of the distortion was due to crystal field splitting of the Pr^{3+} energy levels. In order to investigate this further variable temperature powder X-ray diffraction studies were performed on $Pr_2O_2Fe_2OSe_2$ using the d9 diffractometer, equipped with an Oxford Cryosystems PheniX CCR cryostat, as discussed in section 2.3.3.

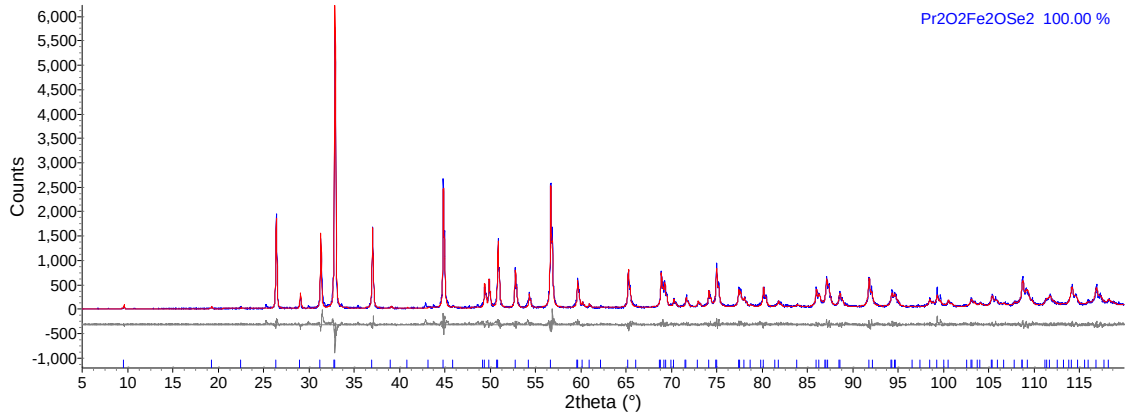

Figure 5.3 *Rietveld plot for $Pr_2O_2Fe_2OSe_2$ at room temperature using X-ray data; observed = blue, calculated = red, difference = grey. DGF031, d5_08003.*

Figure 5.4 shows a surface plot of the data collected for $Pr_2O_2Fe_2OSe_2$ in the region of the {200} reflection (46–48° 2θ). Unlike in $Pr_2O_2Mn_2OSe_2$, no peak splitting was observed at low temperatures, suggesting that this behaviour is not universal for Pr^{3+}-containing materials. *Figure 5.5* shows that the variation of the *a* and *c* cell parameters as a function of temperature. Whilst the variation in the *a* cell parameter appears to be relatively smooth, the change in the *c* cell parameter shows a slight change in thermal expansion on cooling below ~75 K, similar to that observed for $La_2O_2Fe_2OSe_2$ at ~150 K. Plots of cell volume and *c*/*a* ratio can be found in appendix VIII. A strain term to describe peak broadening was also introduced into the refinements, following the observation of peak broadening before the phase transition in $Pr_2O_2Mn_2OSe_2$, and below T_N in $La_2O_2Fe_2OSe_2$. This term is convoluted with the instrumental peak shape with a *tan*(θ) dependency, as shown in *eqn 5.1*, and describes a change in the full width half maximum of the Lorentzian contribution to the overall peak shape.[5] *Figure 5.5* shows that this term varies little with temperature, however any effects may be masked by the higher instrumental contribution to peak shape relative to the high resolution powder diffractometer (HRPD) data used for $Pr_2O_2Mn_2OSe_2$. It is, however, clear that peak splitting is observed in X-ray data collected for $Pr_2O_2Mn_2OSe_2$ but not this material (*Figure 5.4*). Cell parameters for the low temperature structure are given in *Table 5.2*. Whilst the thermal displacement refined for Pr and O(2) sites is as negative at low temperature, they are within one standard uncertainty of zero.

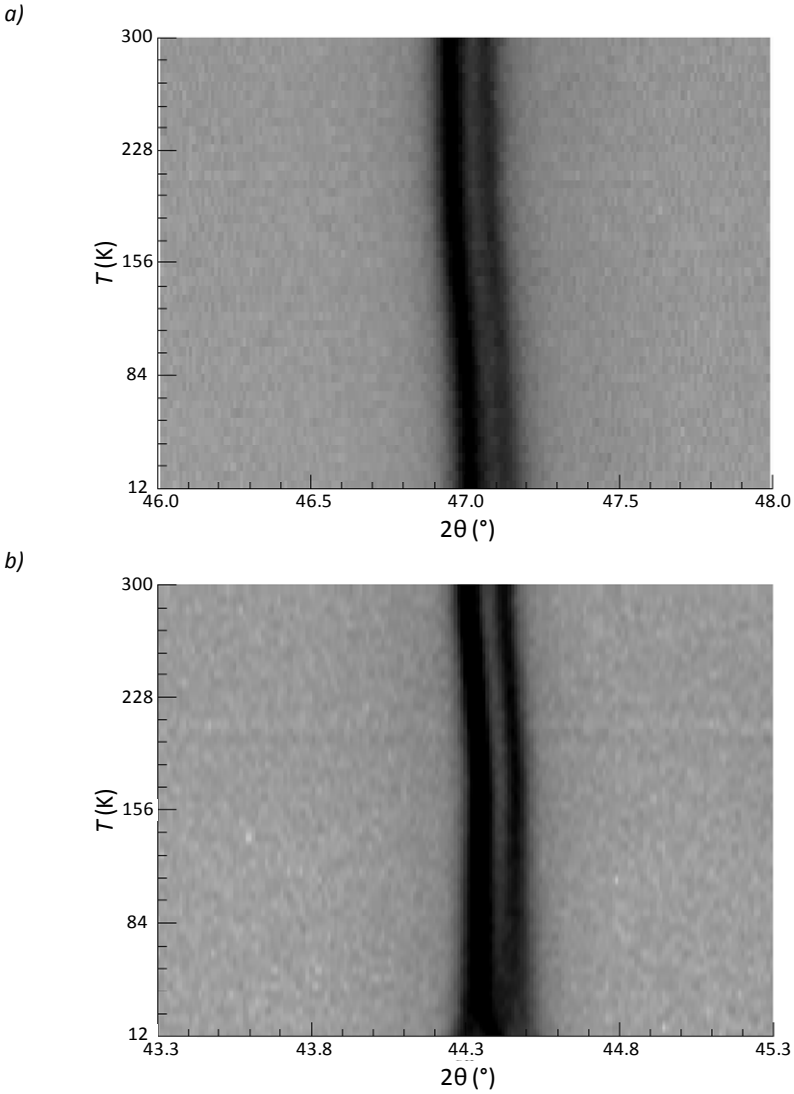

Figure 5.4 *Psuedo-film plot showing the effect of temperature on the {200} reflection of (a) $Pr_2O_2Fe_2OSe_2$ (~47.0° 2ϑ) and (b) $Pr_2O_2Mn_2OSe_2$ (~44.3° 2ϑ); plots show the 46–48° 2ϑ and 43.3–45.3° 2ϑ region of the X-ray data, respectively. DGF031, d9_02807.*

$$lor\_fwhm = Strain\_L \times tan(\theta) \qquad \textbf{eqn 5.1}$$

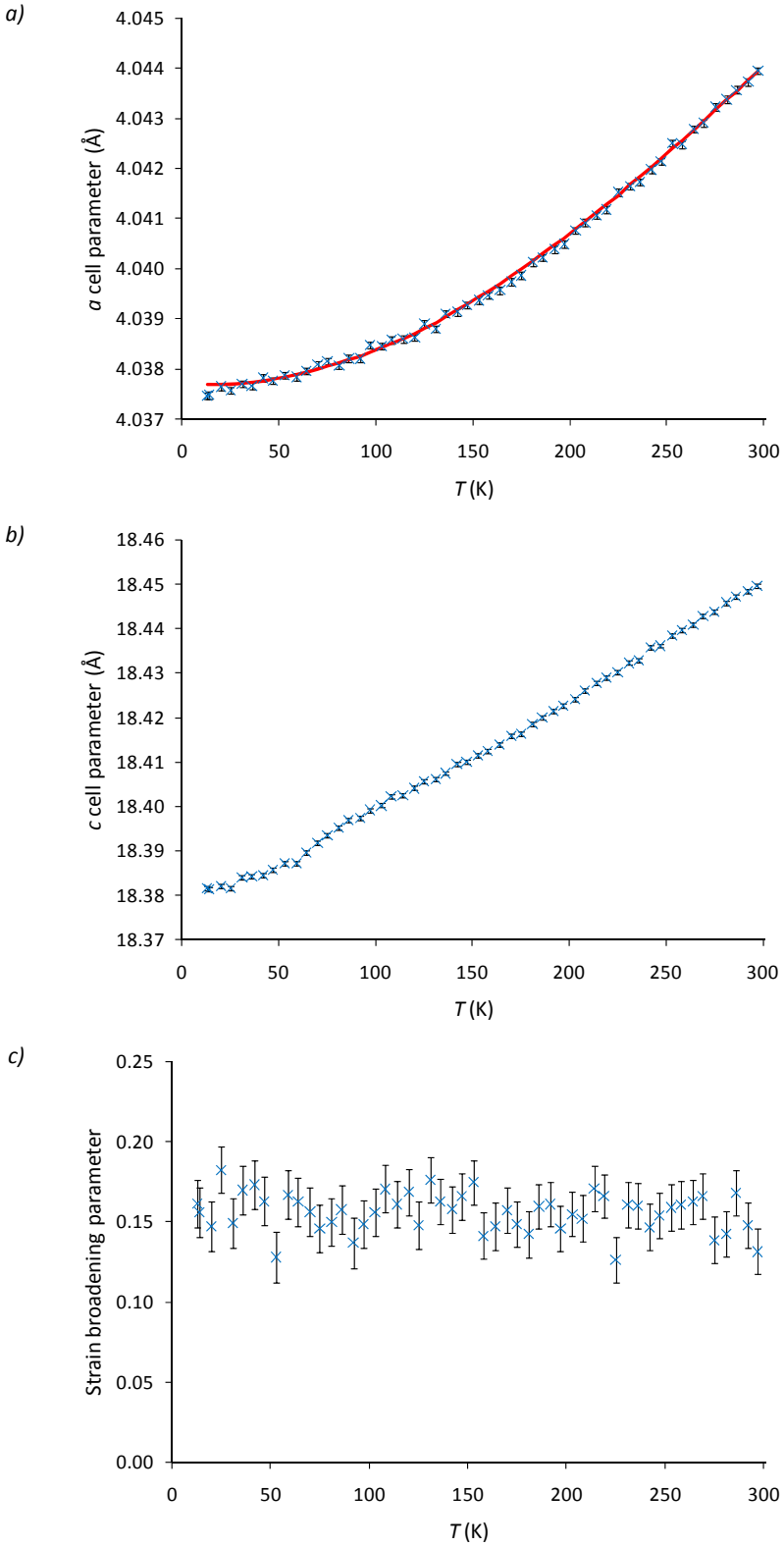

Figure 5.5 *The (a) a cell, (b) c cell and (c) strain broadening parameters for $Pr_2O_2Fe_2OSe_2$ as a function of temperature.*

5.3 Manganese-Iron Materials

Previous work showed that the synthesis of vanadium and chromium containing materials with this structure-type was not possible, and hence no materials with transition metal radii between those of

Mn^{2+} and Fe^{2+} had been prepared.[2] To that end the synthesis of a series of manganese-iron materials, with the general formula $A_2O_2(Mn_{0.5}Fe_{0.5})_2OSe_2$, was attempted. Three materials were successfully prepared, $La_2O_2(Mn_{0.5}Fe_{0.5})_2OSe_2$, $Pr_2O_2(Mn_{0.5}Fe_{0.5})_2OSe_2$, and $Nd_2O_2(Mn_{0.5}Fe_{0.5})_2OSe_2$, however the synthesis of $Sm_2O_2(Mn_{0.5}Fe_{0.5})_2OSe_2$ proved unsuccessful; the lack of formation of the known phase $Sm_2O_2Fe_2OSe_2$ suggests that the experiment should be repeated.

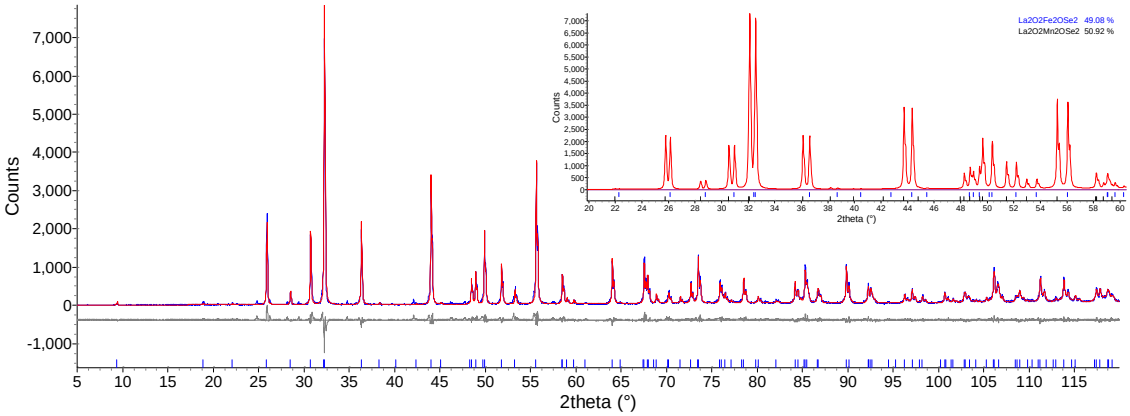

Figure 5.6 *Rietveld plot for $La_2O_2(Mn_{0.5}Fe_{0.5})_2OSe_2$ at room temperature using X-ray data with the calculated pattern for individual $La_2O_2Mn_2OSe_2$ and $La_2O_2Fe_2OSe_2$ inset; observed = blue, calculated = red, difference = grey. DGF118a, d5_07997.*

The synthesis of each phase was confirmed by Rietveld analysis using power X-ray diffraction data. The lack of any major impurities in each preparation, and the observation of only one set of Bragg peaks, suggested that all of the manganese and iron metal had reacted to form a solid-solution. Results from Rietveld refinement of each phase are given in *Table 5.3* and a Rietveld plot for $La_2O_2(Mn_{0.5}Fe_{0.5})OSe_2$ is shown in *Figure 5.6*; plots for $Pr_2O_2(Mn_{0.5}Fe_{0.5})OSe_2$ and $Nd_2O_2(Mn_{0.5}Fe_{0.5})OSe_2$ are given in appendix IX. The inset is a calculated diffraction pattern for a 50:50 mixture of $La_2O_2Mn_2OSe_2$ and $La_2O_2Fe_2OSe_2$ phases using previously refined peak shape and instrumental parameters. Refinement was performed using crystallographic information from $La_2O_2Fe_2OSe_2$, however an Mn^{2+} site with the same coordinates as the Fe^{2+} site was included; occupancies for these two metal sites were set at 0.5, and thermal displacement parameters were constrained to be the same. Due to the similar scattering powers of Mn^{2+} and Fe^{2+} it was not possible to refine site occupancies to determine the true composition, however this would be possible if neutron data were available. A comparison of the cell parameters of $La_2O_2(Mn_{0.5}Fe_{0.5})_2OSe_2$, $La_2O_2Mn_2OSe_2$ and $La_2O_2Fe_2OSe_2$ is given in *Table 5.4*, and shows that the *a* cell parameter is comparable to the average of the two individual phases, suggesting a composition of $La_2O_2(Mn_{0.50}Fe_{0.50})_2OSe_2$. Examination of the *c* cell parameters suggests a stoichiometry closer to $La_2O_2(Mn_{0.69}Fe_{0.31})_2OSe_2$, however the lack of any major impurities in the pattern suggests that a 1:1 ratio of Mn:Fe can be assumed. Similar results were found for the praseodymium containing material, however, as $Nd_2O_2Mn_2OSe_2$ has not been successfully prepared a cell volume of 305.73 $Å^3$ was predicted, based on the contraction observed across the $A_2O_2Fe_2OSe_2$ series. The refined cell volume of 305.72(1) $Å^3$ suggested that the desired stoichiometry of $Nd_2O_2(Mn_{0.5}Fe_{0.5})_2OSe_2$ was, again, achieved.

Table 5.3 *Results from X-ray Rietveld refinements of $A_2O_2(Mn_{0.5}Fe_{0.5})_2OSe_2$ materials at room temperature.*

	La	Pr	Nd
Nuclear symmetry	*I*4/*mmm*	*I*4/*mmm*	*I*4/*mmm*
a (Å)	*4.11210(3)*	*4.07108(5)*	*4.05332(5)*
c (Å)	*18.7723(2)*	*18.6201(4)*	*18.6072(4)*
V (Å^3)	*317.428(6)*	*308.60(1)*	*305.71(1)*
A z (*c*)	*0.18552(6)*	*0.18699(6)*	*0.18721(7)*
Se *z* (*c*)	*0.0982(1)*	*0.1001(1)*	*0.1001(2)*
A U_{iso} (100×Å^2)	*-0.05(3)*	*-0.09(3)*	*0.26(4)*
M U_{iso} (100×Å^2)	*0.60(8)*	*0.47(8)*	*0.7(1)*
Se U_{iso} (100×Å^2)	*0.40(5)*	*0.15(5)*	*0.32(6)*
O(1) U_{iso} (100×Å^2)	*1.3(3)*	*1.1(3)*	*2.7(5)*
O(2) U_{iso} (100×Å^2)	*0.8(4)*	*1.0(5)*	*-2.2(3)*
N^o. variables	*25*	*25*	*33*
R_{wp} (%)	*15.23*	*14.88*	*16.98*
χ^2	*3.40*	*3.01*	*3.72*

Further details are given in appendix IX.

Table 5.4 *Observed and calculated cell parameters for $La_2O_2(Mn_{0.5}Fe_{0.5})_2OSe_2$.*

	Mn (obs)	Fe (obs)	$Mn_{0.5}Fe_{0.5}$ (calc)	$Mn_{0.5}Fe_{0.5}$ (obs)	Mn:Fe Ratio
a (Å)	*4.138921(4)*	*4.08475(1)*	*4.11183(1)*	*4.11209(4)*	*0.50:0.50*
c (Å)	*18.84990(3)*	*18.59736(9)*	*18.7236(1)*	*18.7723(3)*	*0.69:0.31*
V (Å^3)	*322.911(1)*	*310.300(2)*	*316.606(2)*	*317.425(7)*	*0.57:0.43*

5.4 Magnetic Structure of $La_2O_2Co_2OSe_2$

Following the observation that $La_2O_2Mn_2OSe_2$ and $La_2O_2Fe_2OSe_2$ both order with different antiferromagnetic (AFM) structures on cooling, the magnetic structure proposed by Withers for $La_2O_2Co_2OSe_2$ was reinvestigated.[1] The structure was originally described with a magnetic unit cell with $\boldsymbol{k}$ = (½½0) and moments aligned in the *ab* plane, as shown in *Figure 5.7*. The refined moment on the Co^{2+} sites for this model was calculated as 4.81 μ_B at 12 K; the maximum expected moment for a Co^{2+} ion is 3.9 μ_B. Subsequent theoretical studies, published by Wu, suggested, however that the material adopts an AFM6 structure; these LSDA+*U* calculations, with Mott-Hubbard interaction energies (*U*) of 2, 3 and 4 eV, all suggested that the J_1 (nearest neighbour) and J_2' (180° Co-O-Co) interactions should be AFM, whilst the J_2 (~97° Co-Se-Co) interactions are FM.[6] The strongest of these interactions at each value of *U* was the J_2' coupling, suggesting that the Co-O-Co interactions would dominate. Similar work by Fuwa *et al*., suggested that AFM J_1 coupling interactions would dominate, thus producing the AFM1 arrangement seen in $La_2O_2Mn_2OSe_2$.[7] All studies have been conclusive that an AFM structure is adopted, and this is in agreement with susceptibility measurements, however the spin state of the Co^{2+} ion has also been under question, with work by Wang *et al*. suggesting a low spin configuration, and work by Wu and Fuwa *et al.*, suggesting a high spin configuration.[8]

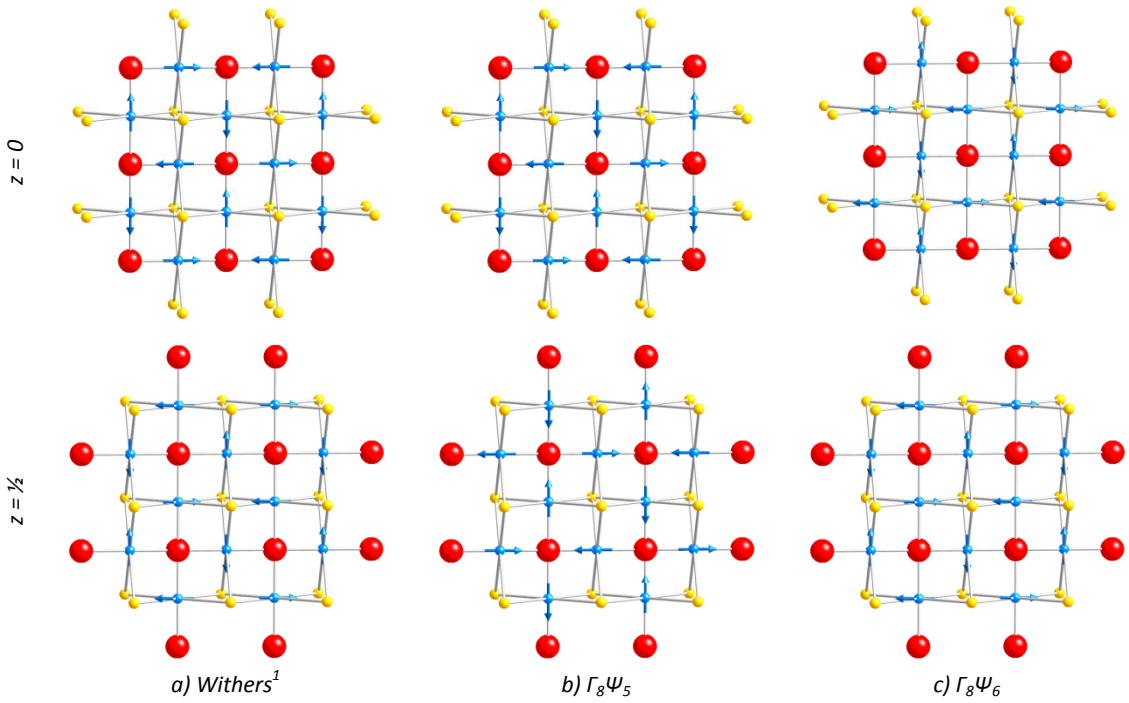

Figure 5.7 *Theoretical magnetic structures for $La_2O_2Co_2Se_2$, showing (a) Withers' reported model, (b) the $\Gamma_8\Psi_5$ and (c) $\Gamma_8\Psi_6$ models suggested from refinements in SARAh; Co = blue, O = red, Se = yellow.*

In order to clarify the arguments presented, Withers' original neutron data were reinvestigated using a similar method to that used for $La_2O_2Mn_2OSe_2$ and $La_2O_2Fe_2OSe_2$ in SARAh Refine.[9] Withers first observed that at 12 K, several new peaks were observed (*Figure 5.8*) consistent with AFM ordering, with an enlarged unit cell of $2a\times2a\times c$; note also the presence of impurity peaks from CoO, present at both room temperature and 12 K. For *I*4/*mmm* symmetry with propagation vector k = (½½0), six basis vectors are produced. The $\Gamma_2\Psi_1$, $\Gamma_2\Psi_2$, $\Gamma_8\Psi_5$ and $\Gamma_8\Psi_6$ basis vectors all describe arrangements with the moments aligned in the *ab* plane, and where all of the 180° Co-O-Co (J_2') interactions are satisfied. The remaining $\Gamma_4\Psi_3$ and $\Gamma_6\Psi_4$ basis vectors describe the moments lying along the *c* axis, again with all of the J_2' interactions satisfied. Initial analysis showed that χ^2 was maximised for larger contributions of $\Gamma_2\Psi_1$ and $\Gamma_2\Psi_2$, and minimised for larger contributions of $\Gamma_8\Psi_5$ and $\Gamma_8\Psi_6$; contour plots for this analysis are given in appendix X. Mixing of the latter two of these basis vectors was then investigated, and results showed, (*Figure 5.9*), that minima were produced when either was present; *i.e.* the statistics suggest that the structures so-derived are equally valid solutions.

The magnetic structures produced by these basis vectors are shown in *Figure 5.7*. Both have moments orientated in the *ab* plane and are related to each other by a rotation of the direction of the moments by ±90°, such that in the $\Gamma_8\Psi_5$ solution moments are directed along the Co-O bonds, and in the $\Gamma_8\Psi_6$ solution they are perpendicular to bonds. Due to the tetragonal nature of the nuclear cell, however, it is not possible to distinguish whether moments point along the *a* or *b* axes. Mössbauer spectroscopy data published for $Nd_2O_2Fe_2OSe_2$, however, demonstrated that Fe^{2+} moments are directed along the Fe-O bonds, and theoretical calculations by Fuwa *et al.* have suggested anisotropy of the Co^{2+} ions directed along the Co-O bonds, suggesting that the $\Gamma_8\Psi_5$ model presented here is correct.[7, 10] In both

arrangements the J_2 and J_2' interactions are all AFM, satisfying the Goodenough rules for 180° interactions between two d^7 cations, whereas the J_1 interactions all have some degree of frustration, with the moments lying perpendicular to each other.[11] These layers propagate in the *c* direction by a translation of (¼,¼,½). A final refined moment of 3.78(6) ì$_B$ for the Co^{2+} ion is consistent with a high spin Co^{2+} ion, confirming arguments by Wu and Fuwa *et al.*, and is closer to an expected μ_{eff} value of 3.9 μ_B.[6, 7] This refined moment compares with a value of 3.4(1) μ_B for CoO at 4.2 K.[12] Results from Rietveld analysis of $La_2O_2Co_2OSe_2$ using 145°, 90° and 44° bank neutron data collected on SEPD at the IPNS at Argonne, are given in *Table 5.5*, and Rietveld plots of the entire data range are given in appendix X. Bond angles and interatomic distances at 12 K can be found in *Table 5.10*. Whilst the final refinement was performed in GSAS, using separate nuclear and magnetic phases (with the magnetic phase described in *P*1), analysis in ISODISTORT suggested that the observed magnetic ordering was consistent with Shubnikov symmetry P_Cmmn with basis vector (-1,1,0)(-1,-1,0)(0,0,1) (labelled by TA / ISODISTORT as space group number 59.415).[13]

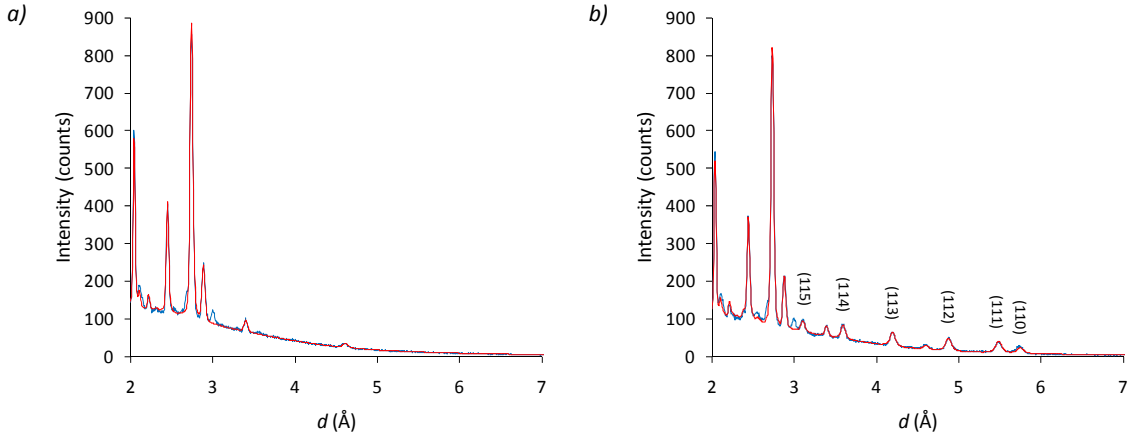

Figure 5.8 *Rietveld plots at (a) room temperature and (b) 12 K, highlighting the magnetic peaks observed in $La_2O_2Co_2OSe_2$; observed = blue, calculated = red, difference = grey.*

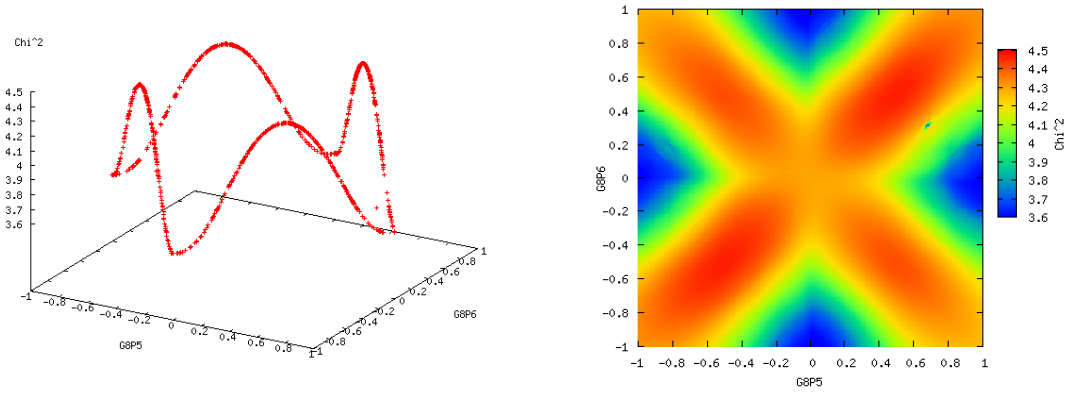

Figure 5.9 *xyz and contour plots showing χ^2 as a function of varying contributions of $\Gamma_8\Psi_5$ and $\Gamma_8\Psi_6$.*

Table 5.5 *Results from neutron Rietveld refinements of $La_2O_2Co_2OSe_2$ at 12 K, with results published by Withers for comparison.*[1]

	$La_2O_2Co_2OSe_2$	Reported	
Temperature	12 K	12 K	*295 K*
Nuclear symmetry	*I4/mmm*	*I4/mmm*	*I4/mmm*
Magnetic symmetry	P_Cmmn	*P4/mmm*	-
a (Å)	*4.0599(3)*	*4.06264(4)*	*4.07162(5)*
c (Å)	*18.377(1)*	*18.3883(3)*	*18.4282(4)*
V (Å^3)	*302.92(2)*	*303.500(7)*	*305.504(8)*
La *z* (*c*)	*0.18317(5)*	*0.18335(7)*	*0.18337(5)*
Se *z* (*c*)	*0.09515(6)*	*0.09525(8)*	*0.09511(7)*
La U_{iso} (100×Å^2)	*0.34(2)*	*0.48*	*1.1*
Co U_{iso} (100×Å^2)	*0.51(5)*	*0.52*	*1.39*
Se U_{iso} (100×Å^2)	*0.36(2)*	*0.47*	*1.19*
O(1) U_{iso} (100×Å^2)	*0.42(3)*	*0.38*	*0.66*
O(2) U_{iso} (100×Å^2)	*0.91(4)*	*1.19*	*2.51*
Co^{2+} *M* (μ_B)	*3.78(6)*	*4.81*	-
N^o. variables	*59*	-	-
R_{wp} (%)	*6.89*	-	-
χ^2	*3.33*	-	-

Statistics for specific banks of data and other information are given in appendix X.

5.5 Structural and Magnetic Comparisons of $A_2O_2M_2OSe_2$-type Materials

In this section we will discuss the trends observed for series of $A_2O_2M_2OSe_2$-type materials on variation of both transition and rare-earth metal radii. These trends will include the variation of lattice parameters across the series, a discussion of the phase diagram for all systems and the magnetic structures adopted by the $La_2O_2M_2OSe_2$ materials; the lattice parameters and *c*/*a* ratios observed for each of the material discussed are given in *Table 5.6*. *Table 5.7* gives the "thickness" of the lanthanide-oxide and metal-oxychalcogenide layers, and their separation, which are defined, alongside bond angle definitions, in *Figure 5.10*.

Table 5.6 *Lattice parameters for known $A_2O_2M_2OSe_2$ materials and those presented in this work at room temperature.*

Material	*a* (Å)	*c* (Å)	*V* (Å^3)	*c*/*a*	Ref.
$La_2O_2Mn_2OSe_2$	*4.138921(4)*	*18.84990(3)*	*322.911(1)*	*4.55430(1)*	
$Ce_2O_2Mn_2OSe_2$	*4.11304(2)*	*18.74100(9)*	*317.043(3)*	*4.55648(3)*	
$Pr_2O_2Mn_2OSe_2$	*4.09739(2)*	*18.69481(9)*	*313.860(3)*	*4.56261(3)*	
$La_2O_2(Mn_{0.5}Fe_{0.5})_2OSe_2$	*4.11210(3)*	*18.7722(2)*	*317.428(5)*	*4.56513(6)*	
$Pr_2O_2(Mn_{0.5}Fe_{0.5})_2OSe_2$	*4.07108(5)*	*18.6201(4)*	*308.604(8)*	*4.5738(1)*	
$Nd_2O_2(Mn_{0.5}Fe_{0.5})_2OSe_2$	*4.05332(5)*	*18.6072(3)*	*305.707(8)*	*4.5906(1)*	
$La_2O_2Fe_2OSe_2$	*4.08475(1)*	*18.59736(9)*	*310.300(2)*	*4.55288(2)*	
$Ce_2O_2Fe_2OSe_2$	*4.05928(9)*	*18.4638(5)*	*304.24(1)*	*4.5485(2)*	
$Pr_2O_2Fe_2OSe_2$	*4.04351(4)*	*18.4476(3)*	*301.618(6)*	*4.56227(9)*	
$Nd_2O_2Fe_2OSe_2$	*4.02816(4)*	*18.4347(3)*	*299.122(6)*	*4.57645(8)*	[3]
$Sm_2O_2Fe_2OSe_2$	*4.00079(7)*	*18.3827(5)*	*294.24(1)*	*4.5948(1)*	[3]
$La_2O_2Co_2OSe_2$	*4.07114(4)*	*18.4270(3)*	*305.412(7)*	*4.52625(9)*	[1]

Table 5.7 *Layer thicknesses and separation for known $A_2O_2M_2OSe_2$ materials.*

Material	A_4O	MSe_4O_2	Separation	Ref.
$La_2O_2Mn_2OSe_2$	*2.3872(3)*	*3.768(2)*	*1.6350(1)*	
$Ce_2O_2Mn_2OSe_2$	*2.3520(8)*	*3.792(2)*	*1.6130(2)*	
$Pr_2O_2Mn_2OSe_2$	*2.3021(5)*	*3.800(2)*	*1.6225(2)*	
$La_2O_2(Mn_{0.5}Fe_{0.5})_2OSe_2$	*2.421(2)*	*3.685(8)*	*1.6401(7)*	
$Pr_2O_2(Mn_{0.5}Fe_{0.5})_2OSe_2$	*2.347(2)*	*3.727(9)*	*1.6181(7)*	
$Nd_2O_2(Mn_{0.5}Fe_{0.5})_2OSe_2$	*2.337(2)*	*3.73(1)*	*1.6198(9)*	
$La_2O_2Fe_2OSe_2$	*2.4415(8)*	*3.585(3)*	*1.6364(3)*	
$Ce_2O_2Fe_2OSe_2$	*2.411(2)*	*3.60(1)*	*1.6099(9)*	
$Pr_2O_2Fe_2OSe_2$	*2.364(2)*	*3.634(7)*	*1.6129(3)*	
$Nd_2O_2Fe_2OSe_2$	*2.348(2)*	*3.636(8)*	*1.6165(7)*	*3*
$Sm_2O_2Fe_2OSe_2$	*2.287(2)*	*3.69(1)*	*1.6083(8)*	*3*
$La_2O_2Co_2OSe_2$	*2.453(5)*	*3.50(2)*	*1.631(2)*	*1*

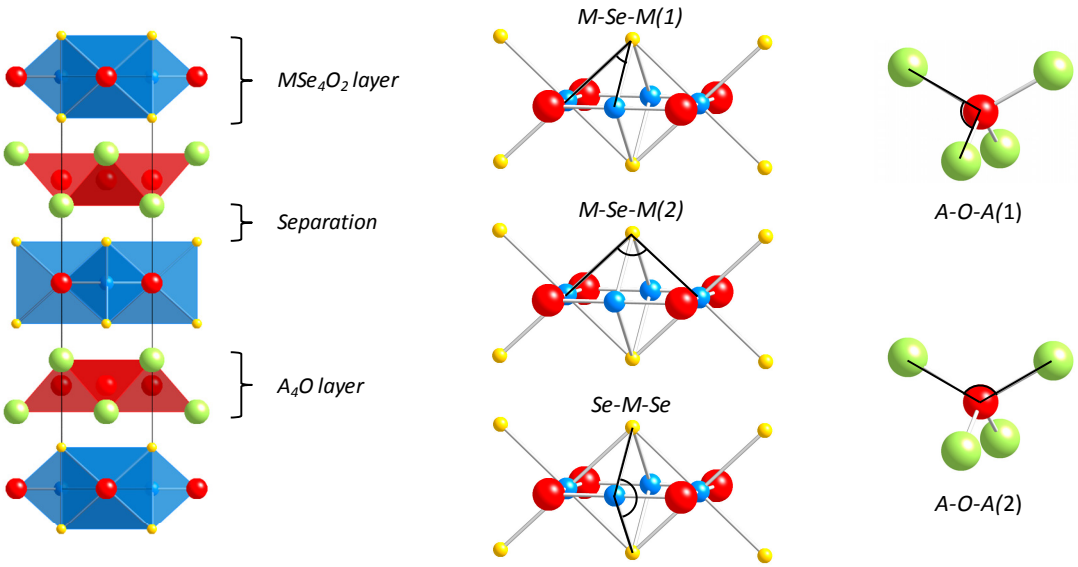

Figure 5.10 *Layer thickness, separation and bond angle definitions for $A_2O_2M_2OSe_2$ materials; A = green, M = blue, O = red, Se = yellow.*

5.5.1 Stability Field for Formation

Figure 5.11 summarises the transition metal and rare-earth metal radii over which the $A_2O_2M_2OSe_2$ structure has been prepared; where successfully prepared phases are shown in black. We can clearly see that these materials form over a narrow range of transition metal radii, with the range of the rare-earth ions possible being largest for iron-containing materials. The red line on the chart is a guide to the eye of where the stability region lies. The synthesis of manganese-iron materials has confirmed that preparation of materials with radii between Fe^{2+} and Mn^{2+} is possible, suggesting that the lack of phase formation for vanadium and chromium-containing materials is not constrained by their respective ionic radii but by the possible formation of other products as discussed below. It is worth mentioning here that the transition metal radii used are high spin, as this is consistent with magnetic measurements of the materials.

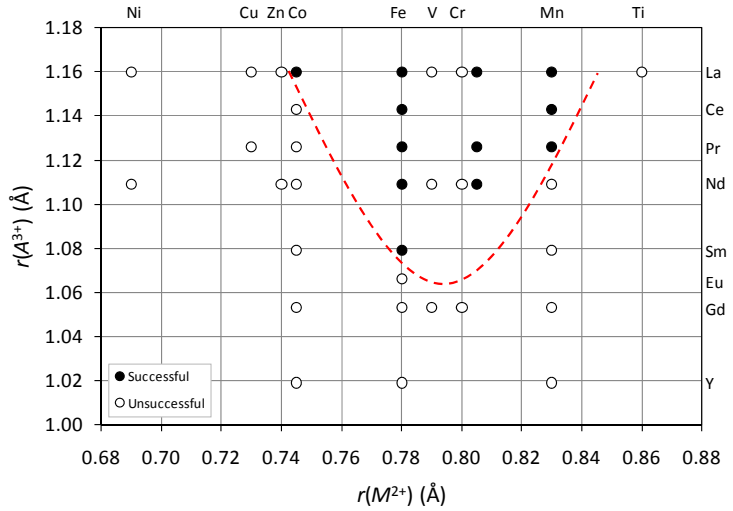

Figure 5.11 *Plot showing materials successfully prepared with respect to rare-earth and transition metal radii; the dotted red line serves as a guide to the eye.*

Figure 5.12 gives a summary of the phases formed when the preparation of the target phase was unsuccessful. These results show that, in general, the phases stable under these conditions were the lanthanide-oxide starting material plus the transition metal monoselenide. For reactions with smaller lanthanides, particularly those involving manganese, the ternary rare-earth oxyselenide was formed, alongside *M*Se and *M*O. For the late transition metals the formation of ZrCuSiAs-related materials, *i.e.* LaOCuSe, PrOCuSe and $La_2O_2ZnSe_2$, was observed. Presumably the high stability of these phases prevents the formation of the $A_2O_2M_2OSe_2$ structure under thermodynamic control. In the case of vanadium and chromium the products formed were controlled by the formation of stable M^{3+} perovskite phases $LaVO_3$ and $LaCrO_3$. Several unknown phases were also observed, especially for syntheses involving vanadium, chromium or titanium. There are, however, several 3-dimensional oxychalcogenides known to exist containing these metals. Further investigation would be required to identify all phases formed which lay outside the scope of this project.

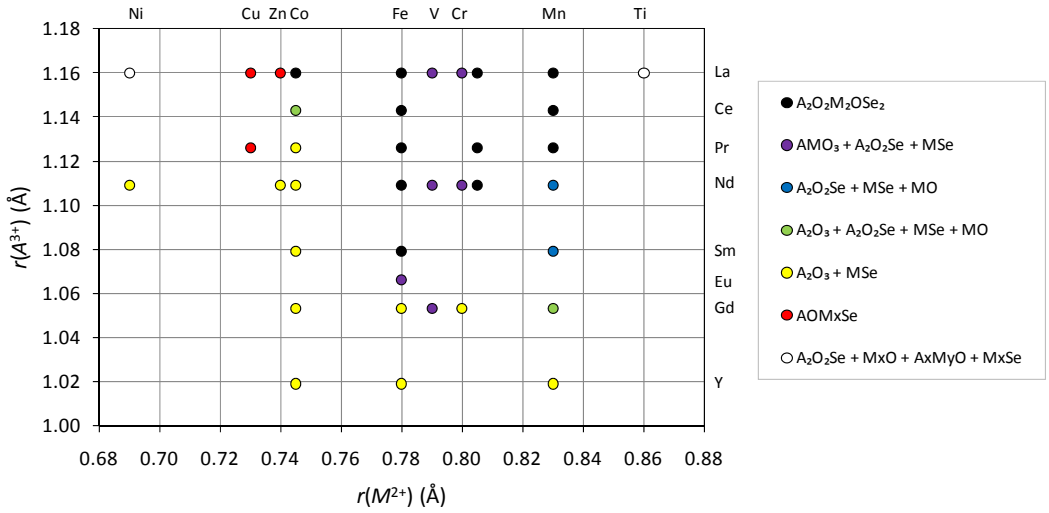

Figure 5.12 *Plot showing all materials prepared in the attempted synthesis of $La_2O_2Fe_2OSe_2$-type materials.*

5.5.2 Variation of Lanthanide Ion

Figure 5.13 shows the variation in cell volume observed across the $A_2O_2Mn_2OSe_2$ and $A_2O_2Fe_2OSe_2$

series, with the trend for *A*OCuSe materials included for comparison; in each series values are normalized relative to the lanthanum-containing material. These results show that cell volume decreases, approximately linearly, with respect to decreasing lanthanide radii, as would be expected from the lanthanide contraction. There is an indication in these materials, and in the *A*OCuSe series, that the lanthanum containing materials have a slightly larger cell volume than that expected for the series. This is derived primarily from a larger *c* lattice parameter, and inspection of inter and intra-layer distances suggests that this is derived from an increased separation of the $[A_2O_2]^{2+}$ and $[MO_2Se_4]^{2-}$ layers, although the cause of this is not known. A similar trend has been noted in the lanthanide monophosphides, although its origin was not discussed.[14] Plots of inter and intra-layer distances, along with lattice parameters, and all bond lengths and angles, are given in appendix XI.

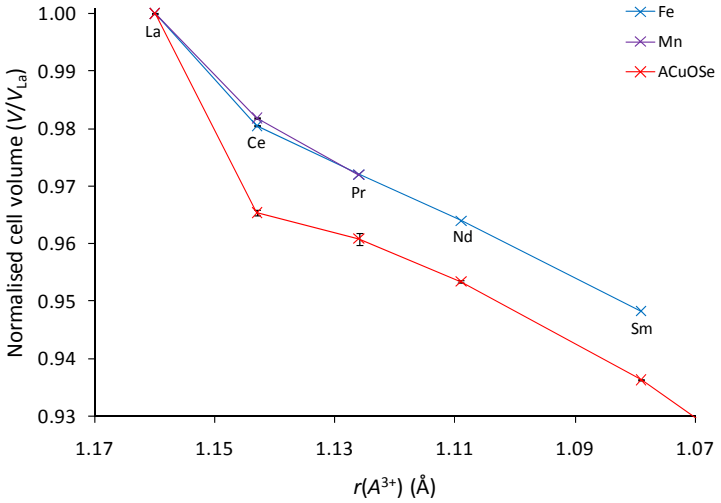

Figure 5.13 *Plot showing the cell volumes of $A_2O_2M_2OSe_2$ (M = Mn, Fe) and AOCuSe materials as a function of lanthanide radius.*[15, 16]

Figure 5.14 shows how the *c*/*a* ratio of the materials change as the size of the lanthanide ion is altered. Both the iron and manganese series of materials show an approximately linear increase of the *c*/*a* ratio with respect to decreasing lanthanide radius. This can be rationalised by the decrease in lanthanide radius causing the $[A_2O_2]^{2+}$ layers to contract, which in turn applies chemical pressure to the transition metal layers. This pressure causes the *M*-O bond length to decrease which, from a bond valence perspective, would cause the *M*-Se distance to increase, leading to an increase in the thickness of these layers along *c*. These results are reflected by the *M*-Se-*M*(1) and *M*-Se-*M*(2) bond angles, shown in *Figure 5.15a* and *b*, which are both seen to decrease with decreasing lanthanide radius, whilst the Se-*M*-Se bond angle, *Figure 5.15c*, is seen to increase; definitions of the bond angles are in *Figure 5.10*. The variation in the Fe-Se bond distance is linear within error, whilst the change Mn-Se bond length is relatively small (*Figure 5.15d*). The overall decrease observed in the *c* cell parameter is therefore much smaller than that observed for *a*, and hence the *c*/*a* ratio increases with decreasing lanthanide radius. The La^{3+} member lies slightly off the expected line as discussed above.

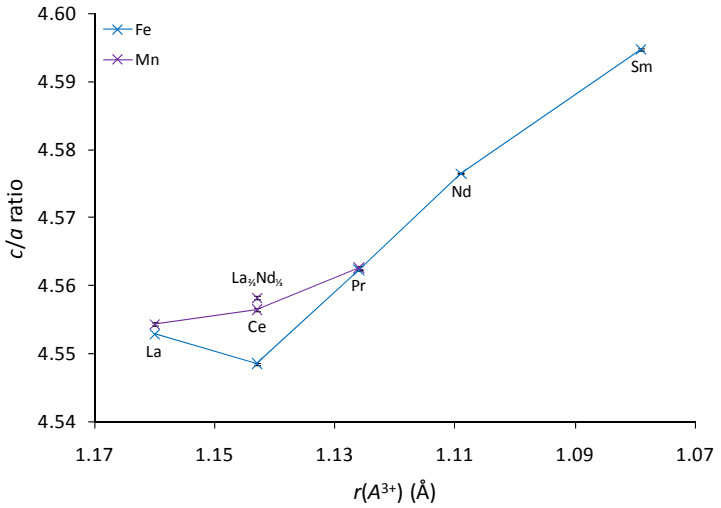

Figure 5.14 *Plot showing the c/a ratios of $A_2O_2M_2OSe_2$ (M = Mn, Fe) materials as a function of lanthanide radius.*

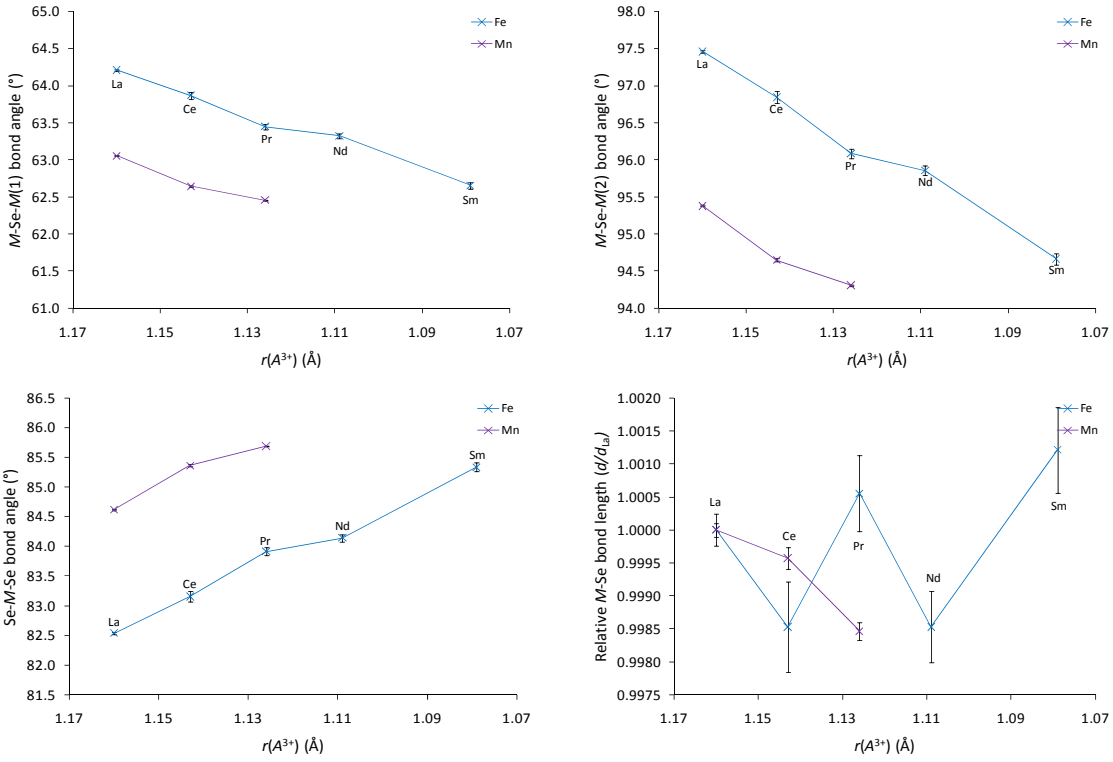

Figure 5.15 *Metal-selenide bond angles (a) M-Se-M(1), (b) M-Se-M(2), (c) Se-M-Se, and (d) relative M-Se bond length, as a function of lanthanide radius.*

5.5.3 Variation of Transition Metal Ion

Figure 5.16a shows the effect of changing transition metal radius on the cell volume of $La_2O_2M_2OSe_2$ materials (M = Mn, $Mn_{0.5}Fe_{0.5}$, Fe, Co), and shows the expected linear increase with increasing transition metal radius. *Figure 5.16b* shows a plot of the *c*/*a* ratio for these materials as a function of transition metal radius, which, unlike that observed on variation of the lanthanide ion, is seen to increase with increasing metal radius. The *c*/*a* ratio of $La_2O_2Mn_2OSe_2$ is again different to that expected. As above plots of inter and intra-layer distances, along with lattice parameters, and all bond lengths and angles, are given in appendix XI.

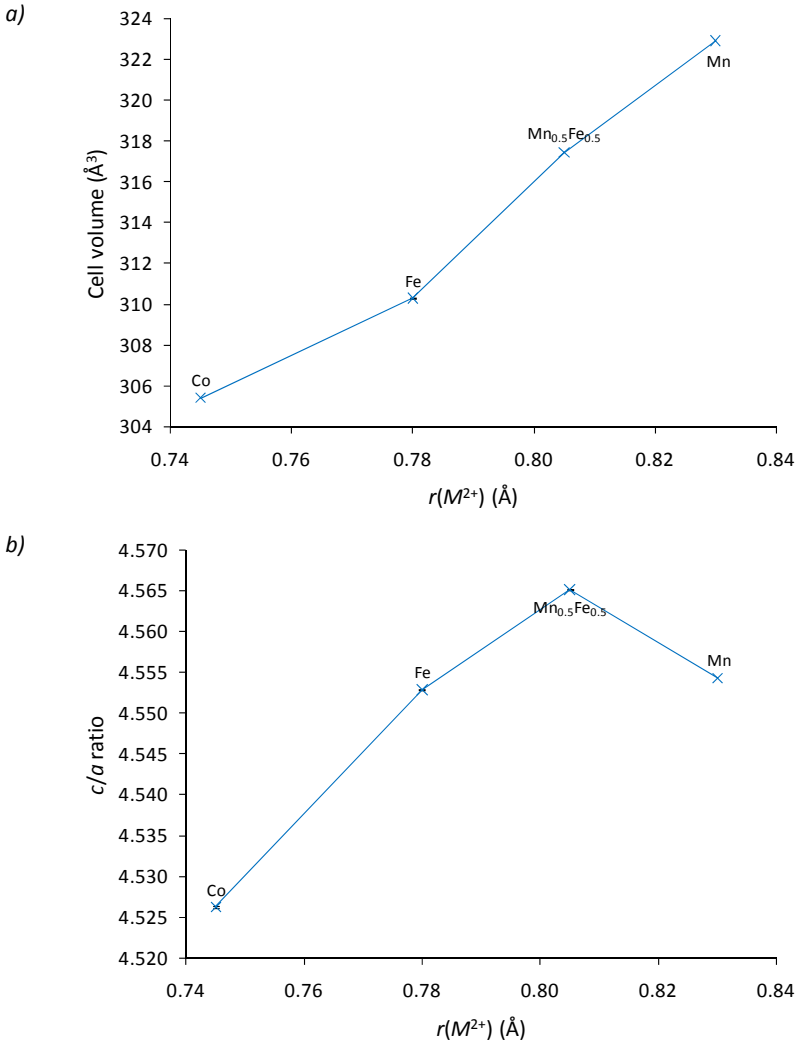

Figure 5.16 *The (a) cell volumes and (b) c/a ratios of $La_2O_2M_2OSe_2$ materials as a function of transition metal radius.*

Figure 5.17 shows the thickness of the lanthanum-oxide and metal-oxychalcogenide layers, and layer separation, as a function of transition metal ion, relative to $La_2O_2Mn_2OSe_2$. The data show that as the size of the transition metal ion, and hence the *a* cell parameter, increases the metal-oxychalcogenide layers get thicker, whilst the lanthanum-oxide layers become shorter along *c* and wider in the *ab* plane. This is presumably driven by the lengthening *M*-Se bond length. The separation of these layers as a function of transition metal radius is also seen to increase, although to a far lesser extent. Both these factors cause *c*/*a* to increase and are only partially compensated by the reduction in width of the $[A_2O_2]^{2+}$ layers.

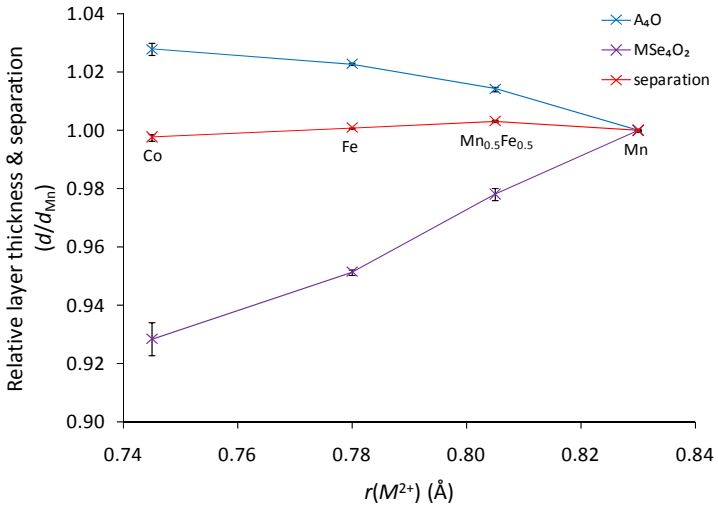

Figure 5.17 *Relative layer thicknesses and separation of $La_2O_2M_2OSe_2$ materials as a function of transition metal radius; A_4O = blue, MSe_4O_2 = purple, separation = red.*

5.5.4 Displacement of the O(2) Ion

As discussed in previous chapters, inspection of thermal displacement parameters for these materials suggests that the O(2) ion is dynamically displaced out of the M^{2+} plane at room temperature and statically displaced at low temperatures, and hence the *M*-O-*M* bond angle distorts away from 180°. One might expect that this would be more pronounced for materials in which the *M*-O-*M* bond is subject to strain, either from decreasing lanthanide, or increasing transition metal, radius. *Table 5.8* gives a summary of the observed U_{iso} parameters O(2) ions in these materials. Note that those derived from X-ray diffraction are less accurate due to the relatively small scattering power of O^{2-} and systematic errors associated with reflection geometry experiments. These values seem to confirm that as the $[A_2O_2]^{2+}$ layers contract and the *a* cell parameter decreases, (the *M*-O bonds become shorter, and more strained) the O(2) ions are more displaced from the *z* = 0.5 plane. The results also show that, for $La_2O_2M_2OSe_2$ materials, as the size of the transition metal is increased, so is the displacement of the O(2) ions. This observation suggests that the distortion of the $[La_2O_2]^{2+}$ layers, brought about by the increase of the transition metal radius, restricts the increase of the *M*-O bonds within the *ab* plane, and consequently the oxide ions are more likely to be displaced above and below the $[M_2O]^{2+}$ layers.

Table 5.8 *O(2) $U_{iso/eq}$ parameters for known $A_2O_2M_2OSe_2$ materials.*

Material	O(2) $U_{iso/eq}$ (100×Å^2)	Measurement
$La_2O_2Mn_2OSe_2$	*3.07(3)*	Neutron
$Ce_2O_2Mn_2OSe_2$	*3.37(4)*	Neutron
$Pr_2O_2Mn_2OSe_2$	*3.71(3)*	Neutron
$La_2O_2Fe_2OSe_2$	*1.17(6)*	Neutron
$Ce_2O_2Fe_2OSe_2$	*2.9(8)*	X-ray
$Pr_2O_2Fe_2OSe_2$	*0.4(4)*	X-ray
$Nd_2O_2Fe_2OSe_2$	*4.1(5)*	X-ray
$Sm_2O_2Fe_2OSe_2$	*7.4(8)*	X-ray
$La_2O_2Co_2OSe_2$	*2.5(1)*	Neutron

5.5.5 Comparison of the Magnetic Structures of $La_2O_2M_2OSe_2$ Materials (*M* = Mn, Fe, Co)

Figure 5.18 shows the magnetic structures observed for $La_2O_2Mn_2OSe_2$, $La_2O_2Fe_2OSe_2$ and $La_2O_2Co_2OSe_2$. Not only do these structures vary for each transition metal involved, the experimental structures of $La_2O_2Fe_2OSe_2$ and $La_2O_2Co_2OSe_2$ also differ to those predicted from theoretical studies; theoretical studies of $La_2O_2Mn_2OSe_2$ have not been reported.[6, 17] The important interactions in these materials are the nearest neighbour (n.n.), J_1, interactions, which involve two direct *M*-*M*, one 90° *M*-O-*M* and two ~64° *M*-Se-*M* interactions per metal ion, and the next nearest neighbour (n.n.n.) interactions, which are split into two ~97° *M*-Se-*M*, J_2, and one 180° *M*-O-*M*, J_2', interaction per metal ion. Goodenough's rules predict each of these interactions to be AFM for each of Mn^{2+}, Fe^{2+} and Co^{2+}.[11]

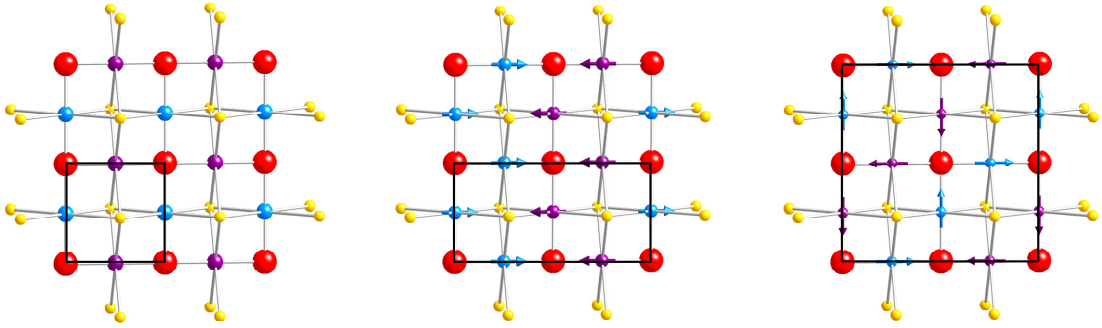

a) $La_2O_2Mn_2OSe_2$ *b) $La_2O_2Fe_2OSe_2$* *c) $La_2O_2Co_2OSe_2$*

Figure 5.18 *Arrangement of the magnetic moments in (a) $La_2O_2Mn_2OSe_2$, (b) $La_2O_2Fe_2OSe_2$ and (c) $La_2O_2Co_2OSe_2$; M = blue/purple, O = red, Se = yellow; magnetic cells are outlined.*

Table 5.9 is a summary of the results from GGA+*U* and LSDA+*U* calculations for both $La_2O_2Fe_2OSe_2$ and $La_2O_2Co_2OSe_2$, and of those for isostructural $Ba_2Se_2Fe_2OSe_2$ and $Sr_2S_2Fe_2OS_2$, performed for U = 3 eV.[18] It can be seen that for $La_2O_2Fe_2OSe_2$ and $La_2O_2Co_2OSe_2$, J_1 is ~-4 meV, J_2 is a small and positive number, and J_2' is large and negative. Note that signs here have been unified such that a negative *J* corresponds to AFM coupling. Work by Zhu *et al.* has produced a phase diagram for $La_2O_2Fe_2OSe_2$ at 0 K (*Figure 5.19*), and shows that three magnetic structures (AFM1, AFM5 & AFM6, *Figure 5.20*) can be adopted depending on the magnitude of the exchange interactions. This work shows that, for small positive values of J_2, the AFM1 arrangement is adopted when $|J_2'|/|J_1| < 1$, and the AFM6 arrangement is adopted when $|J_2'|/|J_1| > 1$. The AFM5 structure is observed when $J_2 < J_2'$ and $|J_2|/|J_1| > 1$, and when $|J_2|/|J_1| < 1$ the AFM6 structure is again adopted. For the $La_2O_2Co_2OSe_2$ system, as U is increased from 2–4 eV $|J_2'|/|J_1|$ remains > 3, whilst for $La_2O_2Fe_2OSe_2$ $|J_2'|/|J_1|$ varies from 2.43 to 0.97 for U = 1.4–4.5 eV, and as such changes the predicted structure from AFM6 to AFM1.

Table 5.9 *Coupling interaction energies calculated for $La_2O_2Fe_2OSe_2$-type materials; negative numbers relate to AFM interactions and positive relate to FM.*

Material	J_1 (meV)	J_2 (meV)	J_2' (meV)	Ref
$La_2O_2Fe_2OSe_2$	*-3.77*	*1.11*	*-4.79*	*17*
$La_2O_2Co_2OSe_2$	*-4.04*	*0.84*	*-12.39*	*6*
$Ba_2Se_2Fe_2OSe_2$	*-2.6*	*2.3*	*-3.5*	*18*
$Sr_2S_2Fe_2OS_2$	*-2.5*	*1.1*	*-4.1*	*18*

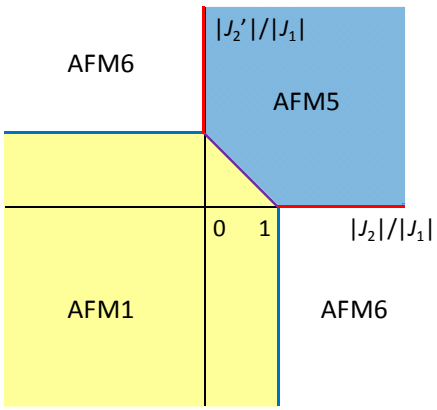

Figure 5.19 *Magnetic phase diagram for $La_2O_2Fe_2OSe_2$ with the AFM1 region shown in yellow, AFM5 shown in blue and AFM6 shown in white, taken from Zhu et al..*[vii]

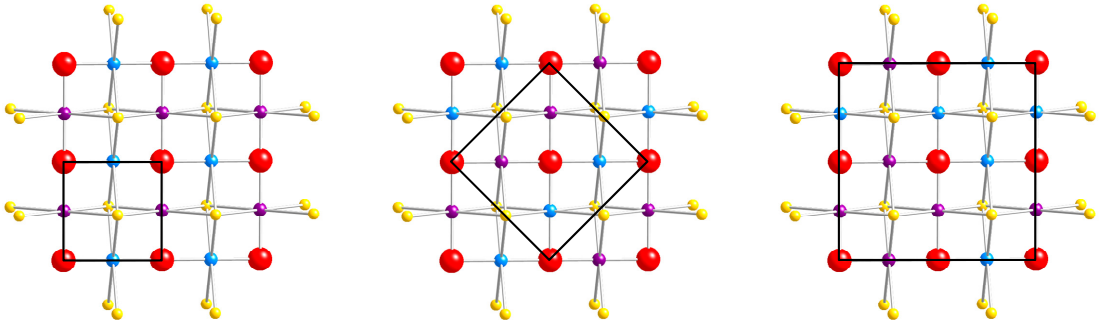

a) AFM1 *b) AFM5* *c) AFM6*

Figure 5.20 *Theoretical magnetic structures for $La_2O_2Fe_2OSe_2$, (a) AFM1, (b) AFM5 and (c) AFM6; Fe = blue/purple, O = red, Se = yellow; magnetic cells are outlined.*

Experimental results show that for $La_2O_2Mn_2OSe_2$ the AFM1 structure is adopted, suggesting that the J_1 interactions dominate, and hence the J_2' interactions are frustrated. Results reported here for $La_2O_2Fe_2OSe_2$ suggest that the material orders with an AFM3 structure, similar to that of $Fe_{1.086}Te$, in which half of all of the interactions are satisfied and half frustrated.[19] In $La_2O_2Co_2OSe_2$, all of the J_2' interactions are satisfied, whilst the J_1 interactions involve moments perpendicular to one another and therefore are all partially frustrated. Note that for $La_2O_2Fe_2OSe_2$ and $La_2O_2Co_2OSe_2$ the experimental results disagree with theory, perhaps because the magnetic cells considered for calculations were too small.

A full understanding of these magnetic structures would require significant theoretical work. Some insight can be gained from chemical considerations, though this is complicated by the variety of potential interaction pathways and their subtle changes as bond lengths and angles are varied. *Table 5.10* shows that the *M-M* bond distance decreases on progression from Mn^{2+} to Fe^{2+} and Co^{2+}, as would be expected from the ionic radii of the metals.[20] Whilst one might expect to see a greater degree of orbital overlap for smaller values of $d_{M\text{-}M}$, contraction of the t_{2g} orbitals with increasing electronegativity competes to make any direct orbital overlap weaker (electronegativities are 1.55 for Mn, 1.83 for Fe and

[vii] Reprinted Figure 5 with permission from J-X. Zhu *et al.*, *Phys. Rev. Lett*, 2010, **104**, 216405. Copyright 2010 by the American Physical Society.

1.88 for Co).[21] On this argument we would expect the strength of the J_1 interactions to increase, as the direct *M*-*M* interactions increase, and hence be strongest in $La_2O_2Mn_2OSe_2$, and decrease in strength from $La_2O_2Fe_2OSe_2$ to $La_2O_2Co_2OSe_2$. If we assume that Goodenough's rule regarding direct cation-cation interactions holds true, then one would expect the J_1 interactions for *M* = Mn to be most strongly AFM.[11] Experimentally we do observe that $La_2O_2Mn_2OSe_2$ adopts the AFM1 structure, in which J_1 interactions are all AFM. For $La_2O_2Co_2OSe_2$ the higher electronegativity would imply weaker direct *M*-*M* interactions yet stronger *M*-O-*M* interactions due to increased covalency. Experimentally J_2' interactions are indeed satisfied in this structure. The coupling interactions in the AFM3 structure adopted by $La_2O_2Fe_2OSe_2$ are all half-satisfied, suggesting that this structure is a compromise between the competing interactions. One might therefore expect that the decrease in lattice parameters observed on variation of the lanthanide ion across the $A_2O_2Fe_2OSe_2$ series, may lead to increased overlap of the Fe^{2+} orbitals, and hence produce a magnetic structure more similar to that of $La_2O_2Mn_2OSe_2$. Studies by Fuwa *et al.*, however, have suggested that $Nd_2O_2Fe_2OSe_2$ orders with $\boldsymbol{k}$ = (½½0) and $Ce_2O_2Fe_2OSe_2$ orders with $\boldsymbol{k}$ = (¼¼0), suggesting more complex magnetic structures.[10] There is clearly a significant body of experimental and theoretical work required to fully understand these complex systems.

Table 5.10 *Selected interatomic distances and bond angles for $La_2O_2M_2OSe_2$ materials at 12 K.*

		$La_2O_2Mn_2OSe_2$	$La_2O_2Fe_2OSe_2$	$La_2O_2Co_2OSe_2$
Bond lengths (Å)	$d_{M\text{-}M}$	*2.92666(1)*	*2.88836(1)*	*2.8708(2)*
	$d_{M\text{-}O}$	*2.06946(1)*	*2.04238(1)*	*2.0300(1)*
	$d_{M\text{-}Se}$	*2.7985(2)*	*2.7172(5)*	*2.6793(1)*
	$d_{A\text{-}O}$	*2.3890(1)*	*2.3794(2)*	*2.3727(1)*
	$d_{A\text{-}Se}$	*3.3524(2)*	*3.3197(4)*	*3.2951(2)*
Bond angles (°)	*M*-Se-*M* (1)	*63.054(6)*	*64.21(1)*	*64.79(3)*
	M-Se-*M* (2)	*95.38(1)*	*97.46(2)*	*98.52(5)*
	Se-*M*-Se	*84.62(1)*	*82.54(2)*	*81.48(5)*
	A-O-*A* (1)	*104.455(4)*	*105.260(9)*	*105.55(2)*
	A-O-*A* (2)	*120.05(1)*	*118.27(2)*	*117.65(5)*

5.6 Conclusions

This chapter describes the preparation of four new materials isostructural with $La_2O_2Fe_2OSe_2$: $Ce_2O_2Fe_2OSe_2$, and three $A_2O_2(Mn_{0.5}Fe_{0.5})_2OSe_2$ phases (*A* = La–Nd). The variable temperature structural properties of $Pr_2O_2Fe_2OSe_2$ have been investigated, and these show similar behaviour to other members of the $A_2O_2Fe_2OSe_2$ family, with a phase transition evidenced by the thermal expansion of the *c* cell parameter at low temperatures. Unlike $Pr_2O_2Mn_2OSe_2$, there was no evidence of peak splitting at low temperature, and also no evidence of peak broadening, however higher quality data would be required to probe any peak broadening present definitively.

Comparison of the successfully prepared $La_2O_2Fe_2OSe_2$-type materials shows that these form over a restricted range of metal radii. The cell volumes for these materials show an approximately linear decrease with decreasing metal radii, although *c*/*a* ratios show that the rate of change of the *c* and *a*

lattice parameters is not always equivalent. These effects have been rationalised based on local bonding requirements.

The magnetic structure of $La_2O_2Co_2OSe_2$ was also investigated, and two statistically equivalent solutions were proposed, labelled $\Gamma_8\Psi_5$ and $\Gamma_8\Psi_6$. These arrangements both contain moments lying in the *ab* plane, and are related by ±90° rotations of the moments. Parallel moments are then seen to order AFM along both *a* and *b*. These results are similar to those previously reported by Withers, however the moments in the plane at $z = ½$ are related by a rotation of 90°. The models here are thus consistent with an equivalent local anisotropy in each layer. Results have also confirmed the high spin nature of the Co^{2+} ion. Comparison of the magnetic structures adopted by $La_2O_2Mn_2OSe_2$, $La_2O_2Fe_2OSe_2$ and $La_2O_2Co_2OSe_2$, suggests that the magnetic structure adopted is critically dependent on the ratio of the J_1 and J_2' interactions, as suggested in theoretical studies by Zhu *et al.*. The structures observed experimentally are not, however, those predicted.

Note that the magnetic structure presented here for $La_2O_2Co_2OSe_2$ was confirmed in a recent publication by Fuwa *et al.*, who also concluded, from electronic structure calculations, that the Co^{2+} moments were directed along the Co-O bonds.[22]

5.7 References

1. N. D. Withers, *Synthesis and Characterisation of New Layered Oxychalcogenide Materials*, Durham University, *Ph.D.*, Durham, 2005.
2. D. G. Free, *Synthesis and Chemistry of New Layered Oxychalcogenides*, Durham University, *M.Chem.*, Durham, 2007.
3. P. Hickey, *Synthesis and Chemistry of New Layered Chalcogenides and Oxychalcogenides*, Durham University, *M.Chem.*, Durham, 2004.
4. J. M. Mayer, L. F. Schneemeyer, T. Siegrist, J. V. Waszczak and B. v. Dover, *Angew. Chem. Int. Ed. Engl.*, 1992, **31**, 1645-1647.
5. A. A. Coelho, *TOPAS Academic: General profile and Structure Analysis Software for Powder Diffraction Data*, Bruker AXS, Karlsruhe, 2010.
6. H. Wu, *Phys. Rev. B*, 2010, **82**, 020410.
7. Y. Fuwa, M. Wakeshima and Y. Hinatsu, *Solid State Commun.*, 2010, **150**, 1698-1701.
8. C. Wang, M.-q. Tan, C.-m. Feng, Z.-f. Ma, S. Jiang, Z.-a. Xu, G.-h. Cao, K. Matsubayashi and Y. Uwatoko, *J. Am. Chem. Soc.*, 2010, **132**, 7069-7073.
9. A. S. Wills, *Physica B*, 2000, **276-278**, 680-681.
10. Y. Fuwa and et al., *J. Phys.: Condens. Matter*, 2010, **22**, 346003.
11. J. B. Goodenough, *Magnetism and the Chemical Bond*, John Wiley & Sons, New York - London, 1963.
12. M. D. Rechtin and B. L. Averbach, *Phys. Rev. B*, 1972, **6**, 4294-4300.
13. B. J. Campbell, H. T. Stokes, D. E. Tanner and D. M. Hatch, *J. Appl. Cryst.*, 2006, **39**, 607-614.
14. O. Schob and E. Parthe, *Acta Cryst.*, 1965, **19**, 214-224.
15. T. Ohtani, M. Hirose, T. Sato, K. Nagaoka and M. Iwabe, *Jpn. J. Appl. Phys.*, 1993, **32 (Suppl. 32-3)**, 316-318.
16. D. O. Charkin, A. V. Akopyan and V. A. Dolgikh, *Russ. J. Inorg. Chem.*, 1999, **44**, 833-837.
17. J. X. Zhu, R. Yu, H. Wang, L. L. Zhao, M. D. Jones, J. Dai, E. Abrahams, E. Morosan, M. Fang and Q. Si, *Phys. Rev. Lett.*, 2010, **104**, 216405.
18. H. Kabbour, E. Janod, B. Corraze, M. Danot, C. Lee, M.-H. Whangbo and L. Cario, *J. Am. Chem. Soc.*, 2008, **130**, 8261-8270.

19. S. Li, C. de la Cruz, F. Q. Huang, Y. Chen, J. W. Lynn, J. Hu, Y. L. Huang, F. C. Hsu, K. W. Yeh, M. K. Wu and P. Dai, *Phys. Rev. B*, 2009, **79**, 054503.
20. R. D. Shannon, *Acta Cryst.*, 1976, **A32**, 751-767.
21. A. L. Allred, *J. Inorg. Nucl. Chem.*, 1961, **17**, 215-221.
22. Y. Fuwa, T. Endo, M. Wakeshima, Y. Hinatsu and K. Choyama, *JACS ASAP Publication*, 2010.

Synthesis and Characterisation of β-$La_2O_2MSe_2$ (*M* = Mn, Fe)

6.1 Introduction

As discussed in the introduction there have been many interesting mixed-anion materials prepared with the ZrCuSiAs structure, the most topical of which are the oxypnictide superconductors. There is also a wide range of oxychalcogenide materials known with this structure and the study of these has been fuelled by their interesting optical and electronic properties. These materials formally contain fluorite-type $[A_2O_2]^{2+}$ layers, separated by anti-fluorite-type $[M_2Q_2]^{2-}$ layers. The most studied oxychalcogenide materials are those containing copper-chalcogenide layers, whilst silver-containing materials have also been reported. In these oxychalcogenides the transition metal formally has a univalent oxidation state. In the oxypnictides the presence of M^{2+} ions (where *M* = Mn–Zn, Ag, Cd, Ru & Os) is balanced by the trivalent pnictide ions, such that the metal-pnictide, $[M_2Pn_2]^{2-}$, layers have the same overall charge as in the oxychalcogenides.[1] Prior to this work there were only two examples of ZrCuSiAs-related oxychalcogenides containing divalent metal ions, $La_2O_2CdSe_2$ and $CeOMn_{0.5}Se$.[2-4] In these materials charge balance is achieved by half-occupation of the metal sites.

In an attempt to prepare potentially interesting new ZrCuSiAs-related oxychalcogenides, in which the transition metal sites are half-occupied, a new oxychalcogenide structure type was formed. In this chapter we will discuss the synthesis, structure solution from X-ray powder diffraction data, and variable temperature structural and magnetic properties, of β-$La_2O_2MnSe_2$. These have since been reported alongside the iron-containing material β-$La_2O_2FeSe_2$ in joint work with Emma McCabe.[5]

6.2 Synthesis and Structure Solution of β-$La_2O_2MnSe_2$

β-$La_2O_2MnSe_2$ was synthesised according to the method outlined in section 2.2.3. This section will discuss the structure solution of β-$La_2O_2MnSe_2$ from laboratory X-ray powder diffraction data, by a combination of charge flipping and direct methods, the refinement of the final model and discussion of the structure obtained. The structure of β-$La_2O_2MnSe_2$ and its relationship with other known oxychalcogenide materials is discussed.

6.2.1 Indexing and Pawley Refinements

β-$La_2O_2MnSe_2$ was synthesised using the technique outlined in section 2.2.3, and the diffraction pattern of the resulting brick-red powder was recorded using the Bruker d8 Advance (“d9”) powder diffractometer. Data were initially collected over the 2θ range 10–90°, in steps of 0.0354° with a collection time of 0.4 s per step (*DGF210*, *d9_03727.raw*). Inspection of these data showed that a crystalline material had been prepared, however the diffraction peaks observed could not be explained by any mixture of known oxide and chalcogenide materials. The pattern could, however, be indexed using TOPAS Academic (TA), which suggested that a cell with dimensions 16.55 × 4.01 × 17.54 Å, and

either *C*222 or *C*222_1 symmetry, explained the observed peaks; several other cells and space groups were also suggested and the results from indexing are given in the e-appendix.[6, 7]

Pawley refinements using the predicted cell and symmetries suggested that the *C*222 and *C*222_1 models both successfully fitted the observed diffraction peaks over the full 2θ range recorded, whilst other suggestions did not. The results of the Pawley refinements in *C*222 and *C*222_1, as well as in *P*222, are shown in *Figure 6.1* and clearly show that centred cells fit the data just as well as the primitive cell. This clearly suggests that *C*-centring is present, and the similarity in the values of R_{wp} achieved by both of the *C*-centred cells suggests that the 2_1 symmetry element of *C*222_1 is also present.

The space group symmetry was further investigated using ExtSym.[8, 9] ExtSym considers *hkl* intensities, obtained from Pawley refinement of a cell in the lowest symmetry group of the crystal system determined from indexing (*i.e.* one with no systematic absences), to predict probable extinction symbols. For *hkl*'s generated by refinement of the indexed cell in *P*222, results suggested that the three most probable extinction symbols were *Cc*--, *C*--2_1 and *C*---, with log-probabilities scores of 305, 298 and 283, respectively (the full output from ExtSym is given in the e-appendix). Pawley refinement using a cell in *Cmc*2_1, which has the *Cc*-- extinction symbol and was one of cells predicted by indexing, was also performed (*Figure 6.1*), however the results suggested that the choice of *C*222_1 was valid.

Note that as all of the peaks in the pattern could be indexed using *C*222_1 symmetry, this suggested that no impurity phases were present. It was therefore assumed that the contents of the cell would be equivalent to that of the target phase, $La_2O_2MnSe_2$. As the calculated cell volume from indexing was approximately eight times larger than that of $CeOMn_{0.5}Se$ (1164 $Å^3$ compared with 147.6 $Å^3$; a factor of 7.9), it was assumed the cell had an overall content of $La_{16}O_{16}Mn_8Se_{16}$.

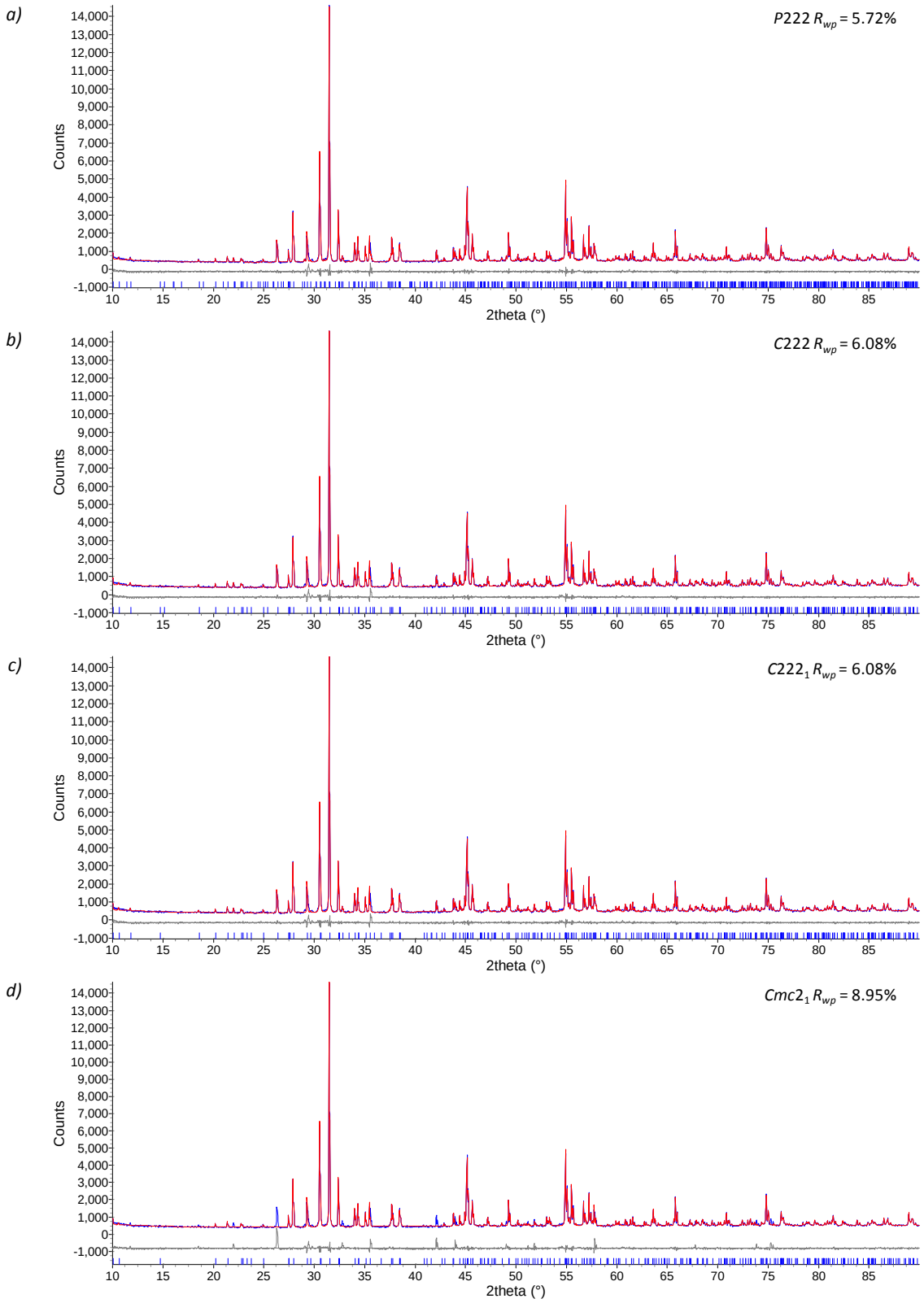

Figure 6.1 *Pawley plots for $La_2O_2Mn_2OSe_2$ at room temperature using (a) P222, (b) C222, (c) $C222_1$ and (d) $Cmc2_1$ symmetry; observed = blue, calculated = red, difference = grey. DGF210, d9_03727.*

6.2.2 Charge Flipping and Direct Methods

After searching the ICSD for materials with similar cell metrics, contents and symmetry to those determined, it was concluded that a new structure type had been prepared, and consequently the arrangement of the atoms within the unit cell was investigated. Two different methods were employed

in the analysis: charge flipping and direct methods.[10, 11] In order to increase the success of these techniques higher quality data were collected, again using the d9 diffractometer, between 5 and 150° 2θ in steps of 0.0205° at a time of 8 s per step (*DGF210*, *d9_03744.raw*). Repetition of the indexing process supported the cell choice, with lattice parameters of 16.55 × 4.01 × 17.54 Å and $C222_1$ or $C222$ symmetry being suggested.

Charge flipping

Charge flipping (section 2.5.5) was performed in TA, with a d_{max} value of 1 Å.[6, 10] Whilst prior knowledge of symmetry is not required for the charge flipping algorithm, it can be built in by the user to increase the speed of structure solution. In addition, if information on the cell contents is included then, following the location of the electron density in the unit cell, atoms can be automatically assigned relative to the electron density present.

Results from repeated charge-flipping runs consistently identified potential positions for the La atoms, whilst there was some ambiguity between the Mn and Se sites due to their similar number of electrons (25 for Mn and 34 for Se). Due to the relatively small electron count of oxygen, O sites were less reliably determined. The structure derived from charge flipping is shown in *Figure 6.2a*, and suggests that the material contains manganese-selenide layers with two distinct Mn sites, separated by layers containing La, O and Se. One of the transition metal sites, Mn(1), appears to be coordinated by four Se and two O atoms, in a distorted octahedral arrangement, and the other, Mn(2), is coordinated by just Se atoms in a distorted trigonal-bipyramidal arrangement. Note that the files used for the charge-flipping routine are given in the e-appendix.

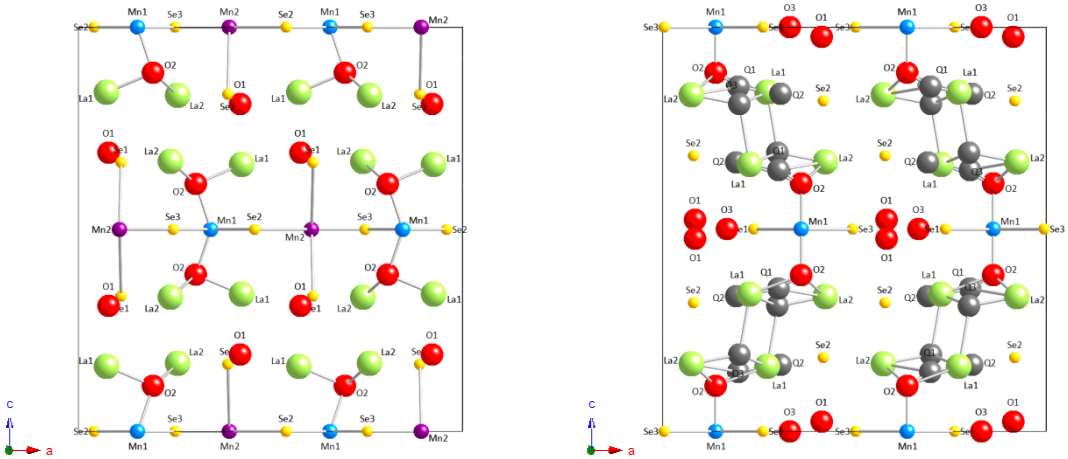

a) charge flipping *b) direct methods*

Figure 6.2 *Structure of β-$La_2O_2MnSe_2$ as determined by (a) charge flipping and (b) direct methods; La = green, Mn = blue, O = red, Se = yellow, Q (unknown atoms) = grey, the unit cell is outlined.*

Direct methods

In order to further clarify the structure obtained from charge flipping, direct methods were employed using the program EXPO (section 2.5.6).[11, 12] EXPO processes extracted structure factor amplitudes by direct methods in order to locate atom positions. Unlike charge flipping, prior knowledge of symmetry is

required, and therefore the same information used in the charge flipping routine was included. The results from this method are shown in *Figure 6.2b*, and are similar to those predicted from charge flipping with Mn/O/Se layers separated by layers of La, O and Se atoms. La positions were the same as proposed by charge flipping and one Mn site (Mn(1)) was similar. Positions of other atoms were less clear and several other areas of electron density were also identified; these are shown by the atoms in grey.

6.2.3 Rietveld Refinements

In order to investigate the results derived from charge flipping and direct methods, trial models were used for Rietveld analysis in TA.[6] The initial refinement of the direct methods model, with fixed thermal displacement parameters, site occupancies and coordinates, gave an R_{wp} of 6.17 % (compared with a value of 3.38 % from a Pawley refinement of the same data). The areas of electron density identified in EXPO as Q(1), Q(2) and Q(3) were described using O atoms. Refinement of thermal displacement parameters for the starting model gave sensible values for the majority of the atoms present, but refined to physically unreasonable values (here limited to B_{iso} = 20 Å^2) for the O(3), Q(1) and Q(2) sites. Inspection of the structure showed that these atom positions sat in close proximity to other ions and they were therefore removed from the refinement. The resulting structure is given in *Figure 6.3a*, and whilst removal of these atoms did result in a slight increase of R_{wp} from 5.15 to 5.27 %, the structure appeared to make more chemical sense.

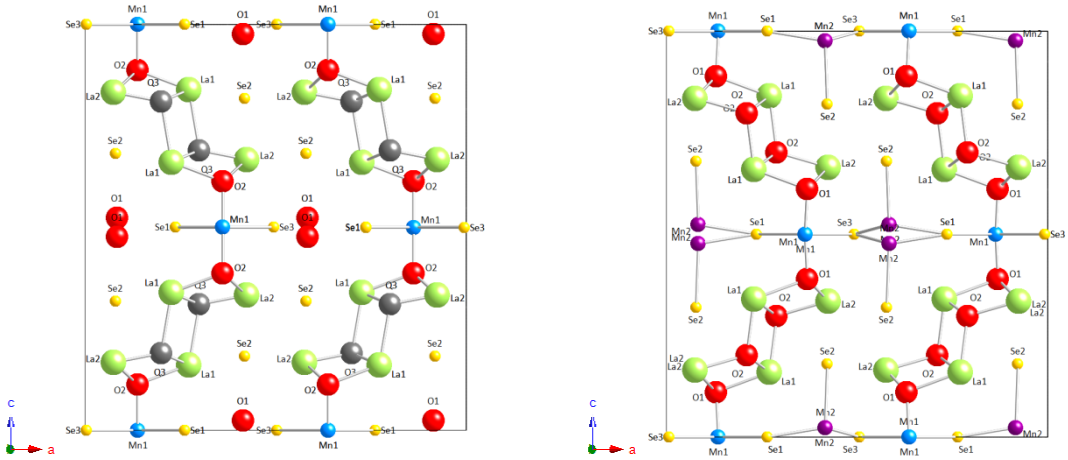

a) after removal of O(3), Q(1) and Q(2) *b) final structure*

Figure 6.3 *Structure of β-$La_2O_2MnSe_2$ (a) after removal of O(3), Q(1) and Q(2) and (b) finally determined; La = green, Mn = blue, O = red, Se = yellow, Q = grey, the unit cell is outlined.*

The main chemically unsatisfying aspect of this model was then the O(1) atom site, which was split above and below the manganese-selenide layers, and surrounded by three Se atoms. Refinement of site occupancies suggested that this O(1) site was predicted as having an occupancy of 1.54 corresponding to ~12 electrons on each site, or ~24 in total across the two neighbouring sites. As it would be unreasonable to find two fully occupied atomic positions in such close proximity, it was assumed that these sites were likely to be two half-occupied Mn sites (with a total of 25 electrons), with the Mn atom randomly disordered above and below the plane at z = 0.5. This assumption is in agreement with the

structure predicted from charge flipping, which contains two Mn sites; one octahedral (Mn(1)) and one pseudo trigonal-bipyramidal (Mn(2)) metal site. At this point it was also assumed that the remaining unknown atom, Q(3), was an O^{2-} ion. The resulting structure is shown in *Figure 6.3b*.

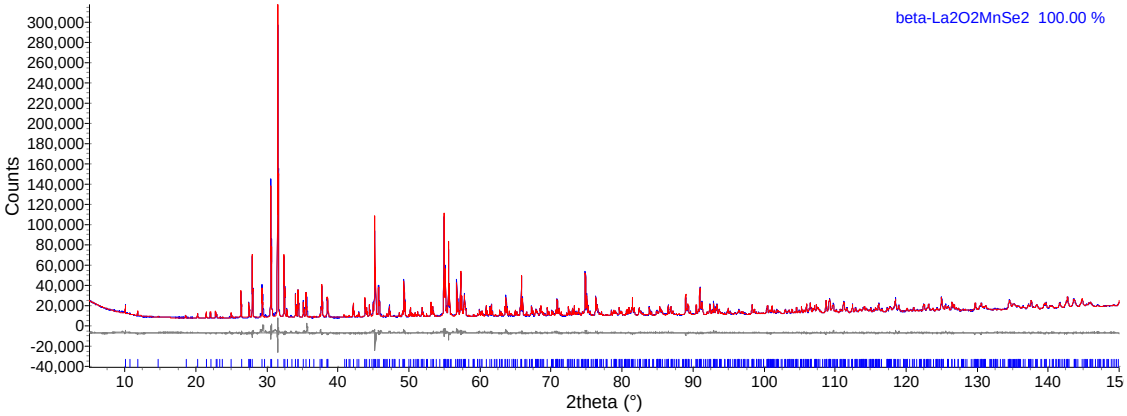

Figure 6.4 *Rietveld plot for β-$La_2O_2MnSe_2$ at room temperature using X-ray data; observed = blue, calculated = red, difference = grey. DGF210, d9_03744.*

The final step in the Rietveld analysis allowed the atomic coordinates to refine, with the Mn(2) site occupancy fixed at 0.5. The resulting fit is given in *Figure 6.4*, and had an R_{wp} of 4.30 %, just 1.08 % larger than that from Pawley refinement.

Neutron data were subsequently collected on HRPD and the final lattice parameters, thermal displacement parameters and atomic coordinates, determined from a combined refinement of X-ray and neutron data, are given in *Table 6.1* and *Table 6.2*, and Rietveld plots for each of the data banks are shown in *Figure 6.5*. An excellent fit is seen for all data sets giving high confidence in the structural model. Note that synthesis of a pure bulk sample for neutron diffraction proved difficult, and hence minor impurity phases are observed in the pattern, not present in the original sample. There was no evidence at room temperature to suggest that the Mn(2) sites were ordered. Refinement of site occupancies on individual atom sites suggested that the material was approximately stoichiometric within the precision of the diffraction data. Fixing the La(1) site occupancy at 1 and allowing other sites to refine gave a refined formula of $La_{1.994(6)}O_{2.06(2)}Mn_{0.99(1)}Se_{2.08(1)}$. Whilst this structural model is basically correct, there are some subtleties which are discussed further on.

Table 6.1 *Lattice parameters and refinement statistics from combined X-ray / neutron Rietveld refinement of β-$La_2O_2MnSe_2$ at 300 K.*

	β-$La_2O_2MnSe_2$
Nuclear symmetry	$C222_1$
a (Å)	*16.54582(8)*
b (Å)	*4.00739(2)*
c (Å)	*17.52752(7)*
V (Å^3)	*1162.172(9)*
N°. variables	*125*
X-ray R_{wp} (%)	*4.82*
HRPD bs R_{wp} (%)	*4.42*
HRPD 90° R_{wp} (%)	*2.60*
HRPD 30° R_{wp} (%)	*9.10*
Total R_{wp} (%)	*4.38*
χ^2	*1.36*

Table 6.2 *Atomic coordinates, occupancies (Occ.) and thermal displacement parameters from combined X-ray / neutron Rietveld refinement of β-$La_2O_2MnSe_2$ at 300K.*

	Wyckoff site	***x***	***y***	***z***	**Occ.**	U_{eq} **(100×Å^2)**
La(1)	*8c*	*0.77042(9)*	*0.009(2)*	*0.15947(8)*	*1*	*0.41(7)*
La(2)	*8c*	*0.5751(1)*	*0.501(1)*	*0.16427(8)*	*1*	*0.45(6)*
Mn(1)	*4a*	*0.6383(3)*	*0*	*0*	*1*	*1.7(3)*
Mn(2)	*8c*	*0.9155(4)*	*0.5*	*0.0232(3)*	*0.5*	*1.4(3)*
Se(1)	*4a*	*0.7641(2)*	*0.5*	*0*	*1*	*0.6(1)*
Se(2)	*8c*	*0.9228(2)*	*0.517(3)*	*0.1801(1)*	*1*	*0.94(9)*
Se(3)	*4a*	*0.5080(2)*	*0.5*	*0*	*1*	*0.6(1)*
O(1)	*8c*	*0.6291(3)*	*0.007(5)*	*0.1129(2)*	*1*	*0.4(1)*
O(2)	*8c*	*0.7096(2)*	*0.515(4)*	*0.2053(2)*	*1*	*0.2(1)*

U_{ij} values and other information are given in appendix XII.

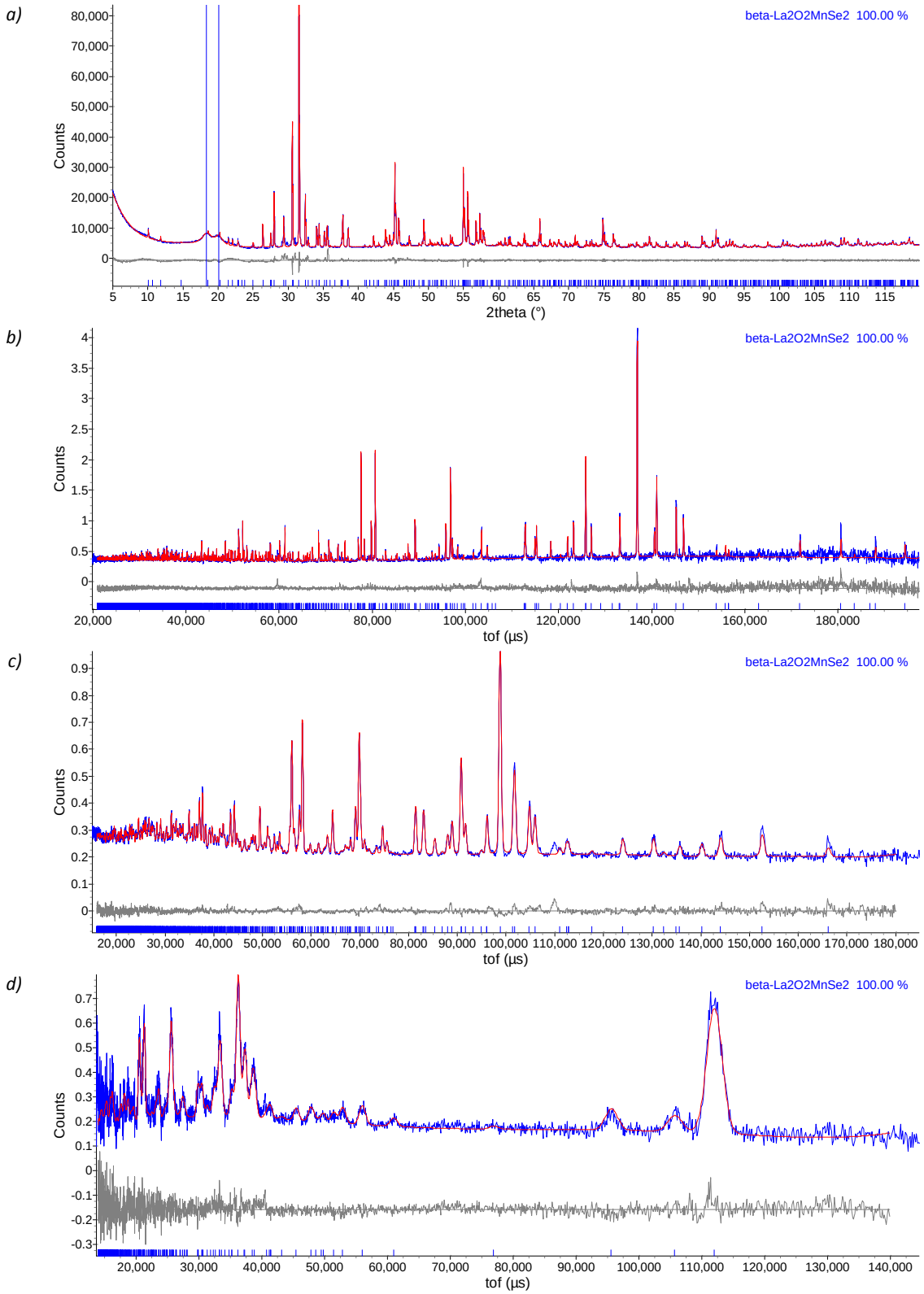

Figure 6.5 *Rietveld plots for β-$La_2O_2MnSe_2$ at room temperature using (a) X-ray, (b) HRPD bs, (c) 90° and (d) 30° bank data; observed = blue, calculated = red, difference = grey. DGF242, d9_04152, hrp45431.*

6.2.4 Structure Description

The final structure is shown in *Figure 6.6*, and has cell contents of $La_{16}O_{16}Mn_8Se_{16}$, which is equivalent to the target composition $La_2O_2MnSe_2$. The difference in structure between this and ZrCuSiAs-related materials has led us to term the material β-$La_2O_2MnSe_2$. The structure can be described by

manganese-selenide layers separated by $La_4O_4Se_3$-type lanthanum-oxyselenide layers. The origin of the difference between this structure and that adopted by the layered oxychalcogenides and oxypnictides will be discussed.

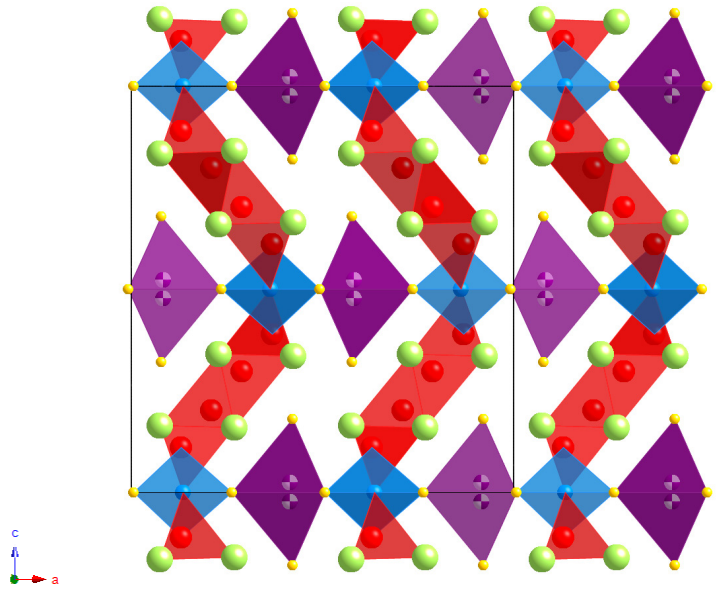

Figure 6.6 *Structure of β-$La_2O_2MnSe_2$; La = green, Mn(1) = blue, Mn(2) = purple; O = red, Se = yellow, the unit cell is outlined; the purple/white colour of the Mn(2) sites shows they are half-occupied.*

The manganese-selenide layers contain Mn^{2+} ions in two different coordination environments, labelled Mn(1) and Mn(2). The Mn(1) site is octahedrally coordinated by four Se^{2-} and two O^{2-} ions. These octahedra then share edges to form chains of edge-sharing octahedra running along the *b* axis (*Figure 6.7a*). The Mn(2) site is best described by two, distorted, face-sharing $MnSe_4$ tetrahedra, in which the Mn^{2+} sites are half-occupied (*Figure 6.7a*). An alternative description, however, is as a distorted trigonal-bipyramid in which the Mn^{2+} site is randomly distributed above or below the trigonal plane. The low temperature ordering of Mn(2), section 6.3, leads us to favour the former description. These tetrahedra, or trigonal-bipyramids, then share corners to produce chains of corner sharing polyhedra, again extending along the *b* axis. These chains are arranged such that they share edges with one adjacent chain of MnO_2Se_4 octahedra, and corners with the remaining octahedral chain; best viewed in *Figure 6.7a*. The octahedrally coordinated Mn^{2+} sites are similar to those observed in materials such as $Gd_4O_4TiSe_4$, and the tetrahedrally coordinated Mn^{2+} sites are similar to those observed in hexagonal MnSe, which is composed of networks of distorted corner-sharing $MnSe_4$ tetrahedra, in which the Mn^{2+} ions lie away from the tetrahedral body centre (*Figure 6.7b*).[13, 14]

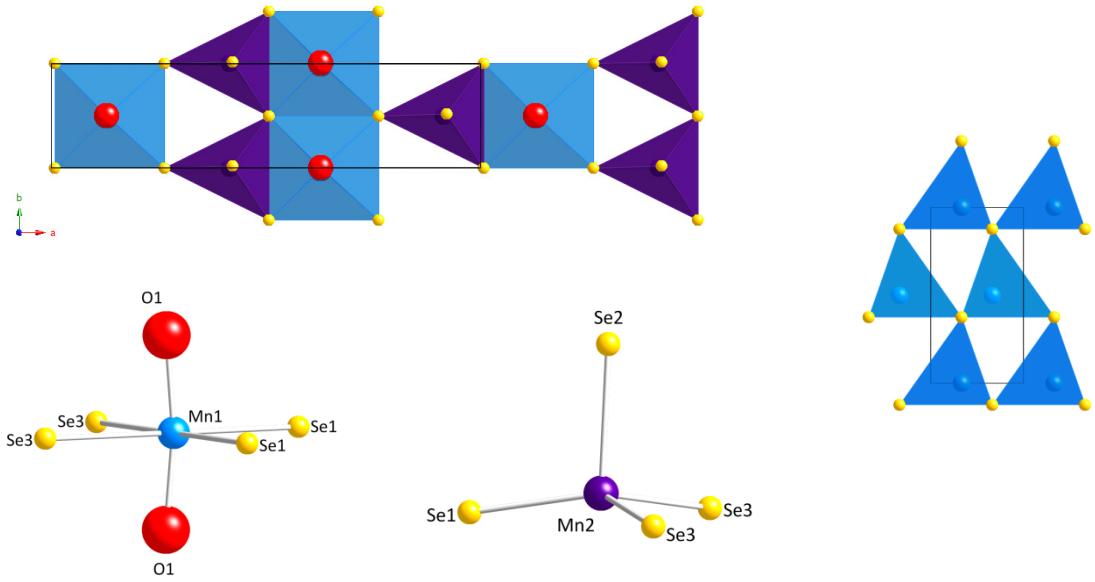

a) β-$La_2O_2MnSe_2$ *b) MnSe*

Figure 6.7 *Coordination of the Mn^{2+} ions in (a) β-$La_2O_2MnSe_2$ and (b) MnSe; Mn(1) = blue, Mn(2) = purple, O = red, Se = yellow.*

The lanthanum-oxychalcogenide layers (*Figure 6.8*) contain fragments of the $[La_2O_2]^{2+}$ layers observed in a large range of oxychalcogenide materials, four La atoms across ($4A_4O$) and extending along the *b* axis. Se^{2-} ions then complete the coordination sphere of the La^{3+} ion producing an arrangement comparable to the structure of $La_4O_4Se_3$ (*Figure 6.8*).[15] These layers are then separated by the manganese-selenide layers such that the $[La_2O_2]^{2+}$ fragments are arranged in a zigzag fashion. $[La_2O_2]^{2+}$ fragments are connected via the octahedrally coordinated transition metal ion, as observed in $Gd_4O_4TiSe_4$.[13]

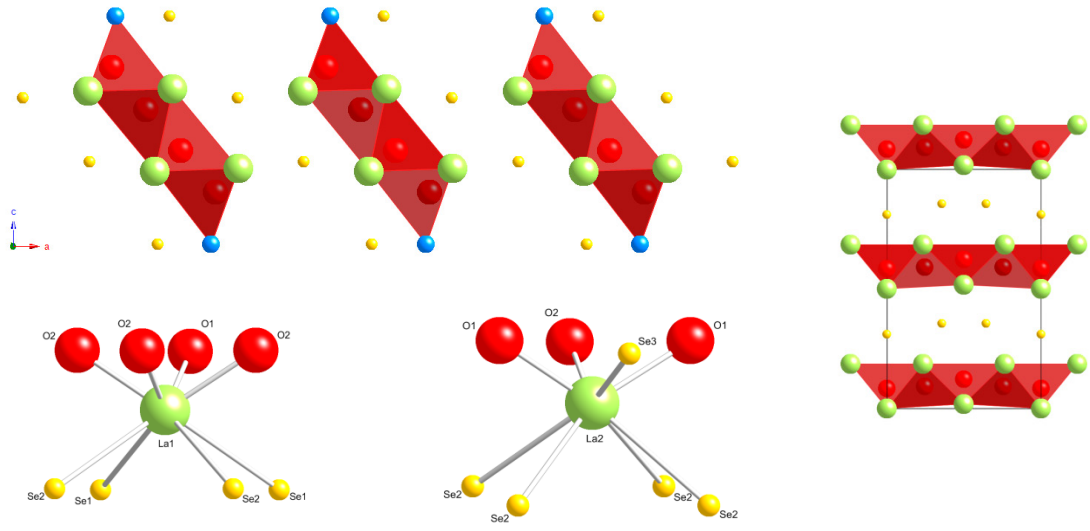

a) β-$La_2O_2MnSe_2$ *b) $La_4O_4Se_3$*

Figure 6.8 *Coordination of the La^{3+} ions in (a) β-$La_2O_2MnSe_2$ and (b) $La_4O_4Se_3$; La = green, O = red, Se = yellow.*

The structure is very similar to that observed for $Gd_4O_4TiSe_4$, where $La_4O_4Se_3$-like layers are connected in a parallel fashion by TiO_2Se_4 octahedra (*Figure 6.9*). In this case, however, the tetrahedral transition metal sites, Mn(2), observed in β-$La_2O_2MnSe_2$ are unoccupied, as the overall charge is balanced by the

tetravalent Ti^{4+} ion. It is therefore not unreasonable to assume that the occupancy of these sites in β-$La_2O_2MnSe_2$ causes the $[La_2O_2]^{2+}$ fragments to align in a zigzag fashion.

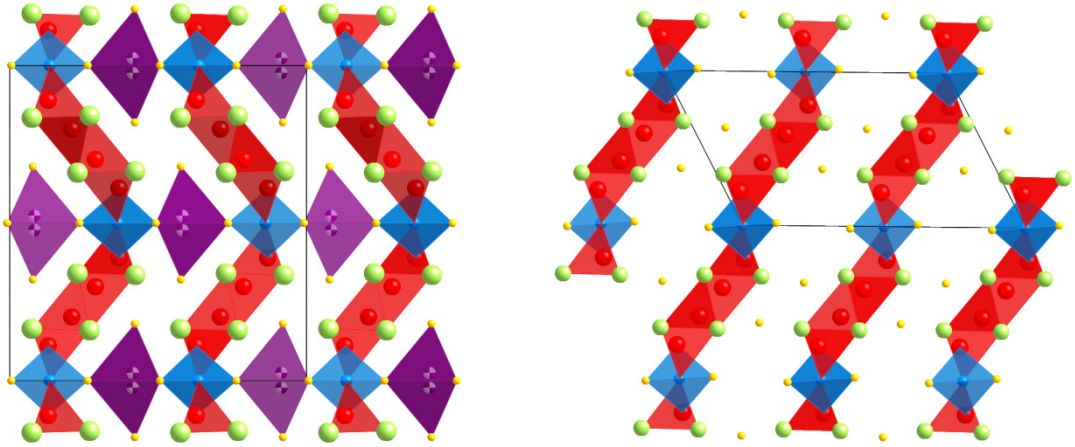

a) β-$La_2O_2MnSe_2$ *b) $Gd_4O_4TiSe_4$*

Figure 6.9 *Comparison of the structures of (a) β-$La_2O_2MnSe_2$ and (b) $Gd_4O_4TiSe_4$; La/Gd = green, Mn(1)/Ti = blue, Mn(2) = purple, O = red, Se = yellow, unit cells are outlined.*

The reason for the remarkable difference between this structure and that adopted by ZrCuSiAs-related $CeOMn_{0.5}Se$ is correctly not understood. It is assumed, however, that larger size of the La^{3+} ion, compared with that of Ce^{3+}, is important. The two structures can be compared by considering breaking of the $[A_2O_2]^{2+}$ layers of $CeOMn_{0.5}Se$ into smaller $4A_4O$ wide fragments, which then rotate by ~48°, such that the terminal O^{2-} sites coordinate with every fourth (previously half-occupied) transition metal site. The coordination of the La^{3+} ions is then retained by displacement of Se^{2-} ions into sites previously half-occupied by Mn^{2+} ions, forming octahedrally and tetrahedrally coordinated Mn^{2+} sites.

Note that structure can be alternatively described by the separation of O^{2-} and Se^{2-} ions into La/Mn(1) and Mn(2) layers, respectively, running perpendicular to *a*.

6.3 Variable Temperature Structural Studies

Variable temperature powder diffraction data were collected for β-$La_2O_2MnSe_2$ on HRPD at the ISIS facility, over the temperature range 6 to 366 K, and backscattering bank data were analysed using the local routine *multitopas*. *Figure 6.10* shows the change in *a*, *b* and *c* cell parameters as a function of temperature; a plot of cell volume as a function of temperature is given in appendix XII. Whilst the thermal expansion of the *b* cell parameter appears to be fairly constant, a distinct phase transition is observed in the *a* and *c* cell parameters at ~300 K. This is most evident in *c*, which on cooling below 300 K begins to increase, until reaching a maximum at ~160 K, after which it begins to decrease again. The transition is observed as a more subtle change in gradient in the *a* cell parameter.

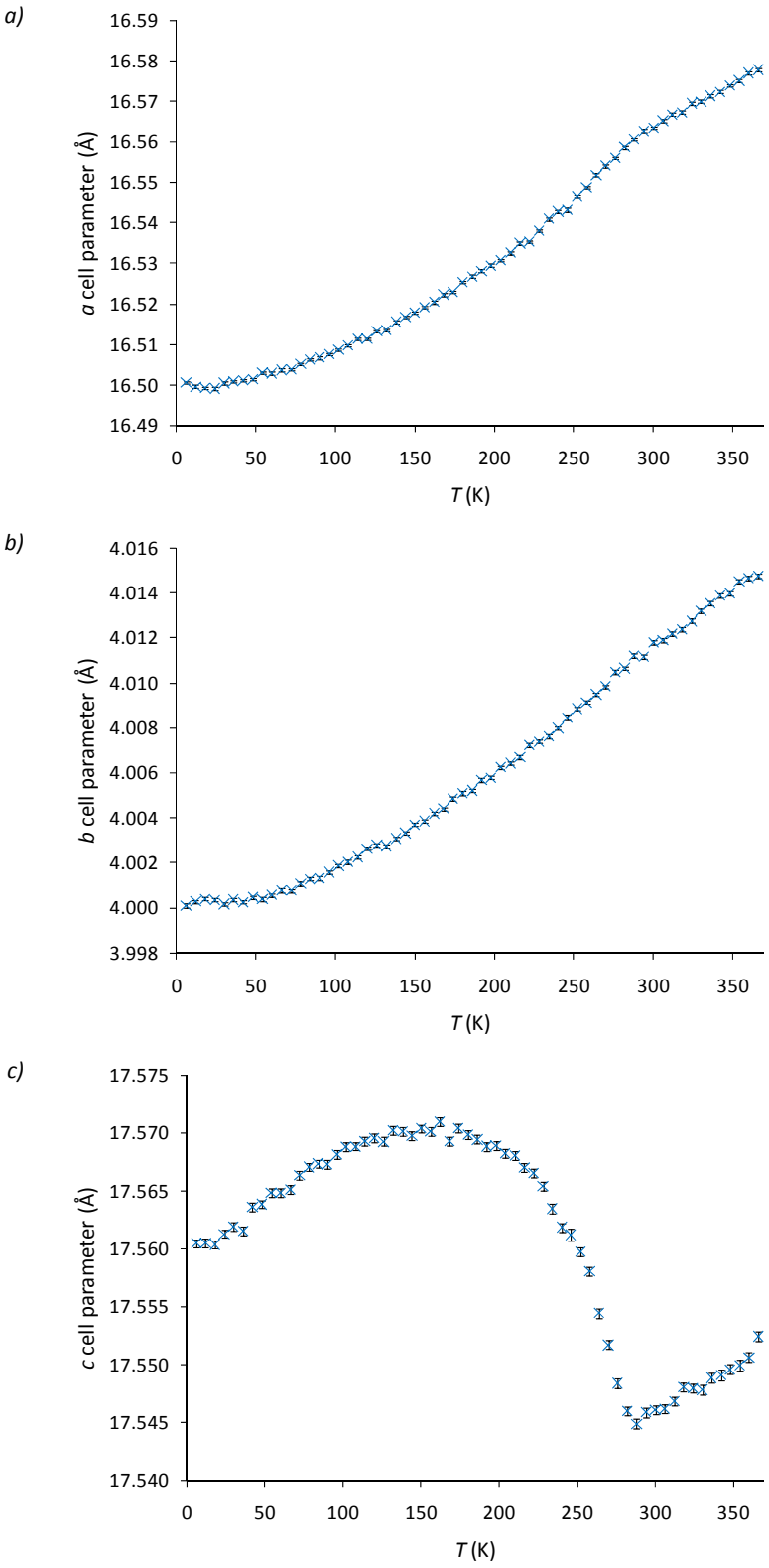

Figure 6.10 *The (a) a (b) b and (c) c cell parameters for* β-$La_2O_2MnSe_2$ *as a function of temperature.*

Investigation of thermal displacement parameters (*Figure 6.11*) shows that the thermal displacement of both Mn(1) and Mn(2) is relatively larger than the other atoms present at room temperature. Values of U_{iso} for these sites, however, do appear to decrease to roughly similar values of the other atoms sites on cooling. There is however a lot of scatter observed in the refined values from these relatively short data collections, reflected in the large error bars.

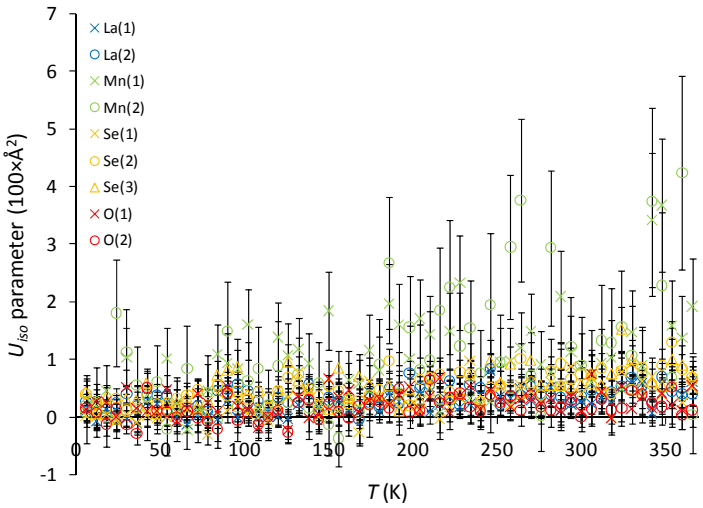

Figure 6.11 *Thermal displacement parameters for β-$La_2O_2MnSe_2$ as a function of temperature.*

Close inspection of high quality neutron and X-ray diffraction data collected at 12 K, showed the presence of an extra reflection at 0.99 Å (~21° 2θ) (*Figure 6.12*). Variable temperature X-ray powder diffraction data, collected over the range 19 to 24° 2θ (*Figure 6.13*), show that this peak appears below approximately 270 K. Collection of X-ray data over a similar range on warming suggested that this transition was fully reversible. Work by Emma McCabe has demonstrated that the appearance of this peak is consistent with ordering of the Mn(2) sites, and distortion mode refinements have shown that the Mn(2) site ordering can be described with the Y3 irreducible representation, giving the structure shown in *Figure 6.14*.[5] It is thought that the change in bonding brought about by the ordering of these Mn(2) is what drives the structural distortion observed in the *c* cell parameter. Emma shows that the ordered low temperature structure has *Pna*2_1 symmetry, and therefore *Ama*2 parent symmetry was adopted for the final room temperature structure reported in the literature; note that *Pna*2_1 is a maximal subgroup of *Ama*2. The final atomic coordinates in this description differ insignificantly from those discussed above. Note also that *Ama*2 has the *A*--*c* extinction symbol (non-standard setting of *Cc*--), which, as discussed earlier, was suggested as a probable extinction symbol by EXPO. Investigation of the amplitude of the Y3 occupancy mode as a function of temperature confirmed ordering of the Mn(2) sites below 270 K is responsible for the phase transition. Full details for the final atomic coordinates, occupancies and thermal displacement parameters for the material at room temperature and 12 K, and the ordering of the Mn(2) ions are given in the literature.[5]

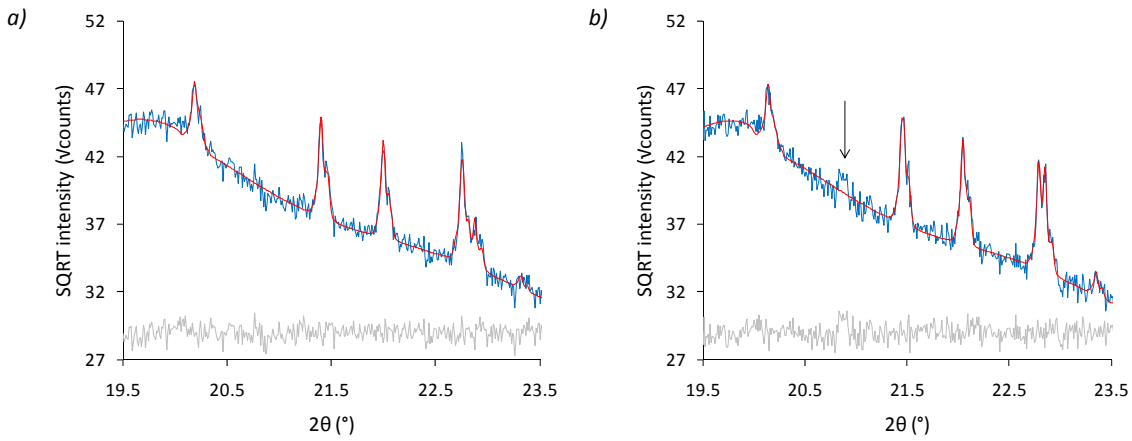

Figure 6.12 *Rietveld plots at (a) 295 and (b) 12 K highlighting the appearance of the superstructure peak at 0.99 Å for β-$La_2O_2MnSe_2$; observed = blue, calculated = red, difference = grey. DGF210, d9_03922.*

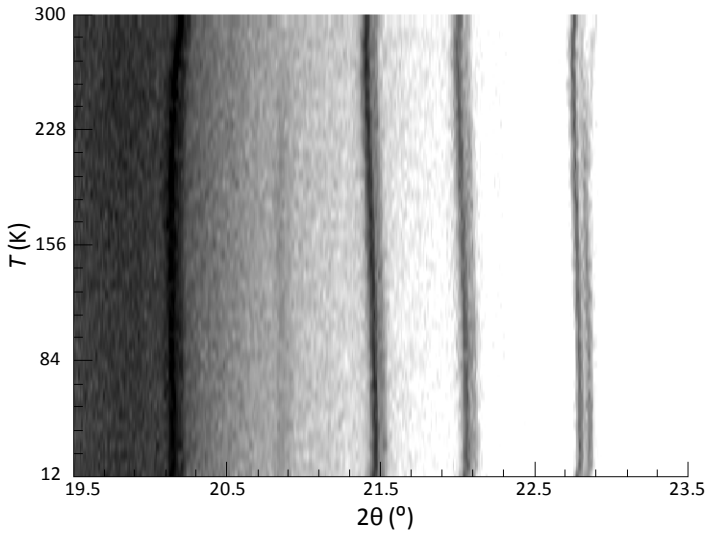

Figure 6.13 *Psuedo-film plot showing the evolution of the superstructure peak at ~21° as a function of temperature in β-$La_2O_2MnSe_2$; plot shows the 19.5–23.5° 2ϑ region of the X-ray data. DGF210, d9_03922.*

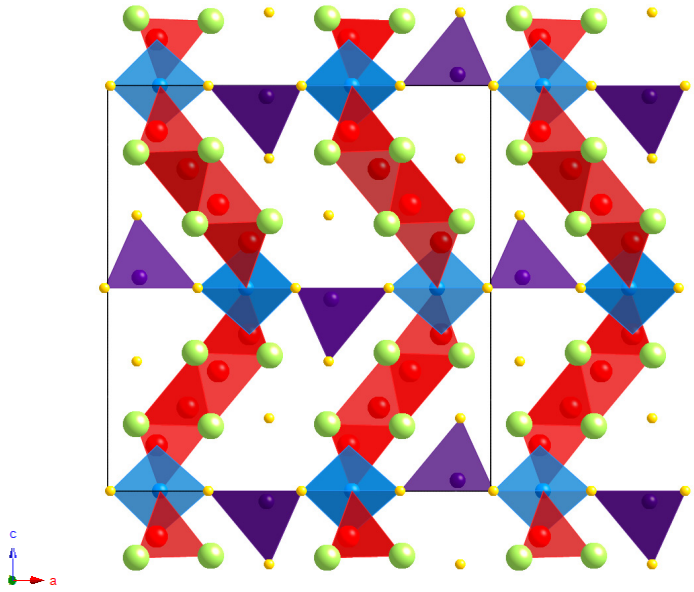

Figure 6.14 *Low temperature structure of β-$La_2O_2MnSe_2$; La = green, Mn(1) = blue, Mn(2) = purple; O = red, Se =*

yellow, the unit cell is outlined.

6.4 Magnetic Properties

In order to investigate the magnetic properties of β-$La_2O_2MnSe_2$, magnetic susceptibility data were collected using a SQUID magnetometer, with the routines outlined in section 2.6.3. *Figure 6.15* shows the magnetisation of β-$La_2O_2MnSe_2$ as a function of applied magnetic field at room temperature. These data suggest that the material is paramagnetic at room temperature, with a calculated moment of 4.36 μ_B per atom, smaller than that expected for a high spin Mn^{2+} ion (5.92 μ_B).

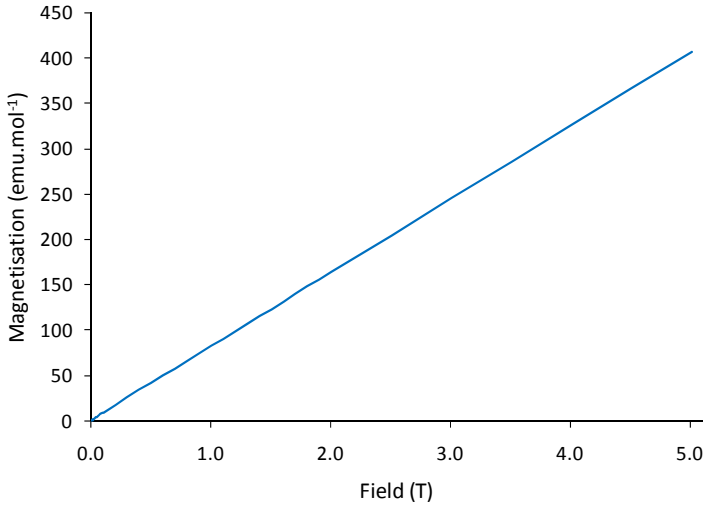

Figure 6.15 *Magnetisation as a function of applied magnetic field at 292 K for β-$La_2O_2MnSe_2$.DGF210ii.*

Figure 6.16 shows the field cooled (FC) and zero-field cooled (ZFC) data, which were collected between 2 and 292 K in 5 K increments, with an applied field of 1000 Oe. These data show that material orders antiferromagnetically with a T_N of ~30 K. A Curie-Weiss fit of the 150–300 K data gave a moment of 5.73 μ_B, which is similar to that expected, and Weiss constant of -154 K.

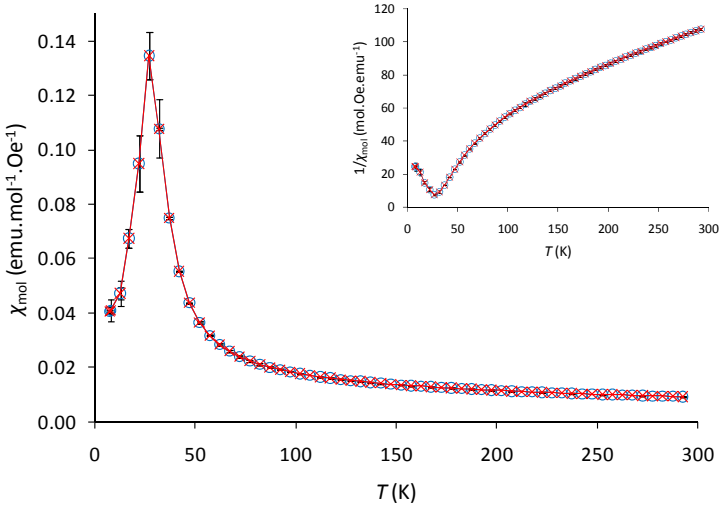

Figure 6.16 *Magnetic susceptibility as a function of temperature for both FC and ZFC experiments on β-$La_2O_2MnSe_2$ with an applied field of 1000 Oe; FC = red, ZFC = blue; inset is inverse susceptibility. DGF210ii.*

Figure 6.17 shows low temperature neutron data recorded by the 30° bank on HRPD. Whilst a new peak is observed at 6.30 Å, and a shoulder is observed on the peak at 7.46 Å, it was not possible to determine any information of the magnetic structure of the material from these features, suggesting that the Mn^{2+} ions are ordered with an incommensurate structure at 12 K.

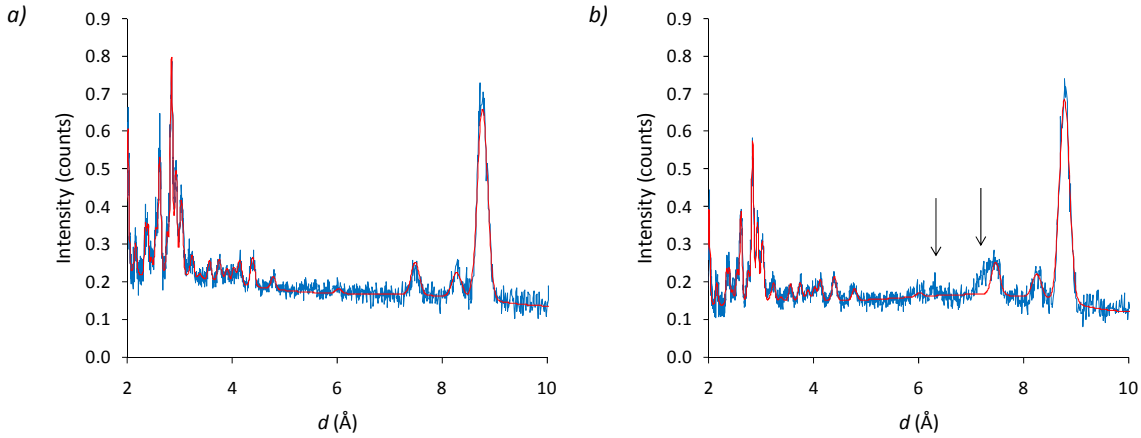

Figure 6.17 *Rietveld plots at (a) 295 and (b) 12 K highlighting the appearance of possible magnetic features at 6.30 and 7.46 Å in the 30° bank HRPD data for β-$La_2O_2MnSe_2$; observed = blue, calculated = red. DGF242, hrp45431 & hrp45369, respectively.*

6.5 β-$La_2O_2FeSe_2$

Further work on the β-$La_2O_2MnSe_2$ family also lead to the preparation of β-$La_2O_2FeSe_2$, and this has been reported in a joint publication with Emma McCabe.[5] High resolution powder diffraction data collected on HRPD at ISIS, and X-ray data collected in house, showed that a material isostructural to β-$La_2O_2MnSe_2$ had been prepared. Close inspection of the data showed that the superstructure peak observed in β-$La_2O_2MnSe_2$ on cooling at 21° 2θ, was present at room temperature in β-$La_2O_2FeSe_2$. This work also showed that the transition metal sites at room temperature ordered in a similar fashion to those in β-$La_2O_2MnSe_2$ below 270 K, via the Y3 occupancy mode. Variable temperature studies demonstrated that the behaviour of the *c* cell parameter of β-$La_2O_2FeSe_2$ follows a similar trend to that of β-$La_2O_2MnSe_2$, although the transition observed at 270 K for the manganese-containing material is observed at the higher temperature of 380 K. This again is consistent with the disorder of the transition metal sites at high temperature.

Similar to β-$La_2O_2MnSe_2$, magnetic susceptibility data collected for β-$La_2O_2FeSe_2$ by Emma McCabe, showed that the material also orders antiferromagnetically on cooling (T_N = 90 K).[5] Neutron data collected at 12 K show evidence for this ordering, with additional peaks observed at 4.53, 4.64, 6.83 and 7.40 Å (*Figure 6.18*). Attempts to index these reflections have been unsuccessful, and therefore the arrangement of the moments in this material is not known. The position of the more intense peaks is similar to those observed for β-$La_2O_2MnSe_2$ (6.30 and 7.46 Å), suggesting that these materials have a similar magnetic structure. Work by Emma McCabe has modelled the intensity of these peaks and demonstrated that they appear below ~90 K, consistent with T_N from susceptibility studies, confirming their likely magnetic origin.

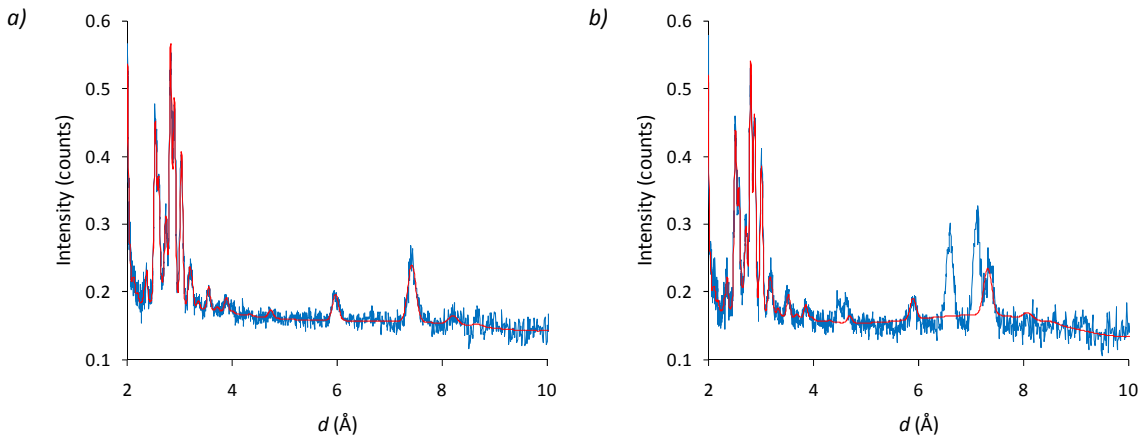

Figure 6.18 *Rietveld plots at (a) 295 and (b) 12 K highlighting the appearance of possible magnetic features at 4.53, 4.64, 6.83 and 7.40 Å in the 30° bank HRPD data for β-$La_2O_2FeSe_2$; observed = blue, calculated = red. DGF233 hrp46218 & hrp45585, respectively.*

6.6 Optical and Electronic Properties

Work by Emma McCabe demonstrated that at room temperature β-$La_2O_2MnSe_2$ was highly insulating (resistance in excess of 6 GΩ), whilst β-$La_2O_2FeSe_2$ was semiconducting with ρ = 10^2 Ωcm.[5] Analysis of data collected between 150 and 300 K gave an activation energy of 0.35 eV for β-$La_2O_2FeSe_2$, suggesting an electronic band gap of 0.70 eV. The resistivity reported for β-$La_2O_2FeSe_2$ (10^2 Ωcm) is similar to that reported for $La_2O_2Fe_2OSe_2$ (10^3 Ωcm) and much larger than those reported for FeSe and LaOFeP (~6×10^{-4} and ~2.5×10^{-4} Ωcm, respectively)[16-18] The electronic band gap calculated for β-$La_2O_2FeSe_2$ (1.1(1) eV) also compares well with that calculated for $La_2O_2Fe_2OSe_2$ (0.19 eV).[19] Optical studies by Emma McCabe for β-$La_2O_2MnSe_2$ suggested an optical band gap of 1.6(1) eV which is comparable to that of $CeOMn_{0.5}Se$ (2.01 eV).[4]

6.7 Conclusions

A new oxychalcogenide structure type has been reported, and is termed β-$La_2O_2MSe_2$ (*M* = Mn, Fe). The structure of β-$La_2O_2MnSe_2$ was solved using a combination of indexing, charge flipping, direct methods and Rietveld refinement, and was found to be similar to that of $Gd_4O_4TiSe_4$, with $La_4O_4Se_3$-type layers separated by a transition metal selenide layer, in which the metal sites are found in two different coordination environments. The first site, *M*(1), is octahedrally coordinated by four Se^{2-} and two O^{2-} ions, and the second, Mn(2), is tetrahedrally coordinated by four Se^{2-} ions. At room temperature, however, the Mn(2) ions are disordered between two adjacent face-sharing tetrahedra. The $La_4O_4Se_3$-type layers consist of $[La_2O_2]^{2+}$ fragments which are joined by the octahedrally coordinated Mn^{2+} ion in a zigzag fashion.

Variable temperature studies have shown that the Mn(2) sites order on cooling, which is apparent by the appearance of a peak at 21° 2θ, and a change in the thermal expansion of the *c* cell parameter. The ordering of these sites has been described in a joint publication with McCabe.[5]

Magnetic susceptibility data have shown that both materials order AFM on cooling, with Néel temperatures of 35 and 90 K, for the manganese and iron-containing materials, respectively. Neutron data have supported this by the appearance of new peaks on cooling, not present in the X-ray data, however there is insufficient information to model the ordering of the Mn^{2+} moments.

6.8 References

1. R. Pottgen and D. Johrendt, *Z. Naturforsch*, 2008, **63b**, 1135-1148.
2. H. Hiramatsu, K. Ueda, T. Kamiya, H. Ohta, M. Hirano and H. Hosono, *J. Phys. Chem. B*, 2004, **108**, 17344-17351.
3. H. Hiramatsu, K. Ueda, T. Kamiya, H. Ohta, M. Hirano and H. Hosono, *J. Mater. Chem.*, 2004, **14**, 2946-2950.
4. I. Ijjaali, K. Mitchell, C. L. Haynes, A. D. McFarland, R. P. van Duyne and J. A. Ibers, *J. Solid State Chem.*, 2003, **176**, 170-174.
5. E. E. McCabe, D. G. Free, B. Mendis, J. Higgins and J. S. O. Evans, *Chem. Mater.*, 2010, **22**, 6171-6182.
6. A. A. Coelho, *TOPAS Academic: General profile and Structure Analysis Software for Powder Diffraction Data*, Bruker AXS, Karlsruhe, 2010.
7. A. A. Coelho, *J. Appl. Cryst.*, 2003, **36**, 86-95.
8. A. J. Markvarsden, K. Shankland, W. I. F. David, J. Johnston, R. M. Ibberson, M. Tucker, H. Nowell and T. Griffin, *J. Appl. Cryst.*, 2008, **41**, 1177-1181.
9. A. J. Markvardsen, W. I. F. David, J. C. Johnson and K. Shankland, *Acta Cryst.*, 2001, **A57**, 47-54.
10. G. Oszlanyi and A. Suto, *Acta Cryst.*, 2004, **A60**, 134-141.
11. A. Altomare, G. Cascarano, C. Giacovazzo, A. Guagliardi, M. C. Burla, G. Polidori and M. Camalli, *J. Appl. Cryst.*, 1994, **27**, 435-436.
12. A. Altomare, M. C. Burla, G. Cascarano, C. Giacovazzo, A. Guagliardi, A. G. G. Moliterni and G. Polidori, *J. Appl. Cryst.*, 1995, **28**, 842-846.
13. A. Meerschaut, A. Lafond, V. Meignen and C. Deudon, *J. Solid State Chem.*, 2001, **162**, 182-187.
14. A. Baroni, *Z. Kristallogr., Kristallgeom., Kristallphys., Kristallchem.*, 1938, **99**, 336-339.
15. J. Dugue, C. Adolphe and P. Khodadad, *Acta Cryst.*, 1970, **B26**, 1627-1628.
16. J. M. Mayer, L. F. Schneemeyer, T. Siegrist, J. V. Waszczak and B. v. Dover, *Angew. Chem. Int. Ed. Engl.*, 1992, **31**, 1645-1647.
17. S. Margadonna, Y. Takabayashi, M. T. McDonald, K. Kasperkiewicz, Y. Mizuguchi, Y. Takano, A. N. Fitch, E. Suard and K. Prassides, *Chem. Commun.*, 2008, 5607-5609.
18. Y. Kamihara, H. Hiramatsu, M. Hirano, K. Kawamura, H. Yanagi, T. Kamiya and H. Hosono, *J. Am. Chem. Soc.*, 2006, **128**, 10012-10013.
19. J. X. Zhu, R. Yu, H. Wang, L. L. Zhao, M. D. Jones, J. Dai, E. Abrahams, E. Morosan, M. Fang and Q. Si, *Phys. Rev. Lett.*, 2010, **104**, 216405.

Synthesis and Characterisation of two new ZrCuSiAs-type Materials

7.1 Introduction

As discussed in the previous chapter there are only two known examples of ZrCuSiAs-related oxychalcogenides that contain a divalent, rather than monovalent, metal ion in their chalcogenide layer: $La_2O_2CdSe_2$ and $CeOMn_{0.5}Se$ (*Figure 7.1*).[1-3] Unlike in the oxypnictide materials, where it is the Pn^{3-} ions that balance the excess transition metal charge, in these material charge balance is achieved by half-occupation of the metal sites in the chalcogenide layers, *i.e.* $[MSe_2]^{2-}$. In known $CeOMn_{0.5}Se$ the transition metal ions are randomly arranged within the chalcogenide layers, whereas in $La_2O_2CdSe_2$ they are ordered such that tetrahedra in the chalcogenide layers share corners not edges, producing the checkerboard arrangement in *Figure 7.1*.

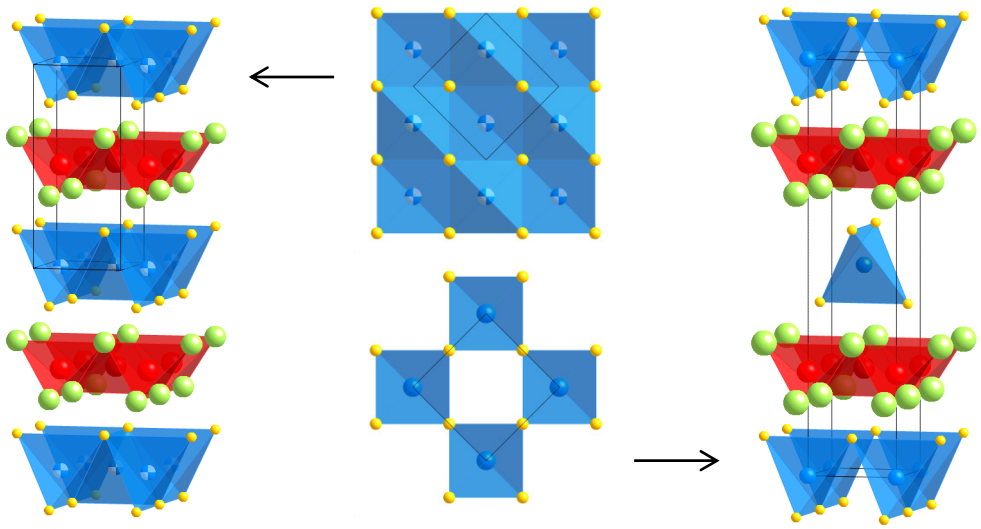

Figure 7.1 *Structures of $CeOMn_{0.5}Se$ & $La_2O_2CdSe_2$, with $[MSe2]^{2-}$ layers highlighted; Cd/Mn = blue, La/Ce = green, O = red, Se = yellow, unit cells are outlined; the blue/white colour of the Mn^{2+} sites shows that they are half-occupied.*

Here we report the synthesis and characterisation of two new ZrCuSiAs-related materials with half-occupied transition metal sites: $Ce_2O_2FeSe_2$ and $La_2O_2ZnSe_2$. In addition the determination of the magnetic structure of $Ce_2O_2FeSe_2$ and variable temperature studies of $La_2O_2ZnSe_2$ will be described. The preparation of an iron-containing ZrCuSiAs-type oxychalcogenide is of particular interest as both structurally related materials CeOFeAs and FeSe have been demonstrated to superconduct at relatively high temperatures (41 and 37 K, respectively).[4, 5]

7.2 $Ce_2O_2FeSe_2$

In an attempt to synthesise a series of iron-based ZrCuSiAs-type oxychalcogenides with potentially interesting magnetic and electronic properties, $Ce_2O_2FeSe_2$ was prepared. Here we will discuss the determination of the room temperature nuclear structure by a combination of indexing, charge flipping and Rietveld refinement, as well as the determination of the magnetic structure observed at 12 K.

7.2.1 Structure Solution

$Ce_2O_2FeSe_2$ was prepared using the method outlined in section 2.2.3. The resulting powder was subsequently characterised using X-ray powder diffraction, which suggested a phase with a similar structure to ZrCuSiAs had been obtained, with some Ce_2O_2Se impurity phase also present. Close inspection showed that extra peaks were present at 4.06 and 5.43 Å (21.8 and 16.3° 2θ, respectively) not predicted by the *P*4/*nmm* tetragonal structure of $CeOMn_{0.5}Se$. These peaks were also not attributable to impurity phases, suggesting the possibility of ordering of the Fe^{2+} sites leading to the enlarged unit cell. Indexing in TOPAS Academic (TA) suggested the peaks at 4.06 and 5.43 Å, together with those already observed for the tetragonal cell, could be described by a cell with dimensions 5.7011 × 5.7201 × 17.3143 Å, with *I*222 symmetry; relating to an approximate $\sqrt{2}a_{tet} \times \sqrt{2}a_{tet} \times 2c$ supercell of the original tetragonal model.[6, 7] The validity of this cell was scrutinised using Pawley refinement in TA, and the R_{wp} of the cell was seen to drop from 5.87 % for the tetragonal (*P*4/*nmm*) model, to 2.42 % for the orthorhombic (*I*222) model (*Figure 7.2*). Note that the results from indexing are given in the e-appendix.

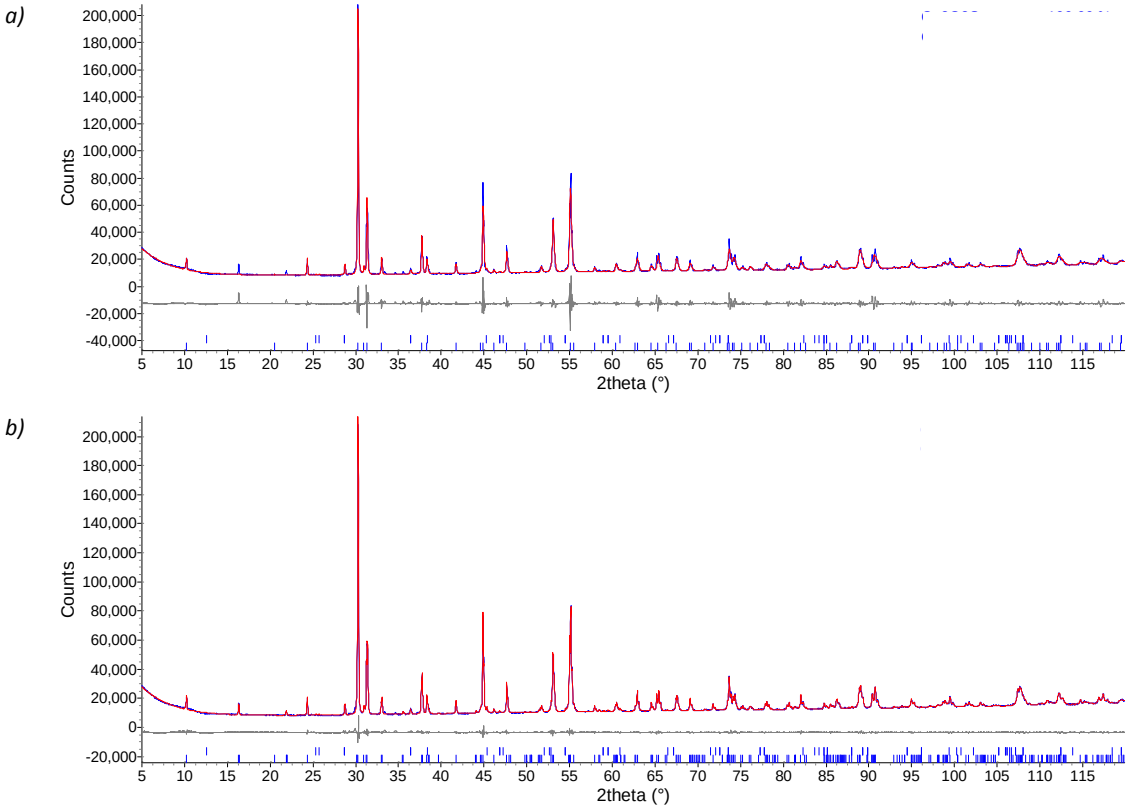

Figure 7.2 *Pawley plots for $Ce_2O_2FeSe_2$ at room temperature using (a) P4/nmm and (b) I222, symmetry with minor impurity phases also modelled; observed = blue, calculated = red, difference = grey. EEM205, d9_04615.*

In order to find out how the Fe^{2+} sites were ordering, charge flipping methods were employed in TA, feeding in information already known about cell dimensions and contents.[8] Charge flipping was successful in locating the $[Ce_2O_2]^{2+}$ layers, and also the positions of the Se^{2-} ions. Possible Fe^{2+} positions, however, were described by a mixture of Fe^{2+} and O^{2-} ions, with varying site occupancies. Rietveld refinement of the model obtained suggested that these oxygen sites were better described by half occupied Fe^{2+} sites, and refinement of site occupancies for all Fe^{2+} sites demonstrated that half of the

sites were empty. The resulting structure is shown in *Figure 7.3* and *Figure 7.4*, and is best described as containing fluorite-type $[Ce_2O_2]^{2+}$ layers separated by 1-dimensional chains of edge-sharing $FeSe_4$ tetrahedra, running along the shorter *a* axis. This "striped" arrangement is different to $La_2O_2CdSe_2$ which is ordered with layers of corner-sharing $CdSe_4$ tetrahedra in a "checkerboard" fashion (*Figure 7.1* & *Figure 7.4*). Note, again, that the files used for charge-flipping are given in the e-appendix.

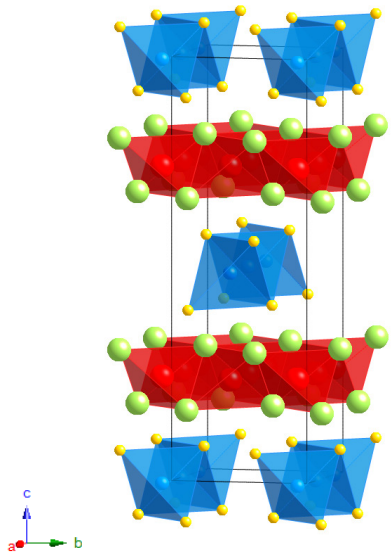

Figure 7.3 *Structure of $Ce_2O_2FeSe_2$; Ce = green, Fe = blue, O = red, Se = yellow, the unit cell is outlined.*

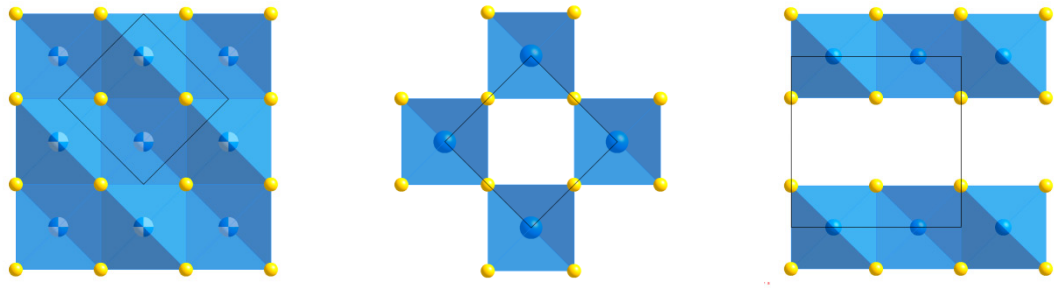

a) $CeOMn_{0.5}Se$ *b) $La_2O_2CdSe_2$* *c) $Ce_2O_2FeSe_2$*

Figure 7.4 *Ordering of M^{2+} ions in $[MSe_2]^{2-}$ layers of (a) $CeOMn_{0.5}Se$, (b) $La_2O_2CdSe_2$ and (c) $Ce_2O_2FeSe_2$; Cd/Fe/Mn = blue, Se = yellow, unit cells are outlined; the blue/white colour of the Mn^{2+} sites shows that they are half-occupied.*

These results are in agreement with those published in joint work with Emma McCabe, which showed that the structure could be described in the space group *Imcb* (the *cab* setting of *Ibam*) or *I*2*cb*, with lattice parameters of $\sim\sqrt{2}a_{tet} \times \sim\sqrt{2}a_{tet} \times 2c$.[9] Ordering of the Fe^{2+} was then identified using distortion mode analysis. For the final analysis the *Imcb* space group was adopted, for which the $\bar{4}m2$ Fe^{2+} sites in *P*4/*nmm* adopt 222 point symmetry. Results from the final Rietveld analysis using a combination of X-ray and neutron diffraction data (HRPD) in the joint publication with Emma McCabe are given in *Table 7.1*; atomic coordinates are given in *Table 7.2*. These refinements included the impurity phase Ce_2O_2Se and a Pawley phase to model V peaks from the HRPD slab can.

Table 7.1 *Results from combined X-ray / neutron Rietveld refinements of $Ce_2O_2FeSe_2$ at room temperature and 12 K.*[9]

	12 K	**300 K**
Nuclear symmetry	*Imcb*	*Imcb*
Magnetic symmetry	P_c2/c	-
a (Å)	*5.67984(3)*	*5.70040(3)*
b (Å)	*5.70565(2)*	*5.71946(3)*
c (Å)	*17.2859(2)*	*17.31342(9)*
V (Å^3)	*560.187(7)*	*564.47(3)*
Ce *y* (*c*)	*0.2517(2)*	*0.2517(2)*
Ce *z* (*c*)	*0.31974(2)*	*0.31956(2)*
Se *y* (*c*)	*0.2421(2)*	*0.2419(2)*
Se *z* (*c*)	*0.08266(4)*	*0.08254(3)*
O *z* (*c*)	*0.24806(8)*	*0.2480(1)*
Ce U_{eq} (100×Å^2)	*0.01(3)*	*0.43(5)*
Fe U_{eq} (100×Å^2)	*0.08(2)*	*0.89(5)*
Se U_{eq} (100×Å^2)	*0.14(1)*	*0.87(4)*
O U_{eq} (100×Å^2)	*0.33(3)*	*0.65(5)*
Fe^{2+} M_y (μ_B)	*3.33(3)*	-
Ce^{3+} M_y (μ_B)	*1.12(2)*	-
R_{wp} (%)	*3.54*	*2.71*
χ^2	*5.24*	*4.41*

Variable temperature studies by Emma McCabe showed that all cell parameters decrease smoothly on cooling, and that no structural phase transitions occur.[9] This work also reported magnetic susceptibility data, which suggested that the material orders antiferromagnetically on cooling, and resistivity studies, which gave a resistivity at room temperature of 20 Ωcm and revealed a band gap of ~0.64 eV. This resistivity is smaller than that observed for β-$La_2O_2FeSe_2$, 10^2 Ωcm.[10] There was no evidence to suggest the onset of superconductivity at low temperatures.

Table 7.2 *Cell coordinates and site occupancies (Occ.) for $Ce_2O_2FeSe_2$.*

	Wyckoff site	***x* (*a*)**	***y* (*b*)**	***z* (c)**	***Occ.***
Ce	*8j*	*0*	*~0.25*	*~0.32*	*1*
Fe	*4a*	*0.25*	*0*	*0*	*1*
O	*8g*	*0.25*	*0.5*	*~0.25*	*1*
Se	*8j*	*0.5*	*~0.24*	*~0.08*	*1*

7.2.2 Magnetic Structure Determination

Analysis of neutron diffraction data collected at 12 K showed the presence of several new peaks at 2.41, 2.56, 3.03, 4.53, 4.65, 5.92, 8.11 and 10.8 Å that were not present in the X-ray data (*Figure 7.5*). These peaks were found to be consistent with a *k*-vector of $\boldsymbol{k}$ = (0½½), and hence a magnetic unit cell of $a \times 2b \times 2c$. Analysis of the data was then performed in SARAh Refine, however due to software restrictions the standard space group setting of *Ibam* was adopted in place of the non-standard setting *Imcb*.[11] For *Ibam* parent symmetry with $\boldsymbol{k}$ = (½½0) one Fe^{2+} site is produced, with a total of six possible basis vectors, labelled by SARAh as $\Gamma_1\Psi_1$, $\Gamma_2\Psi_2$, $\Gamma_3\Psi_3$, $\Gamma_3\Psi_4$, $\Gamma_4\Psi_5$ and $\Gamma_4\Psi_6$. Refinements using a single irreducible representation (irrep) suggested that $\Gamma_3\Psi_3$ best described the ordering of the moments, with a decrease in χ^2 from 3.77, for the nuclear only model, to 3.23; results for the other basis vectors were $\Gamma_1\Psi_1$ = 3.52,

$\Gamma_2\Psi_2$ = 3.71, $\Gamma_3\Psi_4$ = 3.41, $\Gamma_4\Psi_5$ = 3.71 and $\Gamma_4\Psi_6$ = 3.72. The $\Gamma_3\Psi_3$ basis vector describes an arrangement of atoms with Fe^{2+} moments arranged ferromagnetically along the $FeSe_4$ chains, and antiferromagnetically between chains (*Figure 7.8* & *Figure 7.9*), with the moments lying along the *b* axis (of the original unit cell in *Imcb*). Analysis using varying combinations of each of the allowed basis vectors to check for canting of the Fe^{2+} moments suggested that values of χ^2 were consistently lowest with large contributions of $\Gamma_3\Psi_3$ and suggested that the moments were not canted. Contour plots of the $\Gamma_3\Psi_3$ irrep with combinations of the other irreps are shown in *Figure 7.6*; all of the contour plots from this analysis are given in appendix XIII. Canting was also investigated by refinement of each of the M_{xyz} parameters for the Fe^{2+} ion which refined to M_x = 0.6(17), M_y = 2.73(4) and M_z = -0.14(7) μ_B, thus suggesting that the majority of the moment is directed along the *b* axis.

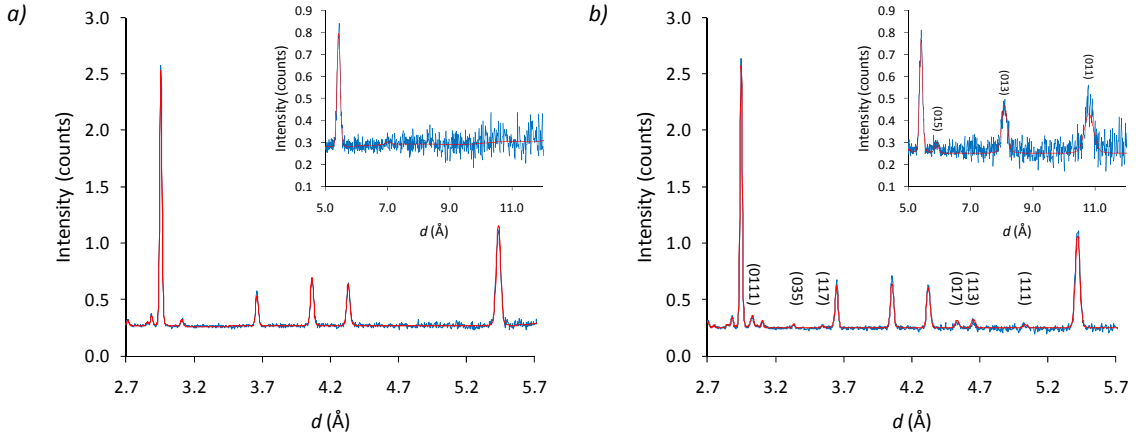

Figure 7.5 *Rietveld plots at (a) 295 and (b) 12 K highlighting the magnetic peaks observed in $Ce_2O_2FeSe_2$ between 2.7 and 5.7 Å (90° HRPD bank), and between 5.0 and 12.0 Å (30° HRPD bank) inset; observed = blue, calculated = red. EEM205, hrp46641 & hrp46672, respectively.*

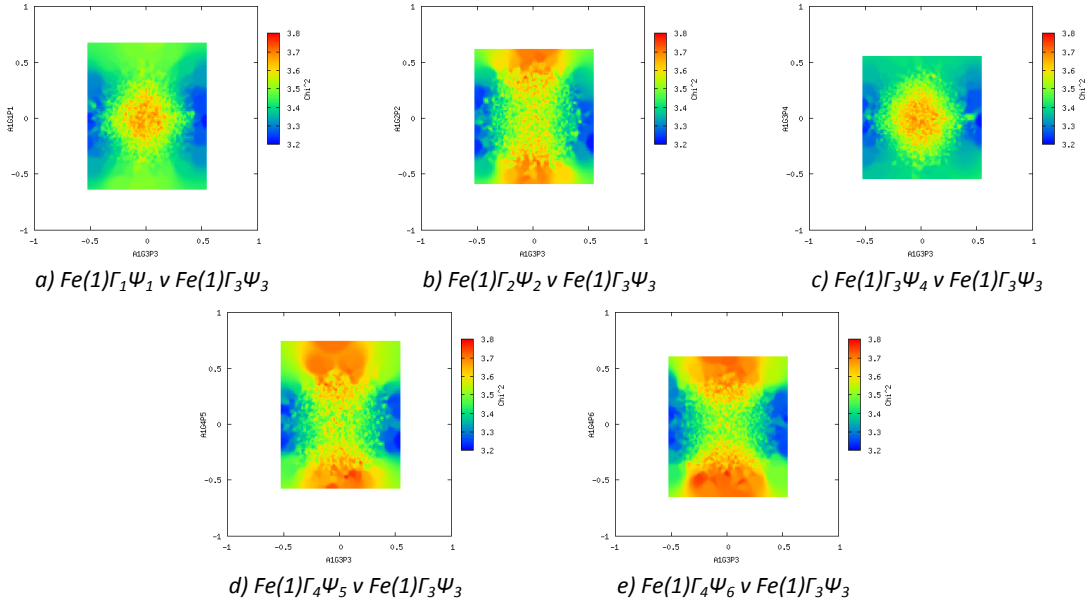

a) Fe(1)$\Gamma_1\Psi_1$ v Fe(1)$\Gamma_3\Psi_3$ *b) Fe(1)$\Gamma_2\Psi_2$ v Fe(1)$\Gamma_3\Psi_3$* *c) Fe(1)$\Gamma_3\Psi_4$ v Fe(1)$\Gamma_3\Psi_3$*

d) Fe(1)$\Gamma_4\Psi_5$ v Fe(1)$\Gamma_3\Psi_3$ *e) Fe(1)$\Gamma_4\Psi_6$ v Fe(1)$\Gamma_3\Psi_3$*

Figure 7.6 *Contour plots showing the change in χ^2 with varying contributions of (a-e) the Fe(1)$\Gamma_3\Psi_3$ basis vector against the Fe(1)$\Gamma_1\Psi_1$, Fe(1)$\Gamma_2\Psi_2$, Fe(1)$\Gamma_3\Psi_4$, Fe(1)$\Gamma_4\Psi_5$ and Fe(1)$\Gamma_4\Psi_6$ basis vectors; low values of χ^2 are shown in blue and large values in red.*

Close inspection of the data showed that intensity for some of the diffraction peaks was still absent, and that other peaks were slightly more intense, notably those at 3.03, 4.65, 5.92 and 8.11 Å (*Figure 7.8*).

Ordering of the rare-earth ions was, therefore, also investigated using SARAh Refine.[11] For *Ibam* parent symmetry with $\boldsymbol{k}$ = (½½0) two independent Ce^{3+} sites are produced (labelled Ce(1) and Ce(2) in *Figure 7.8* and *Figure 7.10*), with a total of six basis vectors each; labelled by SARAh as $\Gamma_1\Psi_1$, $\Gamma_2\Psi_2$, $\Gamma_2\Psi_3$, $\Gamma_3\Psi_4$, $\Gamma_3\Psi_5$ and $\Gamma_4\Psi_6$. Analysis was initially performed by mixing of all twelve basis vectors (six per Ce^{3+} site) and results suggested that lowest values of χ^2 were obtained for a combination of Ce(1)$\Gamma_3\Psi_4$ and Ce(2)$\Gamma_3\Psi_4$; note that the $\Gamma_3\Psi_3$ arrangement for the Fe^{2+} sites was used throughout and contour plots for this analysis are given in appendix XIII. *Figure 7.7* shows contour plots from analysis of the data using both Γ_3 basis vectors allowed for the Ce^{3+} sites, and shows that low values of χ^2 are only obtained when the contribution of the Ce(1)$\Gamma_3\Psi_4$ and Ce(2)$\Gamma_3\Psi_4$ basis vectors are opposite in sign, *i.e.* Ce(1)$\Gamma_3\Psi_4$ - Ce(2)$\Gamma_3\Psi_4$. The resulting arrangement of these moments is given in *Figure 7.8* and *Figure 7.10*.

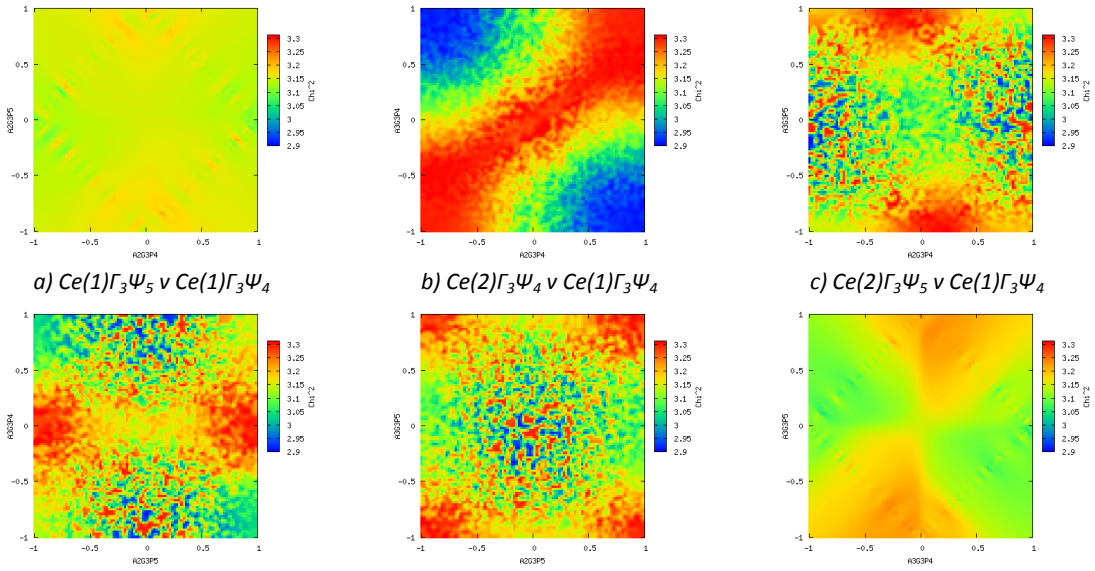

a) Ce(1)$\Gamma_3\Psi_5$ v Ce(1)$\Gamma_3\Psi_4$ *b) Ce(2)$\Gamma_3\Psi_4$ v Ce(1)$\Gamma_3\Psi_4$* *c) Ce(2)$\Gamma_3\Psi_5$ v Ce(1)$\Gamma_3\Psi_4$*

d) Ce(2)$\Gamma_3\Psi_4$ v Ce(1)$\Gamma_3\Psi_5$ *e) Ce(2)$\Gamma_3\Psi_5$ v Ce(1)$\Gamma_3\Psi_5$* *f) Ce(2)$\Gamma_3\Psi_5$ v Ce(2)$\Gamma_3\Psi_4$*

Figure 7.7 *Contour plots showing the change in χ^2 with varying contributions of (a-f) Ce(1)$\Gamma_3\Psi_4$, Ce(1)$\Gamma_3\Psi_5$, Ce(2)$\Gamma_3\Psi_4$, and Ce(2)$\Gamma_3\Psi_5$ basis vectors; low values of χ^2 are shown in blue and large values in red.*

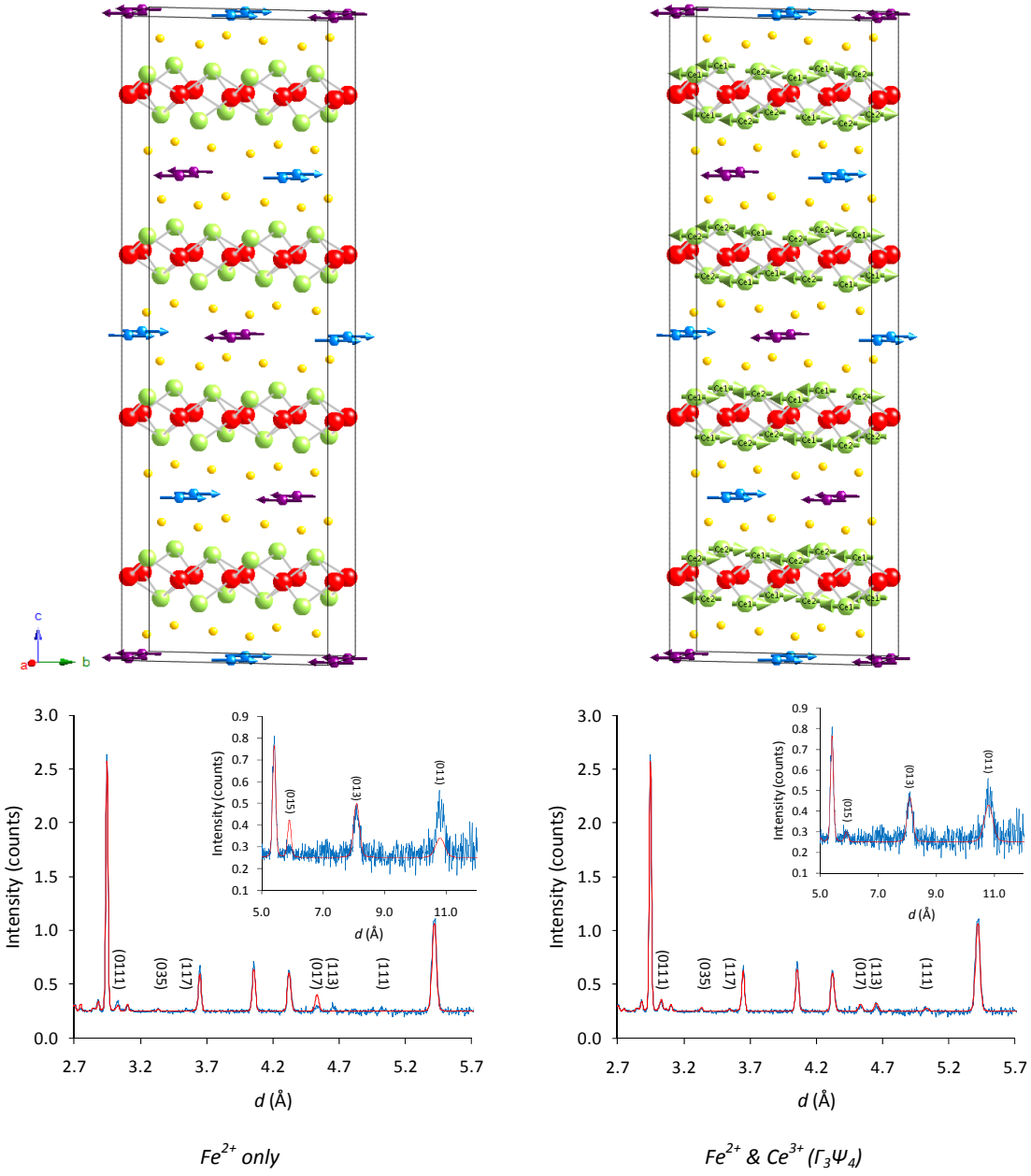

Figure 7.8 *Magnetic structures and Rietveld plots highlighting the magnetic peaks observed in $Ce_2O_2FeSe_2$ for the Fe^{2+} only and the Fe^{2+} & Ce^{3+} models between 2.7 and 5.7 Å (90° HRPD bank), and between 5.0 and 12.0 Å (30° HRPD bank) inset; observed = blue, calculated = red; Fe = blue, Ce = green, O = red, Se = yellow, the unit cell is outlined. EEM205, hrp46672.*

Canting of the Ce^{3+} moments was also investigated in TA using distortion mode refinements, and allowing mixing of the $\Gamma_3\Psi_4$ (labelled by ISODISTORT as mT2+(a,b)[Ce1:j]A''_2(a) and 2(b)) and $\Gamma_3\Psi_5$ (mT2+(a,b)[Ce1:j]A''_4(a) and 4(b)) basis vectors. These results suggested that whilst refinement statistics were improved for the 90° bank neutron data, those for the bs bank data remained essentially unchanged, and those for the 30° data bank worsened. Due to the high weighting of the 90° data the overall refinement statistics were improved, however by only a small amount: R_{wp} decreased from 3.78 to 3.77 % for the uncanted and canted models, respectively. Overall there is little evidence to explicitly state whether canting of the Ce^{3+} moments is present or not, and therefore the uncanted model is reported here. The improvement observed in the refinement statistics for each bank of data for varying models is given in *Table 7.3*.

Table 7.3 *Refinement statistics for bs, 90° and 30° neutron banks for the nuclear and each of the magnetic models used.*

Model	R_{wp} bs	R_{wp} 90°	R_{wp} 30°	R_{wp} total
Nuclear	*4.68*	*4.72*	*10.7*	*4.84*
Fe^{2+} only	*4.48*	*3.75*	*10.1*	*4.20*
Fe^{2+} & Ce^{3+} ($\Gamma_3\Psi_4$)	*4.41*	*3.12*	*8.13*	*3.78*
Fe^{2+} & Ce^{3+} ($\Gamma_3\Psi_4$ & $\Gamma_3\Psi_5$)	*4.41*	*3.09*	*8.30*	*3.77*

The results from the final distortion mode refinement of the structure are given in *Table 7.1* and refinement plots are given in appendix XIII.[9] Note that whilst these refinements were carried out in *P*1 symmetry, analysis in ISODISTORT shows that the arrangement of moments can be described by a cell with P_C2/c symmetry and basis vector (0,-1,1)(1,0,0)(0,0,2).[12] The overall refined moment for the Fe^{2+} site is 3.33(3) μ_B, larger than that observed for $La_2O_2Fe_2OSe_2$ of 2.66(4) μ_B at 12 K (chapter 4), and much larger than that for the poor metal CeOFeAs, which is observed to be 0.94(3) μ_B at 1.7 K.[13]

In CeOFeAs, and related oxypnictides, there are two important magnetic interactions to consider: the nearest-neighbour (n.n.), J_1, and the next nearest neighbour (n.n.n.), J_2, interactions. Due to the reduction in symmetry in these materials from tetragonal to orthorhombic on cooling, the J_1 interactions split into J_{1a} and J_{1b}, where J_{1a} is the coupling along the longer axis (*a*) and J_{1b} is that along the shorter axis (*b*). In CeOFeAs it has been shown that the J_{1a} interactions are AFM and the J_{1b} interactions are FM, whilst the J_2 interactions are all AFM, suggesting that J_2 interactions dominate in these materials. The magnetic structure produced is termed AFM2. In $Ce_2O_2FeSe_2$, however, we have a single J_1 interaction (which in this case is along the *a* axis) and J_2 interactions are absent. The FM ordering along the chains is what one would predict from Goodenough-Kanamori rules for a 90° d^6 species.[14-16] A simple comparison to the CeOFeAs structure would therefore suggest that in CeOFeAs it is the J_{1a} AFM interactions that are frustrated, though various DFT calculations for LaOFeAs predict all J_1 interactions to be AFM.[17, 18] In reality the magnetic interactions in iron-arsenide systems are now thought to be highly anisotropic due to orbital ordering and result from a complex balance of AFM superexchange interactions or moments due to localised electrons and FM double exchange due to delocalisation of itinerant d_{xy}/d_{yz}.[19, 20]

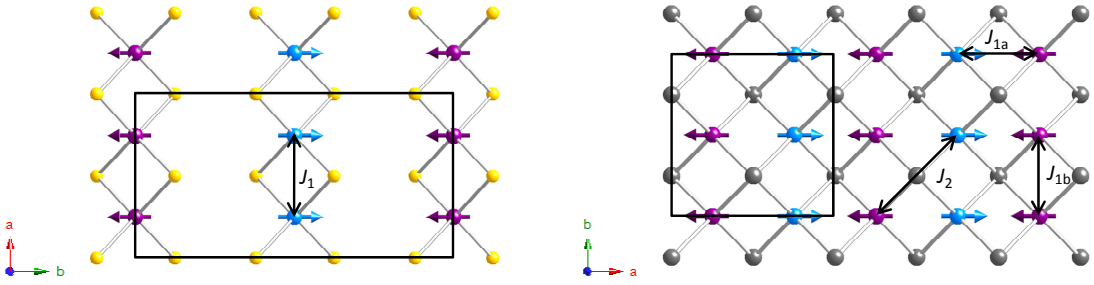

a) $Ce_2O_2FeSe_2$ *b) CeOFeAs*

Figure 7.9 *Magnetic structures for the Fe^{2+} layers in (a) $Ce_2O_2FeSe_2$ and (b) CeOFeAs; Fe = blue/purple, As = grey, Se = yellow, magnetic cells are outlined in black.*

The arrangement of the Ce^{3+} moments also differs between $Ce_2O_2FeSe_2$ and CeOFeAs, with the arrangement of the Ce^{3+} moments in CeOFeAs resembling those of the Fe^{2+} layers, although Ce^{3+}

moments are at 45° to the Fe^{2+} ions in the *ab* plane. The arrangement in $Ce_2O_2FeSe_2$ is more complex. As in the Fe^{2+} layers of CeOFeAs, there are two distinct n.n. interactions (J_{1a} & J_{1b}; where J_{1a} is marginally shorter than J_{1b}), which are shown in *Figure 7.10*. Considering the layers in isolation, these interactions are all frustrated, with any given Ce^{3+} ion having either three FM and one AFM, or one FM and three AFM interactions. The n.n.n. interactions (J_2 & J_2'; where J_2 is shorter than J_2') are also split into two due to slight difference in bond lengths. In this case we observe that the coupling interactions along the longer Ce-Ce distances are AFM, and those along the shorter distances are FM. One might also expect to observed magnetic coupling between the Fe^{2+} and Ce^{3+}, however this cannot be determined from the powder diffraction data available; R_{wp} remains constant on rotation of the Fe^{2+} moments by 180°. Note that simulations in ISODISTORT suggest that one would observe a change in peak intensities for a 180° rotation of the Fe^{2+} moments.

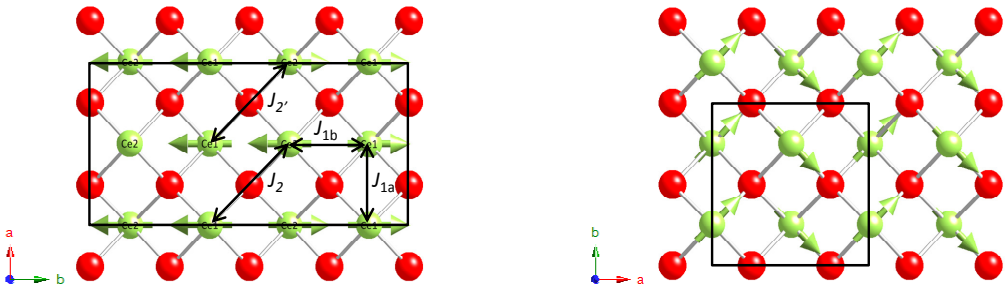

a) $Ce_2O_2FeSe_2$ *b) CeOFeAs*

Figure 7.10 *Magnetic structures for the Ce^{3+} layers in (a) $Ce_2O_2FeSe_2$ and (b) CeOFeAs; Ce = green, O = red, magnetic cells are outlined in black.*

Figure 7.11 shows the change in the modelled magnetic moment on both the Fe^{2+} and Ce^{3+} ions as a function of temperature. The data show that the Fe^{2+} moments begin to order below ~173 K, which is in agreement with results published by McCabe by modelling of peak intensities.[9] This behaviour was modelled as in previous chapters and the results for each ion are given in *Table 7.4*. This ordering temperature is similar to that observed in $CaFe_2As_2$ (173 K) however larger than those observed for CeOFeAs (140 K) and $La_2O_2Fe_2OSe_2$ (90 K). The Ce^{3+} moments appear to order with the same T_N, which compares to values of 4 K in CeOFeAs, 16 K in CeSb, and 50 K in $CeVO_3$.[13, 21, 22] Whilst this value of T_N seems unusually large, this could be driven by the Fe^{2+} ordering. It is, however, possible that the apparent high ordering temperature is due to the relatively low quality of the data for the rapid variable temperature studies and the relatively weak intensity of the magnetic reflections. Experiments are planned to probe this unusual behaviour further.

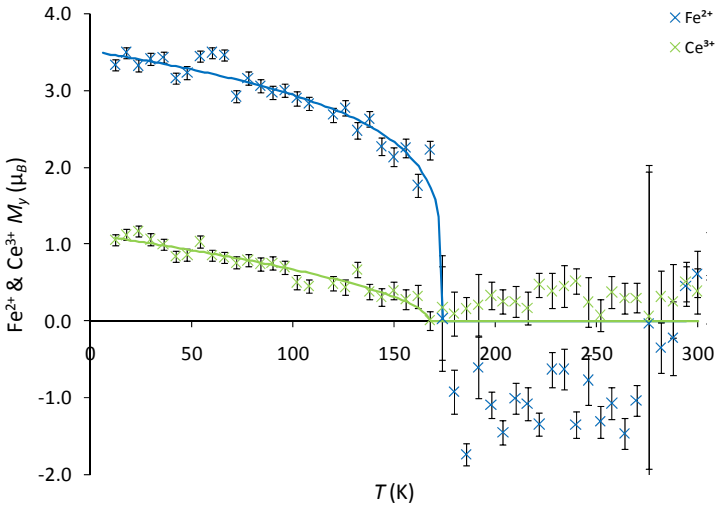

Figure 7.11 *Magnetic moments of Fe^{2+} and Ce^{3+} in $Ce_2O_2FeSe_2$ as a function of temperature; Fe^{2+} = blue, Ce^{3+} = green.*

Table 7.4 *Refined parameters for models of magnetic ordering of Fe^{2+} and Ce^{3+} as a function of temperature in $Ce_2O_2FeSe_2$.*

		Fe^{2+}	Ce^{3+}
M_y	M_0 (μ_B)	*3.52(7)*	*1.15(5)*
	T_N (K)	*174(5)*	*172(8)*
	β	*0.21(3)*	*0.7(1)*

7.3 $La_2O_2ZnSe_2$

$La_2O_2ZnSe_2$ was isolated whilst exploring the formation of M^{2+}-containing ZrCuSiAs-type oxychalcogenides. Synthesis using the procedure outlined in section 2.2.3 produced a white powder, which was subsequently characterised using X-ray diffraction. This section will discuss the room and low temperature structures of $La_2O_2ZnSe_2$ from X-ray diffraction data.

7.3.1 Structure Determination

X-ray data collected at room temperature for $La_2O_2ZnSe_2$ showed that a ZrCuSiAs-related phase had been obtained. Unlike $Ce_2O_2FeSe_2$ there were no peaks observed relating to a ~√2a_{tet} × ~√2a_{tet} based supercell, however there were several unidentified peaks present; notably those at 5.32, 4.45, 3.63, 3.52, 2.81 & 2.53 Å (*Figure 7.12*). These peaks could not be explained by known impurity phases or indexed to a sensible cell. This suggests that the origin of the peaks is from a complex ordering of the Zn^{2+} ions.[6, 7] Work by Tuxworth has further investigated the origin of these peaks, and tentatively concludes that as composition is varied their intensity scales with that of the main phase.[23] As these peaks could not be identified, Rietveld refinements presented in *Table 7.5* were performed in the tetragonal space group *P*4/*nmm* with the Zn^{2+} sites half occupied, as in $CeOMn_{0.5}Se$ (*Figure 7.4a*); cell coordinates are given in *Table 7.6* and a Rietveld plot is given in *Figure 7.12*.[3]

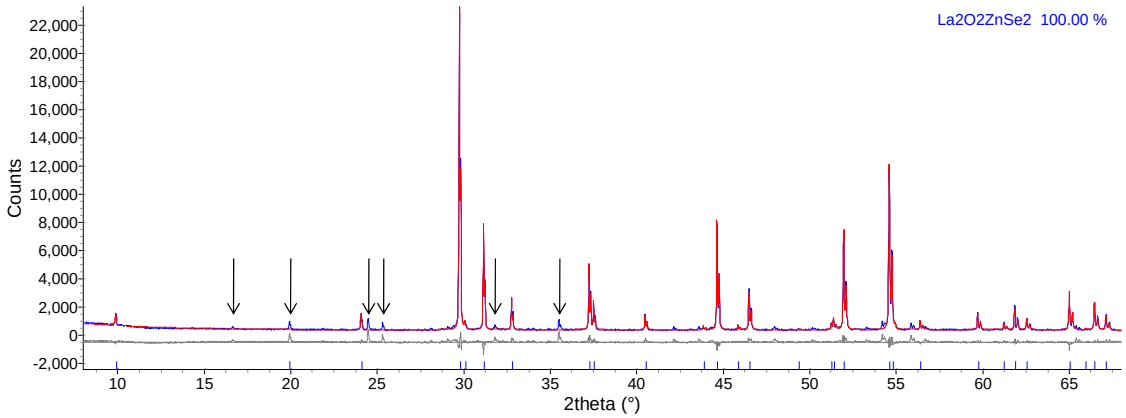

Figure 7.12 *Rietveld plot for $La_2O_2ZnSe_2$ at room temperature; observed = blue, calculated = red, difference = grey; unexplained peaks are indicated by black arrows. DGF217, d9_03766.*

Investigation of data collected at 12 K does not show the presence of any additional peaks over those seen at room temperature, suggesting that the Zn^{2+} ions are either already ordered at room temperature, and therefore are the cause of the un-indexed peaks, or they remain randomly distributed within the chalcogenide layers. Refinement results for the material at 12 K are given in *Table 7.5* and a Rietveld plot is given in appendix XIV.

Table 7.5 *Results from X-ray Rietveld refinements of $La_2O_2ZnSe_2$ at room temperature and 12 K.*

	12 K	**300 K**
Nuclear symmetry	*P4/nmm*	*P4/nmm*
a (Å)	*4.04509(3)*	*4.05267(3)*
c (Å)	*8.8763(1)*	*8.8980(1)*
V (Å^3)	*145.240(3)*	*146.143(3)*
La *z* (*c*)	*0.6392(2)*	*0.6387(2)*
Se *z* (*c*)	*0.1672(3)*	*0.1675(3)*
La U_{iso} (100×Å^2)	*0.00(4)*	*0.41(5)*
Zn U_{iso} (100×Å^2)	*0.3(2)*	*1.1(2)*
Se U_{iso} (100×Å^2)	*0.03(7)*	*0.74(8)*
O U_{iso} (100×Å^2)	*1.8(6)*	*1.3(6)*
N°. variables	*27*	*27*
R_{wp} (%)	*11.95*	*11.46*
χ^2	*1.76*	*1.67*

More information is given in appendix XIV.

Table 7.6 *Cell coordinates and site occupancies (Occ.) for $La_2O_2ZnSe_2$.*

	Wyckoff site	***x* (*a*)**	***y* (*b*)**	***z* (c)**	***Occ.***
La	*2c*	*0.25*	*0.25*	*~0.64*	*1*
Zn	*2a*	*0.75*	*0.25*	*0*	*0.5*
O	*2b*	*0.75*	*0.25*	*0.5*	*1*
Se	*2c*	*0.25*	*0.25*	*~0.17*	*1*

7.3.2 Variable Temperature Studies

Variable temperature data were collected using the d9 diffractometer, and analysed in TA using the local *multitopas* routine.[6, 24] *Figure 7.13* shows the change in *a* and *c* cell parameters as a function of temperature. These results suggest that $La_2O_2ZnSe_2$ contracts with a continual thermal expansion on cooling, which is shown by the solid lines, although there is perhaps a slight hint of a discontinuity below

~135 K observed in both sets of data; results from the modelling of the thermal expansion, using *eqn 3.1* with two Einstein terms, are given in *Table 7.7*. Plots of cell volume and *c*/*a* ratio are given in appendix XIV.

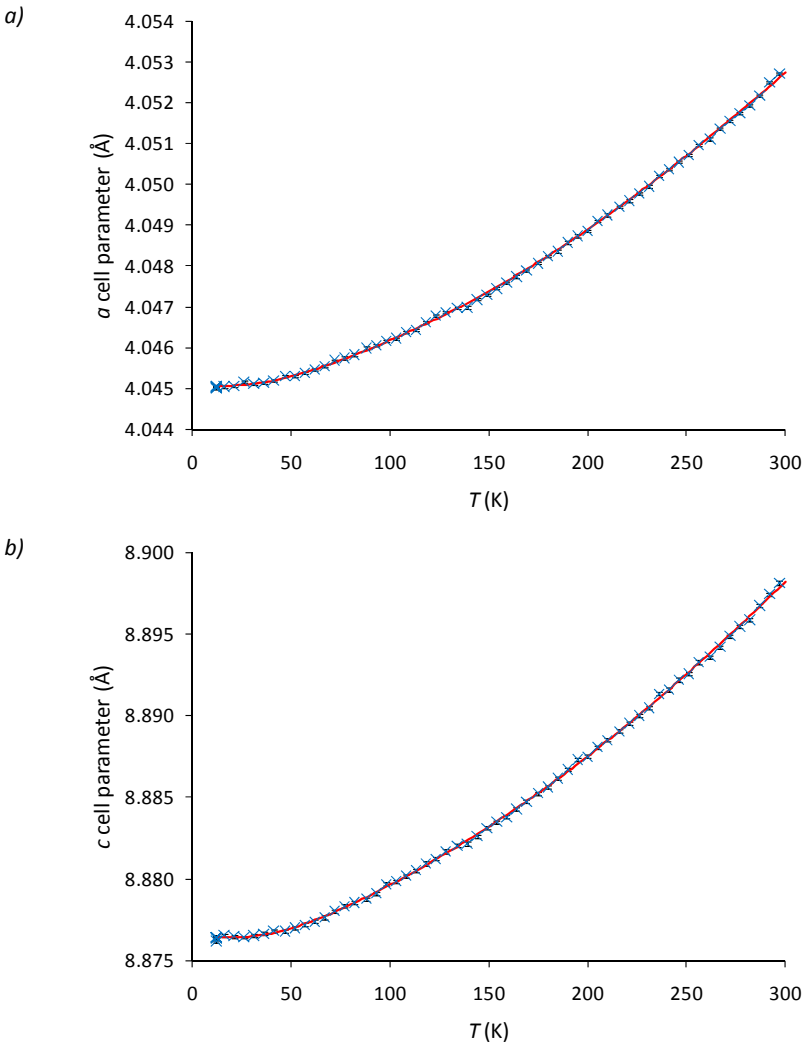

Figure 7.13 *The (a) a and (b) c cell parameters for $La_2O_2ZnSe_2$ as a function of temperature.*

Table 7.7 *Refined parameters for models of thermal expansion for $La_2O_2ZnSe_2$.*

	a	***c***
a_0 or c_0 (Å)	*4.04507(1)*	*8.87642(4)*
C_1 (10^{-6})	*5.8(3)*	*8.6(4)*
θ_1 (K)	*137(9)*	*155(8)*
C_2 (10^{-6})	*8.1(5)*	*9(1)*
θ_2 (K)	*767(63)*	*879(95)*

7.4 Unsuccessful Syntheses

Although β-$La_2O_2MSe_2$ (*M* = Mn, Fe), $Ce_2O_2FeSe_2$ and $La_2O_2ZnSe_2$, were all successfully prepared, the synthesis of further materials by variation of the rare-earth metal proved unsuccessful. Those phases targeted are summarised in *Table 7.8* with the phases formed alongside. These reactions were also repeated at temperatures of 900 and 1000 K, however there was no evidence for the formation of either ZrCuSiAs or β-$La_2O_2MnSe_2$-related materials. Similar to the results presented in chapter 5, the

main products of the reactions were the ternary lanthanide-oxyselenide and metal-selenide, although there was also evidence for formation of known $A_2O_2M_2OSe_2$ materials. Furthermore, several unknown impurity phases were observed, however due to time constraints a full analysis of these as presented in chapter 5 for the $A_2O_2M_2OSe_2$ materials was not performed. Other work by Emma McCabe demonstrated that synthesis of Co, Ni and Cu phases was also not possible; again the main impurities observed were A_2O_2Se and MSe.

Table 7.8 *Results from unsuccessful reactions for $A_2O_2MSe_2$ target phases.*

Material	Products	Conditions (°C)
$Pr_2O_2MnSe_2$	Pr_2O_2Se, MnSe, $Pr_2O_2Mn_2OSe_2$, unknown	1100
$Nd_2O_2MnSe_2$	Nd_2O_2Se, MnSe, unknown	900, 1000, 1100
$Sm_2O_2MnSe_2$	Sm_2O_2Se, MnSe	1100
$Gd_2O_2MnSe_2$	Gd_2O_2Se, MnSe, Gd_2O_3	1100
$Pr_2O_2FeSe_2$	Pr_2O_2Se, FeSe	1100
$Nd_2O_2FeSe_2$	Nd_2O_2Se, $Nd_2O_2Fe_2OSe_2$, unknown	900, 1000, 1100
$Ce_2O_2ZnSe_2$	Ce_2O_2Se, ZnSe, unknown	1100

7.5 Conclusions

Two new oxychalcogenide materials have been synthesised with structures similar to those of the layered ZrCuSiAs-type oxychalcogenides and oxypnictides: $Ce_2O_2FeSe_2$ and $La_2O_2ZnSe_2$. $Ce_2O_2FeSe_2$ has been shown to contain ordered transition metal sites within the chalcogenide layers. These sites order to create 1-dimensional chains of $FeSe_4$ tetrahedra, unlike the Cd^{2+} sites in $La_2O_2CdSe_2$, which order to create corner-sharing tetrahedral layers. Data collected for $La_2O_2ZnSe_2$ suggest that the Zn^{2+} may be ordered at room temperature; however the arrangement of the ions has not yet been unravelled.

Neutron diffraction data collected for $Ce_2O_2FeSe_2$ have demonstrated that both the Fe^{2+} and Ce^{3+} moments order antiferromagnetically on cooling below ~170 K. Analysis of this arrangement in ISODISTORT suggests that both moments order with the mT2+ basis vector (labelled as Fe$\Gamma_3\Psi_3$ and Ce$\Gamma_3\Psi_4$ in SARAh Refine).

7.6 References

1. H. Hiramatsu, K. Ueda, T. Kamiya, H. Ohta, M. Hirano and H. Hosono, *J. Phys. Chem. B*, 2004, **108**, 17344-17351.
2. H. Hiramatsu, K. Ueda, T. Kamiya, H. Ohta, M. Hirano and H. Hosono, *J. Mater. Chem.*, 2004, **14**, 2946-2950.
3. I. Ijjaali, K. Mitchell, C. L. Haynes, A. D. McFarland, R. P. van Duyne and J. A. Ibers, *J. Solid State Chem.*, 2003, **176**, 170-174.
4. G. F. Chen, Z. Li, D. Wu, G. Li, W. Z. Hu, J. Dong, P. Zheng, J. L. Luo and N. L. Wang, *Phys. Rev. Lett.*, 2008, **100**, 247002.
5. S. Medvedev, T. M. McQueen, I. A. Troyan, T. Palasyuk, M. I. Eremets, R. J. Cava, S. Naghavi, F. Casper, V. Ksenofontov, G. Wortmann and C. Felser, *Nat. Mater*, 2009, **8**, 630-633.
6. A. A. Coelho, *TOPAS Academic: General profile and Structure Analysis Software for Powder Diffraction Data*, Bruker AXS, Karlsruhe, 2010.

7. A. A. Coelho, *J. Appl. Cryst.*, 2003, **36**, 86-95.
8. G. Oszlanyi and A. Suto, *Acta Cryst.*, 2004, **A60**, 134-141.
9. E. E. McCabe, D. G. Free and J. S. O. Evans, *Chem. Commun.*, 2011, **47**, 1261-1263.
10. E. E. McCabe, D. G. Free, B. Mendis, J. Higgins and J. S. O. Evans, *Chem. Mater.*, 2010, **22**, 6171-6182.
11. A. S. Wills, *Physica B*, 2000, **276-278**, 680-681.
12. B. J. Campbell, H. T. Stokes, D. E. Tanner and D. M. Hatch, *J. Appl. Cryst.*, 2006, **39**, 607-614.
13. J. Zhao, Q. Huang, C. de la Cruz, S. Li, J. W. Lynn, Y. Chen, M. A. Green, G. F. Chen, G. Li, Z. Li, J. L. Luo, N. L. Wang and P. Dai, *Nature Mater.*, 2008, **7**, 953-959.
14. J. B. Goodenough, *Phys. Rev.*, 1955, **100**, 564-573.
15. J. B. Goodenough, *Magnetism and the Chemical Bond*, John Wiley & Sons, New York - London, 1963.
16. J. Kanamori, *J. Phys. Chem. Solids*, 1959, **10**, 87-98.
17. T. Yildirim, *Phys. Rev. Lett.*, 2008, **101**, 057010.
18. F. Ma, Z. Y. Lu and T. Xiang, *Phys. Rev. B*, 2008, **78**, 224517.
19. C.-C. Lee, W.-G. Yin and W. Ku, *Phys. Rev. Lett.*, 2009, **103**, 267001.
20. Z. P. Yin and W. E. Pickett, *Phys. Rev. B*, 2010, **81**, 174534.
21. B. Rainford and et al., *J. Phys. C. Solid State*, 1968, **1**, 679-683.
22. A. Munoz, J. A. Alonso, M. T. Casais, M. J. Martinez-Lopez, J. L. Martinez and M. T. Fernandez-Diaz, *Phys. Rev. B*, 2003, **68**, 144429.
23. A. Tuxworth, *Synthesis and Characterisation of Layered Oxychalcogenides*, Durham University, *M.Chem.*, Durham, 2010.
24. J. S. O. Evans, *multitopas, FORTRAN 77 routine*, University of Durham, 1999.

Conclusions & Future Work

This thesis has reported the synthesis of several new oxychalcogenide materials. The family of known $La_2O_2Fe_2OSe_2$-type materials has been expanded to include $Ce_2O_2M_2OSe_2$ (*M* = Mn, Fe), $A_2O_2(Mn_{0.5}Fe_{0.5})_2OSe_2$ (*A* = La, Pr, Nd), and $(La_{⅘}Nd_{⅕})_2O_2Mn_2OSe_2$. In work to explore the formation of ZrCuSiAs-related phases with potentially interesting magnetic and electronic properties, two new materials were formed with the general formula $A_2O_2MSe_2$ ($Ce_2O_2FeSe_2$ & $La_2O_2ZnSe_2$), as well as two new materials with a new oxychalcogenide structure type, β-$La_2O_2MSe_2$ (*M* = Mn, Fe). The first family share a ZrCuSiAs-related structure, however with half occupied transition metal sites, whilst the latter example forms a material more similar in structure to $Gd_4O_4TiSe_2$.[1] The variable temperature structural and magnetic properties of the majority of these materials, and others reported in previous work, have also been discussed.

Work with the $A_2O_2Mn_2OSe_2$ (*A* = La–Pr) family has shown that these materials undergo a series of structural transitions on cooling. Inspection of both X-ray and neutron data suggested that the O(2) site (that in the $[Mn_2O]^{2+}$ plane) has a relatively large thermal displacement at both high and low temperatures. We presume that this is a result of local distortion of the Mn-O-Mn bond angle, and modelling of this (although without reduction in symmetry) shows a significant angle increase on cooling. We have no current evidence to suggest that these O(2) displacements are ordered at room temperature, however variable temperature data have demonstrated the appearance of superstructure peaks, in $La_2O_2Mn_2OSe_2$ on $Pr_2O_2Mn_2OSe_2$, that appear at a temperature coincident with the displacement of the oxygen. Work to date has been unable to index these peaks to a commensurate unit cell, and therefore the ordering pattern of these ions is not known. The synthesis of single crystals of these materials is the next essential step in understanding the low temperature structure of these materials, and would also help confirm the orthorhombic structure observed for $Pr_2O_2Mn_2OSe_2$. SQUID magnetometry experiments should also be repeated with purer samples.

The low temperature nuclear and magnetic structures of $La_2O_2Fe_2OS_2$ and $La_2O_2Fe_2OSe_2$ have been determined, and both have been shown to adopt an AFM3 arrangement of moments, similar to that of FeTe.[2] Unlike the manganese-containing materials, these materials do not undergo a clear phase transition coincident with this magnetic ordering, although variable temperature studies have revealed a discontinuity in the thermal expansion of the *a* cell parameter of both materials at T_N that could indicate a subtle structural transition. In addition to this, a slight increase in peak width is observed for $La_2O_2Fe_2OSe_2$ at the same temperature. In FeTe the lowering of symmetry allows the magnetic ordering of the metal ions to be explained by a single irrep, whilst the structure presented here requires two different irreps to describe the ordering of the moments. Once more, single crystal studies are vital to discern if the observations in *a* and peak width are the result of a subtle transition to a lower symmetry cell on cooling below T_N.

Whilst the structural and magnetic properties of a number of $La_2O_2Fe_2OSe_2$-type materials are now known, there has been no work to date concerning doping of these materials, for example with F^- ions, to investigate the possibility of crossing the Mott-insulator to metallic boundary, perhaps allowing superconductivity at low temperatures. Whilst at first hand these materials seem a step away from the iron-arsenide superconductors, the Fe^{2+} layers in $La_2O_2Fe_2OSe_2$ and FeSe are very similar, and various cation and anion doping strategies should be explored.[3, 4] In addition, electronic and magnetic structure calculations for the low temperature structure of $La_2O_2Mn_2OSe_2$ should be performed. This would allow comparison of the band structure and coupling constants with those previously reported for $La_2O_2Fe_2OSe_2$ and $La_2O_2Co_2OSe_2$.[5, 6] The DFT calculations previously reported for these materials should also be repeated to explore whether the magnetic ordering observed is of lower energy than those predicted with the wrong magnetic cell.

A new family of oxychalcogenides with the β-$La_2O_2MnSe_2$ structure has also been described. As discussed, an Fe^{2+} containing analogue has also been produced since.[7] Whilst their nuclear structures at 12 K are known, there is little data available to investigate their magnetic structures, although susceptibility data show both materials order AFM on cooling. In order to understand the magnetic ordering in these systems, therefore, neutron powder diffraction data should be collected at higher *d*-spacings, for example on WISH at the ISIS facility which allows data to be collected as high as 50 Å. In addition, doping strategies should be explored for these materials in order to observe any change in conductivity.

Finally the synthesis of two new ZrCuSiAs-type materials has been reported: $Ce_2O_2FeSe_2$ and $La_2O_2ZnSe_2$. Similar to $La_2O_2CdSe_2$, the metal sites in $Ce_2O_2FeSe_2$ are ordered, although producing a striped, not checkerboard, arrangement of $FeSe_4$ tetrahedra. Whilst a number of unindexed peaks have been observed in $La_2O_2ZnSe_2$, studies so far have not been able to attribute them to order of the Zn^{2+} ions. Single crystal, and neutron powder diffraction, studies for this material could help uncover any ordering that is present, and consequently reveal a new ordering pattern for this family of materials. Again, doping of $Ce_2O_2FeSe_2$ should also be considered, owing to its resemblance to the iron-based superconductors.

References

1. I. Ijjaali, K. Mitchell, C. L. Haynes, A. D. McFarland, R. P. van Duyne and J. A. Ibers, *J. Solid State Chem.*, 2003, **176**, 170.
2. S. Li, C. de la Cruz, F. Q. Huang, Y. Chen, J. W. Lynn, J. Hu, Y. L. Huang, F. C. Hsu, K. W. Yeh, M. K. Wu and P. Dai, *Phys. Rev. B*, 2009, **79**, 054503.
3. F. C. Hsu, J. Y. Luo, K. W. Yeh, T. K. Chen, T. W. Huang, P. M. Wu, Y. C. Lee, Y. L. Huang, Y. Y. Chu, D. C. Yan and M. K. Wu, *P. Natl. Acad. Sci. USA*, 2008, **105**, 14262-14264.
4. S. Margadonna, Y. Takabayashi, M. T. McDonald, K. Kasperkiewicz, Y. Mizuguchi, Y. Takano, A. N. Fitch, E. Suard and K. Prassides, *Chem. Comm.*, 2008, 5607-5609.
5. H. Wu, *Phys. Rev. B*, 2010, **82**, 020410.
6. J. X. Zhu, R. Yu, H. Wang, L. L. Zhao, M. D. Jones, J. Dai, E. Abrahams, E. Morosan, M. Fang and Q. Si, *Phys. Rev. Lett.*, 2010, **104**, 216405.

7. E. E. McCabe, D. G. Free, B. Mendis, J. Higgins and J. S. O. Evans, *Chem. Mater.*, 2010, **22**, 6171-6182.

Appendices

Note that the e-appendix, which can be found on the inside back cover of this thesis, contains all of the data, input files and spreadsheets used for analysis of the data presented within this thesis.

I. Collation of data and analysis for $La_2O_2Mn_2OSe_2$

Results from combined X-ray / neutron Rietveld refinement of $La_2O_2Mn_2OSe_2$ at 12 K and room temperature.

		12 K	295 K
Sample		*DGF109*	*DGF109*
Input file(s)		*combined_riet.inp*	*combined_riet.inp*
Data file(s)		*d9_03049.raw*	*d9_03034.raw*
		hrp39916_bs.xye	*hrp39877_bs.xye*
		hrp39916_90.xye	*hrp39877_90.xye*
Nuclear symmetry		*I*4/*mmm*	*I*4/*mmm*
Magnetic symmetry		*I*4'/*mm'm*	-
a (Å)		*4.12870(1)*	*4.138921(4)*
c (Å)		*18.78115(5)*	*18.84990(3)*
V (Å^3)		*320.146(1)*	*322.911(1)*
La *z* (*c*)		*0.18644(1)*	*0.18668(1)*
Se *z* (*c*)		*0.09999(2)*	*0.09994(2)*
La U_{ij} (100×Å^2)	U_{11}	*0.33(1)*	*0.81(1)*
	U_{22}	$= U_{11}$	$= U_{11}$
	U_{33}	*0.88(2)*	*1.41(2)*
Mn U_{ij} (100×Å^2)	U_{11}	*0.57(3)*	*1.49(3)*
	U_{22}	*0.49(3)*	*1.03(3)*
	U_{33}	*0.83(3)*	*2.40(4)*
Se U_{ij} (100×Å^2)	U_{11}	*0.78(1)*	*1.35(1)*
	U_{22}	$= U_{11}$	$= U_{11}$
	U_{33}	*0.47(2)*	*1.03(3)*
O(1) U_{ij} (100×Å^2)	U_{11}	*0.54(2)*	*0.97(2)*
	U_{22}	*0.32(3)*	*0.73(3)*
	U_{33}	*0.88(2)*	*1.32(3)*
O(2) U_{ij} (100×Å^2)	U_{11}	*0.57(2)*	*0.98(3)*
	U_{22}	$= U_{11}$	$= U_{11}$
	U_{33}	*7.33(7)*	*7.24(7)*
Mn^{2+} M_z (μ_B)		*4.223(7)*	-
N°. variables		*70*	*70*
X-ray R_{wp} (%)		*4.49*	*3.73*
HRPD bs R_{wp} (%)		*5.30*	*4.34*
HRPD 90 R_{wp} (%)		*3.71*	*3.13*
Total R_{wp} (%)		*4.11*	*3.52*
χ^2		*4.52*	*4.51*

Rietveld plots for $La_2O_2Mn_2OSe_2$ at room temperature

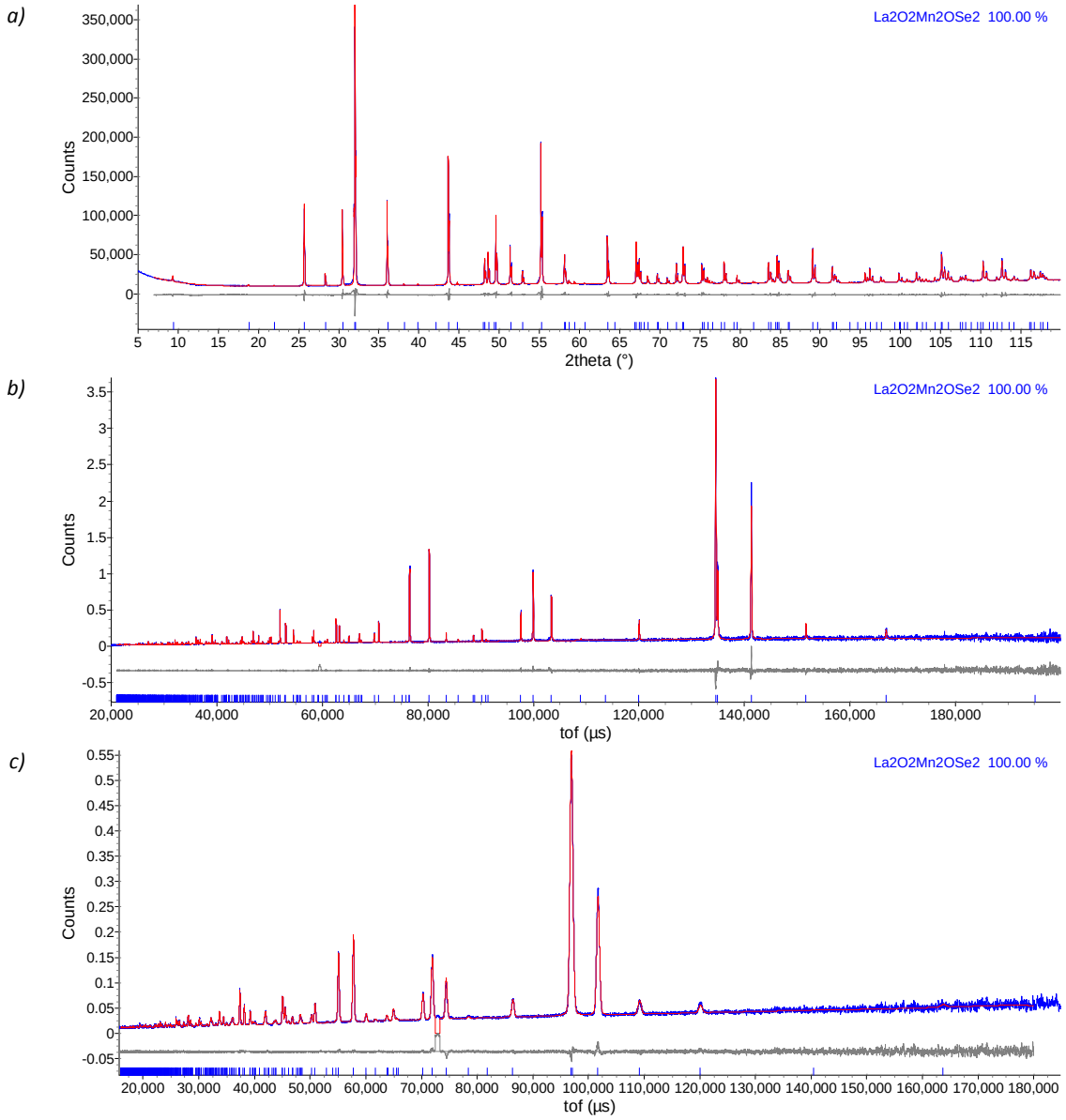

Rietveld plots for $La_2O_2Mn_2OSe_2$ at room temperature using (a) X-ray, (b) HRPD bs and (c) 90° bank data; observed = blue, calculated = red, difference = grey.

Rietveld plots for $La_2O_2Mn_2OSe_2$ at 12 K

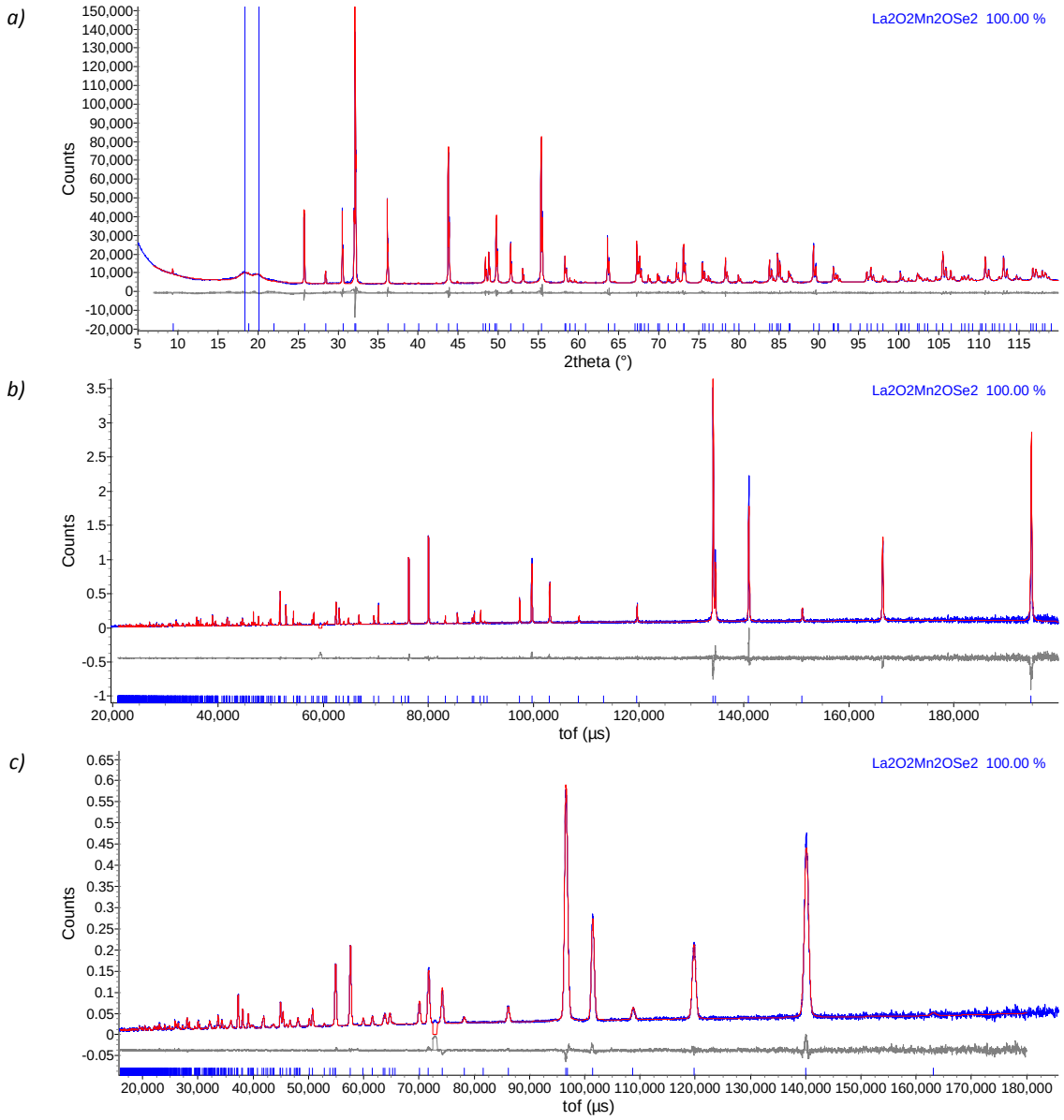

Rietveld plots for $La_2O_2Mn_2OSe_2$ at 12 K using (a) X-ray, (b) HRPD bs and (c) 90° bank data; observed = blue, calculated = red, difference = grey.

Variable temperature plots for $La_2O_2Mn_2OSe_2$

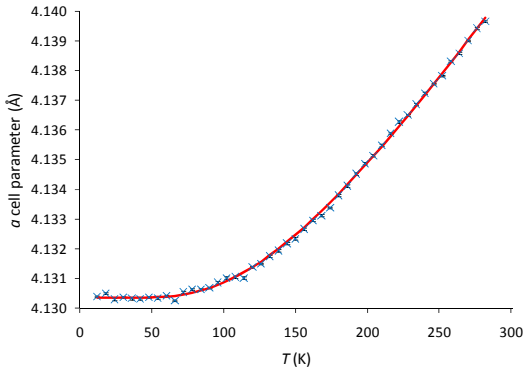

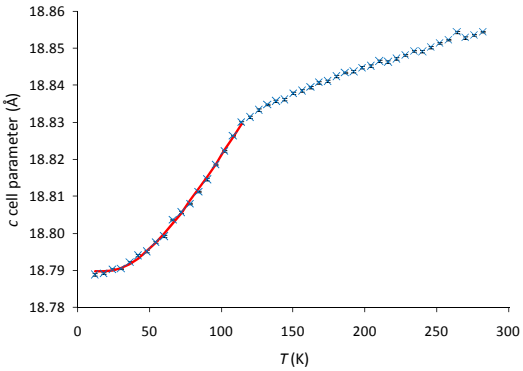

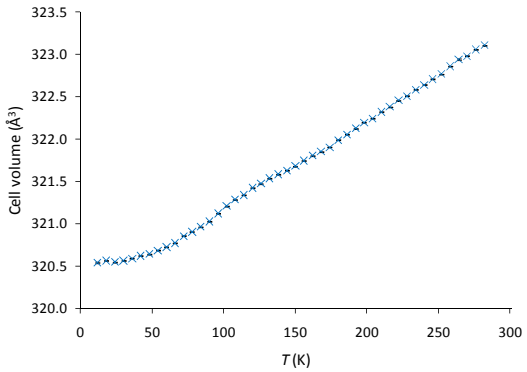

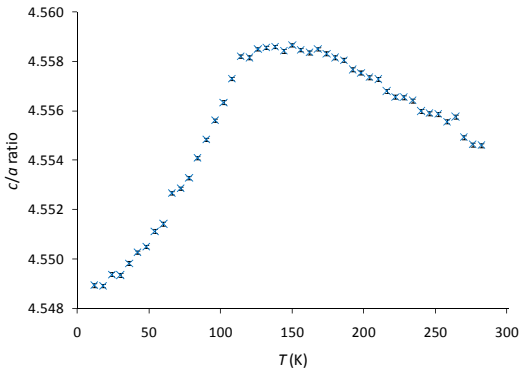

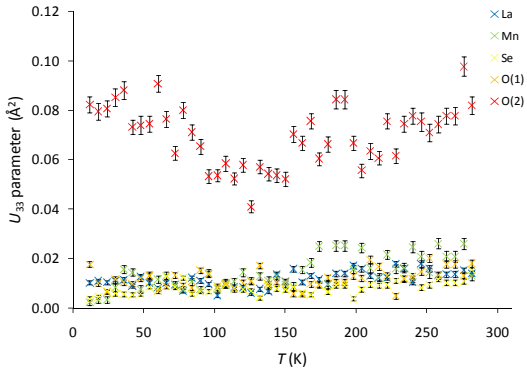

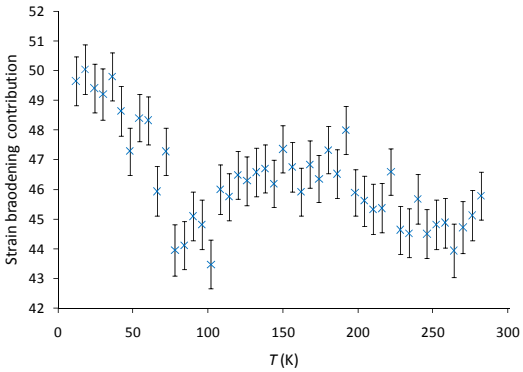

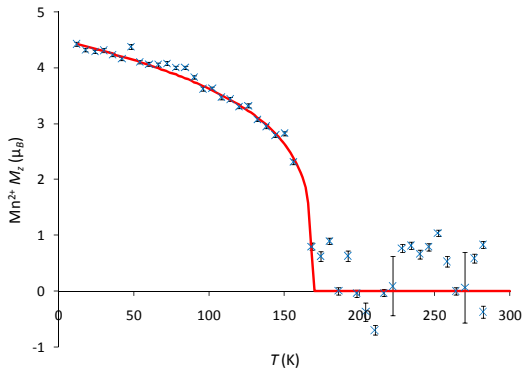

Superstructure peaks in $La_2O_2Mn_2OSe_2$

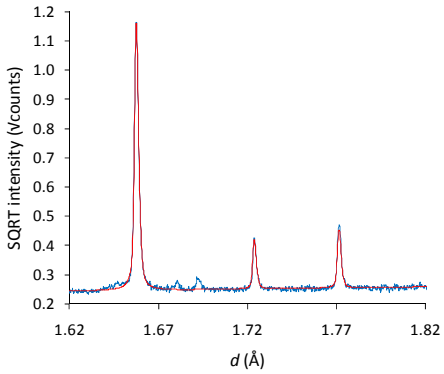

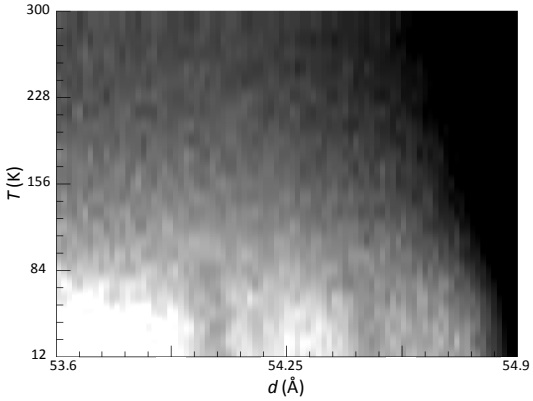

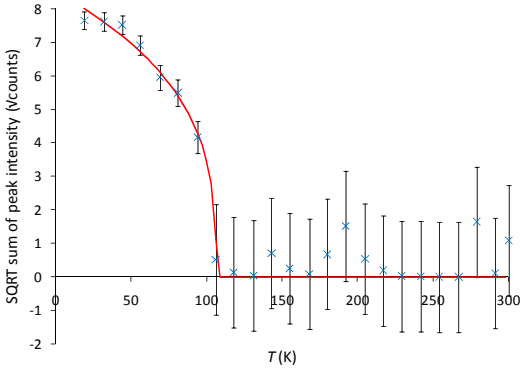

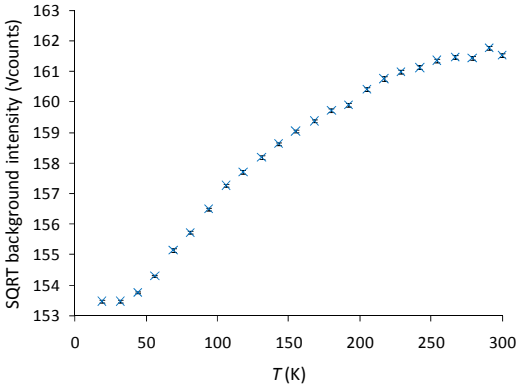

SARAh analysis of $La_2O_2Mn_2OSe_2$ – mixing of all allowed Mn^{2+} basis vectors

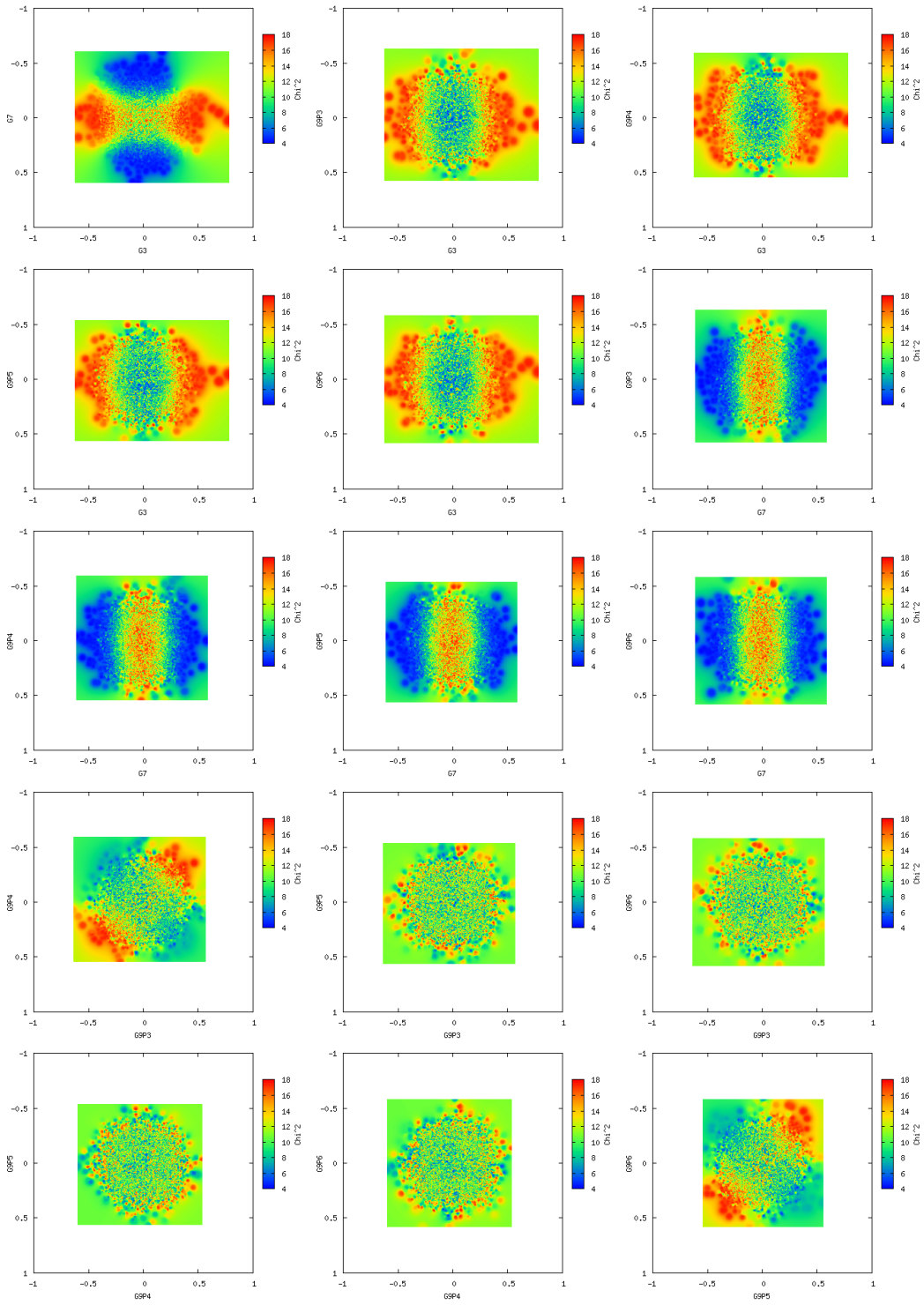

Hysteresis loops for $La_2O_2Mn_2OSe_2$ at 2, 12, 100 and 160 K

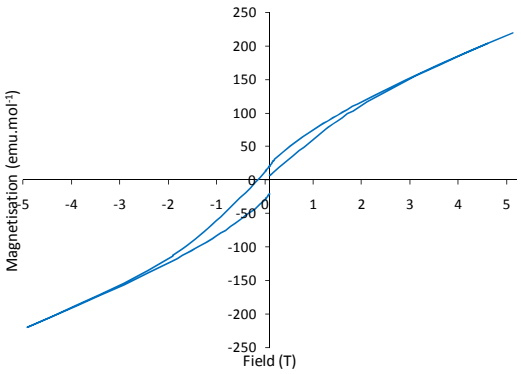

2 K

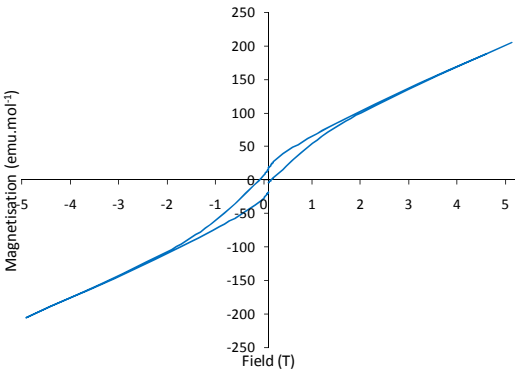

12 K

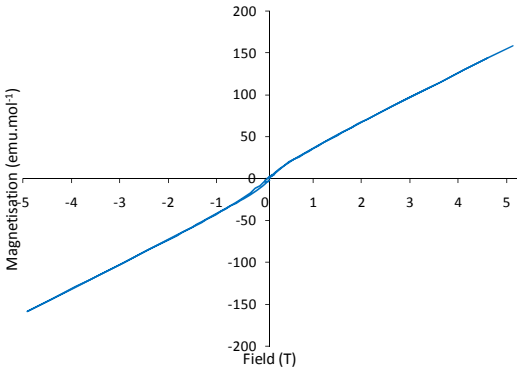

100 K

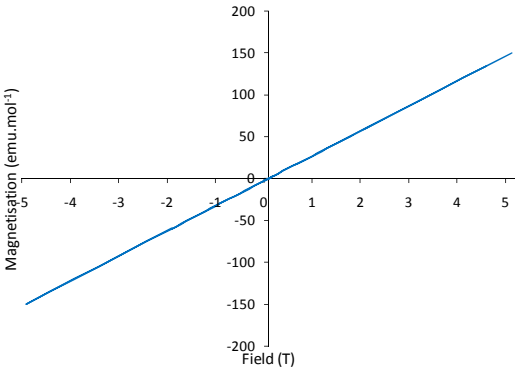

160 K

II. Collation of data and analysis for $Ce_2O_2Mn_2OSe_2$

Results from combined X-ray / neutron Rietveld refinement of $Ce_2O_2Mn_2OSe_2$ at 12 K and room temperature.

		12 K	**295 K**
Sample		*DGF136*	*DGF136*
Input file(s)		*combined_riet.inp*	*combined_riet.inp*
Data file(s)		*d9_03353.raw*	*d9_03354.raw*
		hrp41906_bs.xye	*hrp41875_bs.xye*
		hrp41906_90.xye	*hrp41875_90.xye*
Nuclear symmetry		*I*4/*mmm*	*I*4/*mmm*
Magnetic symmetry		*I*4'/*mm'm*	-
a (Å)		*4.10247(1)*	*4.11304(2)*
c (Å)		*18.70183(8)*	*18.7410(9)*
V (Å^3)		*314.757(2)*	*317.043(3)*
Ce *z* (*c*)		*0.18700(2)*	*0.18725(3)*
Se *z* (*c*)		*0.10089(3)*	*0.10118(3)*
Ce U_{ij} (100×Å^2)	U_{11}	*0.23(2)*	*0.53(2)*
	U_{22}	$= U_{11}$	$= U_{11}$
	U_{33}	*1.03(3)*	*1.46(3)*
Mn U_{ij} (100×Å^2)	U_{11}	*0.76(4)*	*1.31(4)*
	U_{22}	*0.32(3)*	*0.84(4)*
	U_{33}	*0.82(4)*	*2.04(5)*
Se U_{ij} (100×Å^2)	U_{11}	*0.74(2)*	*1.18(1)*
	U_{22}	$= U_{11}$	$= U_{11}$
	U_{33}	*0.63(2)*	*1.03(2)*
O(1) U_{ij} (100×Å^2)	U_{11}	*0.54(2)*	*0.86(2)*
	U_{22}	*0.45(3)*	*0.53(3)*
	U_{33}	*1.06(3)*	*1.38(3)*
O(2) U_{ij} (100×Å^2)	U_{11}	*0.78(3)*	*0.96(3)*
	U_{22}	$= U_{11}$	$= U_{11}$
	U_{33}	*5.91(8)*	*8.2(1)*
Mn^{2+} M_z (μ_B)		*4.023(7)*	-
N^o. variables		*91*	*91*
X-ray R_{wp} (%)		*3.88*	*2.92*
HRPD bs R_{wp} (%)		*4.65*	*4.24*
HRPD 90 R_{wp} (%)		*3.82*	*3.70*
Total R_{wp} (%)		*3.93*	*3.58*
χ^2		*4.38*	*3.67*

Rietveld plots for $Ce_2O_2Mn_2OSe_2$ at room temperature

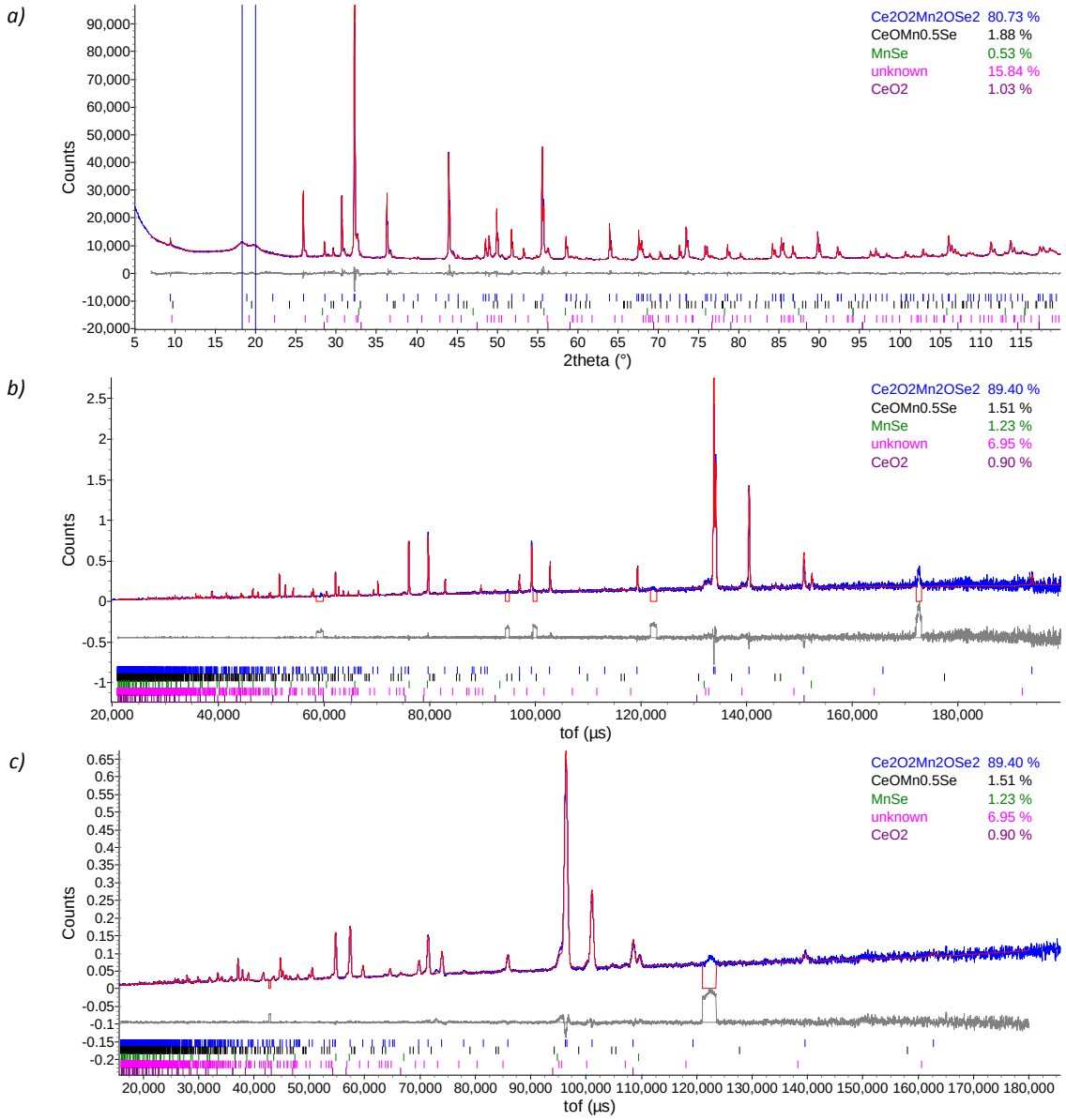

Rietveld plots for $Ce_2O_2Mn_2OSe_2$ at room temperature using (a) X-ray, (b) HRPD bs and (c) 90° bank data; observed = blue, calculated = red, difference = grey.

Rietveld plots for $Ce_2O_2Mn_2OSe_2$ at 12 K

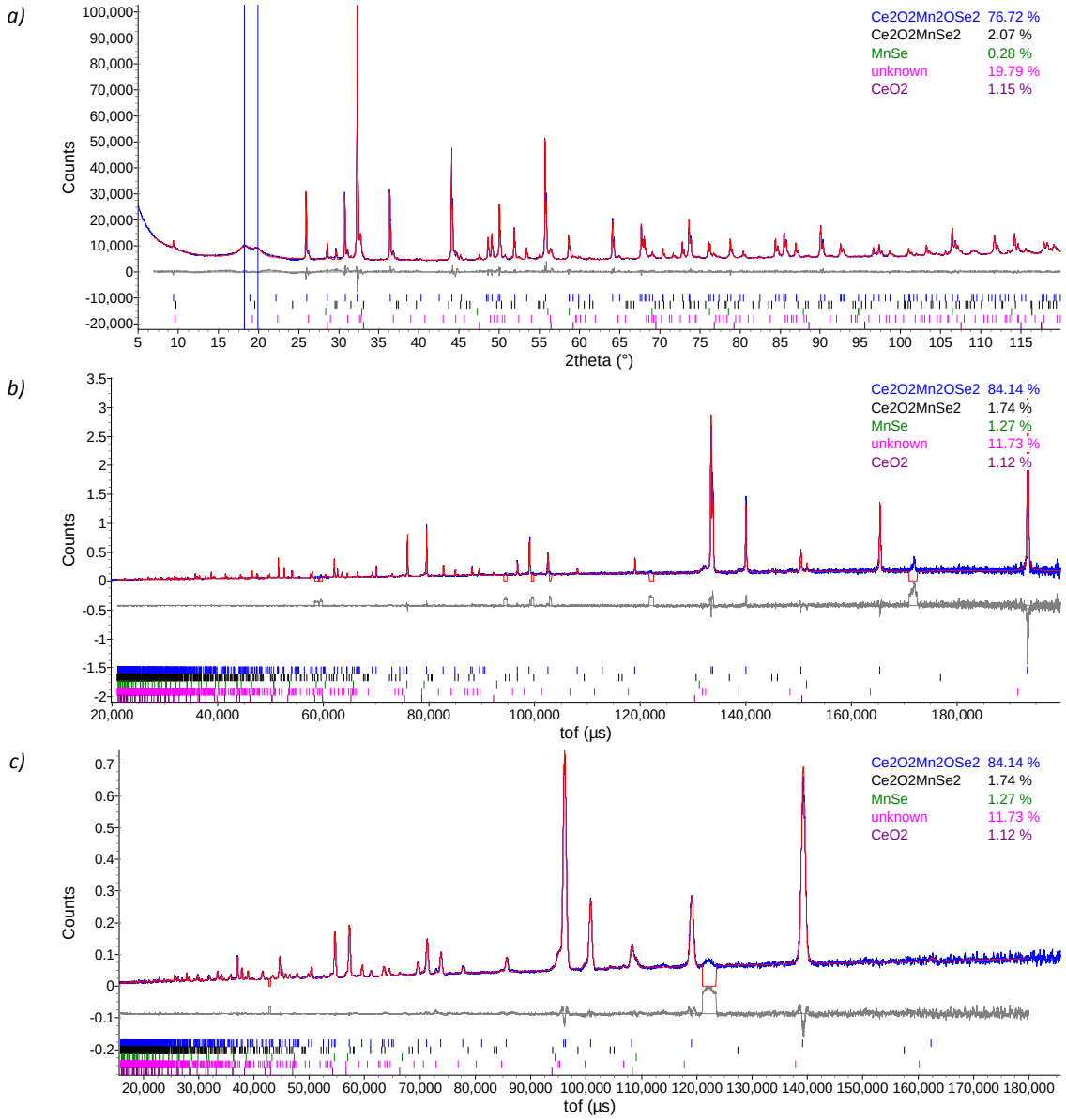

Rietveld plots for $Ce_2O_2Mn_2OSe_2$ at 12 K using (a) X-ray, (b) HRPD bs and (c) 90° bank data; observed = blue, calculated = red, difference = grey.

Variable temperature plots for $Ce_2O_2Mn_2OSe_2$

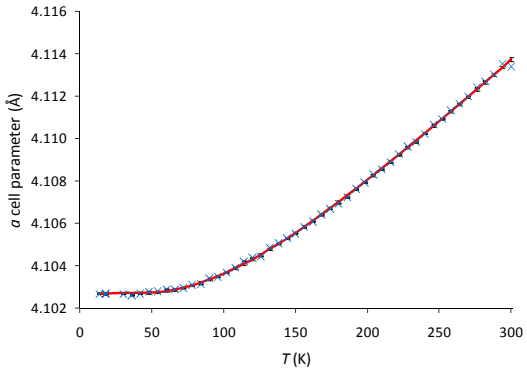

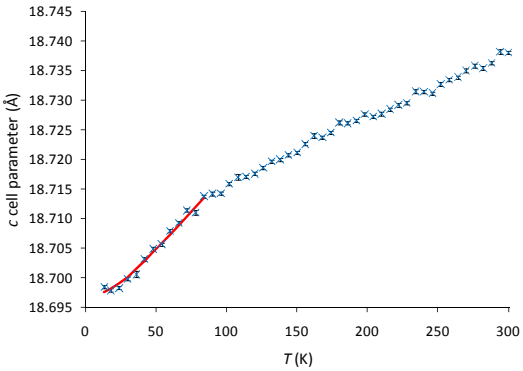

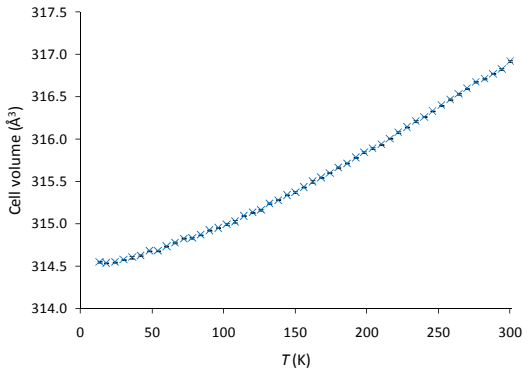

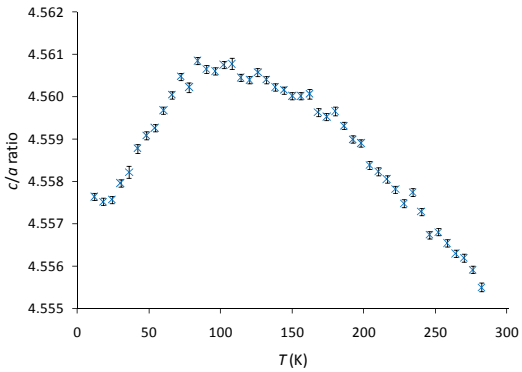

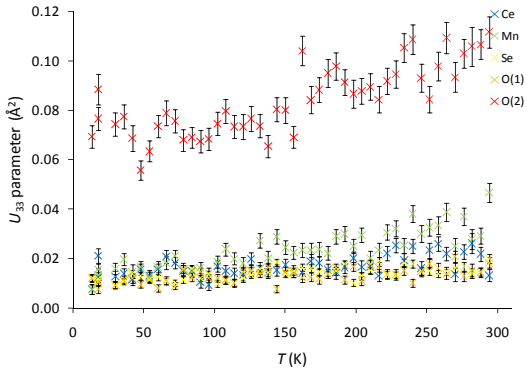

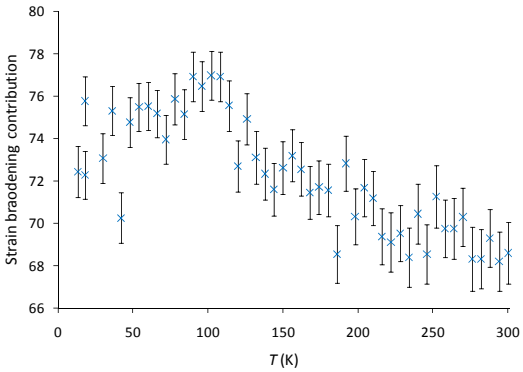

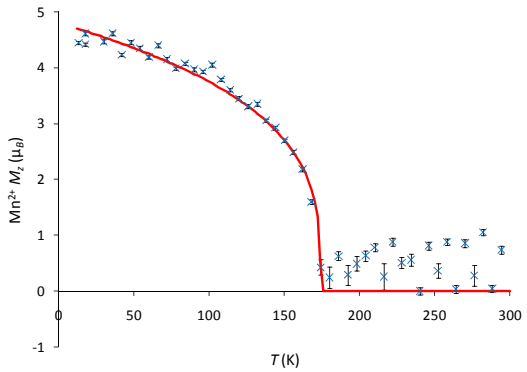

Absence of superstructure peaks in $Ce_2O_2Mn_2OSe_2$

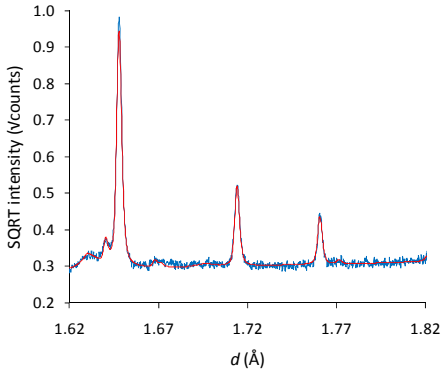

Variable temperature plots for the "unknown" phase in $Ce_2O_2Mn_2OSe_2$ compared with those of $Ce_2O_2Mn_2OSe_2$

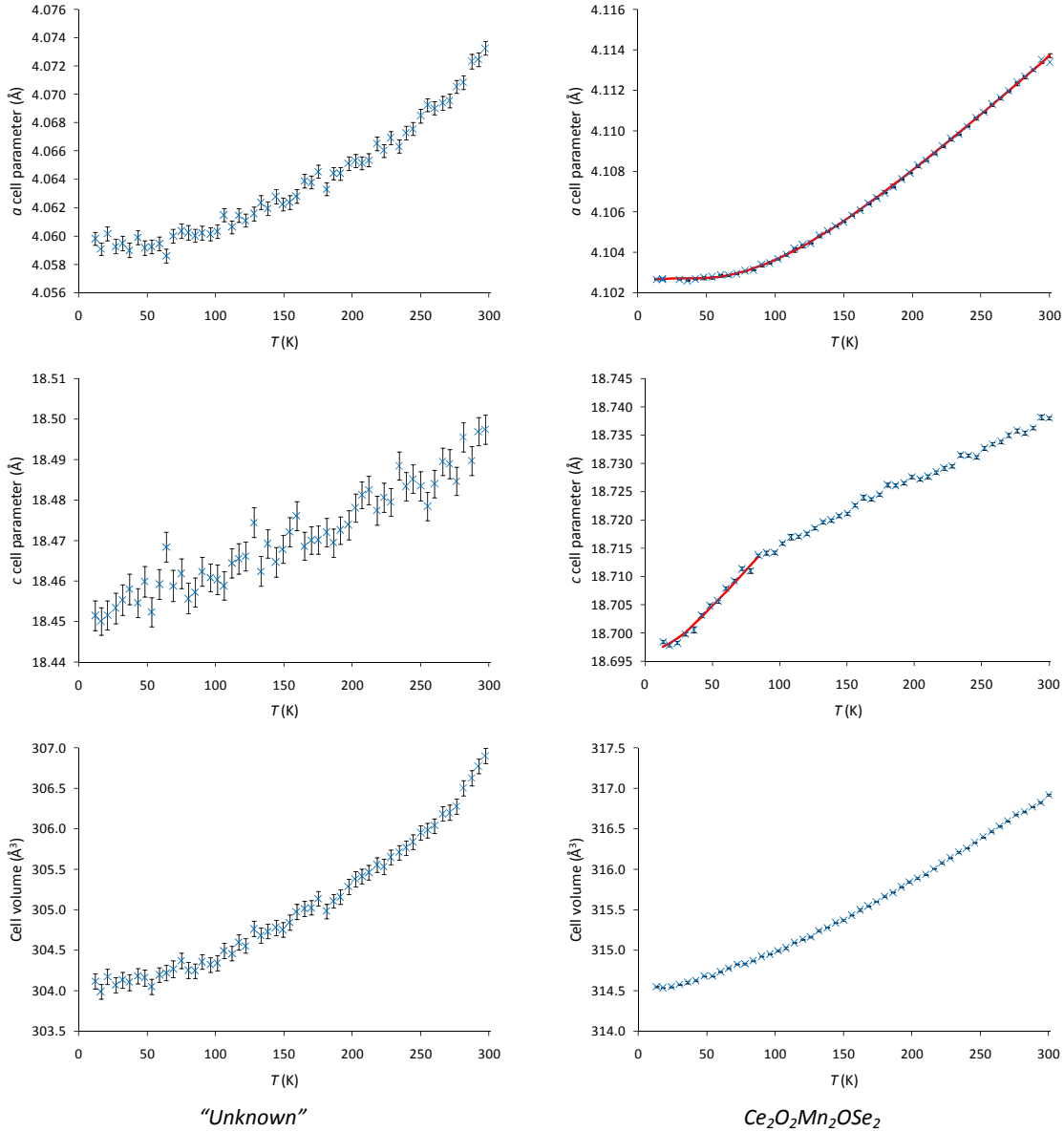

III. Collation of data and analysis for $Pr_2O_2Mn_2OSe_2$

Results from combined X-ray / neutron Rietveld refinement of $Pr_2O_2Mn_2OSe_2$ at 12 K, 72 K and room temperature.

		12 K	72 K	295 K
Sample		*DGF110*	*DGF110*	*DGF110*
Input file(s)		*combined_riet.inp*	*combined_riet.inp*	*combined_riet.inp*
Data file(s)		*d9_02821.raw*	*d9_03391.raw*	*d9_03041.raw*
		hrp39824_bs.xye	*hrp41872_bs.xye*	*hrp39783_bs.xye*
		hrp39824_90.xye	*hrp41872_90.xye*	*hrp39783_90.xye*
Nuclear symmetry		*Immm*	*I4/mmm*	*I4/mmm*
Magnetic symmetry		*Im'm'm*	*I4'/mm'm*	-
a (Å)		*4.08616(3)*	*4.09036(2)*	*4.09739(2)*
b (Å)		*4.09417(4)*	-	-
c (Å)		*18.5539(1)*	*18.58267(1)*	*18.69481(9)*
V (Å^3)		*309.789(6)*	*310.908(4)*	*313.859(3)*
Pr *z* (*c*)		*0.18826(3)*	*0.18799(3)*	*0.18843(2)*
Se *z* (*c*)		*0.10167(3)*	*0.10143(3)*	*0.10164(3)*
O(1) *z* (*c*)		*0.2512(2)*	*0.25*	*0.25*
Pr U_{ij} (100×Å^2)	U_{11}	*0.43(5)*	*0.44(2)*	*0.81(2)*
	U_{22}	*0.68(6)*	*= U_{11}*	*= U_{11}*
	U_{33}	*1.01(4)*	*0.64(3)*	*1.38(3)*
Mn(1) U_{ij} (100×Å^2)	U_{11}	*0.25(9)*	*1.02(4)*	*1.83(4)*
	U_{22}	*0.0(1)*	*0.23(3)*	*0.63(3)*
	U_{33}	*0.6(1)*	*1.19(4)*	*2.31(5)*
Mn(2) U_{ij} (100×Å^2)	U_{11}	*0.5(1)*	-	-
	U_{22}	*3.4(2)*	-	-
	U_{33}	*2.2(2)*	-	-
Se U_{ij} (100×Å^2)	U_{11}	*0.91(5)*	*1.01(2)*	*1.35(2)*
	U_{22}	*1.84(6)*	*= U_{11}*	*= U_{11}*
	U_{33}	*1.29(2)*	*0.89(2)*	*1.21(2)*
O(1) U_{ij} (100×Å^2)	U_{11}	*0.65(6)*	*0.47(2)*	*0.89(2)*
	U_{22}	*0.90(7)*	*0.25(3)*	*0.62(3)*
	U_{33}	*1.15(3)*	*1.05(3)*	*1.31(3)*
O(2) U_{ij} (100×Å^2)	U_{11}	*0.3(1)*	*0.42(3)*	*0.84(3)*
	U_{22}	*1.3(1)*	*= U_{11}*	*= U_{11}*
	U_{33}	*14.4(1)*	*12.8(1)*	*9.44(9)*
Mn^{2+} M_z (μ_B)		*4.219(8)*	*3.838(8)*	-
N^o. variables		*78*	*74*	*68*
X-ray R_{wp} (%)		*5.55*	*3.89*	*3.18*
HRPD bs R_{wp} (%)		*6.37*	*5.55*	*4.53*
HRPD 90 R_{wp} (%)		*4.59*	*4.11*	*3.26*
Total R_{wp} (%)		*4.94*	*4.23*	*3.37*
χ^2		*4.61*	*5.49*	*3.07*

Rietveld plots for $Pr_2O_2Mn_2OSe_2$ at room temperature

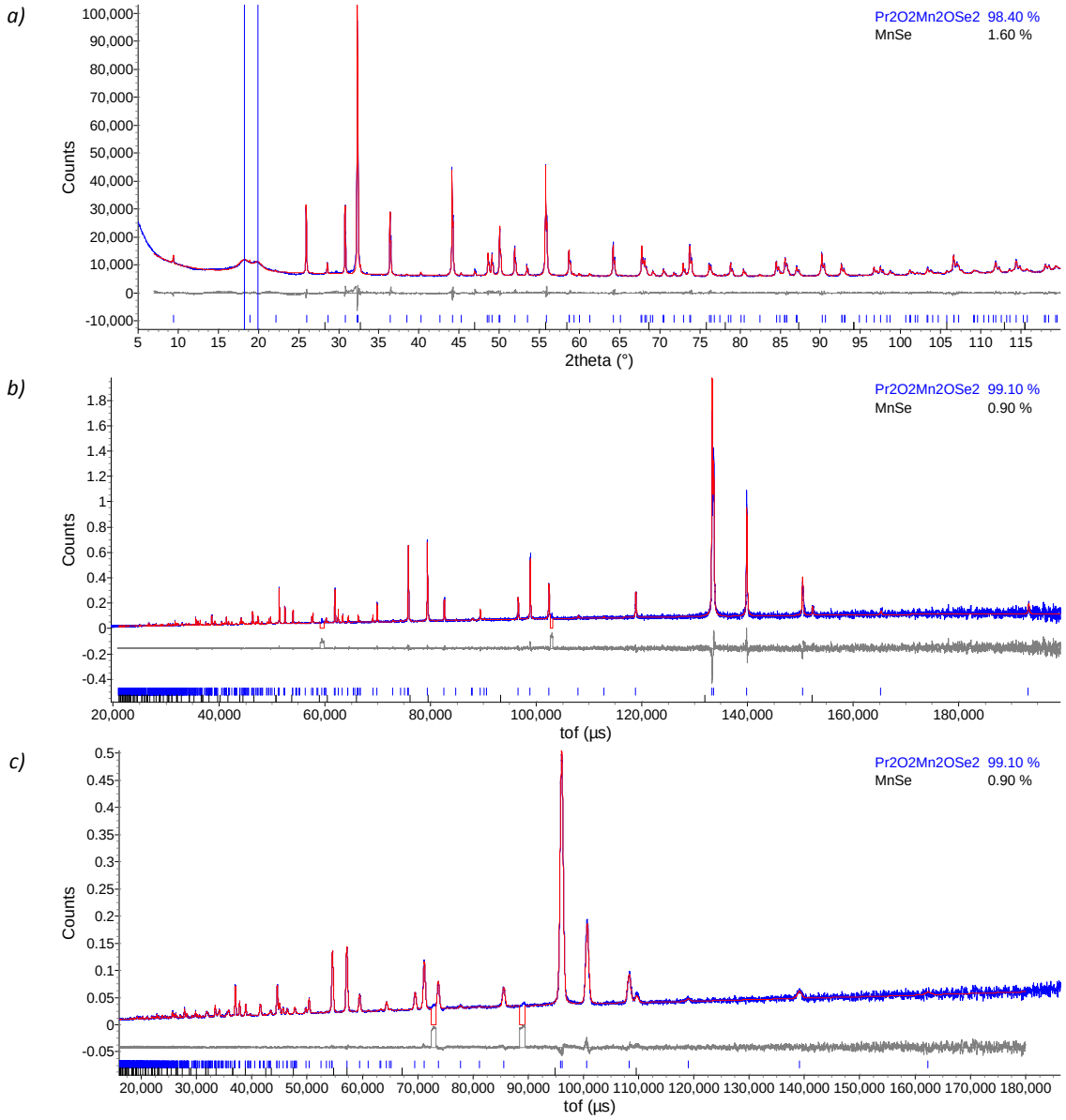

Rietveld plots for $Pr_2O_2Mn_2OSe_2$ at room temperature using (a) X-ray, (b) HRPD bs and (c) 90° bank data; observed = blue, calculated = red, difference = grey.

Rietveld plots for $Pr_2O_2Mn_2OSe_2$ at 72 K

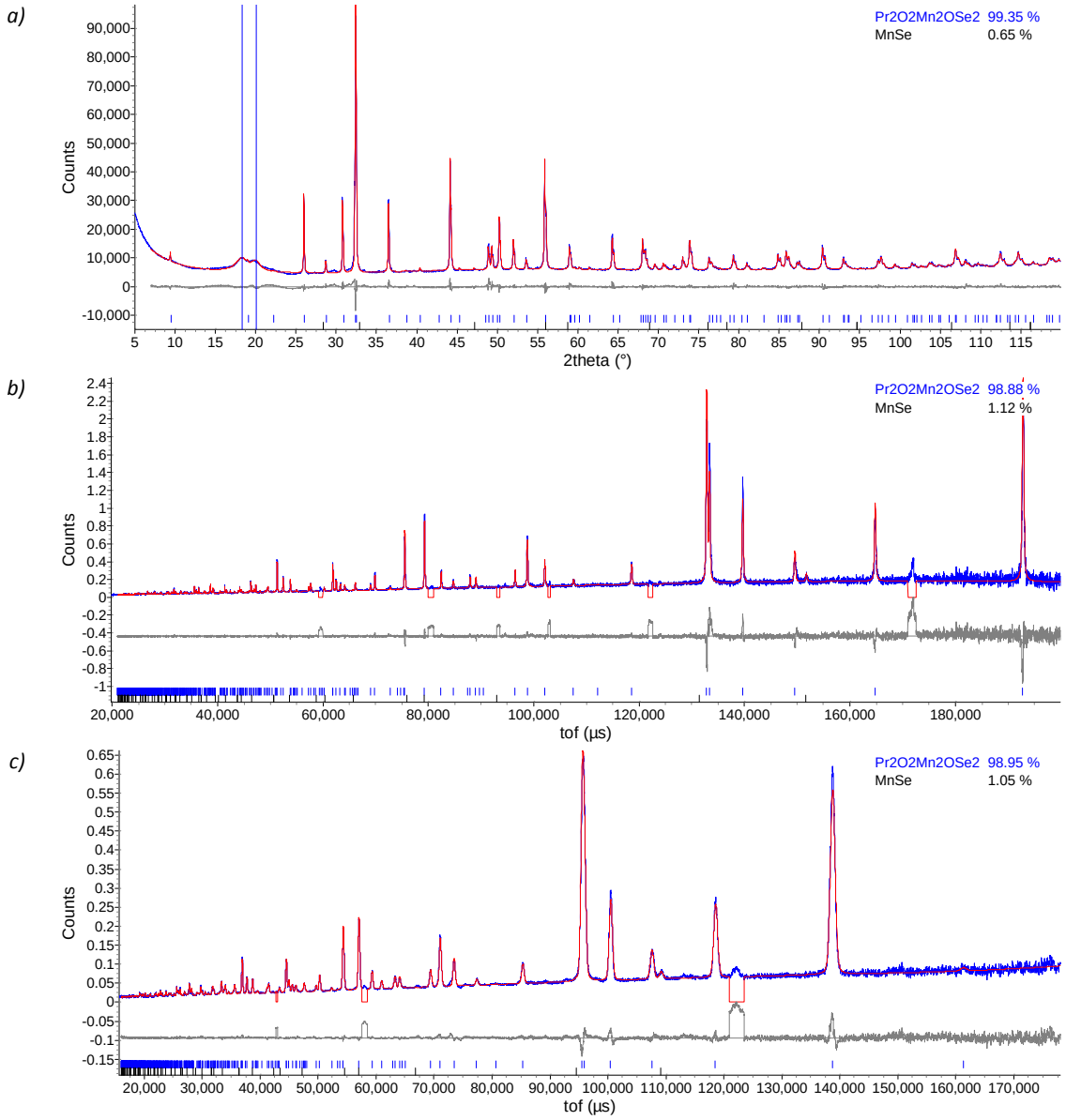

Rietveld plots for $Pr_2O_2Mn_2OSe_2$ at 72 K using (a) X-ray, (b) HRPD bs and (c) 90° bank data; observed = blue, calculated = red, difference = grey.

Rietveld plots for $Pr_2O_2Mn_2OSe_2$ at 12 K

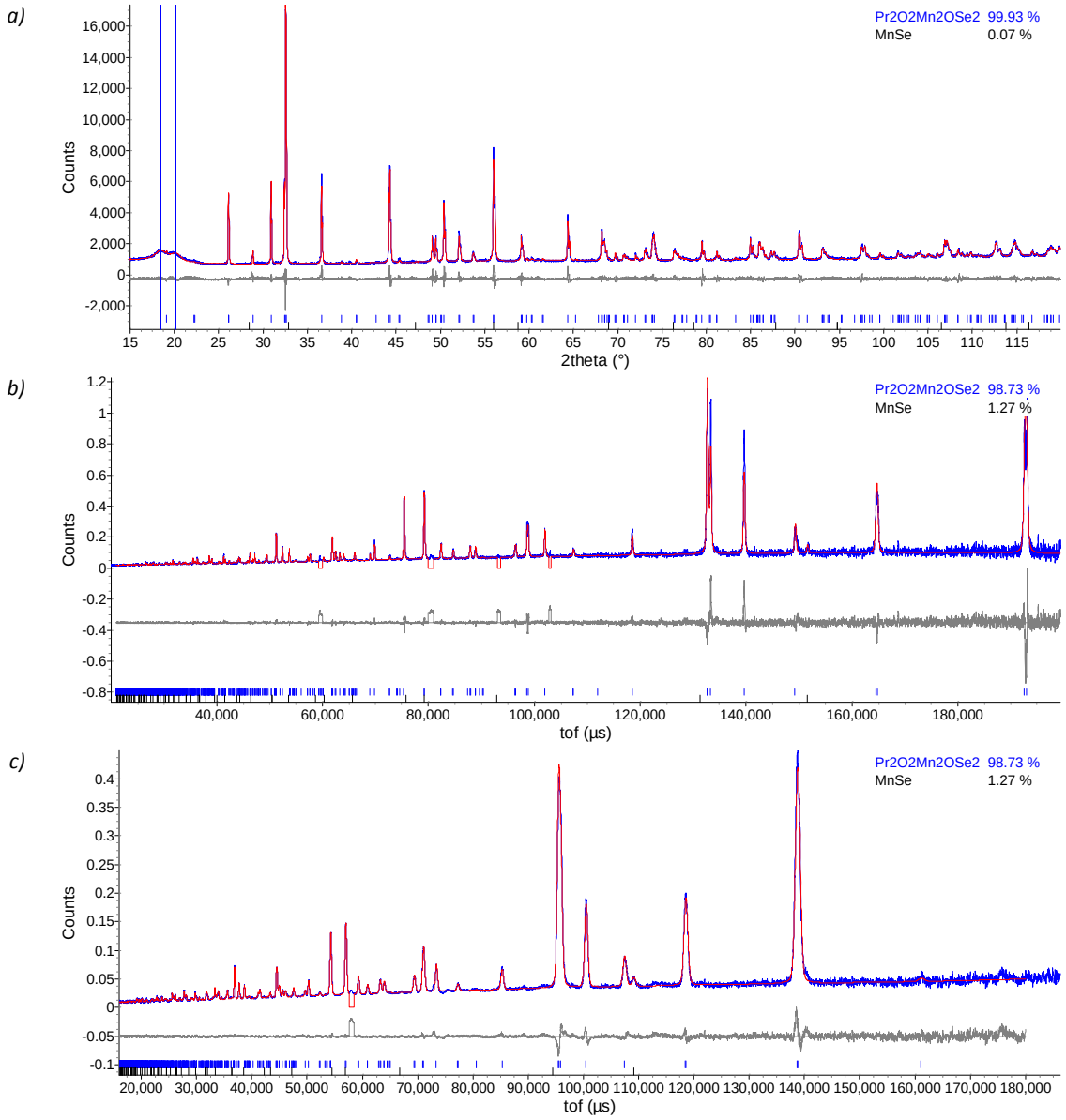

Rietveld plots for $Pr_2O_2Mn_2OSe_2$ at 12 K using (a) X-ray, (b) HRPD bs and (c) 90° bank data; observed = blue, calculated = red, difference = grey.

Variable temperature plots for $Pr_2O_2Mn_2OSe_2$

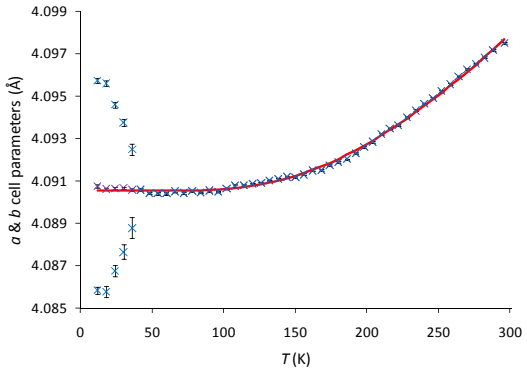

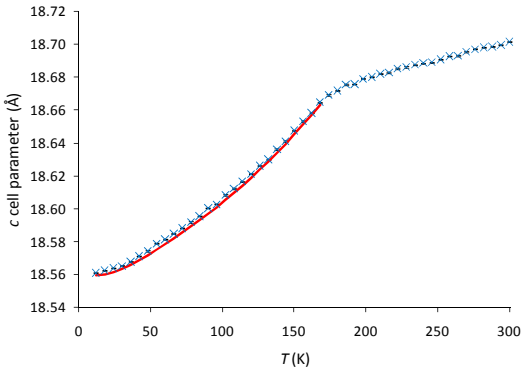

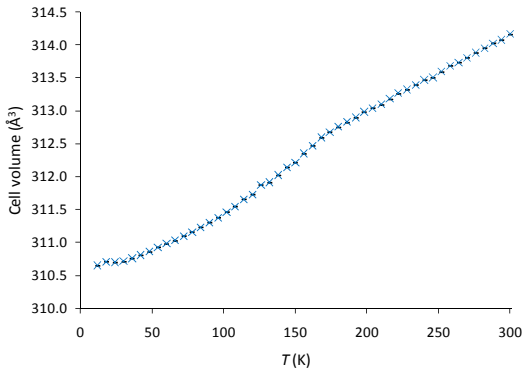

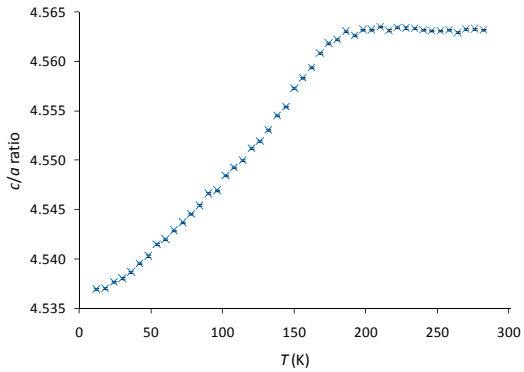

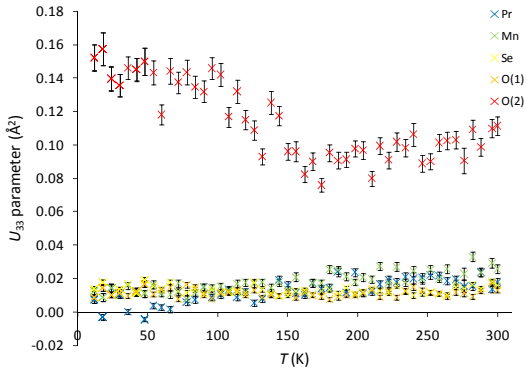

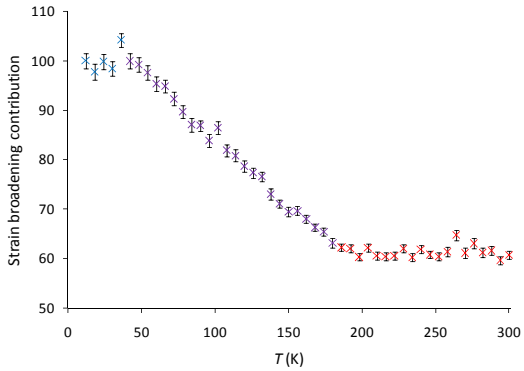

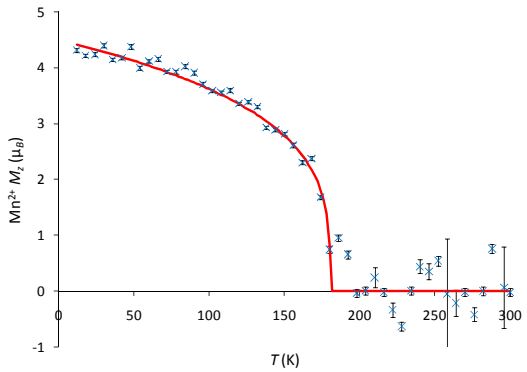

Refinement of the O(2) *z* coordinate in $Pr_2O_2Mn_2OSe_2$

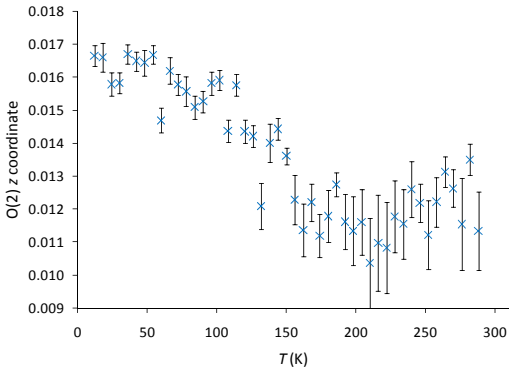

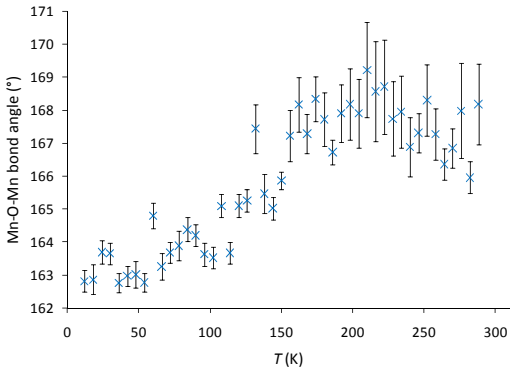

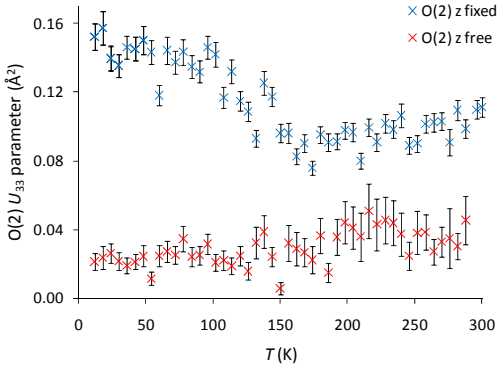

Superstructure peaks in $Pr_2O_2Mn_2OSe_2$

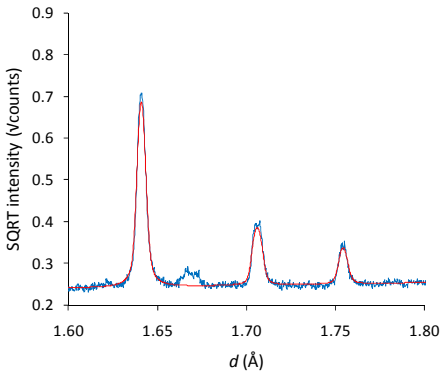

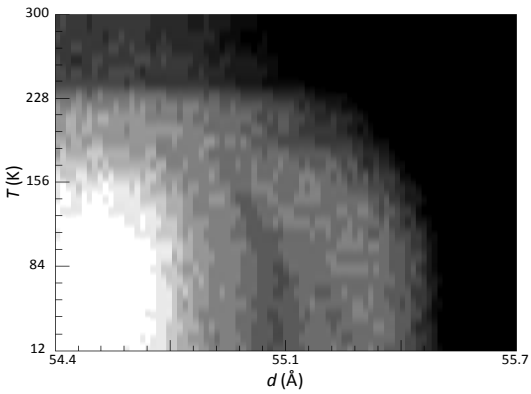

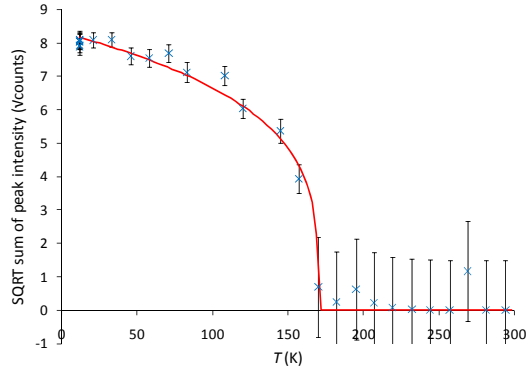

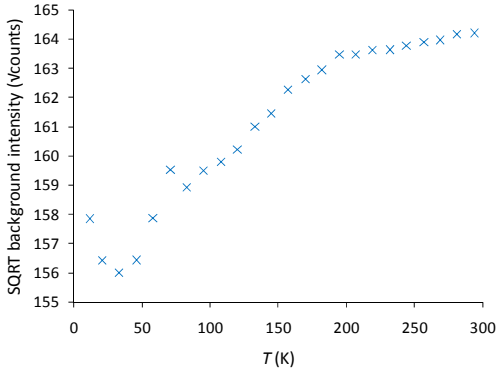

Modelled superstructure peak behaviour in $Pr_2O_2Mn_2OSe_2$

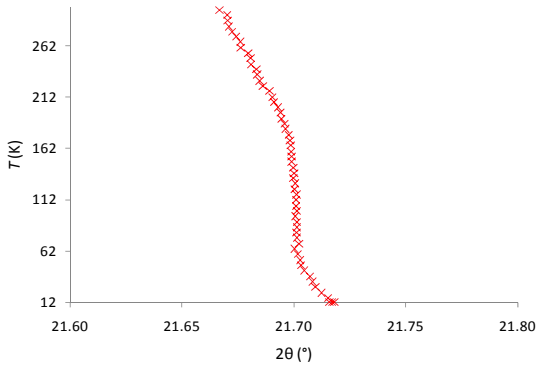

(100)

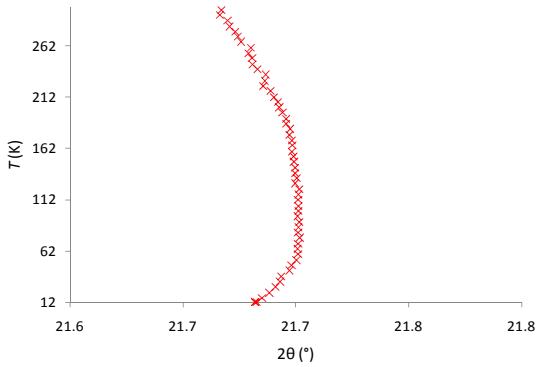

(010)

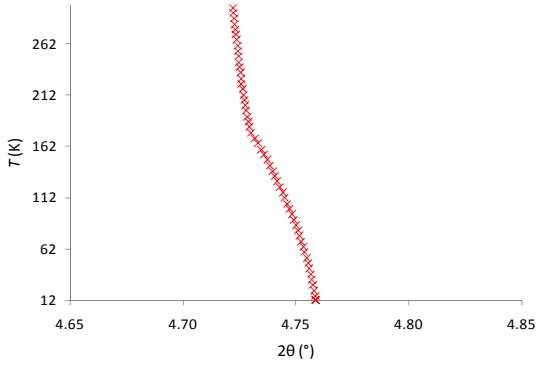

(001)

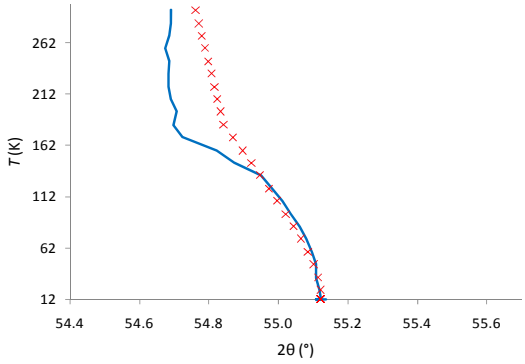

(hkl)

IV. Collation of data and analysis for $(La_{⅔}Nd_{⅓})_2O_2Mn_2OSe_2$

Results from X-ray Rietveld refinement of $(La_{⅔}Nd_{⅓})_2O_2Mn_2OSe_2$ at 12 K and room temperature.

	12 K	**295 K**
Sample	*DGF325*	*DGF325*
Input file(s)	*d9_04883_riet.inp*	*d9_04881_riet.inp*
Data file(s)	*d9_04883.raw*	*d9_04881.raw*
Nuclear symmetry	*I4/mmm*	*I4/mmm*
a (Å)	*4.1115(1)*	*4.1215(1)*
c (Å)	*18.7118(8)*	*18.7863(8)*
V (Å^3)	*316.32(2)*	*319.11(2)*
A z (*c*)	*0.1868(1)*	*0.1874(1)*
Se *z* (*c*)	*0.1004(2)*	*0.1011(2)*
A U_{iso} (100×Å^2)	*0.30(5)*	*0.76(6)*
Mn U_{iso} (100×Å^2)	*0.7(1)*	*1.7(1)*
Se U_{iso} (100×Å^2)	*0.62(8)*	*1.2(1)*
O(1) U_{iso} (100×Å^2)	*1.6(5)*	*0.0(4)*
O(2) U_{iso} (100×Å^2)	*2.7(9)*	*3(1)*
N°. variables	*29*	*29*
R_{wp} (%)	*9.37*	*9.25*
χ^2	*1.34*	*1.34*

Rietveld plots for $(La_{⅔}Nd_{⅓})_2O_2Mn_2OSe_2$ at room temperature and 12 K

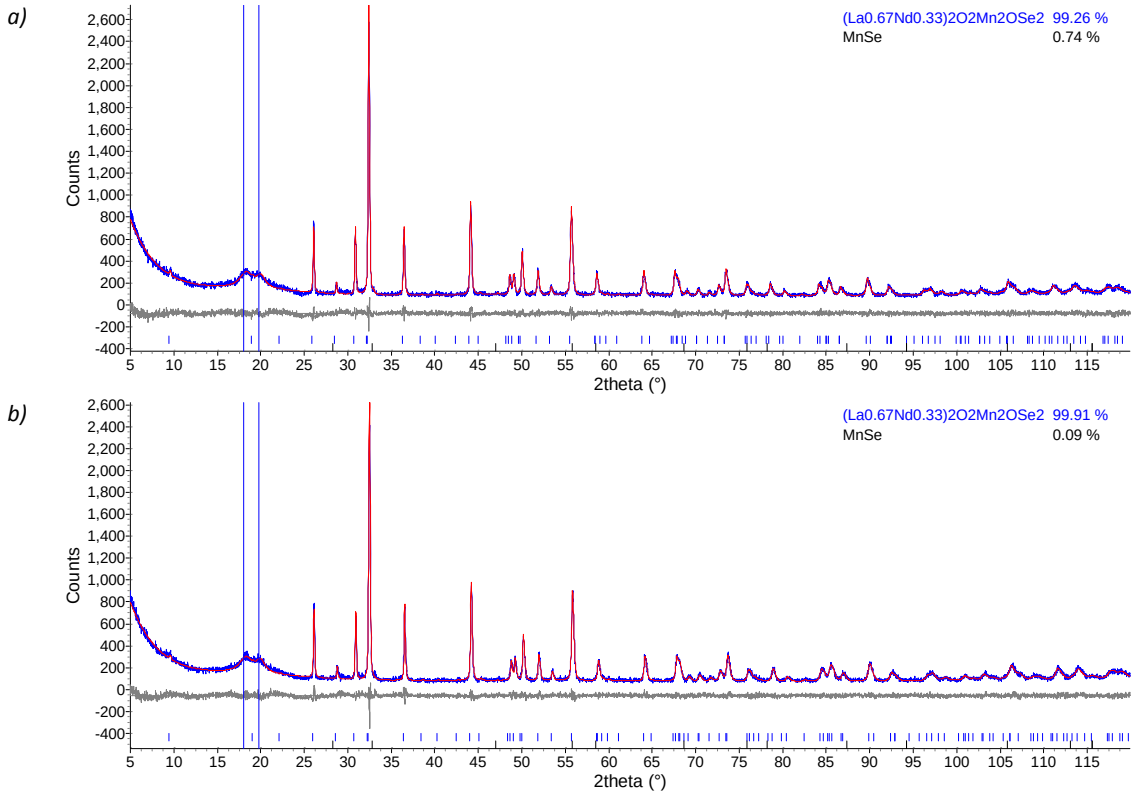

Rietveld plots for $(La_{⅔}Nd_{⅓})_2O_2Mn_2OSe_2$ at (a) room temperature and (b) 12 K; observed = blue, calculated = red, difference = grey.

V. Collation of data and analysis for $La_2O_2Fe_2OS_2$

Results from combined X-ray / neutron Rietveld refinements of $La_2O_2Fe_2OS_2$ at room temperature and 12 K.

		12 K	295 K
Sample		*DGF306*	*DGF306*
Input file(s)		*combined_riet.inp*	*combined_riet.inp*
Data file(s)		*d9_04646_sum.raw*	*d9_04634_sum.raw*
		hrp46728_b1_TOF.xye	*hrp46778_b1_TOF.xye*
		hrp46728_b2_TOF.xye	*hrp46778_b2_TOF.xye*
		hrp46728_b3_TOF.xye	*hrp46778_b3_TOF.xye*
Nuclear symmetry		*I*4/*mmm*	*I*4/*mmm*
Magnetic symmetry		P_s1	-
a (Å)		*4.03287(4)*	*4.04042(5)*
c (Å)		*17.8140(2)*	*17.8803(2)*
V (Å^3)		*289.727(6)*	*291.895(8)*
La *z* (*c*)		*0.18054(3)*	*0.18075(3)*
S *z* (*c*)		*0.0937(1)*	*0.0936(1)*
La U_{ij} (100×Å^2)	U_{11}	*0.77(2)*	*0.49(4)*
	U_{22}	$= U_{11}$	$= U_{11}$
	U_{33}	*0.97(5)*	*0.47(5)*
Fe U_{ij} (100×Å^2)	U_{11}	*1.09(3)*	*1.14(5)*
	U_{22}	$= U_{11}$	*0.48(5)*
	U_{33}	*1.17(5)*	*1.41(5)*
S U_{ij} (100×Å^2)	U_{11}	*1.19(6)*	*1.05(7)*
	U_{22}	$= U_{11}$	$= U_{11}$
	U_{33}	*0.96(7)*	*0.9(1)*
O(1) U_{ij} (100×Å^2)	U_{11}	*0.87(4)*	*0.39(6)*
	U_{22}	$= U_{11}$	*0.43(7)*
	U_{33}	*0.96(7)*	*0.84(7)*
O(2) U_{ij} (100×Å^2)	U_{11}	*0.66(5)*	*0.36(6)*
	U_{22}	$= U_{11}$	$= U_{11}$
	U_{33}	*1.9(1)*	*3.4(1)*
Fe^{2+} M_x (μ_B)		*2.60(3)*	-
N°. variables		*96*	*96*
X-ray R_{wp} (%)		*3.40*	*3.17*
HRPD bs R_{wp} (%)		*5.93*	*5.19*
HRPD 90 R_{wp} (%)		*3.71*	*2.89*
HRPD 30 R_{wp} (%)		*7.24*	*8.31*
Total R_{wp} (%)		*3.99*	*3.49*
χ^2		*5.49*	*3.46*

Variable temperature plots for $La_2O_2Fe_2OS_2$

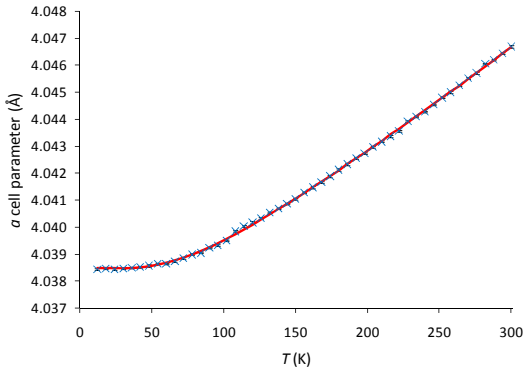

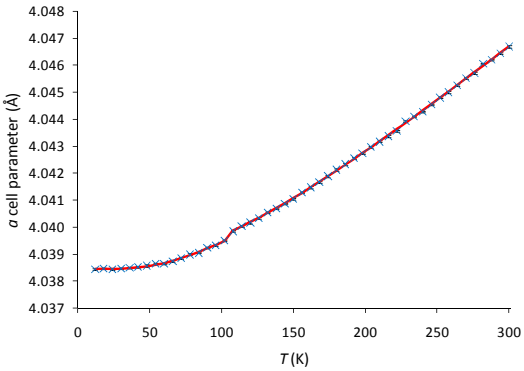

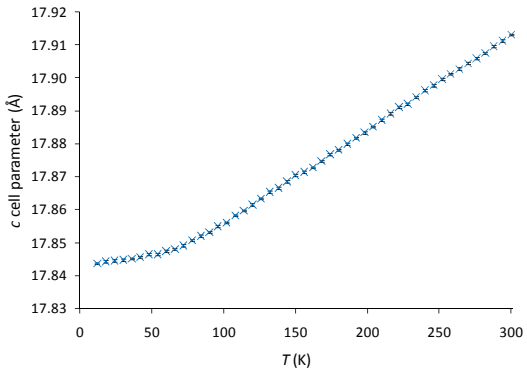

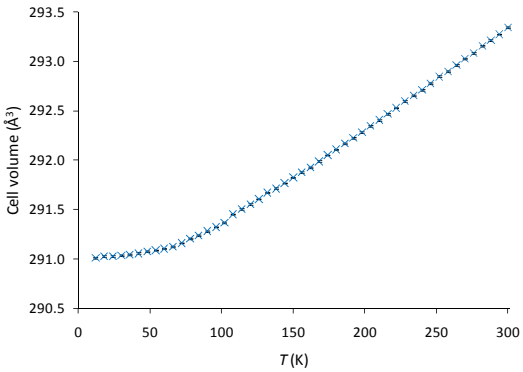

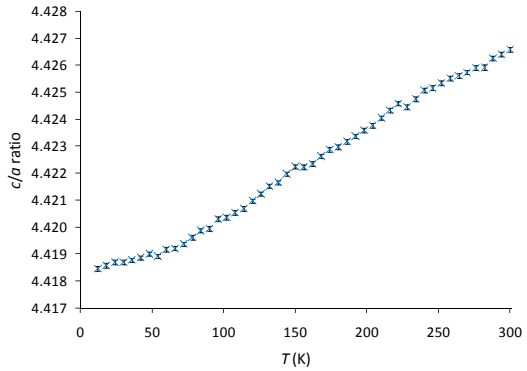

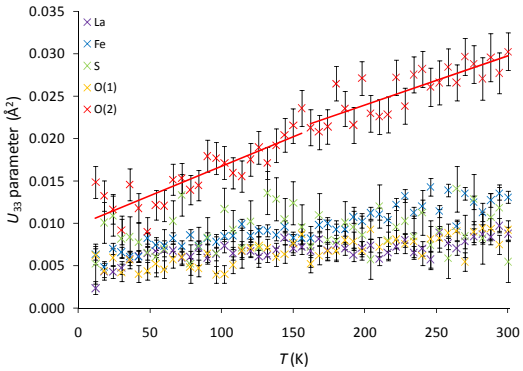

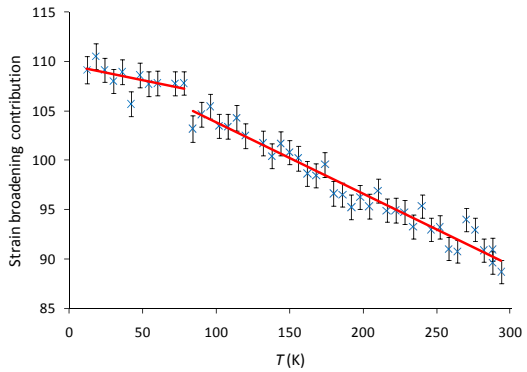

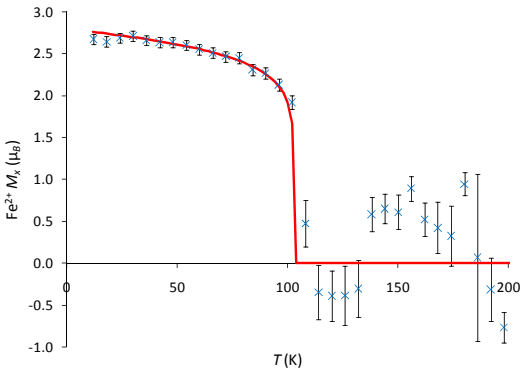

VI. Collation of data and analysis for $La_2O_2Fe_2OSe_2$

Results from combined X-ray / neutron Rietveld refinement of $La_2O_2Fe_2OSe_2$ at 12 K and room temperature.

		12 K	**295 K**
Sample		*DGF213*	*DGF213*
Input file(s)		*combined_riet.inp*	*combined_riet.inp*
Data file(s)		*d9_04095.raw*	*d9_04096.raw*
		hrp45526_b1_TOF.xye	*hrp45577_b1_TOF.xye*
		hrp45526_b2_TOF.xye	*hrp45577_b2_TOF.xye*
		hrp45526_b3_TOF.xye	*hrp45577_b3_TOF.xye*
Nuclear symmetry		*I4/mmm*	*I4/mmm*
Magnetic symmetry		P_S1	-
a (Å)		*4.03287(4)*	*4.08475(1)*
c (Å)		*17.8140(2)*	*18.59736(9)*
V (Å^3)		*289.727(6)*	*310.301(3)*
La *z* (*c*)		*0.18054(3)*	*0.18436(3)*
Se *z* (*c*)		*0.0937(1)*	*0.09637(4)*
La U_{ij} (100×Å^2)	U_{11}	*0.75(2)*	*0.41(3)*
	U_{22}	$= U_{11}$	$= U_{11}$
	U_{33}	*0.70(3)*	*0.23(4)*
Fe U_{ij} (100×Å^2)	U_{11}	*0.86(2)*	*0.61(5)*
	U_{22}	$= U_{11}$	*0.47(5)*
	U_{33}	*1.01(3)*	*1.00(5)*
Se U_{ij} (100×Å^2)	U_{11}	*0.79(2)*	*0.59(4)*
	U_{22}	$= U_{11}$	$= U_{11}$
	U_{33}	*0.86(3)*	*0.45(5)*
O(1) U_{ij} (100×Å^2)	U_{11}	*0.89(3)*	*0.32(6)*
	U_{22}	$= U_{11}$	*0.25(8)*
	U_{33}	*1.06(4)*	*0.84(7)*
O(2) U_{ij} (100×Å^2)	U_{11}	*0.91(4)*	*0.46(7)*
	U_{22}	$= U_{11}$	$= U_{11}$
	U_{33}	*1.32(6)*	*2.6(1)*
Fe^{2+} M_x (μ_B)		*2.69(4)*	-
N^o. variables		*88*	*88*
X-ray R_{wp} (%)		*2.99*	*2.96*
HRPD bs R_{wp} (%)		*4.68*	*5.80*
HRPD 90 R_{wp} (%)		*3.63*	*3.33*
HRPD 30 R_{wp} (%)		*9.43*	*13.77*
Total R_{wp} (%)		*3.40*	*3.29*
χ^2		*4.06*	*2.88*

Variable temperature plots for $La_2O_2Fe_2OSe_2$

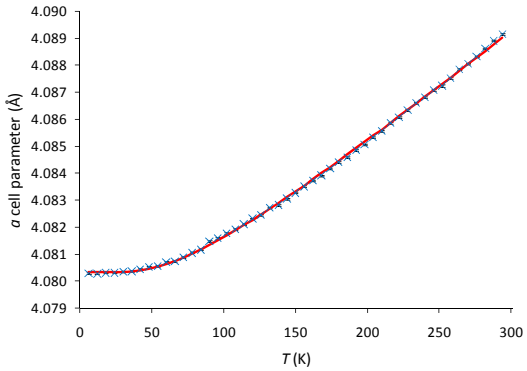

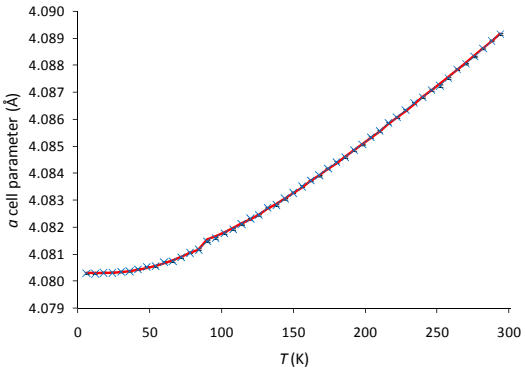

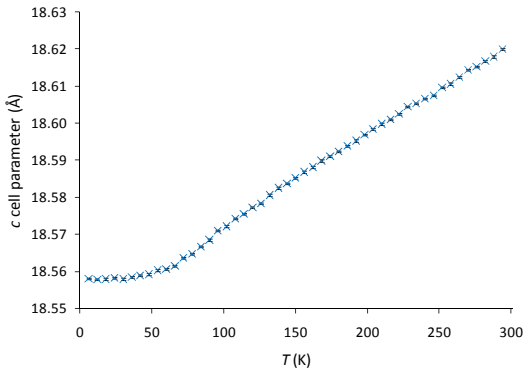

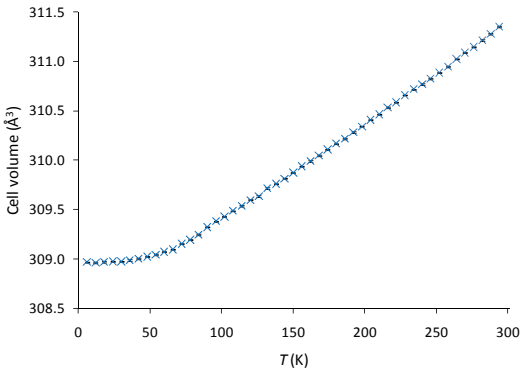

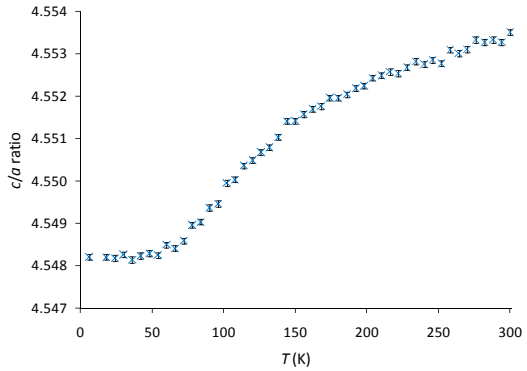

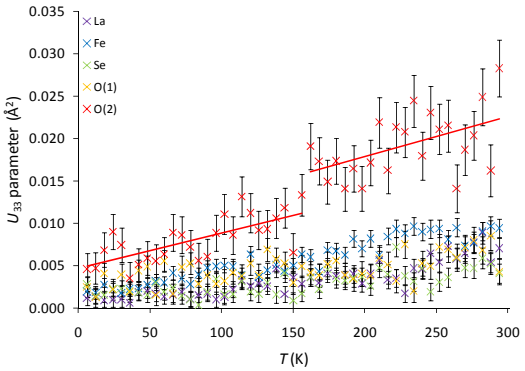

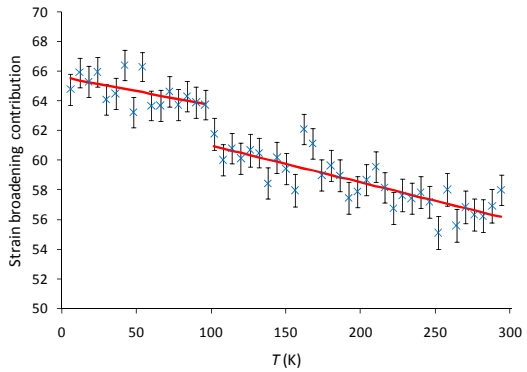

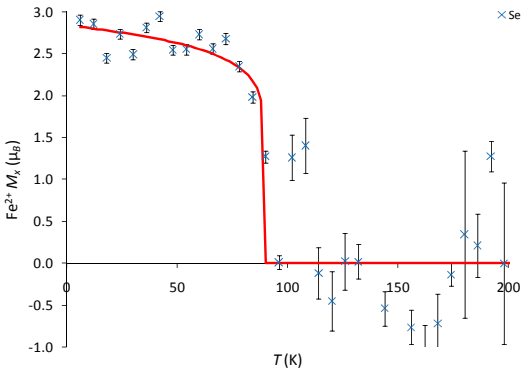

SARAh analysis of $La_2O_2Fe_2OSe_2$ – mixing of all allowed Fe^{2+} basis vectors

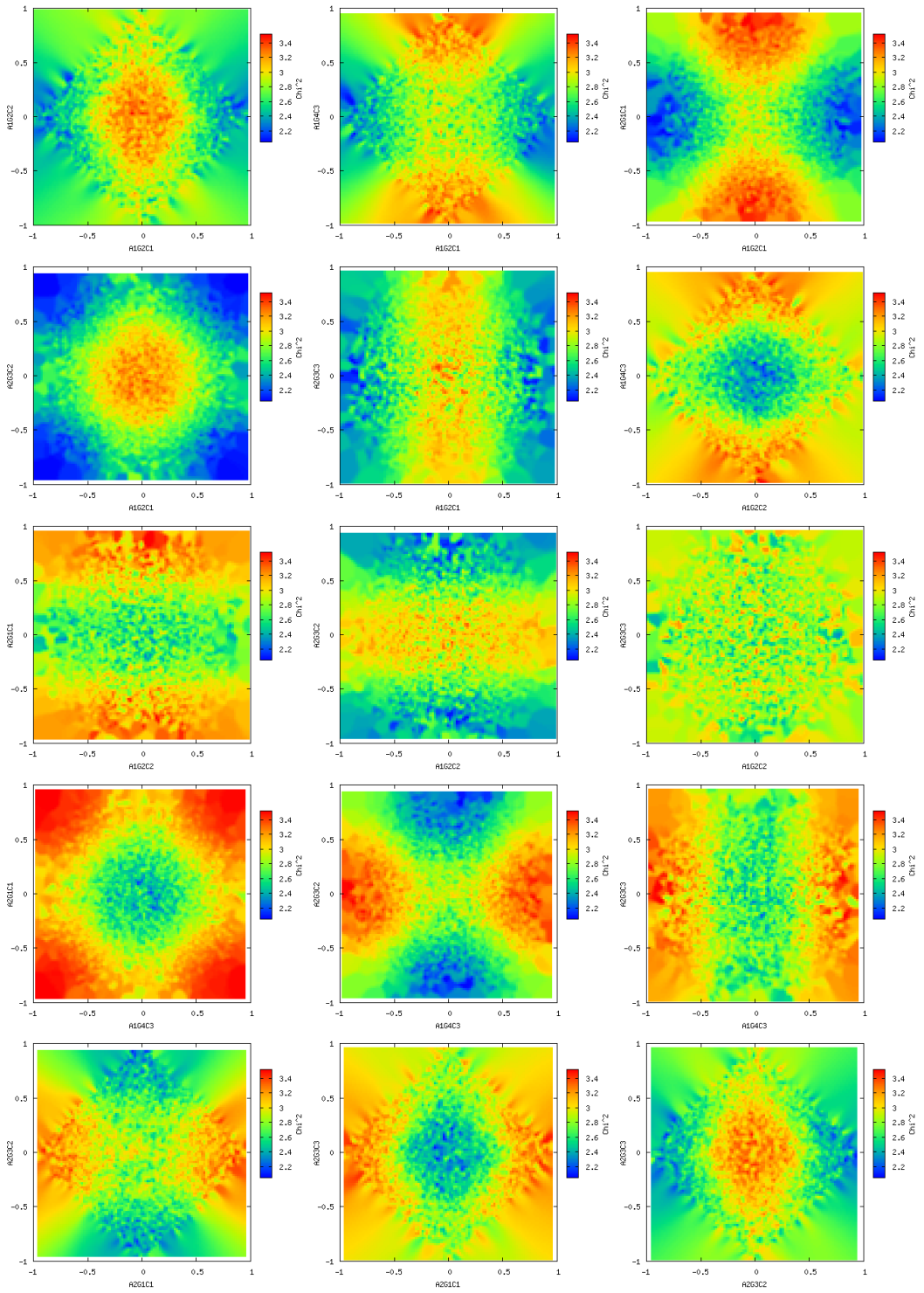

VII. Collation of data and analysis for $Ce_2O_2Fe_2OSe_2$

Results from X-ray Rietveld refinement of $Ce_2O_2Fe_2OSe_2$ at room temperature.

	295 K
Sample	*DGF306*
Input file(s)	*d9_03016_riet.inp*
Data file(s)	*d9_03016.raw*
Nuclear symmetry	*I*4/*mmm*
a (Å)	*4.05928(9)*
c (Å)	*18.4638(5)*
V (Å^3)	*304.24(2)*
Ce *z* (*c*)	*0.18471(8)*
Se *z* (*c*)	*0.0975(2)*
Ce U_{iso} (100×Å^2)	*0.48(5)*
Fe U_{iso} (100×Å^2)	*0.9(1)*
Se U_{iso} (100×Å^2)	*0.77(8)*
O(1) U_{iso} (100×Å^2)	*1.6(4)*
O(2) U_{iso} (100×Å^2)	*2.9(8)*
N^o. variables	*28*
X-ray R_{wp} (%)	*4.34*
χ^2	*3.94*

VIII. Collation of data and analysis for $Pr_2O_2Fe_2OSe_2$

Results from X-ray Rietveld refinement of $Pr_2O_2Fe_2OSe_2$ at 12 K and room temperature.

	12 K	**295 K**
Sample	*DGF031*	*DGF031*
Input file(s)	*d9_02807_lt_riet.inp*	*d9_02807_rt_riet.inp*
Data file(s)	*d9_02807_lt.raw*	*d9_02807_rt.raw*
Nuclear symmetry	*I4/mmm*	*I4/mmm*
a (Å)	*4.03756(4)*	*4.04351(4)*
c (Å)	*18.3837(3)*	*18.4476(3)*
V (Å^3)	*299.689(7)*	*301.618(7)*
Pr *z* (*c*)	*0.18581(6)*	*0.18593(6)*
Se *z* (*c*)	*0.0983(1)*	*0.0985(1)*
Pr U_{iso} (100×Å^2)	*-0.03(3)*	*0.29(3)*
Fe U_{iso} (100×Å^2)	*0.18(7)*	*0.67(7)*
Se U_{iso} (100×Å^2)	*0.28(5)*	*0.77(6)*
O(1) U_{iso} (100×Å^2)	*0.4(3)*	*0.6(3)*
O(2) U_{iso} (100×Å^2)	*-0.3(4)*	*0.4(4)*
N^o. variables	*26*	*26*
X-ray R_{wp} (%)	*4.81*	*4.70*
χ^2	*1.69*	*1.68*

Variable temperature plots for $Pr_2O_2Fe_2OSe_2$

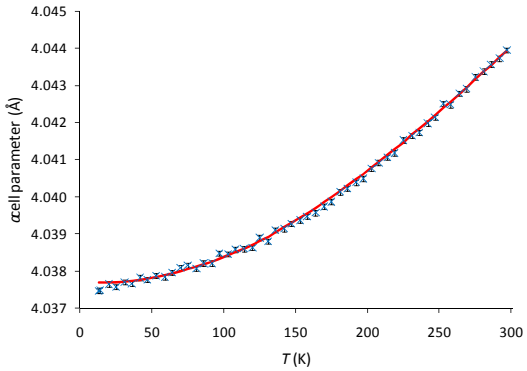

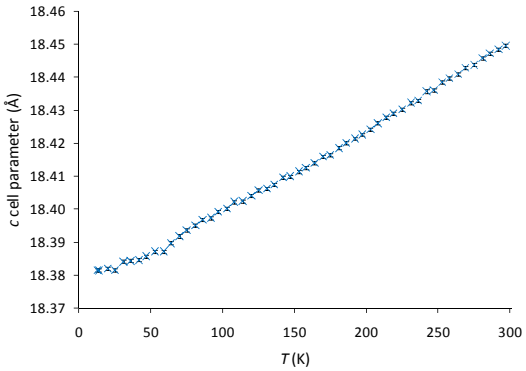

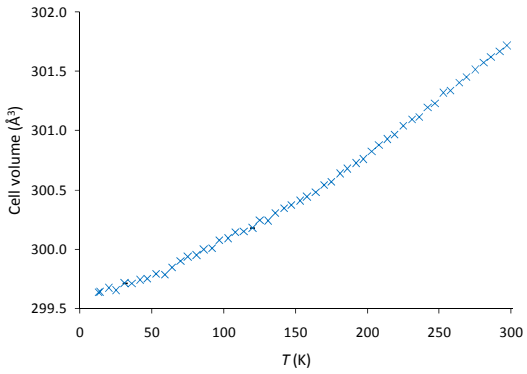

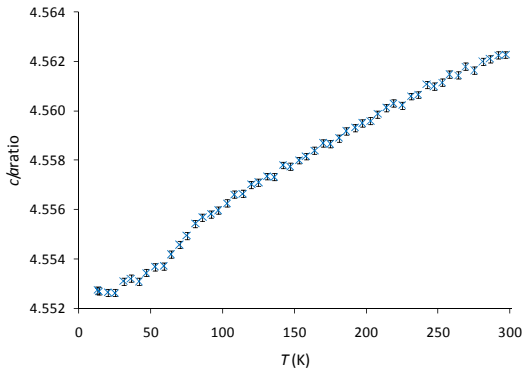

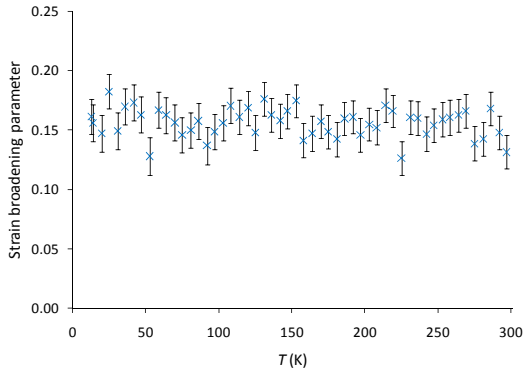

IX. Collation of data and analysis for $A_2O_2(Mn_{0.5}Fe_{0.5})_2OSe_2$

Results from X-ray Rietveld refinement of $A_2O_2(Mn_{0.5}Fe_{0.5})_2OSe_2$ materials at room temperature.

	La	**Pr**	**Nd**
Sample	*DGF118a*	*DGF118b*	*DGF118c*
Input file(s)	*d5_07997_riet.inp*	*d5_07998_riet.inp*	*d5_08000_riet.inp*
Data file(s)	*d5_07997.raw*	*d5_07998.raw*	*d5_08000.raw*
Nuclear symmetry	*I*4/*mmm*	*I*4/*mmm*	*I*4/*mmm*
a (Å)	*4.11210(3)*	*4.07108(5)*	*4.05332(5)*
c (Å)	*18.7723(2)*	*18.6201(4)*	*18.6072(4)*
V (Å^3)	*317.428(6)*	*308.60(1)*	*305.71(1)*
La *z* (*c*)	*0.18552(6)*	*0.18699(6)*	*0.18721(7)*
Se *z* (*c*)	*0.0982(1)*	*0.1001(1)*	*0.1001(2)*
A U_{iso} (100×Å^2)	*-0.05(3)*	*-0.09(3)*	*0.26(4)*
M U_{iso} (100×Å^2)	*0.60(8)*	*0.47(8)*	*0.7(1)*
Se U_{iso} (100×Å^2)	*0.40(5)*	*0.15(5)*	*0.32(6)*
O(1) U_{iso} (100×Å^2)	*1.3(3)*	*1.1(3)*	*2.7(5)*
O(2) U_{iso} (100×Å^2)	*0.8(4)*	*1.0(5)*	*-2.2(3)*
N^o. variables	*25*	*25*	*33*
X-ray R_{wp} (%)	*15.23*	*14.88*	*16.98*
χ^2	*3.40*	*3.01*	*3.72*

Rietveld plots for $A_2O_2(Mn_{0.5}Fe_{0.5})_2OSe_2$ materials at room temperature

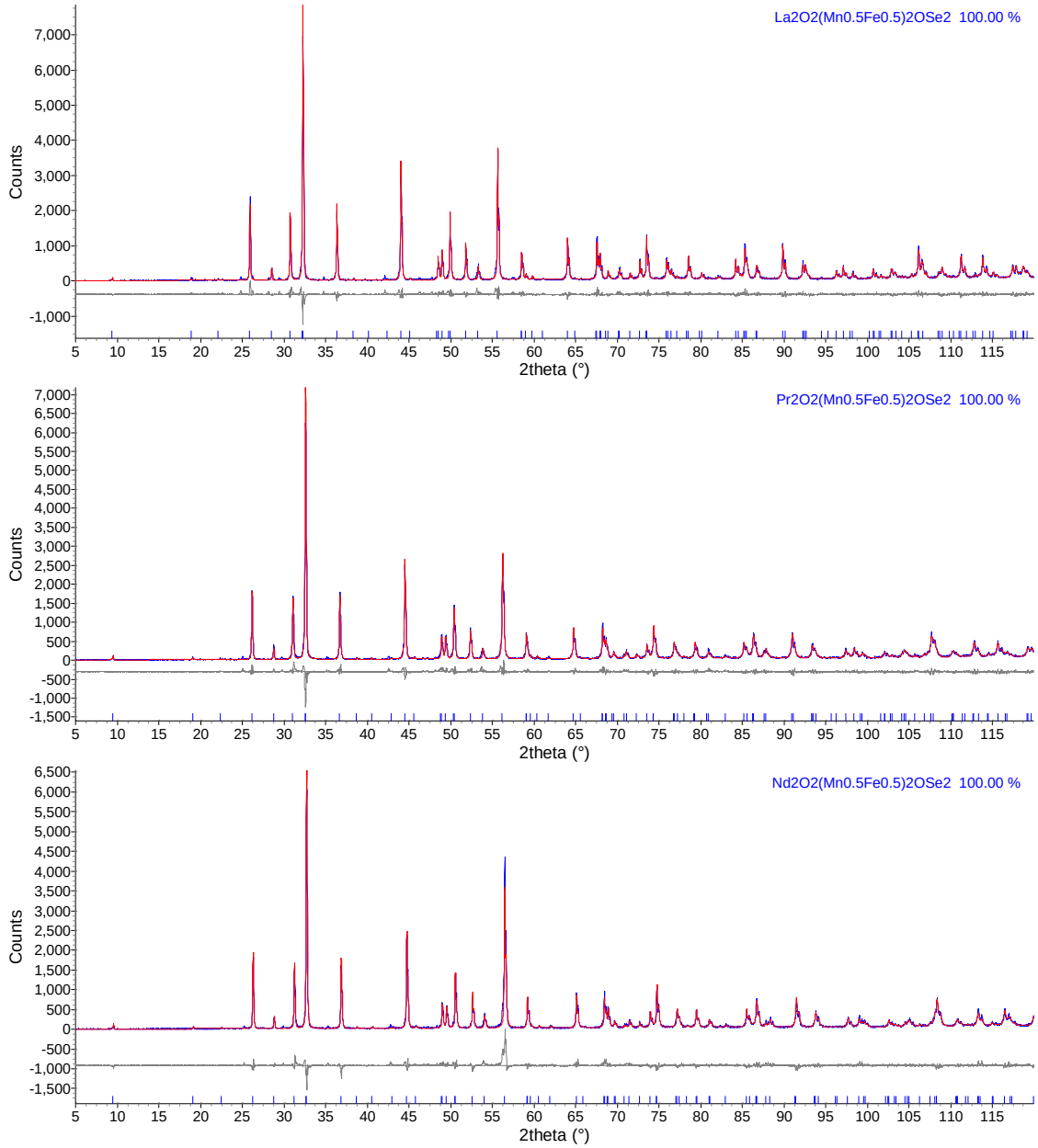

Rietveld plots for (a) $La_2O_2(Mn_{0.5}Fe_{0.5})_2OSe_2$, (b) $Pr_2O_2(Mn_{0.5}Fe_{0.5})_2OSe_2$ and (c) $Nd_2O_2(Mn_{0.5}Fe_{0.5})_2OSe_2$ at room temperature using X-ray data; observed = blue, calculated = red, difference = grey.

X. Collation of data and analysis for $La_2O_2Co_2OSe_2$

Results from neutron Rietveld refinement of $La_2O_2Co_2OSe_2$ at 12 K.

	12 K
Sample	*NDW328*
Input file(s)	*SEPD21196_RIET.EXP*
Data file(s)	*sepd21196.gdat*
Nuclear symmetry	*I4/mmm*
Magnetic symmetry	*$P_C mmn$*
a (Å)	*4.0599(3)*
c (Å)	*18.377(1)*
V (Å^3)	*302.92(2)*
La *z* (*c*)	*0.18317(5)*
Se *z* (*c*)	*0.09515(6)*
La U_{iso} (100×Å^2)	*0.34(2)*
Co U_{iso} (100×Å^2)	*0.51(5)*
Se U_{iso} (100×Å^2)	*0.36(2)*
O(1) U_{iso} (100×Å^2)	*0.42(3)*
O(2) U_{iso} (100×Å^2)	*0.91(4)*
Co^{2+} $M_{x,y}$ (μ_B)	*3.78(6)*
N^o. variables	*59*
SEPD 145 R_{wp} (%)	*6.17*
SEPD 90 R_{wp} (%)	*7.84*
SEPD 44 R_{wp} (%)	*7.26*
Total R_{wp} (%)	*6.89*
χ^2	*3.33*

Rietveld plots for $La_2O_2Co_2OSe_2$ at 12 K

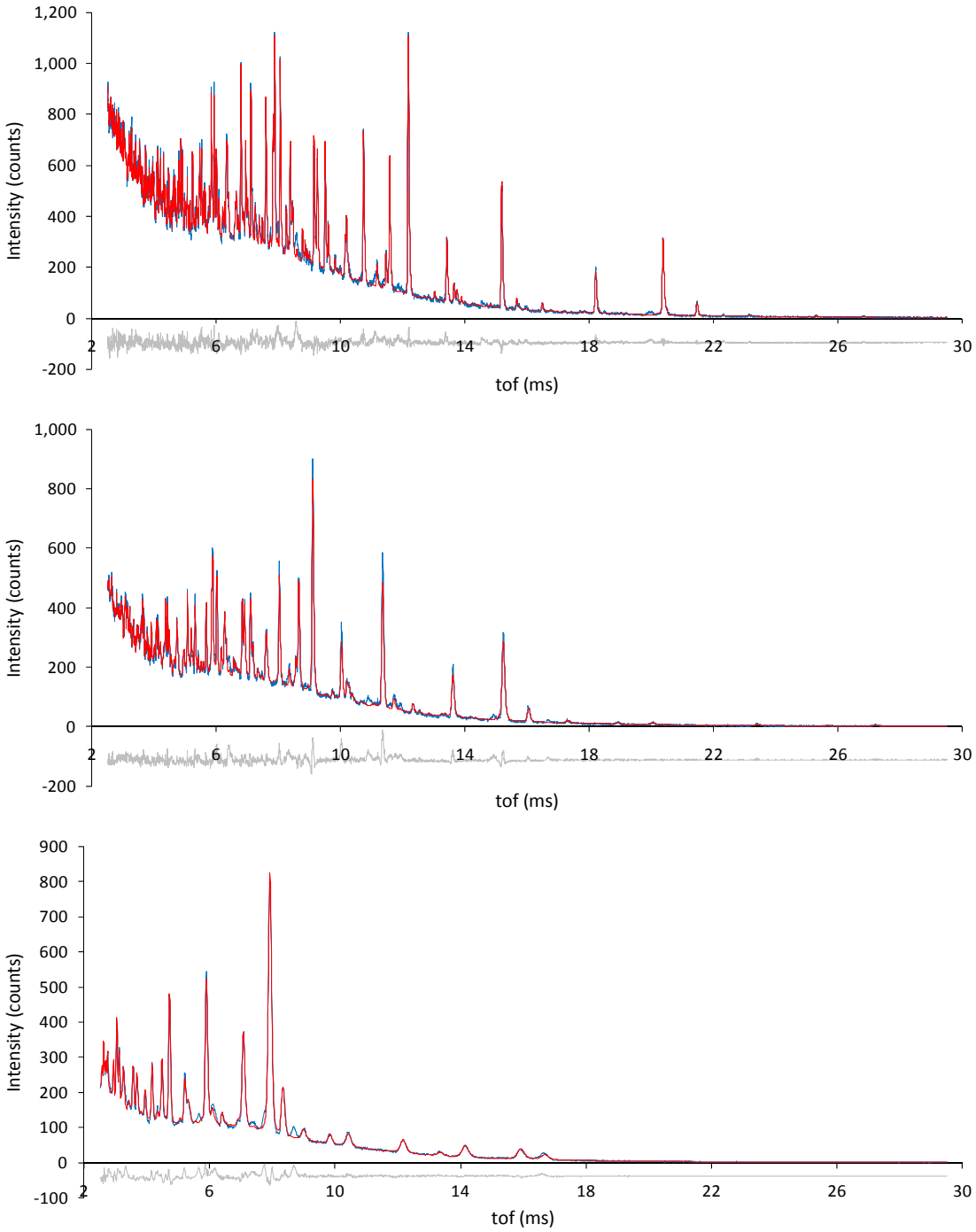

Rietveld plots for $La_2O_2Co_2OSe_2$ at 12 K using (a) 145°, (b) 90°, and (c) 44° bank SEPD data; observed = blue, calculated = red, difference = grey.

SARAh analysis of $La_2O_2CoOSe_2$ – mixing of all allowed Co^{2+} basis vectors

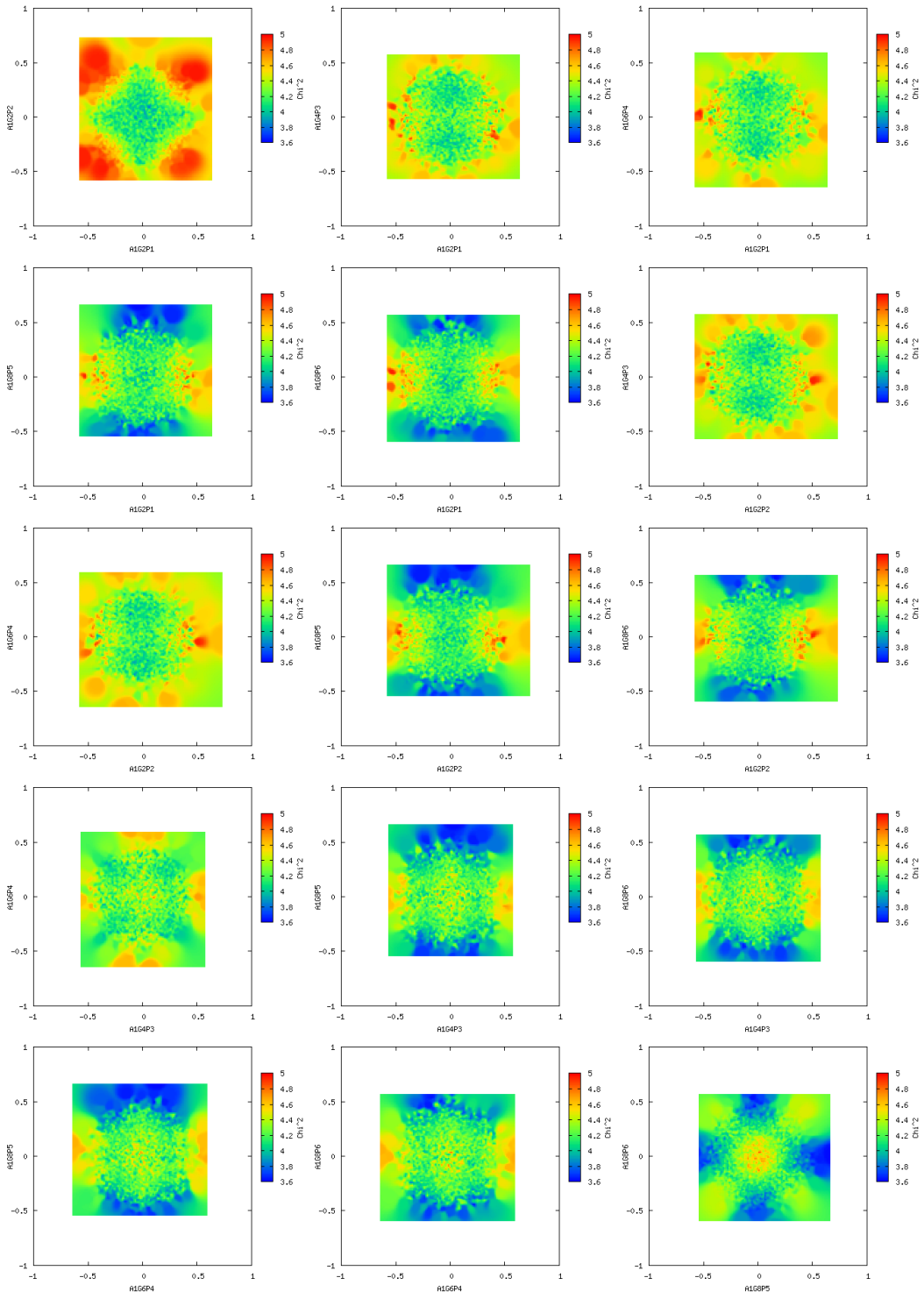

XI. Collation of data and analysis for Structural Comparisons

Lattice parameters – variation of *A*

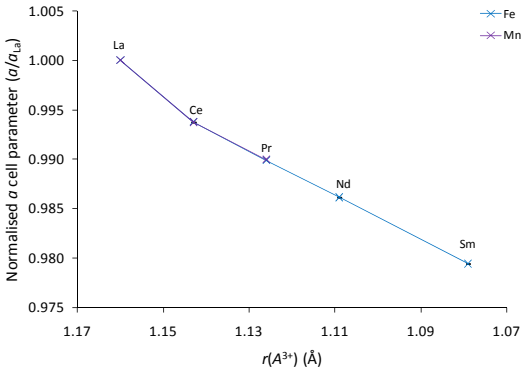

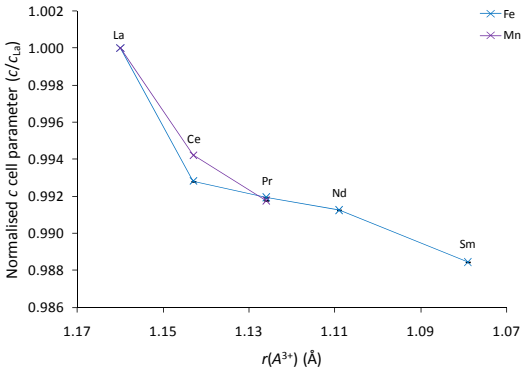

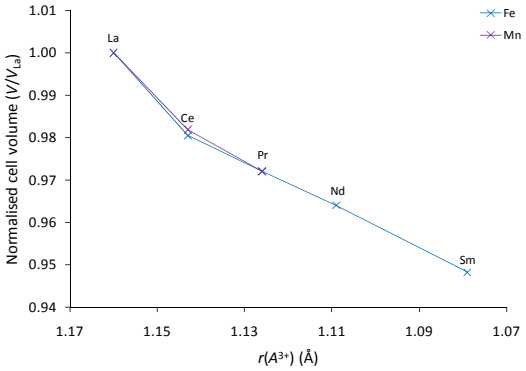

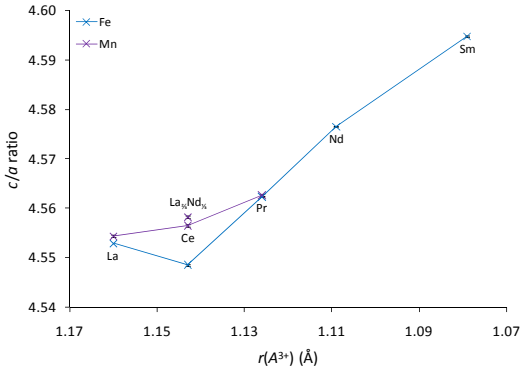

Lattice parameters – variation of *M*

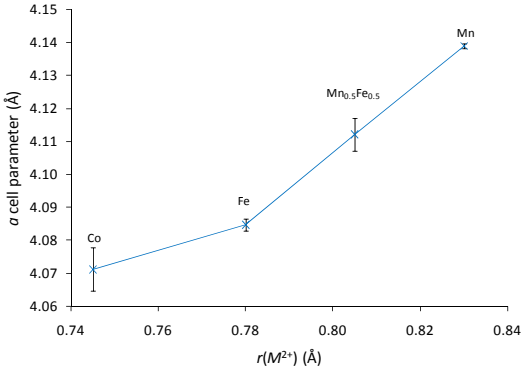

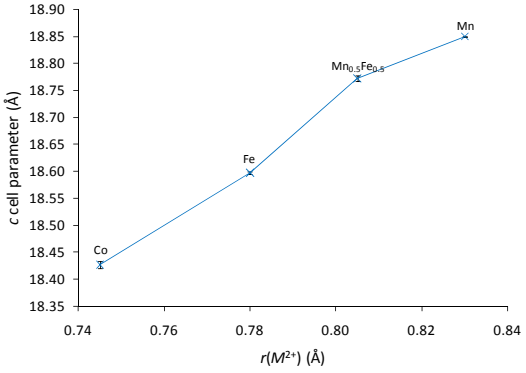

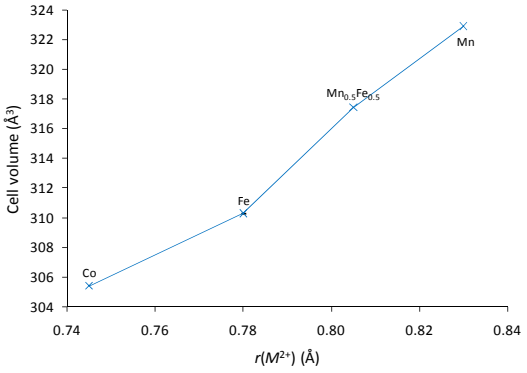

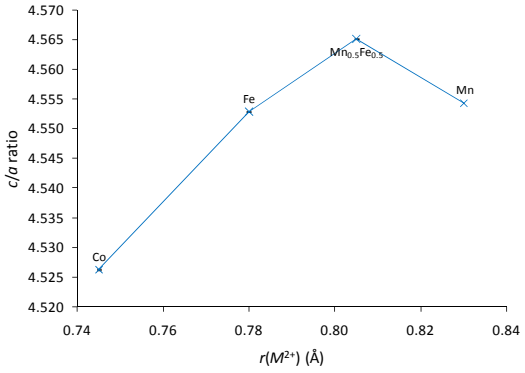

Bond lengths – variation of *A*

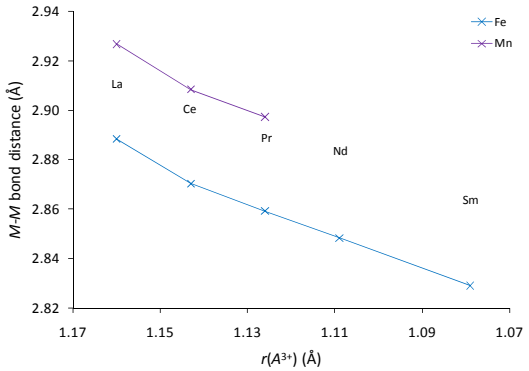

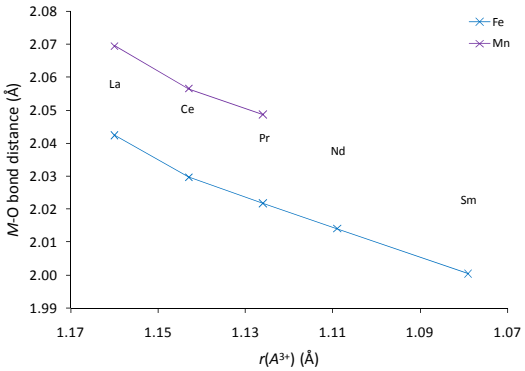

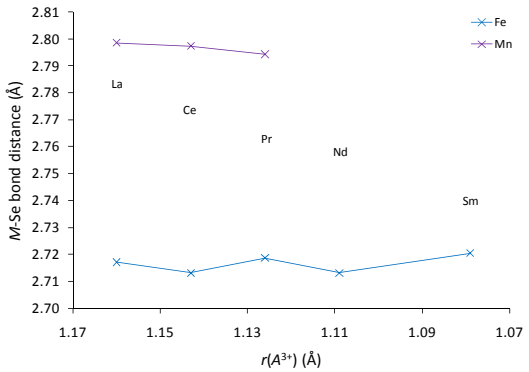

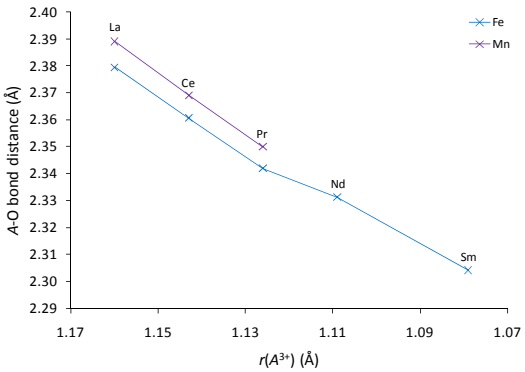

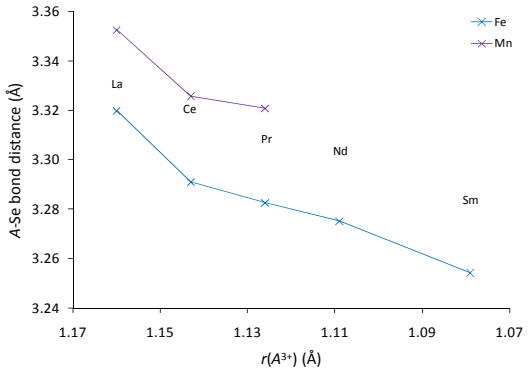

Bond lengths – variation of *M*

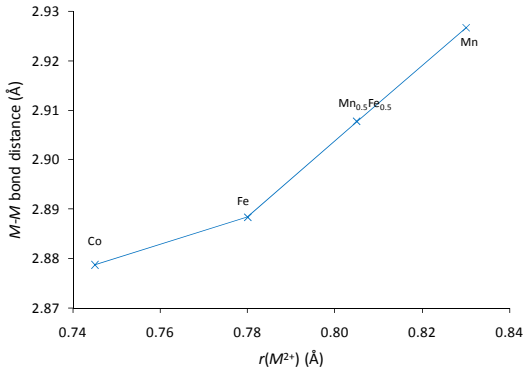

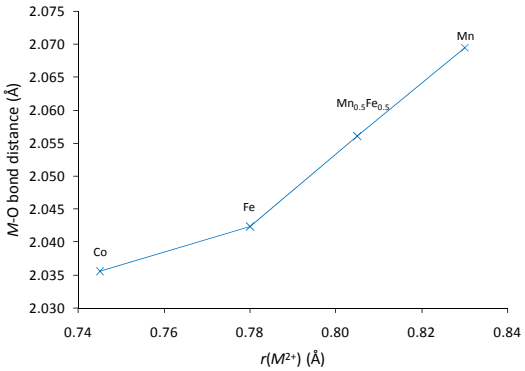

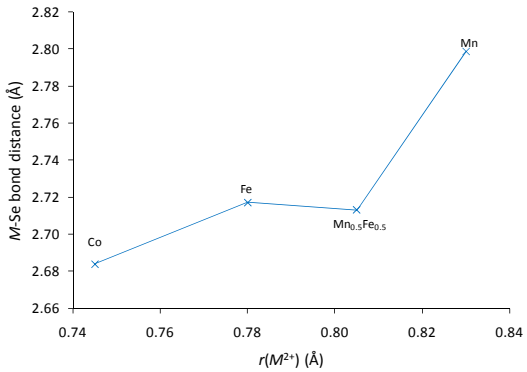

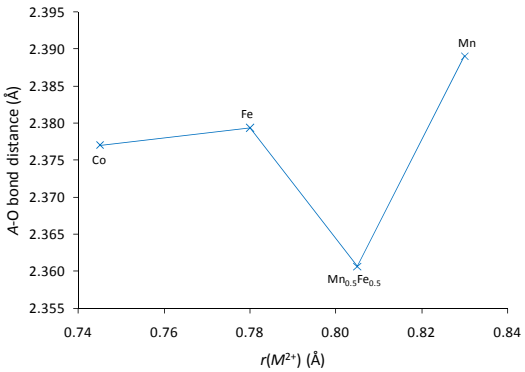

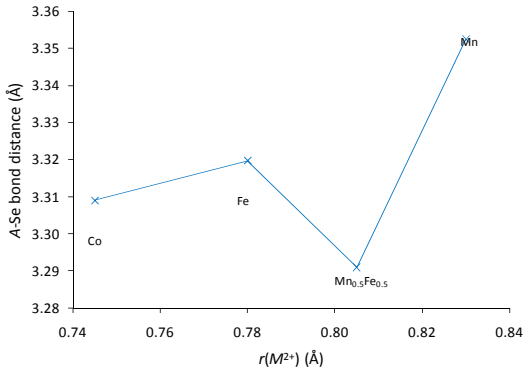

Bond angles – variation of *A*

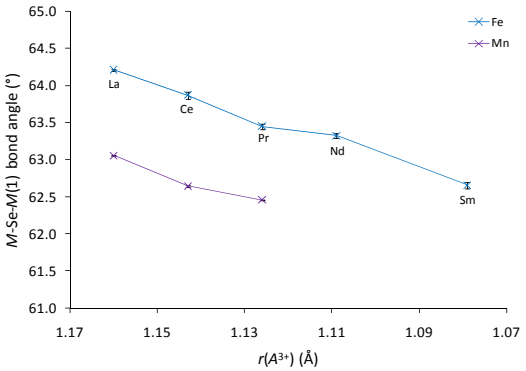

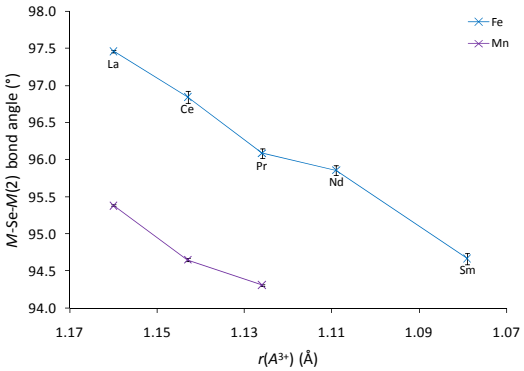

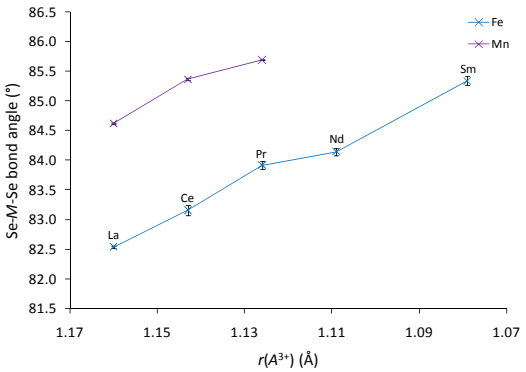

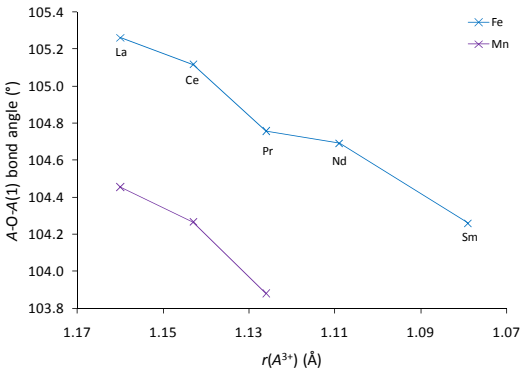

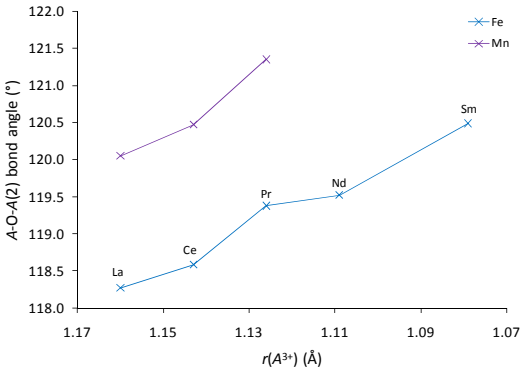

Bond angles – variation of *M*

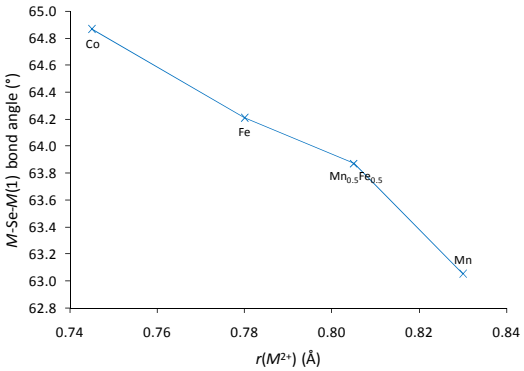

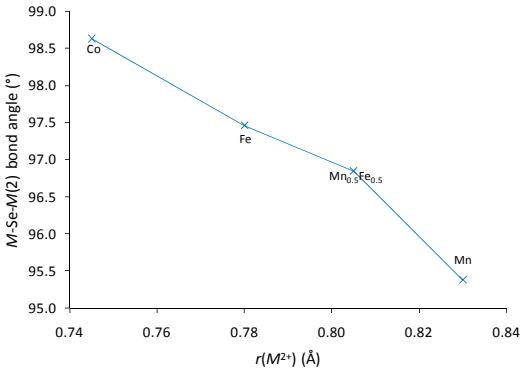

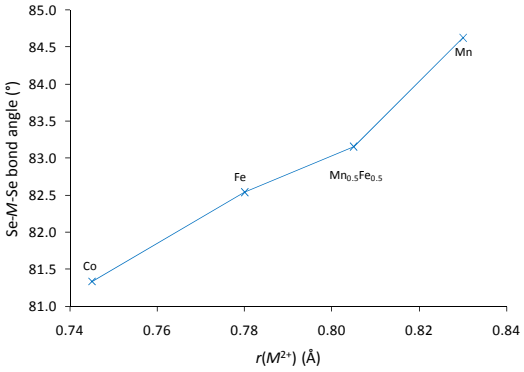

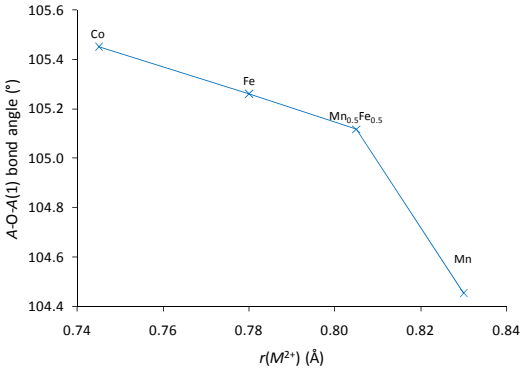

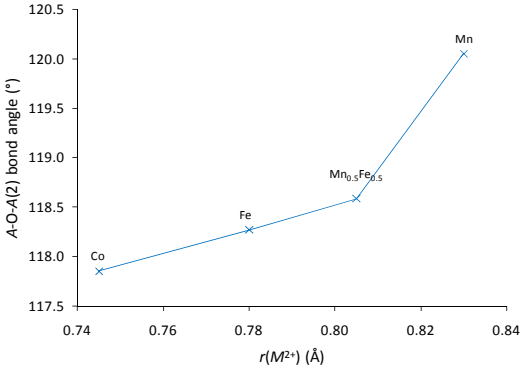

Layer thicknesses and separation – variation of *A*

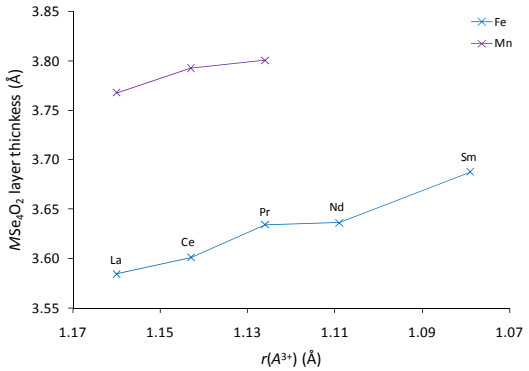

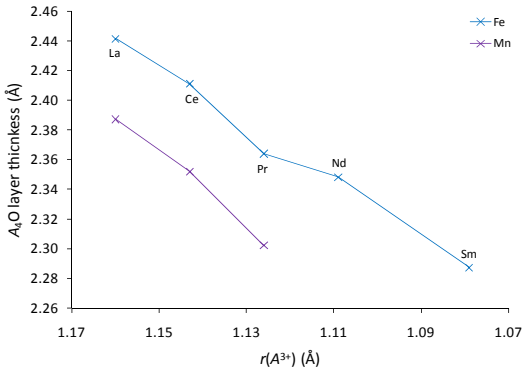

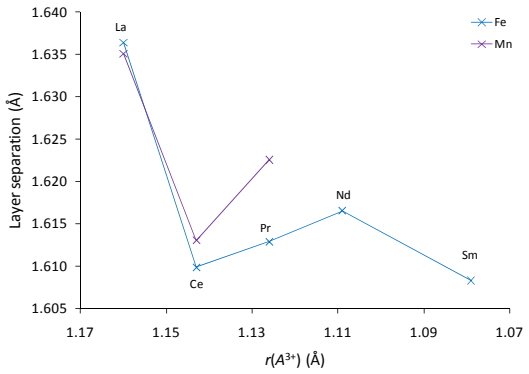

Layer thicknesses and separation – variation of *M*

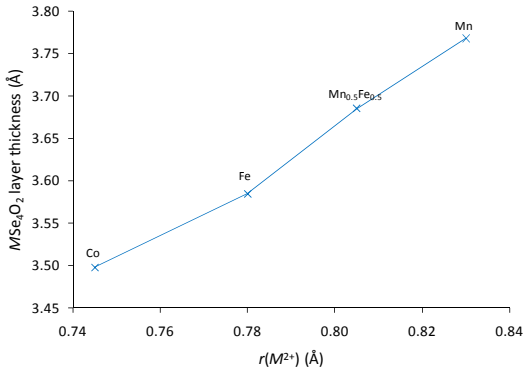

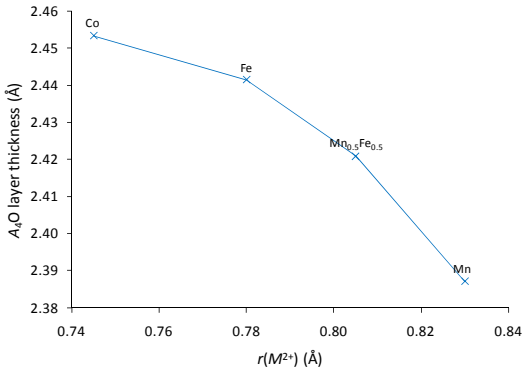

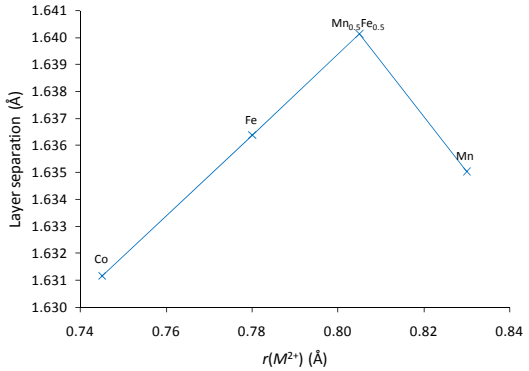

XII. Collation of data and analysis for β-$La_2O_2MnSe_2$

Lattice parameters and refinement statistics from combined X-ray / neutron Rietveld refinement of β-$La_2O_2MnSe_2$ at room temperature.

	300 K
Sample	*DGF242*
Input file(s)	*combined_riet.inp*
Data file(s)	*d9_04152.raw*
	hrp45431_b1_TOF.xye
	hrp45431_b2_TOF.xye
	hrp45431_b3_TOF.xye
Nuclear symmetry	*C*222_1
a (Å)	*16.54582(8)*
b (Å)	*4.00739(2)*
c (Å)	*17.52752(7)*
V (Å^3)	*1162.172(9)*
N°. variables	*125*
X-ray R_{wp} (%)	*4.82*
HRPD bs R_{wp} (%)	*4.42*
HRPD 90° R_{wp} (%)	*2.60*
HRPD 30° R_{wp} (%)	*9.10*
Total R_{wp} (%)	*4.38*
χ^2	*1.36*

Atomic coordinates, occupancies (Occ.) and thermal displacement parameters from combined X-ray / neutron Rietveld refinement of β-$La_2O_2MnSe_2$ at room temperature.

	Wyckoff site	***x***	***y***	***z***	**Occ.**	U_{ij} **(100×Å^2)**		
						U_{11}	U_{22}	U_{33}
La(1)	*8c*	*0.77042(9)*	*0.009(2)*	*0.15947(8)*	*1*	*0.2(1)*	*0.6(1)*	*0.4(1)*
La(2)	*8c*	*0.5751(1)*	*0.501(1)*	*0.16427(8)*	*1*	*0.29(9)*	*0.2(1)*	*0.9(1)*
Mn(1)	*4a*	*0.6383(3)*	*0*	*0*	*1*	*0.2(3)*	*3.4(4)*	*1.6(4)*
Mn(2)	*8c*	*0.9155(4)*	*0.5*	*0.0232(3)*	*0.5*	*0.6(4)*	*1.0(3)*	*2.6(7)*
Se(1)	*4a*	*0.7641(2)*	*0.5*	*0*	*1*	*0.2(2)*	*0.6(2)*	*1.0(2)*
Se(2)	*8c*	*0.9228(2)*	*0.517(3)*	*0.1801(1)*	*1*	*0.8(1)*	*0.2(2)*	*1.8(2)*
Se(3)	*4a*	*0.5080(2)*	*0.5*	*0*	*1*	*0.6(2)*	*0.2(2)*	*0.9(2)*
O(1)	*8c*	*0.6291(3)*	*0.007(5)*	*0.1129(2)*	*1*	*0.4(2)*	*0.5(3)*	*0.3(2)*
O(2)	*8c*	*0.7096(2)*	*0.515(4)*	*0.2053(2)*	*1*	*0.1(2)*	*0.0(3)*	*0.3(2)*

Variable temperature plots for β-$La_2O_2MnSe_2$

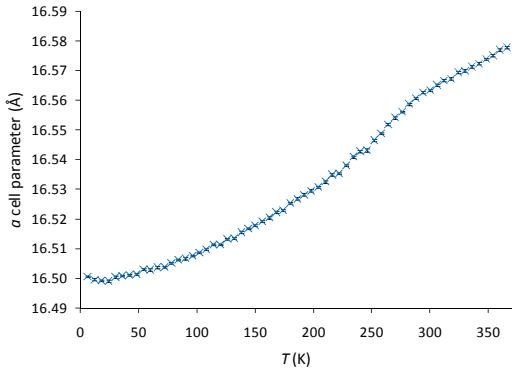

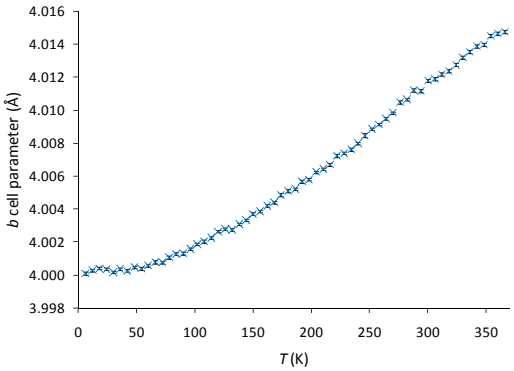

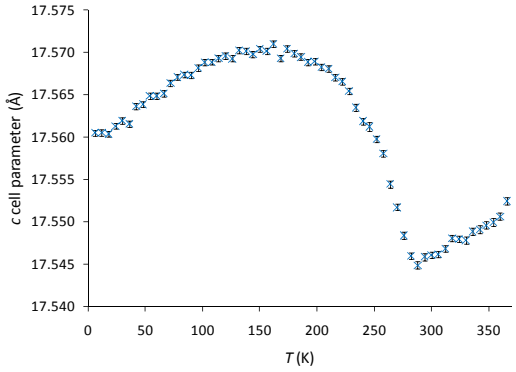

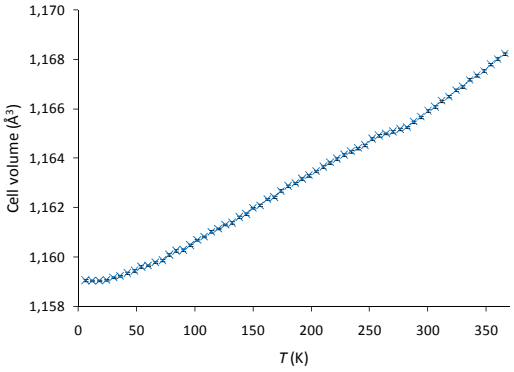

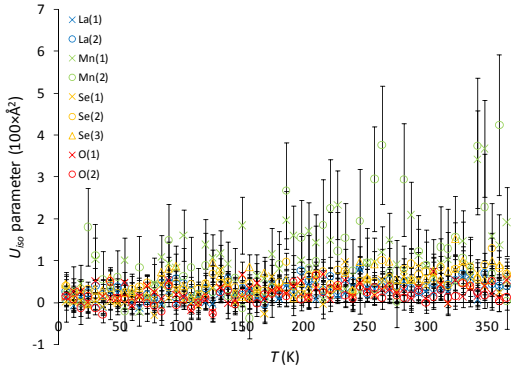

XIII. Collation of data and analysis for $Ce_2O_2FeSe_2$

Published results from combined X-ray / neutron Rietveld refinement of $Ce_2O_2FeSe_2$ at 12 K and room temperature.

	12 K	**300 K**
Sample	*EEM205*	*EEM205*
Nuclear symmetry	*Imcb*	*Imcb*
Magnetic symmetry	*P_c2/c*	-
a (Å)	*5.67984(3)*	*5.70040(3)*
b (Å)	*5.70565(2)*	*5.71946(3)*
c (Å)	*17.2859(2)*	*17.31342(9)*
V (Å^3)	*560.187(7)*	*564.47(3)*
Ce *y* (*c*)	*0.2517(2)*	*0.2517(2)*
Ce *z* (*c*)	*0.31974(2)*	*0.31956(2)*
Se *y* (*c*)	*0.2421(2)*	*0.2419(2)*
Se *z* (*c*)	*0.08266(4)*	*0.08254(3)*
O *z* (*c*)	*0.24806(8)*	*0.2480(1)*
Ce U_{eq} (100×Å^2)	*0.01(3)*	*0.43(5)*
Fe U_{eq} (100×Å^2)	*0.08(2)*	*0.89(5)*
Se U_{eq} (100×Å^2)	*0.14(1)*	*0.87(4)*
O U_{eq} (100×Å^2)	*0.33(3)*	*0.65(5)*
Fe^{2+} M_y (μ_B)	*3.33(3)*	-
Ce^{3+} M_y (μ_B)	*1.12(2)*	-
R_{wp} (%)	*3.54*	*2.71*
χ^2	*5.24*	*4.41*

Note that an example input file for the distortion mode refinements can be found in the e-appendix.

Rietveld plots for $Ce_2O_2Fe_2OSe_2$ at 12 K

a)

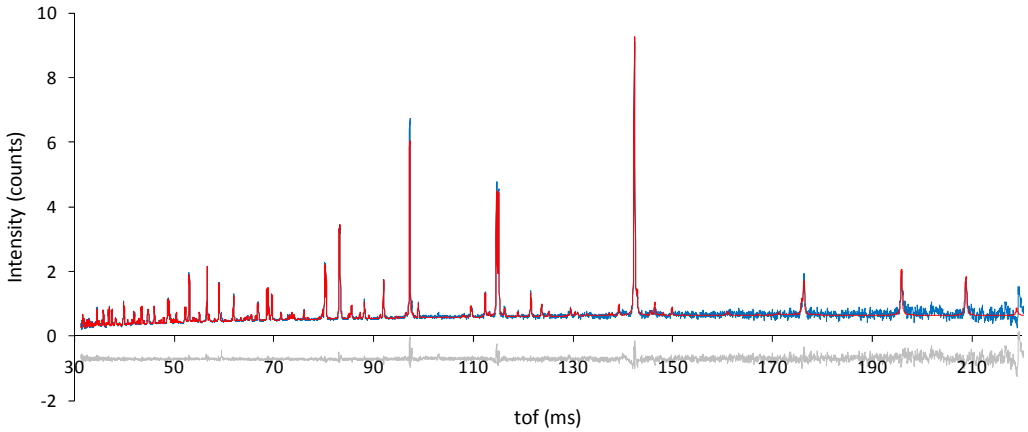

b)

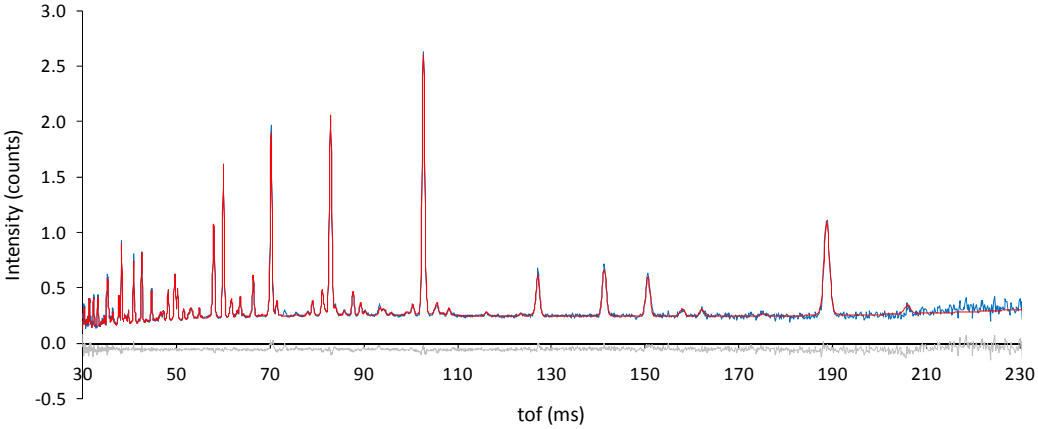

c)

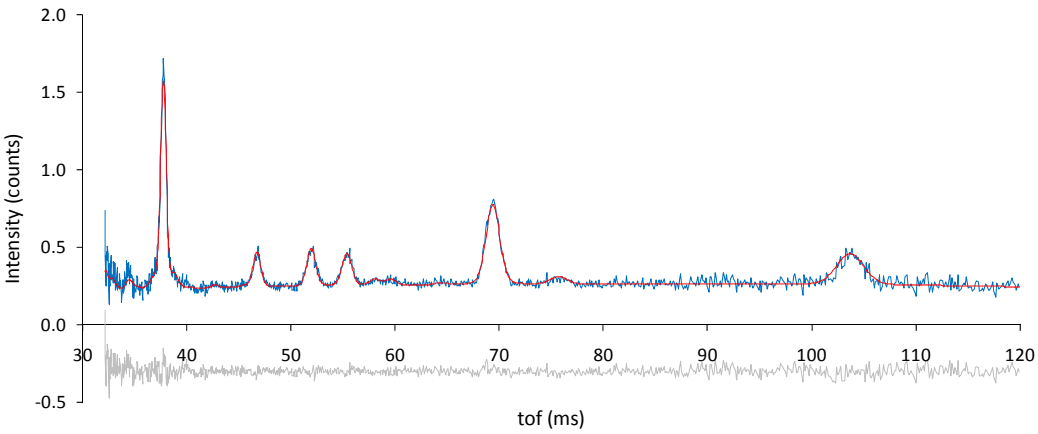

Rietveld plots for $Ce_2O_2FeSe_2$ at 12 K using (a) HRPD bs, (b) 90° and cd) 30° bank data; observed = blue, calculated = red, difference = grey.

SARAh Analysis for $Ce_2O_2FeSe_2$ – mixing of all allowed Fe^{2+} basis vectors

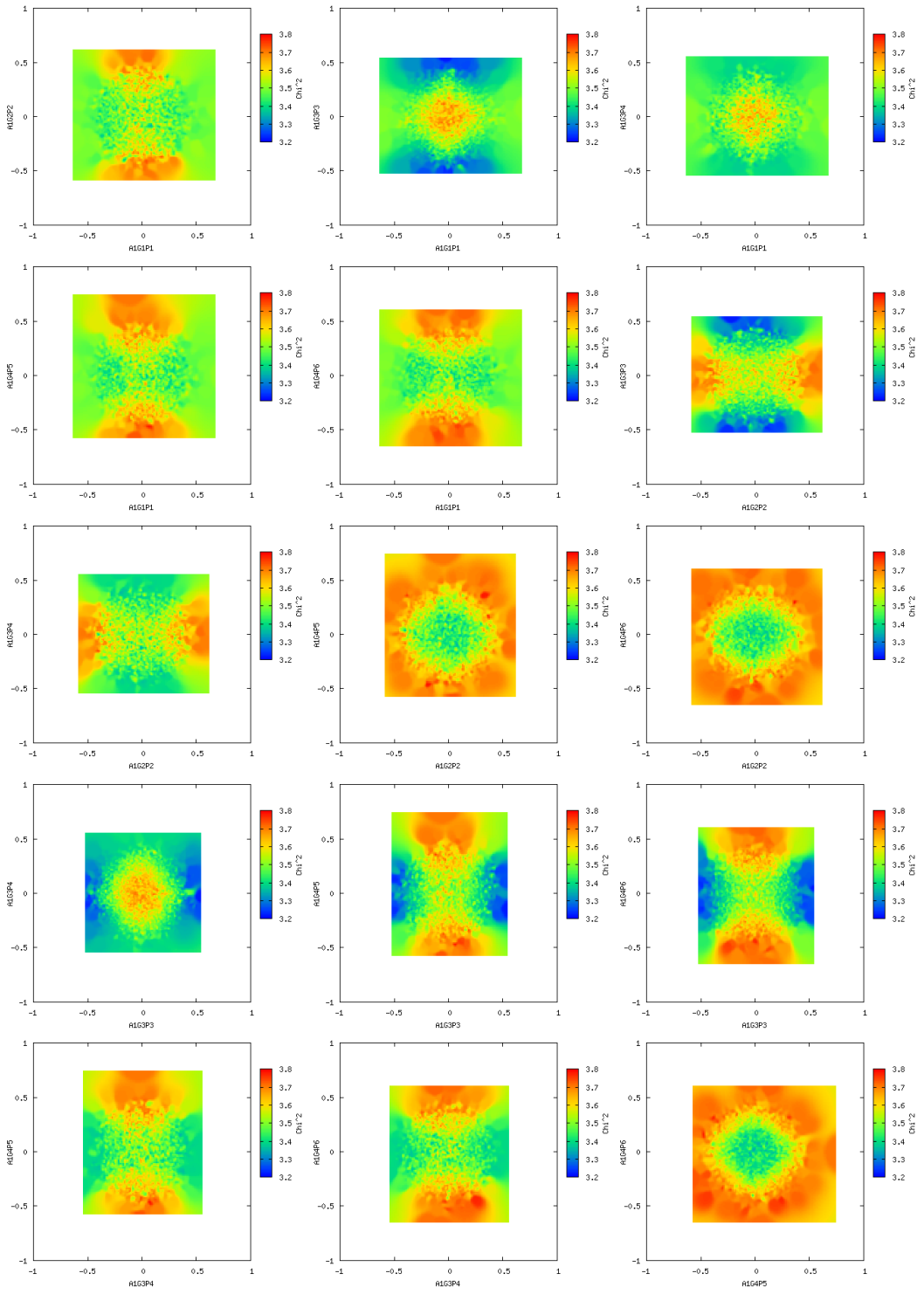

SARAh Analysis for $Ce_2O_2FeSe_2$ – mixing of Fe(1)$\Gamma_3\Psi_3$ with all allowed Ce^{3+} basis vectors

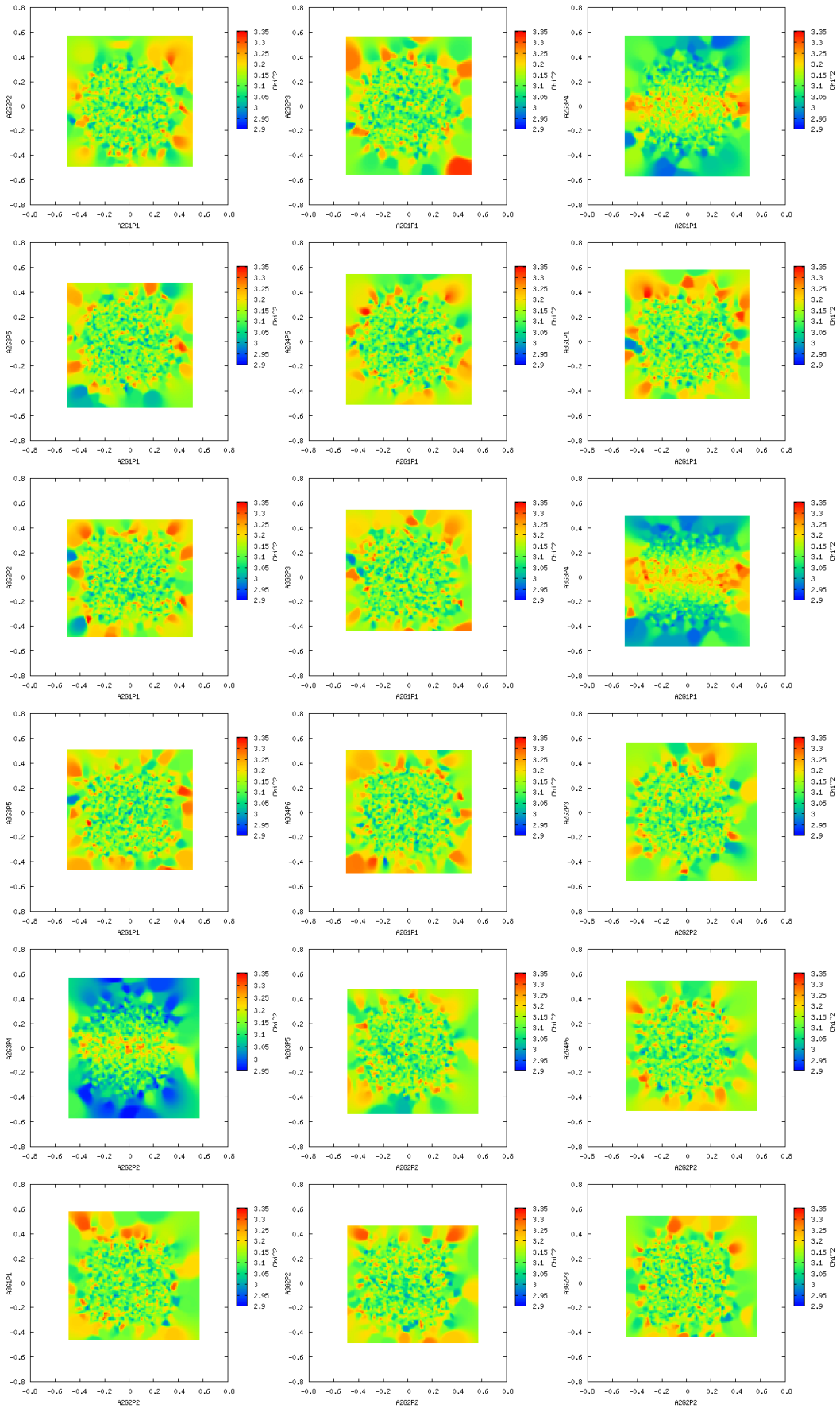

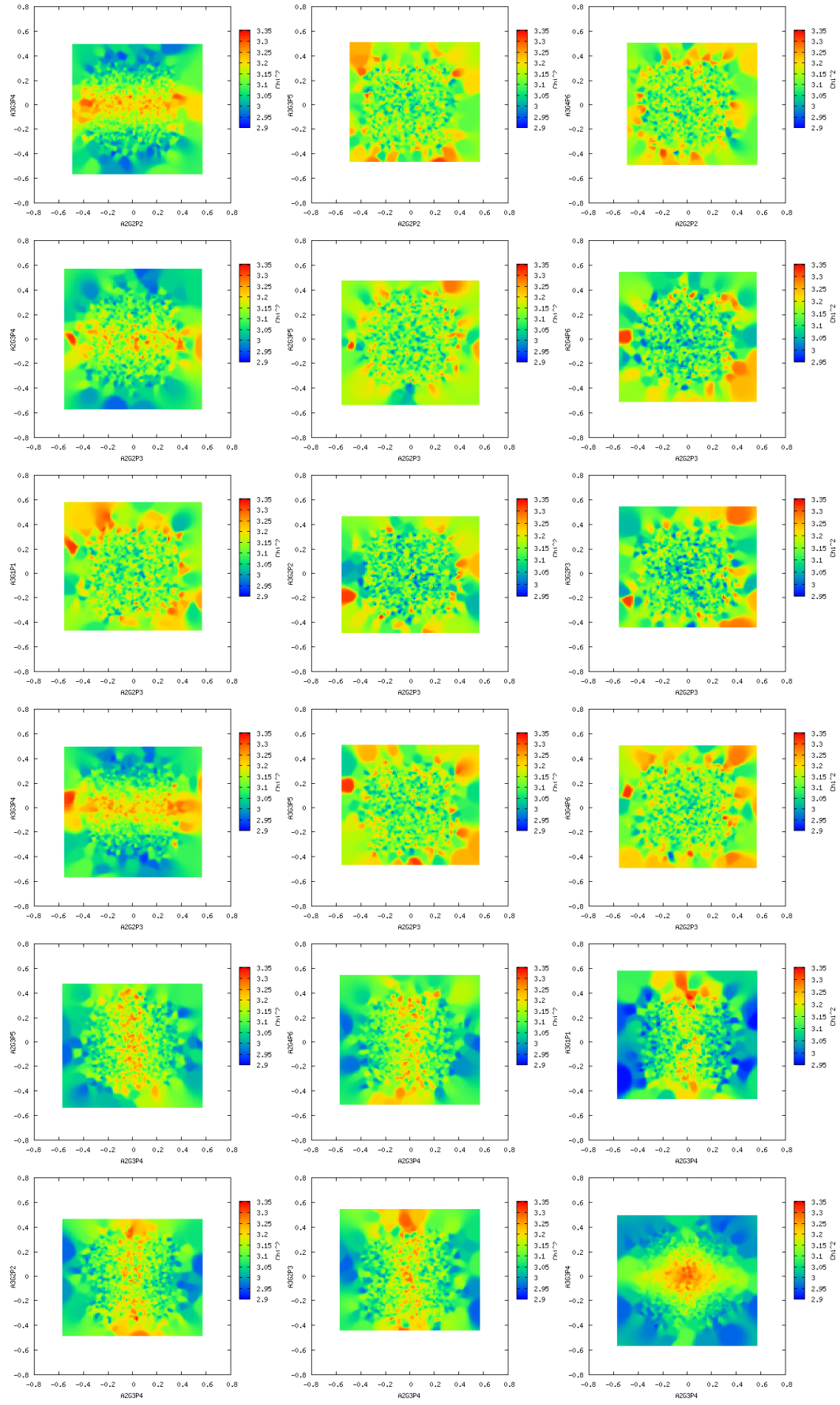

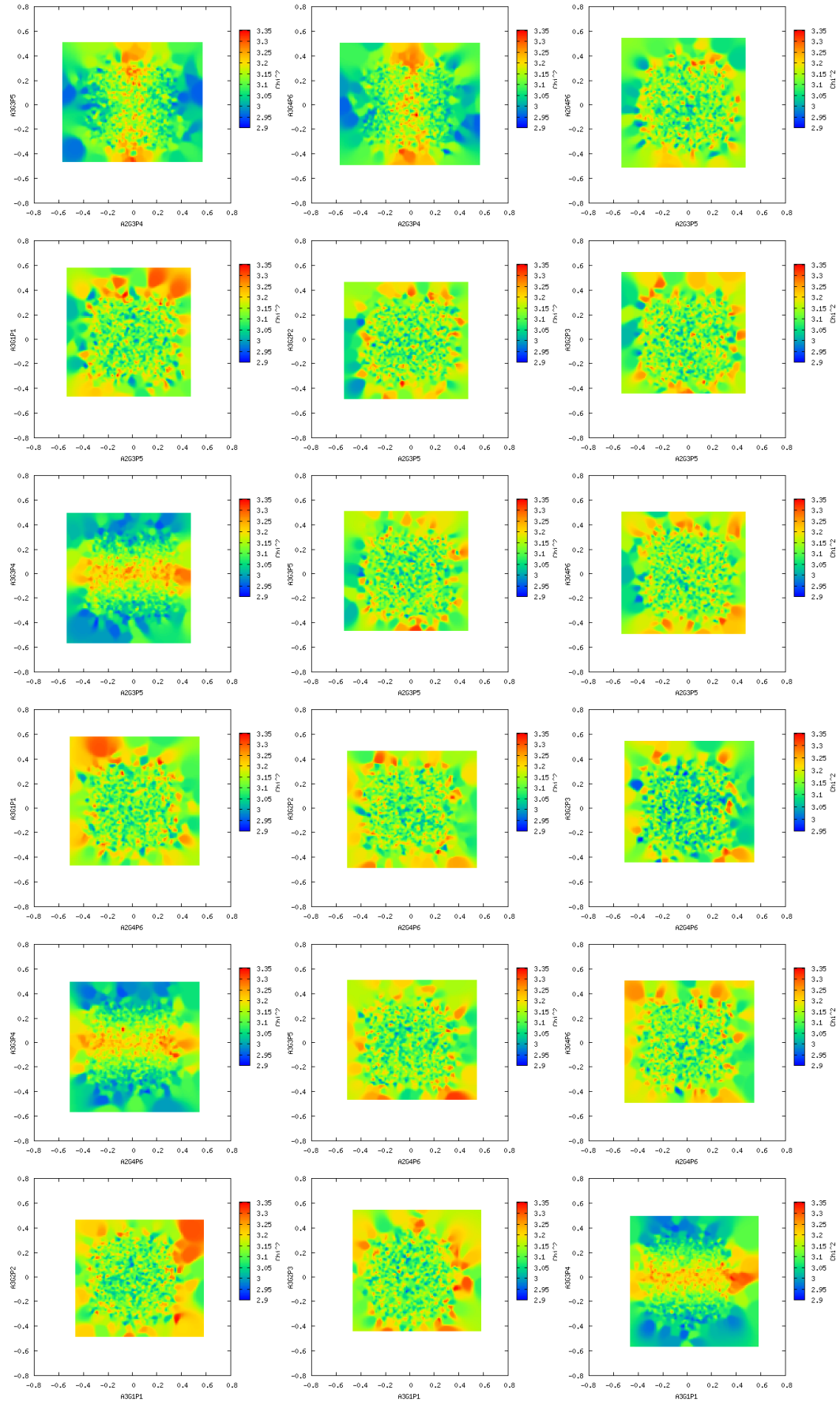

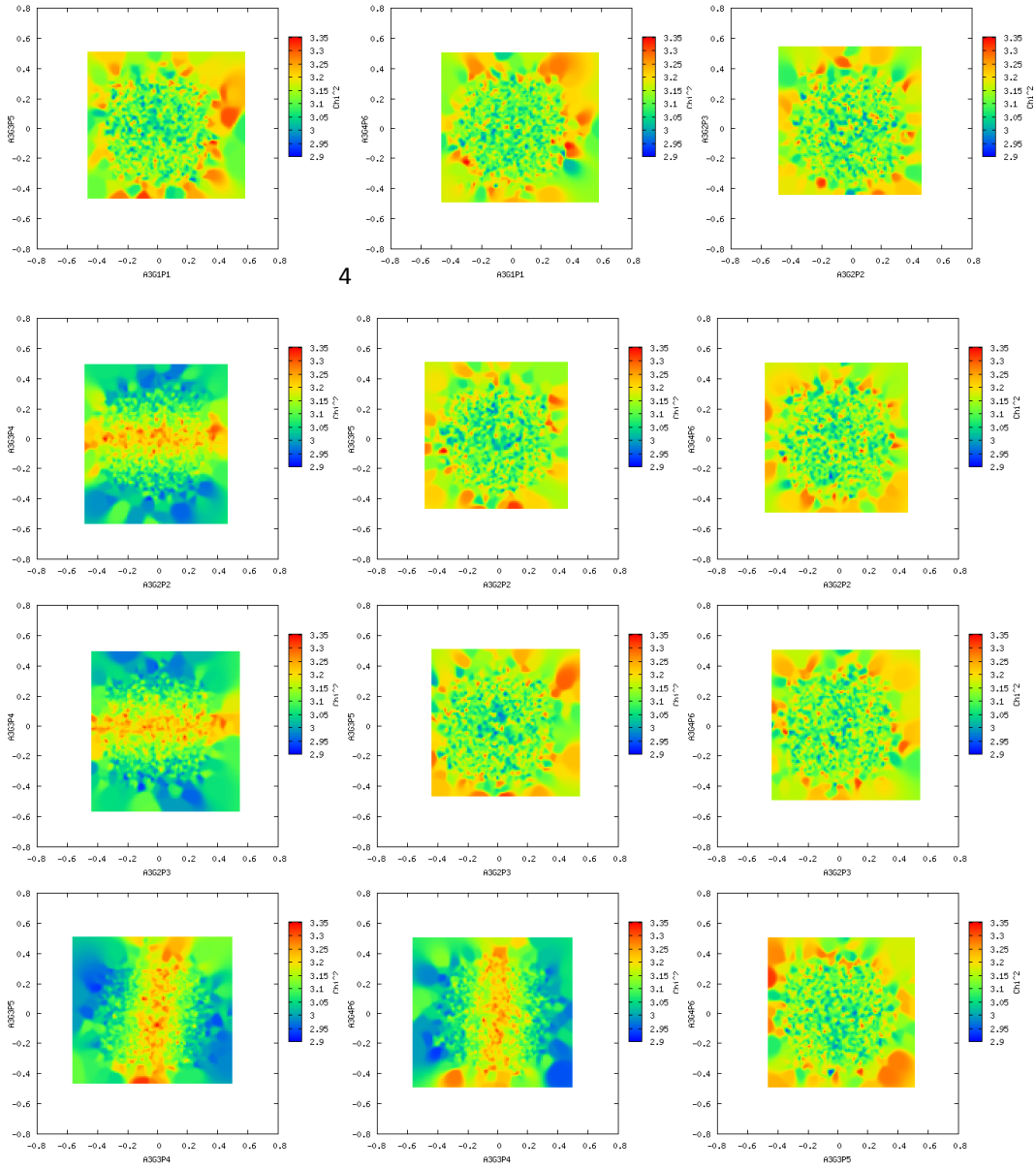
A3G1P1
A3G1P1
A3G2P2
A3G3P4
A3G3P5
A3G4P6
A3G2P2
A3G2P2
A3G2P2
A3G3P4
A3G3P5
A3G4P6
A3G2P3
A3G2P3
A3G2P3
A3G3P5
A3G4P6
A3G3P4
A3G3P4
A3G3P5
Chi^2

4

XIV. Collation of data and analysis for $La_2O_2ZnSe_2$

Results from X-ray Rietveld refinement of $La_2O_2ZnSe_2$ at 12 K and room temperature.

	12 K	**300 K**
Sample	*DGF217*	*DGF217*
Input file(s)	*d9_04436_lt_riet.inp*	*d9_04436_rt_riet.inp*
Data file(s)	*d9_04436.raw* *(range 60)*	*d9_04436.raw* *(range 1)*
Nuclear symmetry	*P4/nmm*	*P4/nmm*
a (Å)	*4.04509(3)*	*4.05267(3)*
c (Å)	*8.8763(1)*	*8.8980(1)*
V (Å^3)	*145.240(3)*	*146.143(3)*
La *z* (*c*)	*0.6392(2)*	*0.6387(2)*
Se *z* (*c*)	*0.1672(3)*	*0.1675(3)*
La U_{iso} (100×Å^2)	*0.00(4)*	*0.41(5)*
Zn U_{iso} (100×Å^2)	*0.3(2)*	*1.1(2)*
Se U_{iso} (100×Å^2)	*0.03(7)*	*0.74(8)*
O U_{iso} (100×Å^2)	*1.8(6)*	*1.3(6)*
N^o. variables	*27*	*27*
R_{wp} (%)	*11.95*	*11.46*
χ^2	*1.76*	*1.67*

Rietveld plots for $La_2O_2ZnSe_2$ at room temperature and 12 K

a)

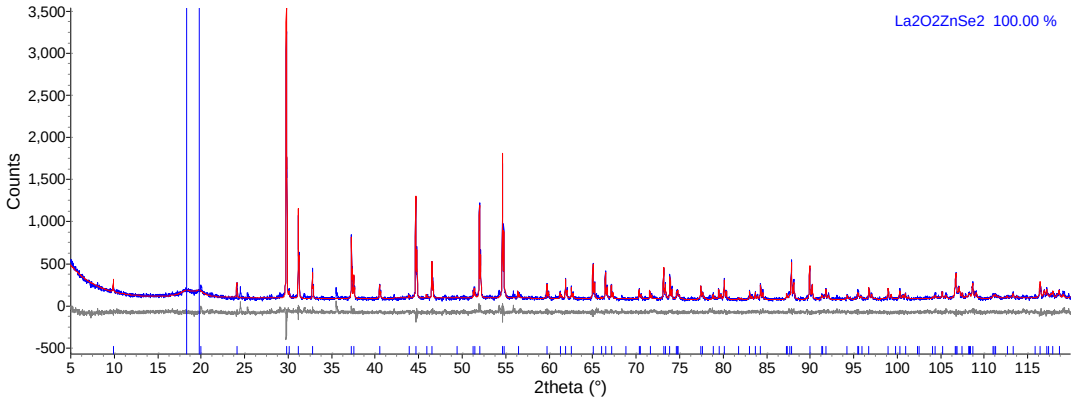

b)

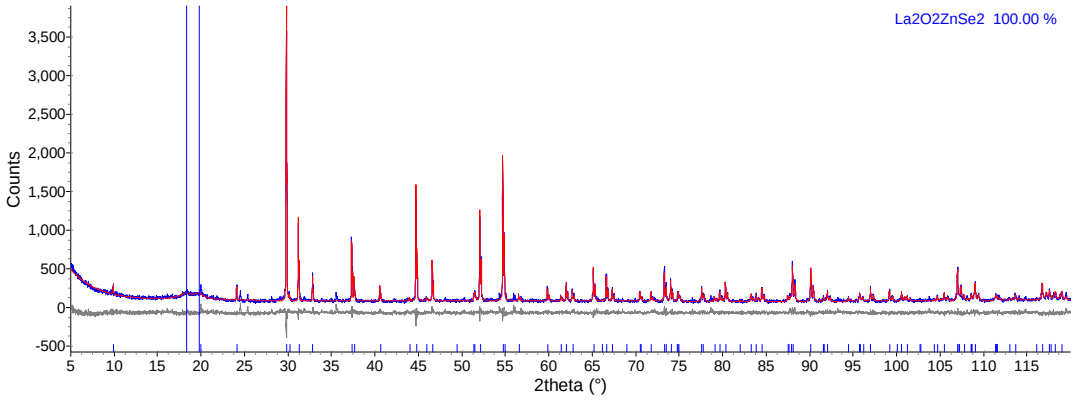

Rietveld plots for $La_2O_2ZnSe_2$ at (a) room temperature and (b) 12 K; observed = blue, calculated = red, difference = grey.

Variable temperature plots for $La_2O_2ZnSe_2$

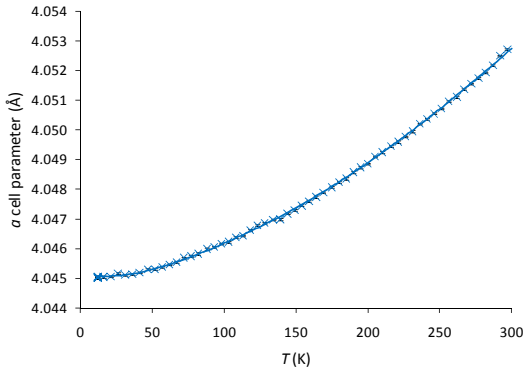

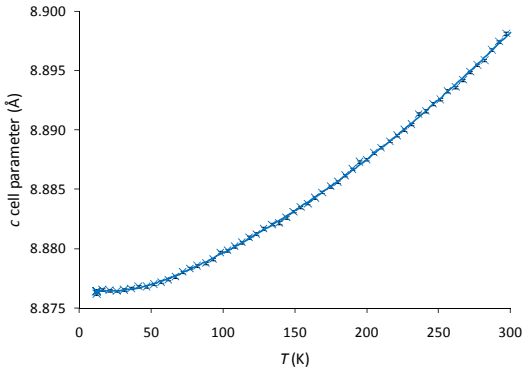

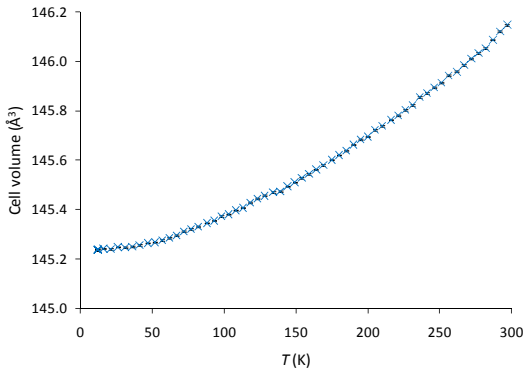

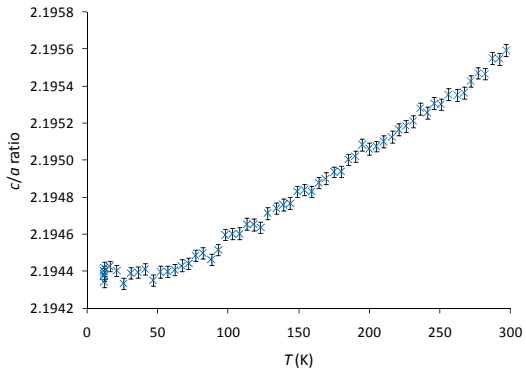

Index to the e-Appendix

A hyperlinked version of this file can be found in the e-Appendix, e-Appendix.htm.